STEREOCOMPLEX POLY (METHYL METHACRYLATE) FIBERS AND SELF-REINFORCED COMPOSITES AND STRUCTURAL COLOR OF BUTTERFLIES AND BEETLES – CHARACTERIZATION, REPLICATION AND MIMICRY

A Dissertation
Presented to
The Academic Faculty

by

Matija Črne

In Partial Fulfillment
of the Requirements for the Degree
Doctor of Philosophy in Polymer Chemistry in the
School of Chemistry and Biochemistry

Georgia Institute of Technology
August 2009

STEREOCOMPLEX POLY (METHYL METHACRYLATE) FIBERS AND SELF-REINFORCED COMPOSITES AND STRUCTURAL COLOR OF BUTTERFLIES AND BEETLES – CHARACTERIZATION, REPLICATION AND MIMICRY

Approved by:

Dr. Mohan Srinivasarao, Advisor
School of Polymer, Textile and Fiber Engineering
Georgia Institute of Technology

Dr. David Collard
School of Chemistry and Biochemistry
Georgia Institute of Technology

Dr. Anselm Griffin
School of Polymer, Textile and Fiber Engineering
Georgia Institute of Technology

Dr. Jung Ok Park
School of Polymer, Textile and Fiber Engineering
Georgia Institute of Technology

Dr. Laren Tolbert
School of Chemistry and Biochemistry
Georgia Institute of Technology

Date Approved: May, 1st 2009

Science is practical in the highest sense of the word.

If the assignment consists of reaching a given aim, then it is sometimes easier to *circumvent* prevailing difficulties rather than to *attack* them; since the former is frequently possible when the latter exceeds our energy. Yet, we would be compelled to confine ourselves to direct confrontation if there were no connection between that which is occurring and that which will take place.

This connection is real; in its over-all effect it is termed the relation between cause and effect. It is the task of Science to elucidate this connection in all its details.

Jacobus Henricus van't Hoff, "Imagination in Science"

Not all those who wander are lost.

J.R.R. Tolkien, "The Lord of the Rings"

To my wonderful family, father Slavko, mother Cirila and sister Alenka.

PREFACE

This thesis is composed of two parts. Part A deals with the production, structure and properties of stereocomplex poly (methyl methacrylate) (PMMA) fibers and self-reinforced composites. Part B deals with the structural color of butterflies and beetles, its characterization, replication and mimicry.

The work described in Part A was done in collaboration with prof. Dr. Satyendra Kumar's research group from Kent State University. Dr. Shin-woong Kang in prof Kumar's research group performed the X-ray measurements at the Advanced Photon Source in Argonne, Ill. We also collaborated on mechanical characterization of electrospun stereocomplex PMMA fibers with prof. Dr. Larry Bottomley's group. Mr. Kane Barker performed atomic force microscopy experiments.

Part A is further divided into chapters. In Chapter 1 an introduction to the stereocomplex PMMA is given with some emphasis on the basic structure, properties in solution and mechanical properties. A brief introduction to self-reinforced composites is also given.

In Chapter 2 we describe our efforts toward producing oriented stereocomplex PMMA fibers by wet spinning. The mechanical properties, crystallization and thermal stability are discussed.

In Chapter 3 we describe gel spinning as a method for production of oriented stereocomplex PMMA fibers. Again, mechanical properties and thermal stability are emphasized. In addition, we discuss the gelation properties and the basic structure of the stereocomplex PMMA. In Chapter 4 we describe the electrospinning method of

stereocomplex fiber production. The influence of gelation is discussed, along with the differences from the atactic PMMA polymer solutions.

In Chapter 5 we describe the production of self-reinforced composites based on stereocomplex PMMA fibers. The fiber stability towards temperature and solvent plays an important role in composite preparation and properties.

Through the study of polymers and composites I had become involved particularly with the optical methods of characterizing them. In our laboratory we had some specimens of butterflies and beetles and we were interested in the structures that give rise to their brilliant colors. It turns out that chitin is a composite of a poly (N-glucosamide) and various proteins and that orientation and nanostructure have an important role in structural color features[1]. As polymer and material chemists we were particularly interested in replicating or artificially making these structures. However, we must first be able to characterize them. In order to characterize the structural color, we present here first in Chapter 6 a brief survey of the structural color features.

In Chapter 7 we describe a simple, yet powerful microscopy method of characterizing the structural color features of microscopic objects. This characterization technique was used throughout the rest of the work in the area of replication, characterization and mimicry of the naturally occurring sctructural color features.

In Chapter 8 we describe the effort towards making rutile titania replicas of the brilliant blue scales of *Morpho rhetenor*. This work was done in collaboration with Dr. Michael Weatherspoon and Dr. Yunnan Fang in prof. Dr. Kenneth Sandhage research group. The sol-gel coating work was done by Dr. Weatherspoon for the brown scales and

Dr. Fang for the blue scales. We were able to replicate the brown and blue scales of *Morpho rhetenor* in rutile titania.

In Chapter 9 we describe the characterization of structural color features on the surface of the jewel beetle *Chrysina gloriosa.* Dr. Vivek Sharma helped out with the Voronoi analysis of the pattern formation and helpful discussions on the optical properties of the cholesteric liquid crystals. Dr. Jung Ok Park assisted us with the confocal microscopy. We were able to identify the focal conic defects on the free surface of a cholesteric phase as responsible for the color of the beetle *Chrysina gloriosa*.

In Chapter 10 we describe our efforts in building the structural color features of the butterfly *Papilio palinurus* from the bottom-up. The work was done in collaboration with John Blair from prof. Dr. Christopher Summers research group, who preformed the atomic layer deposition coating. Dr. Vivek Sharma assisted with the initial multilayer calculations and breath figure templated self-assembly and Dr. Jung Ok Park with the confocal microscopy and breath figure templated self-assembly. We were able mimic the optical effects seen on the butterfly *Papilio palinurus*.

ACKNOWLEDGEMENTS

I wish to thank my parents, Slavko and Cirila Črne, without whose love and devotion I would not have had the opportunity to develop into a scientist. I also would like to thank my family in the United States of America, uncle Stan Jakopin and aunt Jerica Jakopin who provide me with a home away from home on another continent. My sister Alenka has always been there for me and I would like to thank her also. My wonderful friends Dr. Igor Vilfan and Dr. Vivek Sharma have been a tremendous help during my PhD. We discussed science, partied and endured together. Dr. Ralph Mueller, David Leung, Dr. Linda Manning, Peter Boozeroij and Dr. Robert Kriegel were also happily involved.

I would like to thank my collaborators, Dr. Shin-woong Kang, Dr. Satyendra Kumar, Dr. Michael Weatherspoon, Dr. Yunnan Fang, Dr. Kenneth Sndhage, John Blair, Dr. Christopher Summers, Kane Barker and Dr. Larry Bottomley for all their help and patience.

Our group members Dr. Jong Seung Park, Dr. Kyoungweon Park, Min Sang Park, Beom-jin Yoon, Xuxia Yao and Minsu Lee were the most pleasant people to work with. I am grateful to Dr. Han Gi Chae and countless other people who helped with some instrument access or in any other way. .

Finally, I wish to thank my mentors, Dr. Mohan Srinivasarao and Dr. Jung Ok Park for reigniting my passion for science and sharing not only their technical knowledge, but also their lifetime scientific experience with me.

TABLE OF CONTENTS

Page

ACKNOWLEDGEMENTS viii

LIST OF TABLES xiii

LIST OF FIGURES xiv

LIST OF SYMBOLS AND ABBREVIATIONS xx

SUMMARY xxi

CHAPTER

PART A : STEREOCOMPLEX POLY (METHYL METHACRYLATE) FIBERS AND SELF-REINFORCED COMPOSITES

1 INTRODUCTION TO PMMA STEREOCOMPLEX AND SELF-REINFORCED COMPOSITES 1

1.1. Definition and Basic Structure of Stereocomplex 1

1.2. PMMA Stereocomplex properties 4

1.2.1. PMMA Stereocomplex Dilute Solutions 4

1.2.2. PMMA Stereocomplex Gels 7

1.2.3. PMMA Stereocomplex Crystallization 9

1.2.4. PMMA Stereocomplex Mechanical Properties 10

1.2.5. Stereocomplex PMMA Chirality 11

1.3. Self-reinforced Composites 12

2 PMMA STEREOCOMPLEX FIBERS *via* WET SPINNING 14

2.1. Introduction to wet spinning 14

2.2. Experimental 14

2.3. Results 16

2.3. Discussion 28

2.3. Conclusions 35

3 PMMA STEREOCOMPLEX FIBERS *via* GEL SPINNING 36

3.1. Introduction to Gel Spinning 36

3.2. Experimental 38

3.3. Results and Discussion 39

3.4. Conclusions 54

4 ELECTROSPINNING STEREOCOMPLEX SOLUTIONS, WHICH FORM PHYSICAL GELS 56

4.1. Introduction 56

4.2. Results 58

4.3. Discussion 64

4.4. Conclusions 67

5 SELF-REINFORCED COMPOSITE BASED ON STEREOCOMPLEX PMMA FIBERS 69

5.1. Introduction 69

5.2. Experimental 70

5.3. Results 73

5.4. Discussion 78

5.5. Conclusions 82

REFERENCES PART A 83

PART B : STRUCTURAL COLOR OF BUTTERFLIES AND BEETLES – CHARACTERIZATION, REPLICATION AND MIMICRY 97

6 INTRODUCTION TO STRUCTURAL COLOR OF BUTTERFLIES AND BEETLES 98

6.1. Structural Color 98

6.2. Thin Film 99

6.3. Multilayer 101

6.4. Diffraction Grating 103

6.5. Photonic Crystal 105

6.5.1. 1D Phoonic Crystal 106

6.5.2. 2D Photonic Crystal 106

6.5.3. 3D Photonic Crystal 108

6.6. Cholesteric Liquid Crystal 111

6.7. Combinations 114

6.8. Replication and Mimicry 115

7 MICROSCOPY METHOD FOR THE CHARACTERIZATION OF STRUCTURAL COLOR ON A SINGLE SCALE 118

7.1. Introduction 118

7.2. Experimental 124

7.3. Results 125

7.4. Discussion 134

7.5. Conclusions 136

8 MODIFICATION AND REPLICATION OF THE STRUCTURAL COLOR FEATURES OF THE BUTTERFLY *Morpho rhetenor* 138

8.1. Structural Color on the Wings of *Morpho rhetenor* 138

8.2. Methods Used for Replication and Characterization 140

8.3. Coating Results 122

8.4. Discussion of *Morpho rhetenor* replication 145

8.5. *Morpho rhetenor* replication - Conclusions 145

9 IDENTIFICATION OF STRUCTURES RESPONSIBLE FOR THE COLOR OF AN IRIDESCENT BEETLE *Chrysina (Plusiotis) gloriosa* 148

9.1. Introduction 148

9.2. Results 149

9.3. Discussion 163

9.4. Conclusions 170

10 MIMICRY OF THE STRUCTURAL COLOR FEATURES OF THE BUTTERFLY *Papilio palinurus* BY BOTTOM-UP SELF-ASSEMBLY 171

10.1. Structural Color on the Wings of *Papilio palinurus* 171

10.2. Self-assembly Methods for Mimicry of the Structural Color features of *Papilio palinurus* 175

10.2.1. Breath figure templated assembly 176

10.2.2. Multilayer Reflectance Simulation 177

10.2.3. Atomic Layer Deposition (ALD) 180

10.3. Characterization of the Artificial Structures 181

10.4. Conclusions 188

REFERENCES PART B 190

LIST OF TABLES

Page

Table 1.1: Classification of the solvents according to complexation strength 5

Table 2.1: Summary of experiments optimizing wet-spinning conditions. 19

Table 4.1: The melting temperatures of the electrospun stereocomplex fibers from the DSC traces in Figure 4.6 and the corresponding oil bath temperatures. 63

Table 4.2: The critical overlap concentration C* and intrinsic viscosity [η] in DMF 65

LIST OF FIGURES

Page

Figure 1.1: (A) Schematic model of an organized junction composed of the merging of three fibrils (helices) and (B) the mechanism of a proto-junction transformation into an effective junction upon gel swelling. Both figures taken from Guenet 8

Figure 2.1: Wet-spinning apparatus. The polymer solution is in the syringe. The solution is slowly injected directly into a coagulation bath. The syringe needle is dipped nto the coagulation bath. The fiber formed is wound up. 16

Figure 2.2: DSC analysis of the wet-spun stereocomplex fibers before and after annealing at 140°C for varying length of annealing time. All the curves shown were obtained on the first heating run at 20ºC/min. 20

Figure 2.3: Crystallization kinetics of wet-spun stereocomplex PMMA fibers. The enthalpy of melting of the peak at 172°C is plotted against time. Stereocomplex fibers were spun at different pick-up ratios (4 m/min for SC fiber-1 and 11.9 m/min for SC fiber-2). All samples were annealed at 140ºC. 20

Figure 2.4: X-ray diffractogram of the annealed stereocomplex fiber. Broad Peaks at angles correspond to the spacings: 22.0, 7.8, 6.4, (~4.5), and 3.0 (Å). 22

Figure 2.5: SEM images of the wet-spun stereocomplex PMMA fiber at different magnifications. There are plenty of microcrystallites on the surface. Scale bars in left and right image represent 10 μm and 1 μm, respectively. 23

Figure 2.6: Optical micrographs of the atactic melt-spun fiber (left) and stereocomplex wet-spun fiber (right). We can see that the surface of the stereocomplex fiber is rougher than the atactic PMMA fiber. 23

Figure 2.7: The DSC curves for the thermal annealing of atactic, syndiotactic and isotactic PMMA fibers acquired by the same experimental conditions of wet spinning as the stereocomplex fibers. Only isotactic PMMA fibers show a small endothermic peak. 25

Figure 2.8: Mechanical testing of wet-spun PMMA stereocomplex fibers. Each color represents a single filament test sample. 26

Figure 2.9: Heating the wet-spun stereocomplex fibers at 5ºC/min. […] 27

Figure 3.1: Illustration of three different concentration regimes and the influence on fiber formation. […] 38

Figure 3.2: X-ray powder diffractogram of stereocomplex PMMA obtained by evaporating a DMF solution. Sharp peaks indicate orientational order of lattice. Peaks correspond to the spacings of 21.9, 7.9, 6.2, 5.6, 4.5, and 3.0 (Å). 40

Figure 3.3: X-ray powder diffractogram of stereocomplex PMMA obtained from evaporating an acetone solution. Sharp peaks indicate orientational order of lattice. Peaks correspond to the spacings of 21.9, 7.9, 6.2, 5.6, 4.5, and 3.0 (Å). 40

Figure 3.4: Gel-spinning apparatus. […] 41

Figure 3.5: A 3D reconstruction (left) of the stretched gel-spun fiber from a series of confocal microscopy images in xy planes (right) in false colors. Z-axis direction is the fiber axis direction. 43

Figure 3.6: The results of mechanical testing of gel-spun stereocomplex PMMA fibers. Each color represents the results of a tensile test. The average modulus is 2.5 GPa. 46

Figure 3.7: X-ray diffractogram in 2D (left) and 3D (right) of a gel-spun stereocomplex PMMA fiber. The fiber axis is denoted by the double-headed arrow. 47

Figure 3.8: The full range X-ray diffractogram of the gel-spun stereocomplex PMMA fiber. The fiber axis is denoted by the double-headed arrow. 47

Figure 3.9: The intensity vs. 2θ angle plots for the diffractogram from Figure 3.8.[…] 49

Figure 3.10: : The full range X-ray diffractogram of a melt-spun atactic PMMA fiber. The double-heade arrow denotes the fiber direction. 50

Figure 3.11: The DSC analysis of gel-spun fibers made from a 20% DMF […] 51

Figure 3.12: images of the gel-spun fiber at different magnifications. […] 52

Figure 3.13: Results from drawing the isotactic : atactic PMMA stereocomplex gel-spun fiber. […] 53

Figure 4.1: A schematic diagram of the electrospinning apparatus. […] 58

Figure 4.2: Gelation temperature at different concentration of 1:2 iso:syn-PMMA solutions in DMF. […] 59

Figure 4.3: The effect of temperature and concentration of the spinning solution on the morphology of the electrospun stereocomplex PMMA. […] 60

Figure 4.4: The results of fiber diameter measurements of electrospun fibers. Scale bars indicate one standard deviation. […] 61

Figure 4.5: The melting enthalpy of electrospun fibers at various spinning temperatures. […] 62

Figure 4.6: Representative DSC traces for 7.5 wt% stereocomplex solution in DMF. […] 63

Figure 4.7: X-ray diffractogram of electrospun stereocomplex fibers. 64

Figure 4.8: The summary of the process occurring during electrospinning. […] 67

Figure 5.1: (A, B) Self-reinforced PMMA composites with stereocomplex PMMA fibers and a-PMMA by hot compaction after 15min in heat press at 3bar and 160ºC. 74

Figure 5.2: SEM images of the fracture surface from Figure 5.1C and 5.1D. […] 75

Figure 5.3: Temperature measurement during MMA polymerization.[…] 76

Figure 5.4: Atactic PMMA fiber (left fiber) and stereocomplex PMMA fiber (right fiber) under crossed polarizers under the bone cement setting conditions.[…] 77

Figure 6.1: Schematic diagram for thin film interference. […] 100

Figure 6.2: The silvery butterfly *A. argenteus:*.[…] 101

Figure 6.3: Schematic of a multilayer stack 102

Figure 6.4: Micrographs of the butterfly *Papilio palinurus:*[…] 103

Figure 6.5: Schematic of a reflective diffraction grating 104

Figure 6.6: A) SEM of diffraction grating on *Sphaeridiinae gen. sp.,* scale bar 20μm and (B) habitus view of the same specimen[…] 105

Figure 6.7: Schematic of a 2D photonic crystal. […] 107

Figure 6.8: (A) 2D arrangement of inverse cylinders in the butterfly *Papilio nireus,* scale bar 1.4 μm and (B) the same cylinders in SEM, tilted view, scale bar 1μm. 108

Figure 6.9: The three different cubic packing systems and the corresponding skeleton modes […] 110

Figure 6.10: The structure of cholesteric liquid crystals.[…] 113

Figure 7.1: The variables in BRDF. […] 120

Figure 7.2: The conjugate planes in a reflected light microscope. […] 122

Figure 7.3: The aluminum mirror in inverse space under normal incidence […] 124

Figure 7.4: The scattering pattern of *M. rhetenor* (A) and *P. palinurus* (B) 127

Figure 7.5: Diffraction images in transmission for *Morpho rhetenor* (left) and *Papilio palinurus* (right). […] 128

Figure 7.6: The illumination path ray diagrams for incoming light (red) and reflected light (yellow) from a mirror and the resulting image in inverse space. […] 130

Figure 7.7: Examination of a single scale of *Morpho rhetenor*. […] 130

Figure 7.8: *Papilio palinurus* single scale examined with light beam incoming from the left side of the image at $\phi_i = 30^o$. […] 131

Figure 7.9: 3D reconstruction of laser scanning confocal images of a scale of *Papilio palinurus*. […] 132

Figure 7.10: The butterfly *Doxocopa seraphina* and the corresponding microscope inverse space images. 133

Figure 8.1: TEM image of the tree-like structures responsible for the blue reflection of *Morpho rhetenor*. Scale bar 800nm. Adopted from Vukusic *et al.* 139

Figure 8.2: The scheme of the replication process. […] 141

Figure 8.3: Reflectance spectra of coated *Morpho rhetenor* with different number of sol-gel coatings and the rutile replica after the chitin was removed. 142

Figure 8.4: The real space (left) and inverse space (or Q-space, right) images of the *Morpho rhetenor* scale replicated with rutile titania. 143

Figure 8.5: Raman spectrum of the *Morpho rhetenor* replicated scale. 144

Figure 8.6: The calculated reflectance spectra. […] 145

Figure 9.1: The beetle *Chrysina gloriosa* viewed through a left handed circular polarizer and right handed circular polarizer, as indicated by the symbols. 148

Figure 9.2: *Chrysina gloriosa* under microscope with open aperture (column A), with closed aperture (B) and with dark field illumination (C). 150

Figure 9.3: Open aperture stop microspectrophotometric investigation. […] 151

Figure 9.4: Normal incidence narrow incident beam (closed aperture) microspectrophotometric investigation. […] 152

Figure 9.5: Dark field microspectroscopic investigation. The black squares indicate the sampled area. […] 153

Figure 9.6: Narrow incident beam (closed aperture) microspectrophotometric investigation at 25º angle of incidence. […] 154

Figure 9.7: Inverse space image (A) and real image indicating the illuminated area (B) under normal incidence. The bright white spot in the middle of the inverse space picture is the incident beam. 155

Figure 9.8: : Inverse space image under crossed polarizers, with the directions indicated by the arrows. The original image (XPOL) was split into three components: blue, green and red. The intensity of the red component image was also adjusted to make the color more visible. 156

Figure 9.9: Q-space analysis at 30º incident angle. (A)-above is the Q-space image and (A)-below the surface plot of the luminance (intensity). (B)-above the real space image of the area analyzed and (B)-below the surface plot of the luminance (intensity). 157

Figure 9.10: The elytra with immersion oil and a cover slip on top. (A) With closed aperture stop, (B) with open aperture stop and (C) in dark field. Images B and C appear washed out due to some light reflecting from the top of the cover slip. 159

Figure 9.11: Inverse space images of the immersion oil covered elytra under normal illumination. […] 160

Figure 9.12: The elytra with left handed circular analyzer in place (A) with closed aperture stop, (B) with open aperture stop and (C) in dark field. 160

Figure 9.13: Confocal micrographs in fluorescence mode at higher magnification to show detailed structures inside each cell. […] 162

Figure 9.14: Side views (xz section) of the skeleton obtained in reflection mode (A) and in fluorescence mode (B) […] 162

Figure 9.15: The SEM images of the broken elytra. […] 163

Figure 9.16: A comparison between our (A) data from characterization of *Chrysina gloriosa* and (B) the structures in a paper by Meister *et al*. 164

Figure 9.17: (A) Cholesteric helix at the surface with the helix axis oriented at angle θ to the surface normal and incoming light at angle ϕ. (B) Schematic of a layered structure of a focal conic defect at the surface. […] (C) Ray diagram for a spherical mirror for an incident parallel beam. (D) Ray diagram for a light source present between the sphere center and the point of focus. 166

Figure 10.1: (A) The mechanism of light reflection in a microbowl. […] 172

Figure 10.2: (A) The reflectance spectra of microbowls on the surface of a scale of *Papilio Palinurus.* […] (B) Confocal micrograph of a wing scale of *Papilio palinurus* obtained in fluorescence mode. […] (C) Optical micrograph of *Papilio palinurus* obtained in polarized light. […] 173

Figure 10.3: The colors of *Papilio palinurus* in the CIE chart […] 175

Figure 10.4: The steps in making an artificial butterfly wing by self assembly: […] 176

Figure 10.5: The structure of the breath figure templated assembly, (A) before and (B) after peeling off the top half 177

Figure 10.6: Calculated reflectance spectra for 5 alternating TiO_2/Al_2O_3 layers 20 nm each. 179

Figure 10.7: Calculated reflectance spectra for 8 alternating TiO_2/Al_2O_3 layers 20 nm each. 179

Figure 10.8: ALD process. The precursor is deposited on the surface, where it reacts with the nucleophilic groups. The surface is purged of the un-adsorbed precursor and hydrolyzed by water vapor. This process is repeated until a desired thickness is achieved. […] 180

Figure 10.9: The ALD coated porous polymer film with the light coming from behind the camera (A) and from the side (B) […] 181

Figure 10.10: Micrographs of the peeled breath figures coated with 5 alternating TiO_2/Al_2O_3 layers 20 nm thick. An image taken (A) with only the polarizer in the light path, and (B) under crossed polarizers. […] 182

Figure 10.11: A) The reflectance spectra of the peeled and ALD coated (5 layers) breath figure templated assembly and (B) the corresponding CIE diagram […] 183

Figure 10.12: Micrographs of the peeled breath figures coated with 8 alternating TiO_2/Al_2O_3 layers 20 nm thick (A) Image taken with only the polarizer in the light path, and (B) Image taken under crossed polarizers. 185

Figure 10.13: (A) The reflectance spectra of the peeled and ALD coated (8 layers) breath figure templated assembly and (B) the corresponding CIE diagram […] 186

Figure 10.14: Micrographs of unpeeled ALD coated breath figure: (A) under normal illumination, (B) under crossed polarizers, and (C) under dark field illumination. 187

LIST OF SYMBOLS AND ABBREVIATIONS

η	viscosity
σ	surface tension
U	velocity of fluid jet
We	Weber number
Oh	Ohnesorge number
Mw	weight-awerage molecular weight
T_m	melting point
T_g	glass transition temperature
Λ_{max}	glamaximum draw ratio
M_e	entanglement molecular weight
E	Young's modulus
ϕ_i	incident angle
ϕ_r	reflected angle
θ_i	incident angle projection
θ_r	reflected angle projection
PMMA	poly(methyl methacrylate)
Iso-PMMA	isotactic poly(methyl methacrylate)
Syn-PMMA	syndiotactic poly(methyl methacrylate)
MMA	methyl methacrylate
DMF	dimethylformamide
DSC	differential scanning calorimetry
PDI	polydispersity index
SEM	scanning electon microscopy
AFM	atomic force microscopy

SUMMARY

This thesis is divided into two parts. Part A describes our effots in producing stereocomplex PMMA fibers for the purpose of reinforcing PMMA materials. These kinds of composites are known as “self-reinforced” composites. We were successful in producing stereocomplex PMMA fibers with three different methods – wet spinning, gel spinning and electrospinning. Gel spinning and electrospinning produced the most crystalline fibers. Steroecomplex PMMA fibers were further shown to be resistant to high temperature and also to hot monomer solvent during bulk polymerization.

Part B describes our efforts in characterizing, replicating and mimicking structural color features of butterflies and beetles. We have developed a simple method of characterizing the bidirectional reflectance distribution function of microscopic objects such as butterfly wing scales. We used this method to characterize structural color features resulting from the replication of butterfly *Morpho rhetenor* , mimickry of butterfly *Papilio palinurus* and also the native structural color features of *Chrysina* gloriosa, which were shown to be cholesteric focal conic defects lined on the surface.

PART A

STEREOCOMPLEX POLY (METHYL METHACRYLATE) FIBERS AND SELF-REINFORCED COMPOSITES

CHAPTER 1

INTRODUCTION TO PMMA STEREOCOMPLEX AND SELF-REINFORCED COMPOSITES

1.1. Definition and Basic Structure of Stereocomplex

Poly(methyl methacrylate) (PMMA) is used in many applications in everyday life, for example, as plexiglass, bone cement or tooth fillings, etc. We are used to thinking about PMMA as an amorphous, brittle, glassy polymer whose main advantage is the ease of polymerization. However, the monomeric units are prochiral and, hence, the resulting polymer chain contains a series of chiral centers, which can be arranged in three different ways: i) randomly arranged in the atactic PMMA (a-PMMA), ii) all having the same configuration (R or S) in an isotactic PMMA (iso-PMMA), and iii) regularly alternating chiral centers in a syndiotactic PMMA (syn-PMMA). Both stereoregular forms of PMMA adopt helical structures[2-4] and are crystalline[5], while the most common, a-PMMA is amorphous. An even more exciting structure, known as the stereocomplex[6], forms via a stereo-specific interaction when the two stereoregular form of PMMAs are mixed together. The phenomenon of stereocomplexation in PMMA has been reviewed in 2003 by Slager and Domb[7], te Nijenhuis[8] in 1997, and Spevacek[9] in 1987.

A polymer stereocomplexation is defined as "a stereoselective interaction between two complementing stereoregular polymers, that interlock and form a new composite, demonstrating altered physical properties in comparison to parent polymers"[7]. The stereocomplex components can thus be a pair of enantiomeric, optically active

polymers[10] or a pair of isotactic and syndiotactic, not necessarily optically active polymers[11].

The PMMA stereocomplex was first observed in 1958 by Fox[5] and its structure and properties have been extensively studied[9,12-15]. Previous reports showed that the two polymer chains form a double helix[12,13], where the syndiotactic chain wraps around the isotactic chain in a 1:2 iso:syn ratio[9,14]. The basic structure of the PMMA stereocomplex has remained a riddle ever since Fox *et al.* discovered a crystalline form of PMMA in 1958[5]. Liquori *et al.* later proposed on the basis of X-ray analysis that the crystalline form of PMMA is in fact a structure resulting from an interaction between isotactic PMMA and syndiotactic PMMA chains[16]. The resulting structure was named "stereocomplex" and the basic structure was proposed to be a combination of isotactic PMMA helices with the straight syndiotactic PMMA chains running in the grooves of the helices. At the time, the isotactic PMMA chains were thought to form a 5/2 (monomer units/ pitch units) helix with a pitch of 10.5Å[17]. Bosscher and Challa[13] performed an X-ray analysis in 1982 and concluded that the stereocomplex probably consisted of a double-stranded helix in which the isotactic chain is in a 30/4 helix and the syndiotactic in 60/4 helix with the real fiber period being 4 x 18.4Å = 73.6 Å. The structure was revisited by Shoemaker and Challa in their analysis of the fiber X-ray pattern in 1989 and they proposed a double helix model[18] that was accepted until recently. In this model, the isotactic PMMA chain forms a 9/1 helix with a pitch of 18.4Å and the syndiotactic PMMA chain wraps around with 18/1 helix also with 18.4Å pitch. The stoichiometry is thus 1:2 isotactic : syndiotactic. These results were also supported by the modeling of the conformations of isotactic PMMA and

syndiotactic PMMA where it was discovered, that the most stable dihedral angles drive both polymers to make such helices[19]. Finally, Kumaki *et al.* have proposed a new model in 2007 based on their AFM analysis of Langmuir-Blodgett films of stereocomplex PMMA. The model is based on a double helix composed of two isotactic PMMA chains, which is similar to the structure of pure crystalline isotactic PMMA[2]. The syndiotactic PMMA chain then wraps around the isotactic PMMA double helix forming a triple helix. The stoichiometric ratio remains 1:2 isotactic : syndiotactic due to the larger diameter of the syndiotactic helix. This structure explains a number of previously reported results. The template polymerization, where the growing PMMA chain in the presence of isotactic PMMA polymer becomes syndiotactic[20-22] can be explained by the fact that the syndiotactic PMMA chain is on the outside of the triple helix. Likewise, the substitution of methyl ester groups in the syndiotactic PMMA chain by larger groups (ethyl, propyl) does not disturb the stereocomplex formation, while the substitution of the ester groups in the isotactic PMMA chain prevent the stereocomplex formation[23]. The proposed structure might also account for a number of conflicting reports regarding the stereocomplex stoichiometry. Since there are three polymer chains in the stereocomplex structure, two of which are isotactic and one syndiotactic, measurement of colligative properties might have resulted in a reverse stoichiometric ratio[21,24].

We will touch upon the basic stereocomplex structure in Chapter 3 where we analyze the X-ray spectra of gel-spun stereocomplex PMMA fibers.

1.2. PMMA Stereocomplex properties

The stereocomplex introduces a whole new array of interesting properties to PMMA[9]. Atactic PMMA does not crystallize, but stereocomplex PMMA helices can pack together and form crystals with a well-defined melting point[5]. The stereocomplex forms in the bulk after lengthy annealing, while it forms very quickly in solution. The complexation in solution is strongly solvent dependant[21]. These properties have been recently utilized in various attempts to produce new supramolecular structures. For example, the stereocomplex formation has been used to form non-ionic layer-by-layer assembly to produce hollow microparticles[25] and protein scaffolds[26], while the physical gelation has been used to produce a highly porous interconnected network[27].

1.2.1. PMMA Stereocomplex Dilute Solutions

In dilute solutions well below C* the stereocomplex molecules are far enough apart that no entanglements are present. Dilute solution studies were performed mainly for the purpose of determining the stoichiometric ratio of isotactic to syndiotactic PMMA and to assess the influence of the solvent on stereocomplex formation[9].

An early report by Chiang[28] studied the effect of temperature on stereocomplex formation of dilute solutions in dimethylformamide (DMF). They observed a decrease in viscosity at lower temperatures and ascribed it to stereocomplex formation. The bonding of chains into a stereocomplex reduces the number of polymer chains in the solution, thus reducing viscosity. When these solutions were heated above 90ºC, the intrinsic viscosity increased from 0.43dl/g to 0.71dl/g. When the solutions were subsequently cooled down,

the viscosity drop was only observed at 70ºC. The decrease in intrinsic viscosity was also observed by Liu and Liu[29] who used it to determine the stoichiometric ratio of isotactic PMMA : syndiotactic PMMA and found it to be 1:2. Furthermore, they observed that this decrease of viscosity was more pronounced in some solvents than others and that when the decrease was not large, the stoichiometric ratio was also harder to determine and might be closer to 1:1 for those solvents. Vorenkamp, Bosscher and Challa[30] later classified various solvents according to their "stereocomplexation strength". They sorted the solvents into three categories – strongly complexing, weakly complexing and non-complexing (**Table 1.1**). It is interesting to note that tetrachloromethane is a strongly complexing solvent, while in general the more polar solvents are strongly complexing. Chloroform and dichloromethane do not promote stereocomplex formation. The monomer, methyl methacrylate (MMA) is a strongly complexing solvent explaining the phenomenon of template polymerization[22,31-38], where the MMA monomer is polymerized in the presence of a stereoregular PMMA chain. It was found that in the presence of iso-PMMA, the polymerized chain was mainly syn-PMMA. Schomaker and Challa[39-41] as well as Mrkvickova *et al.* [42-44] have done further studies confirming the 1:2 iso:syn ratio and examining the kinetics of the complexation.

Table 1.1: Classification of the solvents according to complexation strength[30].

Strongly complexing	Weakly complexing	Non-complexing
tetrachloromethane (CCl_4)	benzene	chloroform
acetonitrile	toluene	dichloromethane
dimethylformamide (DMF)	*o*-dichlorobenzene	
acetone	benzaldehyde	
dimethylsulfoxide (DMSO)	dioxane	
methyl isobutyrate	thiophene	
tetrahydrofuran (THF)		
methyl methacrylate (MMA)		

Kitayama, Hatada *et al.*[45-48] have prepared molecularly monodisperse 50mers of isotactic and syndiotactic PMMA and studied the stereocomplex formation using gel permeation chromatography in tetrahydrofuran (THF). They have found the stoichiometric ratio of iso : syn to be 1:2.

Recently Kumaki *et al.*[11,49] have done some studies of stereocomplex dilute solutions in chloroform. Even though chloroform is a non-complexing solvent, they observed stereocomplex formation when chloroform solutions were compressed in a Langmuir-Blodgett trough. The stereocomplex thin films were imaged by AFM and the basic structure of stereocomplex was thus explored. Furthermore, the influence of molecular weight was examined. It was found, that iso-PMMA molecules of different molecular weights will self-sort so that chains with similar molecular weight will form a double helix. The syn-PMMA will then wrap around the iso-PMMA until al the space is filled. The higher molecular weigh component thus determines the helix size.

1.2.2. PMMA Stereocomplex Gels

Concentrated stereocomplex solutions in strongly-complexing solvents form thermoreversible physical gels. The crosslinking points in these physical gels have been shown to be bundles of helices[50]. Even though the PMMA stereocomplex has been studied for a couple of decades[9], the gel state has been little studied. The first experimental results were obtained as either a function of temperature[51] or ageing time[52]. In the 1990s, Guenet *et al.* have contributed to the understanding of the molecular structure of the stereoregular PMMA gels by doing neutron scattering experiments[53,54], and swelling and rheological experiments[55], using PMMA with 67% syndiotactic and 18% isotactic content. It has to be pointed out that such polymer is not the most appropriate for the study of stereocomplex formation, because the length of stereoregular sequences is rather short[9].

Prylik and Rehage[51] have used a 1:1 mixture of isotactic and syndiotactic PMMA in their study of PMMA gels. They have measured the elastic and viscous modulus at different temperatures in *o*-xylene and determined the gel point from the point where the curves cross. The crossover sol-gel temperature was found to be 90ºC. It was also determined, that there are some nuclei left even when the gel is heated well above the gelation temperature, resulting in a much faster gel formation on cooling. We have determined the sol-gel transition temperatures for a range of concentrations of stereocomplex PMMA in DMF in Chapter 4.

Gelation usually proceeds very rapidly, when long syndiotactic sequences are present. The rapid gelation process was explained by Schomaker[56]. He suggested that the complexation could start with the formation of a kink in syn-PMMA, which then wraps around the iso-PMMA chain. This stereocomplex nucleus can then grow through simple rotation, resulting in two helices of opposite handedness growing away from the kink site.

The current understanding of PMMA gel structure, according to Guenet[50], is that it can be described by the Jones and Marques theory[57]. This theory describes a gel as a collection of rigid rods connected by flexible junctions. First, the rigid helices are formed, which later aggregate to form junctions.

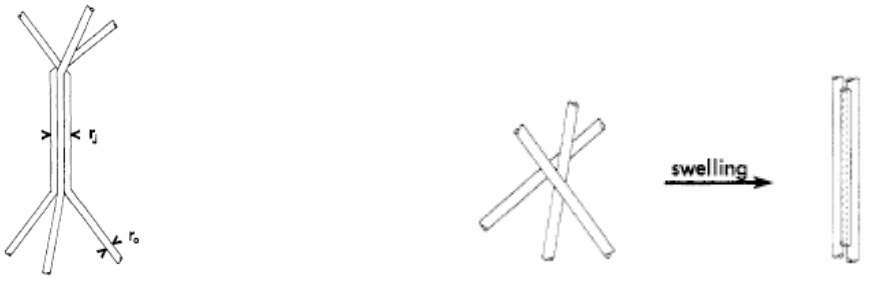

A **B**

Figure 1.1: (A) Schematic model of an organized junction composed of the merging of three fibrils (helices) and (B) the mechanism of a proto-junction transformation into an effective junction upon gel swelling. Both figures taken from Guenet[54] (Used by permission, © American Chemical Society).

In 2005 Kumaki *et al*. have discovered that stereocomplex PMMA forms gels also in ionic liquids[58], opening a route to thermoreversible ion gels.

1.2.3. PMMA Stereocomplex Crystallization

Stereocomplex PMMA crystals can be obtained from solutions by evaporating the solvent, or from the melt. Crystallization from the melt is a very slow process[30,59-62]. The stoichiometry affects the highest obtained melting enthalpy[63], with the highest obtained at iso : syn = 1:2 ratio. The temperature at which crystallization is carried out also affects the melting enthalpy, with the highest enthalpy of -16J/g obtained after 7 days at the crystallization temperature of 140ºC[63]. There is also some debate on the melting point of the stereocomplex. Most researchers report values of either ~180ºC or >210ºC [9,62,64,65]. Presumably, the melting peak around 180ºC is due to stereocomplex crystallites and the peak at 237ºC due to the stereocomplex helix itself dissociating[64,66]. Later, the melting peak at the lower temperature was assigned to a fringed-micellar mode of stereocomplex crystallization, while the higher melting point is the result of lamellar crystallization[62]. Finally, the melting peak with a peak at 162ºC and the highest tail end up to 170ºC was assigned to the crystallization of isotactic PMMA and the higher melting peak to the stereocomplex[65].

The crystallization from solution proceeds much faster and the melting enthalpies obtained are about twice as large compared to the stereocomplexes from melt crystallization[30,63]. The solvent chosen needs to be one of the strongly complexing solvents in order to achieve the highest crystallinity. The highest enthalpies of melting are in the -40J/g range[30,59,67].

The crystallinity percentage is harder to assess. So far the 100% has not been determined and neither has the full enthalpy of melting. Therefore the value of melting enthalpy is usually reported. A further complication is that the isotactic PMMA itself also crystallizes and melts in the same temperature range, often obscuring the value of stereocomplex melting enthalpy[59,65]. In their investigation, Konnecke and Rehage assigned the value of -24 J/g as the enthalpy of stereocomplex formation[59,68]. In terms of energy per monomer unit, that would be 2.4 kJ/mol or 0.57 kcal/mol. The order of magnitude is comparable to the hydrogen bonding strength, which would be 2~10kcal/mol[69]. However, since the stereocomplex interaction is not directional or monomer specific like hydrogen bonding, we have to keep that in mind when using these numbers.

1.2.4. PMMA Stereocomplex Mechanical Properties

There have been very few reports where the mechanical properties of PMMA stereocomplex were investigated. There are three examples of stereocomplex fibers in the literature[13,16,30]. In two of the cases, the fibers were made by stretching 5% DMF gels[16,30] and in one case, by stretching 3% acetone gel[18]. Even though short stereocomplex PMMA fibers were made by stretching gels in order to perform X-ray analysis, no continuous fibers were made.

Allen *et al.* investigated some mechanical properties of stereocomplex using dynamic mechanical analysis[70]. They formed the stereocomplex in an unconventional manner by treating solid blocks of isotactic and syndiotactic PMMA blend with methanol. Methanol is a non-solvent for PMMA and yet promotes stereocomplex

formation. We used this to our advantage in wet-spinning sterocomplex PMMA fibers in Chapter 2. The polymers used in the study of Allen *et al*. were not highly stereoregular, however they observed a significant increase in fracture toughness upon adding isotactic PMMA to atactic PMMA. They did not use a highly syndiotactic polymer in their study.

Although not a study on stereocomplex itself, Urbanek *et al.* have determined the crystalline modulus of isotactic PMMA[71]. Together with modeling the iso-PMMA as a double helix they reported a maximum theoretical modulus of 20 GPa.

1.2.5. Stereocomplex PMMA Chirality

Isotactic PMMA exists in two enantiomeric forms – the L and D. However, syndiotactic PMMA is mesomeric. The stereocomplex PMMA forms a helical structure. Because helices can twist clockwise or anti-clockwise, the stereocomplex PMMA is a great candidate for making chiral materials[72].

Wulff and Zweering have synthesized enantiomerically pure isotactic PMMA and complexed it with syndiotactic PMMA[73]. They reported a rather low value of optical rotation for the enantiomerically iso-PMMA pure ($[\alpha]^{20}$ = -3.0º at 365 nm) and the stereocomplex ($[\alpha]^{20}$ = -5.1 at 365 nm). The value also decreased with increasing the molecular weight. The low value is not surprising, because PMMA is known to have low birefringence[74], therefore also the optical rotation of the enantiomer will be low.

Recently, Kawauchi *et al*. have developed a procedure for controlling the helix sense of stereocomplex PMMA[75,76], reminiscent of the helical polymers and the sergeants

and soldiers methodology developed by Green and co-workers[77]. The helix handedness is controlled by introducing a small molecule (*R* or *S*-1-phenylethanol) in a weakly complexing solvent (toluene). First, the complex between syn-PMMA and C_{60} buckminsterfullerene is synthesized[76]. This complex has been shown to follow the sergeants and soldiers principle. Next, the C_{60} molecules are replaced by iso-PMMA. It is quite surprising that the double iso-PMMA helix can replace the C_{60} molecules in the interior of the syn-PMMA helix while the latter retains its handedness. Another pathway is to introduce the chiral molecule and syn-PMMA, thus biasing the helix, and then introduce the iso-PMMA. This method promises a versatile route to chiral optical materials.

1.3. Self-reinforced Composites

When a composite consists of the same polymer as a matrix and reinforcing fiber, it is called self-reinforced composite or single-polymer composite. One of the main problems in self-reinforced PMMA composites using only a-PMMA is the temperature stability of oriented a-PMMA fibers[78]. At the temperatures required for the composite processing, which is far above the glass transition temperature (T_g) of a-PMMA, most of the chain orientation in a-PMMA fibers is lost. In order to form self-reinforced PMMA composites, one needs to maintain the rigid fiber characteristics even at the processing temperature.

PMMA fibers have been used in making self-reinforced composites before. Gilbert's group was successful in melt-spinning atactic PMMA fibers[79] to make an improved self-reinforced composite[78,80-85]. Particularly the fracture toughness was

improved immensely[80]. The processing temperature and time had a substantial influence on the composite properties. It was found that the processing temperature needed to be kept below 128ºC in order to retain atactic PMMA fiber orientation and thus reinforcing characteristics[78]. The processing time also had to be a short as possible[82,83]. One can clearly expect the need of a special processing equipment that will have to handle very high torque, because the melt viscosity of a-PMMA may be very high at 128C, which is not far above its T_g (T_g = 105°C)[86]. However, Jagger *et al.* have tried to achieve a similar result with chopped-up atactic PMMA fibers immersed in MMA monomer and polymerized at 100°C [87]. Their results indicate, that the fibers introduced into the self-reinforced composite this way do not improve the material properties. Their reasoning is that there is a problem with the interface between the fibers and the polymer matrix. They have been successful in alleviating this problem by coating the PMMA fibers with rubber[88]. Jagger and co-workers also proposed an explanation for Gilbert's[78,81-84] success. They point out that the fibers Gilbert's self-reinforced composite were not at random orientations, but rather bunched together. However, Gilbert's self-reinforced composite was processed above the PMMA glass transition temperature, while the composite made by Jagger *et al.* composite was processed below T_g. Processing the composite above T_g might lead to chain interconnection even between fiber surface and the polymer matrix, thus improving the interface contact. Furthermore, the composite made by Jagger *et al.* was made in the presence of MMA monomer, which was polymerized. MMA is a good solvent for PMMA and at elevated temperatures it is plausible that the oriented PMMA fibers would have dissolved.

CHAPTER 2

PMMA STEREOCOMPLEX FIBERS *via* WET SPINNING

2.1. Introduction to wet spinning

Wet spinning is a fiber-forming process where the polymer is dissolved in a good solvent and the resulting solution is extruded into a non-solvent. Diffusion of the solvent from the stream of polymer solution into the coagulation bath results in fiber formation. Since the nature of the solvent greatly influences the stereocomplex formation[89], we decided to examine how the wet spinning process affects the stereocomplex fiber formation. The advantage of wet spinning over melt spinning in this case is, that the melt spinning temperature required for processing is at least 230ºC, which is well beyond the stereocomplex melting point[90]. Because the stereocomplex takes a long time to form after melting it at such a high temperature[56,62,65], our goal was to achieve stereocomplex formation during the fiber spinning process. Wet spinning was chosen because the stereocomplexation behavior can be controlled by solvent choice.

2.2. Experimental

Atactic-PMMA samples of 3 different molecular weights (Mw) and polydispersity index (PDI) (Mw = 996,000, PDI = 5.7; Mw = 350,000, PDI = 3.4; Mw=15,000, PDI = 1.3) were purchased from Aldrich Chemical Co. Dimethyl formamide (DMF), dichloromethane and methanol were purchased from Acros Organics. Isotactic-PMMA ((Mw = 300,000, PDI = 9.4, isotactic triads: >95%) and syndiotactic-

PMMA (Mw = 50,000, PDI = 1.3, syndiotactic triads: 85%) were purchased from Scientific Polymers Co. All reagents were used without further purification.

Fiber was spun using KDS100 syringe pump (KD Scientific). Differential scanning calorimetry (DSC) was carried out with Seiko DSC 220. Hitachi S800 FEG scanning electron microscope (SEM) was used for the fiber surface imaging, and Leica RDX polarized light microscope was used for the fiber diameter measurements and birefringence observation. Synchotron X-ray crystallography was done using Advanced Photon Source at Argonne National Lab at 0.765335Å along with Mar 3450 area detector.

Isotactic-PMMA and syndiotactic-PMMA (iso-PMMA and syn-PMMA below) were dissolved in dichloromethane to make a 30 wt% solution with iso-:syn-PMMA ratio of 1:2. Noncomplexing and non-gelating solvent was chosen in order to keep the solution viscosity low. The resulting solution was spun from a syringe with 12 gage needle at a speed of 4 ml/h into a cold (-20°C) methanol bath. The needle was bent at a 90deg angle with slight curvature, so that the resulting filament was flowing out of the needle parallel to the ground and the force exerted by the pick-up reel was parallel with the flow direction. The length of the bath was 90 cm and the pickup speeds were 4m/min and 11.9 m/min.

DSC analysis was performed with a heating rate of 20ºC/min. The heating continued until 230ºC, the temperature was kept there for 5min, then the sample was cooled down at -20ºC/min until It reached 40ºC. The temperature was kept at 40 ºC for 5 minutes and then the cycle was repeated twice more. Only the curves obtained during the first heating cycle were relevant for stereocomplex formation analysis.

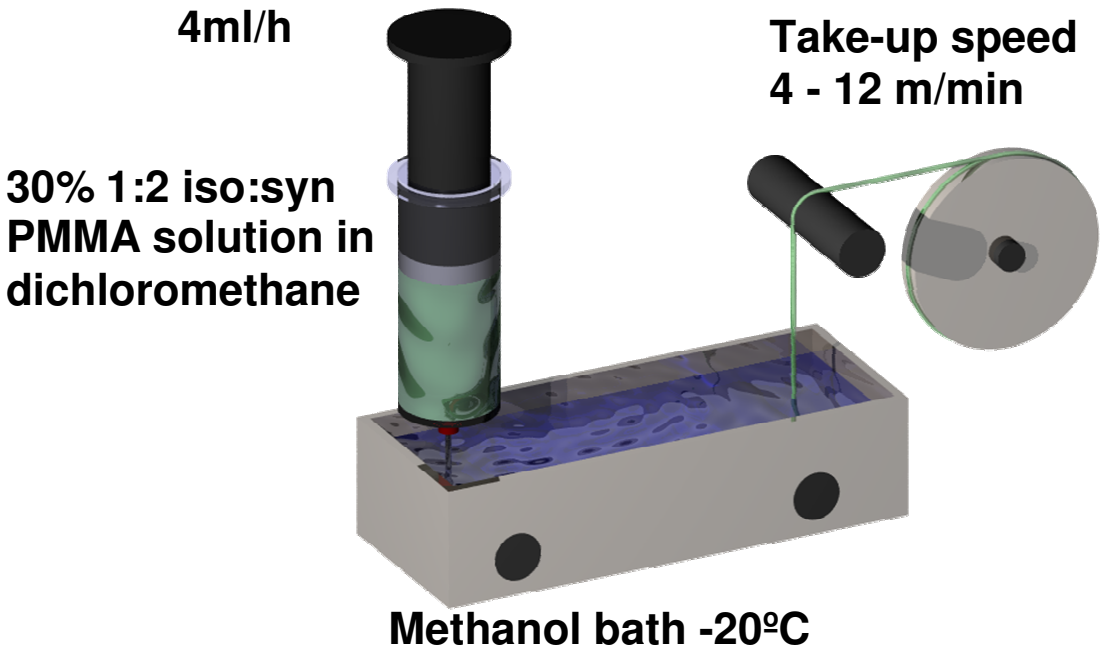

Figure 2.1: Wet-spinning apparatus. The polymer solution is in the syringe. The solution is slowly injected directly into a coagulation bath. The syringe needle is dipped nto the coagulation bath. The fiber formed is wound up.

2.3. Results

Stereocomplex PMMA solutions form physical gels and the gelation strength depends upon the solvent used[30]. The characteristics of physical gels are reversible crosslinks that form the gel network[91]. Such gels are therefore thermoreversible. Dichloromethane is a non-complexing solvent and no gel is formed in this solvent[30]. The mixture of iso- and syn-PMMA in dichloromethane does not form a stereocomplex and is therefore liquid, and easily flows at any temperature. This is the reason we chose dichloromethane as the spinning dope. Multiple concentrations were tried. The 5%, 10%, 15% and 25% by weight stereocomplex PMMA solutions in dichloromethane were not

viscous enough for fiber spinning (**Table 1.1**). The fluid jet of these solutions would always break into droplets *via* Rayleigh instability. The 30% stereocomplex PMMA solution in dichloromethane was viscous enough that the fluid jet did not break up immediately after the solution was passed through a syringe needle.

The next parameter to be defined was the composition of the coagulation bath. Results are summarized in **Table 2.1**. At first, various compositions of dimethylformamide/water were tried. When the water concentration was low, a brittle skin formed on the outside of the fiber, while the inside was still liquid. These fibers would then break. When the water concentration was higher, the whole fiber would quickly phase separate and the resulting bright white fibers were extremely brittle. Differential scanning calorimetry (DSC) analysis showed no endothermic transitions. After discovering that methanol worked very well as the coagulation bath, the fine tuning of DMF-water composition was abandoned. Petrolether was also tried as the coagulation bath, following a previously reported case of spinning SBR/PMMA (polystyrene-butadiene/polymethyl-methacrylate) core-shell particles[92]. However, in our system, petrolether did not seem to be a good coagulation bath. The polymer was readily phase separated into flakes at virtually every concentration. Methanol was chosen because it is a non-solvent for PMMA and it is also known to promote crystallization of the stereocomplex[70]. It has shown itself to be the best coagulation bath. The fluid jet of dichloromethane solution in methanol was stable and formed a continuous fiber.

After spinning the PMMA fibers from a 30 wt% in dichloromethane 1:2 iso-:syn-PMMA spinning dope into a cold methanol coagulation bath, we have determined that the stereocomplex did not form during the spinning process. Instead of an endothermic peak at around 180ºC[62,64,65], the DSC analysis showed a broad endothermic peak at 155ºC (**Figure 2.2**). We reasoned that a longer residential time in the coagulation bath would promote stereocomplex formation. We have attempted to spin the fiber at as low an extrusion speed as possible and as long a residential time in the coagulation time as our apparatus had allowed. The lowest extrusion speed in order to get a stable fiber stream in the coagulation bath was 4 mL/h. We had a 90 cm long coagulation bath and we tried to lengthen the residential time by lowering the pick-up speed from initial 11.9 m/min to 4 m/min. The residential time in the coagulation bath at the slowest possible pick-up speed was 15s.

Table 2.1: Summary of experiments optimizing wet-spinning conditions.

Coagulation bath composition	Spinning dope concentration (w/w 1:2 isotactic:syndiotactic PMMA in CH_2Cl_2)				
	5 %	10 %	15 %	20 %	30 %
water	Flaky precipitate	Flaky precipitate	Flaky precipitate	Flaky precipitate	Flaky precipitate
DMF:H_2O 50:50	Flaky precipitate	Flaky precipitate	Drops precipitate	Pearls on a string precipitate	Brittle white fibers
DMF:H_2O 60:40	Flaky precipitate	Flaky precipitate	Drops precipitate	Pearls on a string precipitate	Brittle white fibers
DMF:H_2O 90:10	Flaky precipitate	Flaky precipitate	Drops with white skin	Pearls on a string with white skin	Jet develops thin white skin and breaks
petrolether	Flaky precipitate	Flaky precipitate	Flaky precipitate	Flaky precipitate	Flaky precipitate
methanol	Flaky precipitate	Flaky precipitate	Drops precipitate	Pearls on a string	**Smooth, stable fiber**

The fibers formed by the wet spinning process from a non-complexing solvent into a complexing non-solvent were annealed in a vacuum oven at 140^{o}C and their thermal behavior is shown as a function of annealing time in **Figure 2.2.** Upon annealing of the as-spun fibers, the melting point increased to 172°C. The annealing temperature we used was 140 ºC, because that temperature was shown to yield the most stereocomplex crystallization without the isotactic PMMA crystallization[62,65] We can also note that the melting peak position shifts from higher temperature to lower values with increasing the crystallization time.

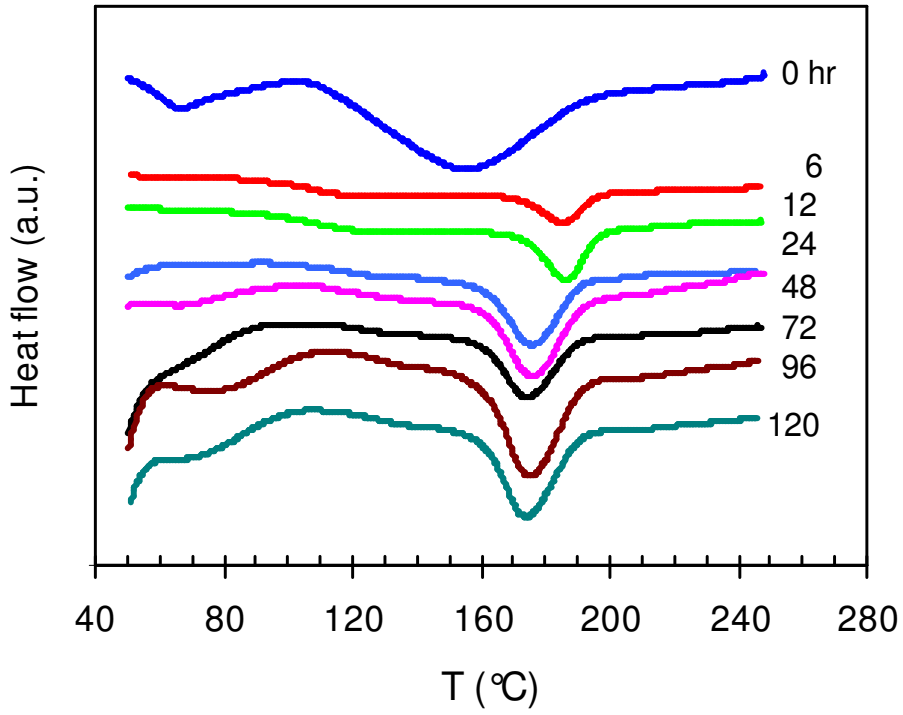

Figure 2.2: DSC analysis of the wet-spun stereocomplex fibers before and after annealing at 140°C for varying length of annealing time. All the curves shown were obtained on the first heating run at 20ºC/min.

We examined whether the wet spinning had any effect on the crystallization time. The enthalpy of the melting for fibrous stereocomplex PMMA mixture and non-fibrous iso-:syn-PMMA 1:2 mixture is compared in **Figure 2.3**. The non-fibrous mixture of iso-/syn-PMMA exhibits an induction time at the annealing temperature of 140°C. After 12 hours no endothermic peak is detectable by DSC. After 24 hours we can detect a melting peak at 172ºC. We did not determine the precise length of the induction time, but it lies between 12 and 24 hours. After the induction period the crystallization proceeds and reaches a maximum enthalpy of melting (12 J/g) after 6 days. The fibrous material does

not exhibit any induction time and the crystalline fraction reaches a maximum enthalpy of melting (15 J/g) after 3-4 days.

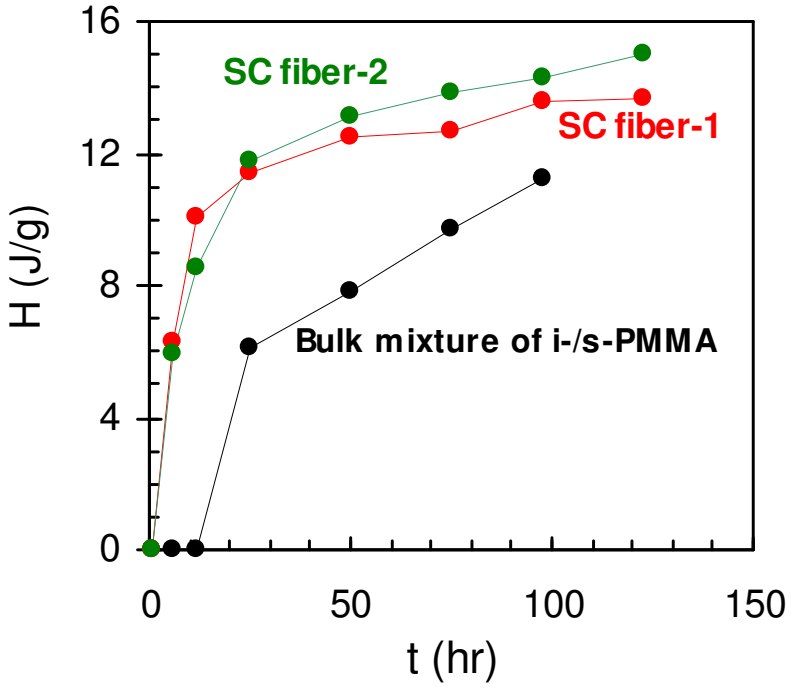

Figure 2.3: Crystallization kinetics of wet-spun stereocomplex PMMA fibers. The enthalpy of melting of the peak at 172°C is plotted against time. Stereocomplex fibers were spun at different pick-up ratios (4 m/min for SC fiber-1 and 11.9 m/min for SC fiber-2). All samples were annealed at 140ºC.

Synchrotron X-ray analysis of the annealed wet-spun stereocomplex PMMA fiber has not shown significant crystalline peaks (see **Figure 2.4**). Similar result has been reported previously for stereocomplex PMMA samples with a comparable enthalpy of melting, where the lack of the crystalline peaks was explained as due to the small crystallite sizes[65].

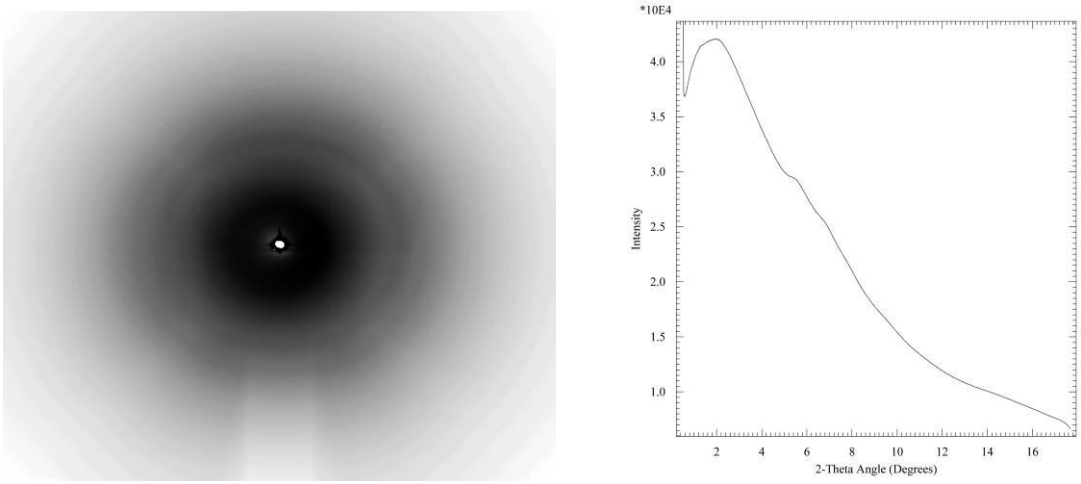

Figure 2.4: X-ray diffractogram of the annealed stereocomplex fiber. Broad Peaks at angles correspond to the spacings: 22.0, 7.8, 6.4, (~4.5), and 3.0 (Å).

To examine the effect of molecular orientation in the fiber, we have spun the fiber at as slow a pick-up rate as possible and at the highest pick-up rate without fiber breakage (4m/min for SC fiber-1 and at 11.9m/min for SC fiber-2 in **Figure 2.3**). If methanol induces crystal formation on the fiber surface, the resulting small crystallites act as nucleation sites for further stereocomplex crystallization.

SEM images of the fiber surface show a presence of 1 μm sized crystallites (see **Figure 2.5**). We have attempted spinning the fibers using a non-complexing non-solvent petroleum ether as the coagulation fluid, to test this hypothesis. Unfortunately, in that case, powdery flakes appeared instead of fibers.

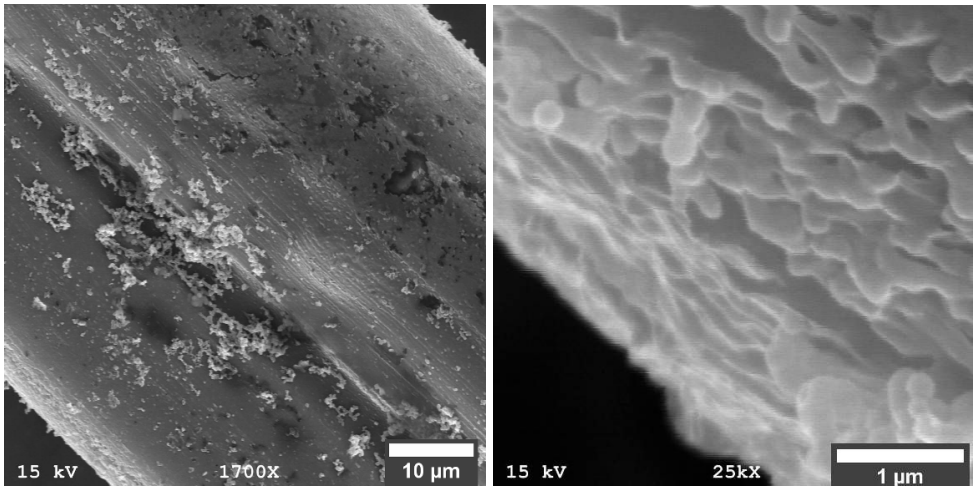

Figure 2.5: SEM images of the wet-spun stereocomplex PMMA fiber at different magnifications. There are plenty of microcrystallites on the surface. Scale bars in left and right image represent 10 µm and 1 µm, respectively.

Another piece of evidence for the formation of microcrystallites comes from the comparison of a stereocomplex fiber with an atactic-PMMA fiber that was wet-spun at the same conditions. Optical micrographs (**Figure 2.6**) indicate the surface of the atactic PMMA fiber is smooth, while the surface of the stereocomplex fiber is rough, with features on the order of one micron.

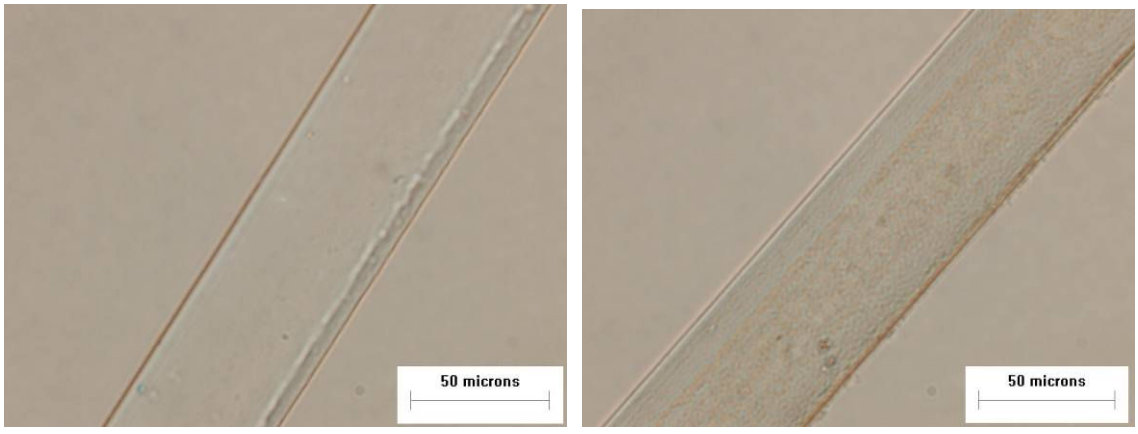

Figure 2.6: Optical micrographs of the atactic melt-spun fiber (left) and stereocomplex wet-spun fiber (right). We can see that the surface of the stereocomplex fiber is rougher than the atactic PMMA fiber.

We have tried to crystallize the atactic-PMMA fiber and did not see any crystallization, as expected. Therefore we can say that only the stereocomplex mixture forms microcrystallites in the cold methanol bath. We have also done control experiments by spinning isotactic-PMMA fibers and syndiotactic-PMMA fibers (see **Figure 2.7**). When subjected to the same experimental conditions, these fibers did not crystallize and their surfaces were smooth with no microcrystallites present. The isotactic-PMMA fibers showed a small endothermic peak at 168ºC after 7 days of annealing, but the enthalpy of melting was very small, about 1 J/g.

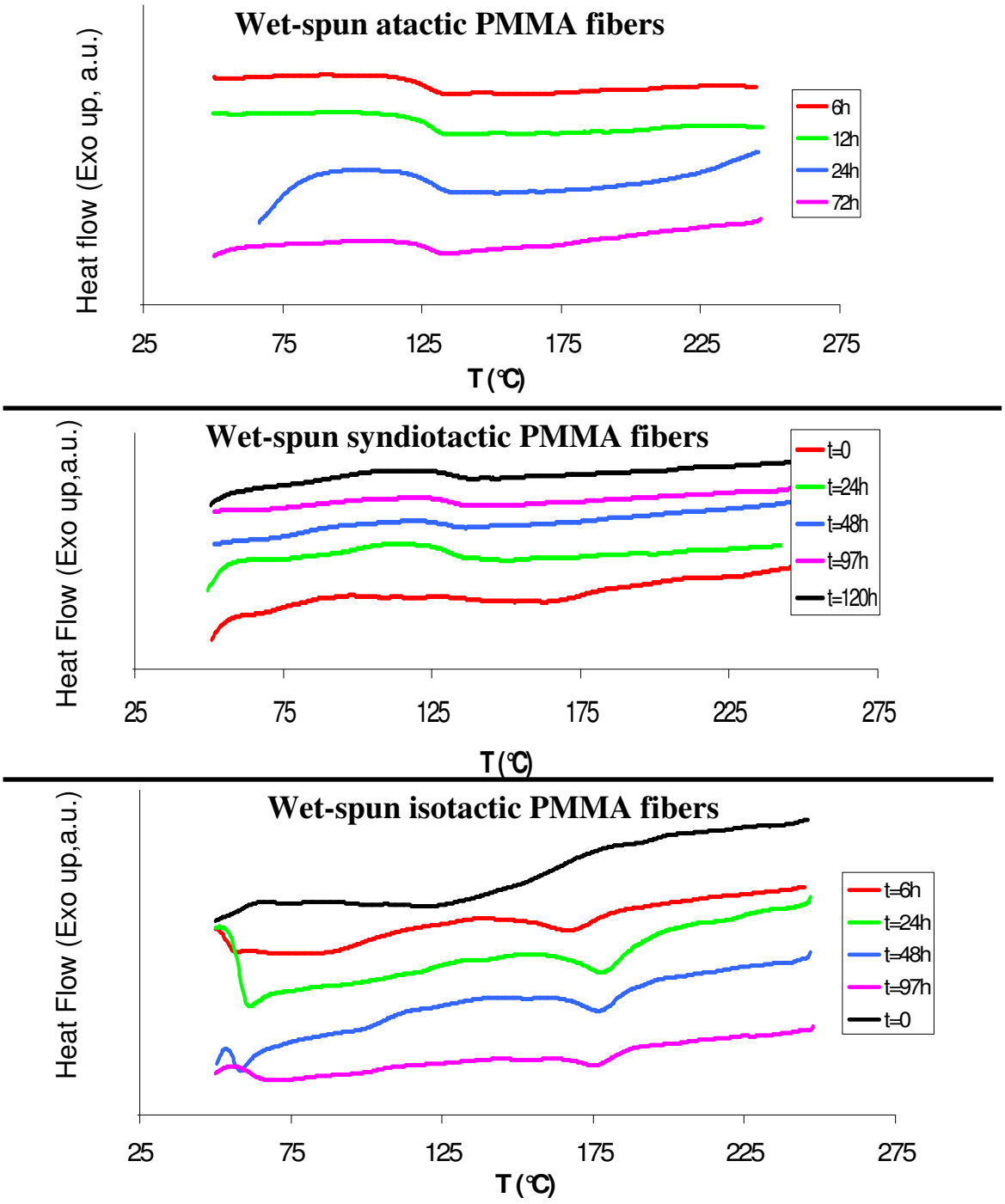

Figure 2.7: The DSC curves for the thermal annealing of atactic, syndiotactic and isotactic PMMA fibers acquired by the same experimental conditions of wet spinning as the stereocomplex fibers. Only isotactic PMMA fibers show a small endothermic peak.

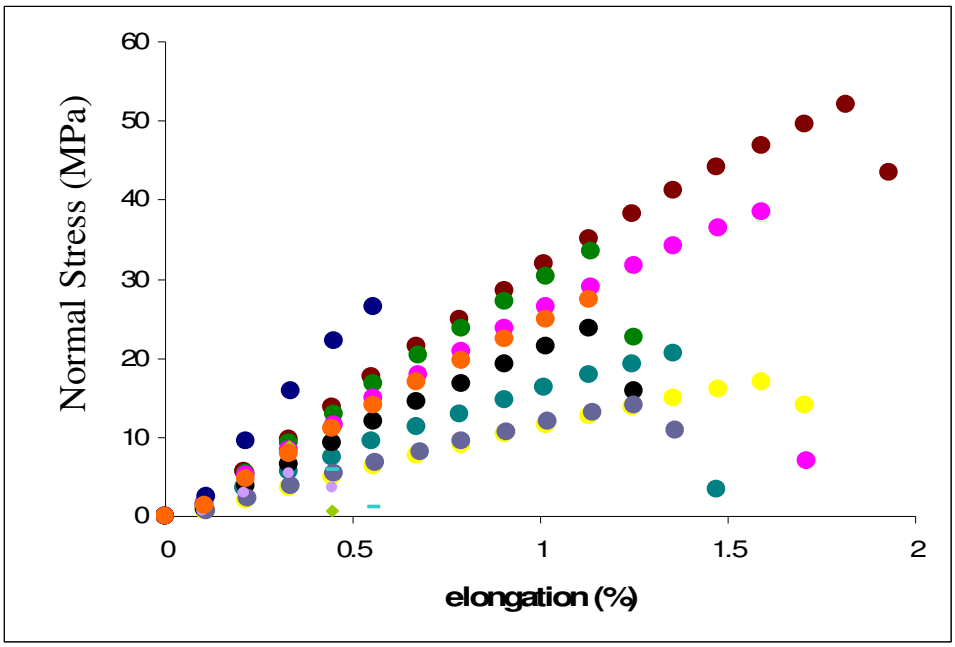

Figure 2.8: Mechanical testing of wet-spun PMMA stereocomplex fibers. Each color represents a single filament test sample.

The mechanical testing of individual fibers (**Figure 2.8**) has revealed that the orientation did increase the modulus. The modulus tested ranged between 1~4 GPa.

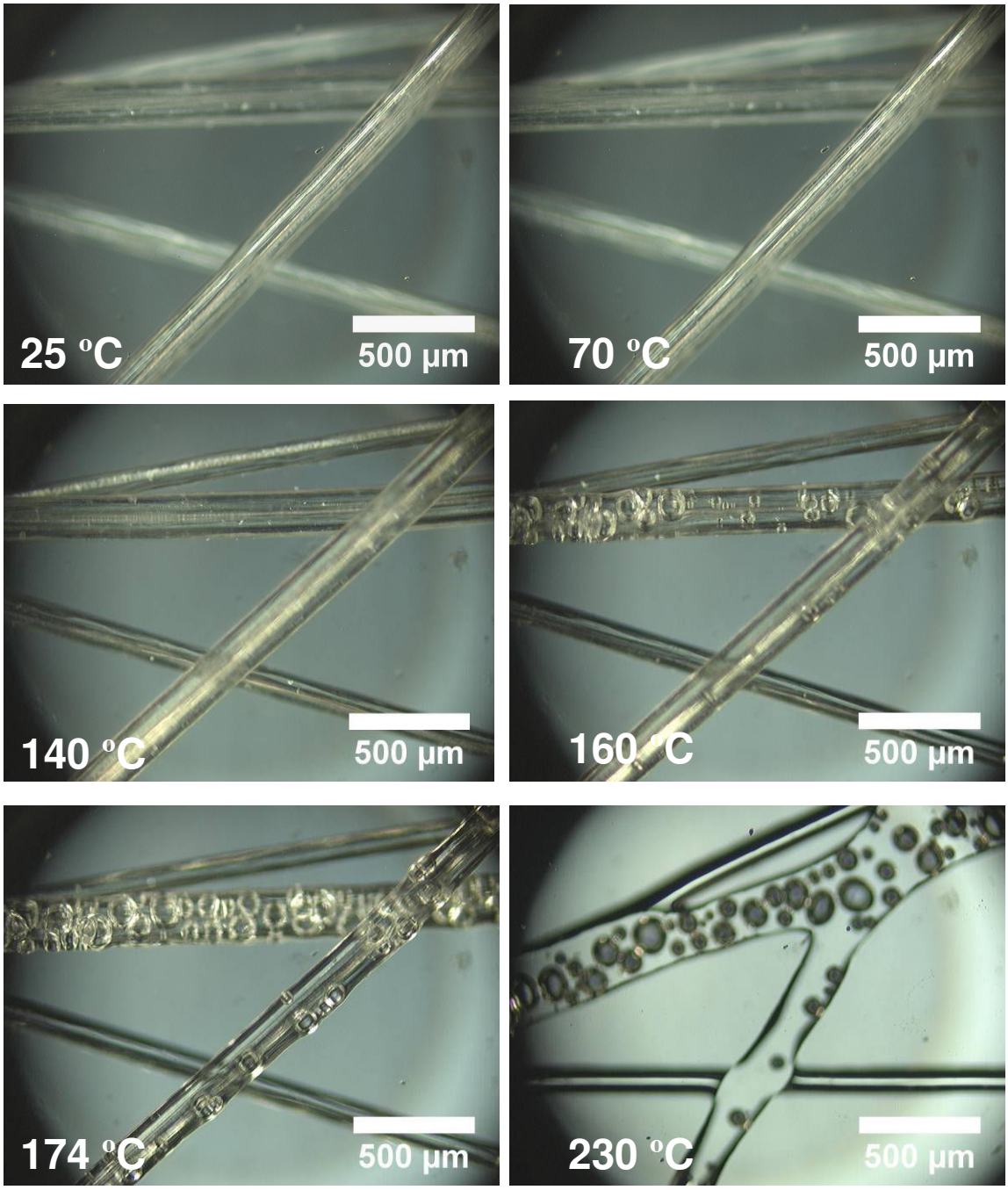

Figure 2.9: Heating the wet-spun stereocomplex fibers at 5ºC/min. The fibers maintain their shape even at high temperatures. Around 160ºC, the surface of the fibers starts to develop bubbles. Above 200ºC the fibers start losing their shape, eventually resulting in an unoriented melt.

In order to test for the stability of the sterocomplex fibers at high temperature, we heated them at 5ºC/min in a Linkam hot stage and observed the changes under a microscope (**Figure 2.9**). The stereocomplex fibers stayed integral up until a temperature close to the melting point of the stereocomplex. During heating, some bubbles occurred on the fiber surface, which are most likely due to the solvent trapped within the polymer network.

2.4. Discussion

Wet spinning of PMMA stereocomplex was developed in order to circumvent the long annealing times necessary for forming the PMMA stereocomplex directly in the melt. It was reasoned that melt spinning the stereocomplex PMMA would have resulted in amorphous fibers that would have had to be annealed for a very long time in order to achieve crystalline stereocomplex fibers.

The choice of dichloromethane as the solvent was made because PMMA stereocomplex does not form in this solvent. High concentrations of PMMA stereocomplex in DMF or other stereocomplex promoting solvents result in a gel, which does not flow. Therefore it is not possible to process stereocomplex solutions in DMF without heat treatment.

The concentration of stereocomplex PMMA was important for fiber spinning. If the concentration is too low, the fluid jet is unstable and instead of a smooth filament

only droplets are formed. The force that drives the fluid into spherical droplets is the surface tension and this is known as Rayleigh instability[93]. As the concentration is increased, the viscosity of the fluid also increases. At some point, the viscosity is high enough that the jet becomes kinetically stable and does not break up into droplets immediately. It is the time scale of this brake-up that depends on the fluid viscosity. Thermodynamically, the cylindrical filament is not the most stable form. In our experiment, the concentrations below 20% in dichloromethane all yielded droplets at the timescales needed for the experiment[91,93,94]. At 20% the Rayleigh instability was trapped and pearls-on-a-string type fiber was made when the jet passed through cold methanol. When dichloromethane diffuses out of the filament and all that is left is the PMMA, the filament is kinetically trapped. When the concentration of stereocomplex PMMA is 30%, the fluid jet remains in the smooth cylindrical form for the duration of the experiment.

Methanol has proven to be the best for the coagulation bath among the solvents we tried. The problem with the DMF-water mixtures appeared to be that the phase separation would occur too fast. When the water concentration was low, a brittle skin formed on the outside of the fiber, while the inside was still liquid. These fibers would then break. When the water concentration was higher, the whole fiber would quickly phase separate and the resulting bright white fibers were extremely brittle. These fibers also contained no stereocomplex as evidenced by DSC. This behavior suggests that as soon as the water diffused into the fiber, phase separation would occur. The phase separation was too fast to allow stereocomplex formation. Dichloromethane/water/DMF/PMMA is a quaternary system, hence the phase diagram is

certainly complicated and it is hard to be too specific about the reason for such behavior. The immiscibility of dichloromethane and water might have been problematic in this complicated mixture. The DMF-water mixtures were thus found to complicate the fiber-spinning process without any benefits. Petrolether has been reported to have been used as the coagulation bath in wet-spinning of SBR/ PMMA core-shell particles into fibers[92]. Most likely the presence of SBR blocks influenced the phase separation behavior of the polymer. In the case of stereocomplex PMMA, there are no solubilizing SBR blocks present and therefore the phase separation is faster. Therefore flaky precipitate was formed when petrolether was used as the coagulation bath. Petrolether was thus found to be unsuitable as the coagulation bath liquid for stereocomplex fiber spinning. Methanol is miscible with dichloromethane and PMMA is not soluble in methanol. Thus, diffusion of dichloromethane out of the filament and of methanol into the filament is facilitated. Because methanol does not dissolve PMMA, phase separation occurs wherever the methanol concentration within the filament becomes large enough. The PMMA fiber is thus formed from the outside in.

The mechanism of fiber formation is tightly linked to the resulting fiber properties[95]. The formation of the polymer fiber from outside in means that the sections of the fiber that are further away from the centre have spent a longer time in the presence of non-solvent. Furthermore, the polymer chains are stretched during the fiber forming process, which gives the fibers greater strength in the axial direction[95]. In addition to Young's modulus, orientation might also affect the crystallization behavior.

The polymer chains in the filament are deformed in two stages – first, when they are pushed through the spinneret and second, when the filament is stretched in the coagulation bath. In our spinning experiment, a higher rate of extrusion was not available, because then also the pick-up rate has to be higher to compensate. This leads to a shorter residence time in the coagulation bath. The shorter residence time means that the non-solvent methanol cannot diffuse fully into the filament and the resulting fiber was too soft to be spun. In addition to that, high die-swell at high extrusion rates prevented using higher extrusion rates. The resulting swollen filament could not be stretched, because the thin skin formed on the outside would break and then the soft liquid inside would pinch, breaking the filament. Therefore the filament stretching was only tested by keeping the extrusion rate the same and varying the pick-up speed. The pickup speed was varied from the highest possible speed that allowed the filament to be continuously wound up without braking (11.9 m/min), to the lowest possible speed, where the pick-up speed was roughly matched with the extrusion rate (4.0 m/min). In this set-up, the filament stretching and the residence time in the coagulation bath are varied in conjunction. The lower the pick-up speed, the longer the residence time.

The DSC analysis of the as-spun fibers has shown no stereocomplex formation. There was a broad peak present at 155ºC, but no characteristic stereocomplex PMMA peak around 172ºC[62,64,65]. The presence of the peak at 155ºC has prompted us to investigate the behavior of theses fiber upon thermal annealing. Previous studies[62,64,65] on the crystallization of stereocomplex PMMA have shown that thermal history and crystallization temperature have a significant effect on the crystallization rate. The

optimum temperature in order to achieve maximum crystallinity was shown to be 140ºC[62,65] and that was the temperature used for our experiments.

The location of the melting peak is drifting towards lower values as the crystallization time gets longer and longer (**Figure 2.2**). It appears that the stereocomplex crystals initially formed are larger than the crystals formed after prolonged crystallization. This behavior would be consistent with the mechanism proposed by Schomaker and Challa[62]. They have proposed that the melting peak at high temperatures (>200ºC) is the result of lamellar crystal growth and the melting peak at lower temperature (~180ºC) is the result of fringe-micellar crystallite growth[62].

When we compare the crystallization rates of unoriented stereocomplex PMMA mixtures to the wet-spun stereocomplex PMMA fibers, we notice a much faster crystallization rate at the start of the process (**Figure 2.3)**. The unoriented stereocomplex PMMA mixtures exhibit a 12 to 24 hour induction time, while the wet-spun fibers begin crystallizing immediately. There are two possibilities for explaining the faster stereocomplex formation in fibers compared to the non-aligned material in bulk or sheet form. The first is that the molecular orientation during fiber spinning brings the polymer chains into a favorable conformation for further stereocomplex formation during the annealing process. The second explanation is that the fiber formation in the methanol coagulation bath produced nucleation sites for further crystallization. Fibers produced at 4 m/min and at 11.9 m/min exhibited very similar crystallization behavior. The fiber spun at a higher rate reached slightly higher final crystallinity, but the fiber spun at the lower rate exhibited slightly faster crystallization during the first day. This is consistent with the proposed fiber-forming mechanism, where methanol initiates fiber formation from the

outside into the center of the filament. The fiber spun at a lower rate spends more time in the coagulation bath and therefore the microcrystallites have more time to grow. The microcrystallites act as nucleation sites during the crystallization process. Therefore, the initial crystallization rate is higher for the fiber that has spent more time in the coagulation bath. The final crystallinity after 7 days of annealing of the more oriented fiber was found to be higher, implying that the final crystallinity of the fiber is affected by the chain orientation. It is also possible, that the initial crystal growth out of the microcrystallites is lamellar, resulting in higher melting temperature than the subsequent fringe-micellar grown crystals[62].

The evidence for this mechanism is the presence of small microcrystallites on the surface of the wet-spun stereocomplex fiber. Rough surface was observed on the surface of stereocomplex fibers under the optical microscope and more clearly under SEM. This roughness was not present on the atactic PMMA wet-spun fiber that was made under the exact same conditions. Since atactic PMMA is amorphous, there is no possibility of microcrystallites being present. Therefore it was concluded that the rough surface of the stereocomplex fiber were small microcrystallites of stereocomplex PMMA.

The mechanical properties of the oriented stereocomplex PMMA fibers were tested before and after crystallization. Tensile testing has shown superior quality of these fibers compared to bulk atactic, unoriented PMMA. Young's modulus of unoriented PMMA is typically 1 GPa[79,83] and the stereocomplex PMMA fibers have a maximum modulus of 3~4 GPa after crystallization. These values are also comparable to the

oriented atactic PMMA fibers obtained by melt spinning (3.5 GPa)[79]. Threefold increase of Young's modulus over bulk material shows that these oriented stereocomplex PMMA fibers may be used as the reinforcement material. A major difference between the stereocomplex PMMA fibers and atactic PMMA fibers is in their brittleness. The stereocomplex PMMA fibers break between 1% and 2% elongation, testifying to their brittleness. The atactic PMMA fibers are not quite as brittle, reaching elongation at break of up to 10%. This can be attributed to the presence of the crystalline fraction in the stereocomplex PMMA fibers. The oriented crystalline domains increase the strength in the longitudinal direction of the fiber. However, the crystalline regions cannot be stretched and therefore the failure mode for stereocomplex PMMA fibers is brittle fracture. Tensile testing has also shown that the wet-spun stereocomplex PMMA fibers were not as uniform as the microscopic inspection led us to believe. The modulus of the fibers tested had a very broad range.

The temperature stability of the stereocomplex PMMA fibers is important for their use as a reinforcement material. The composite has to be processed at a high enough temperature to allow the matrix polymer to flow. Previous work on self-reinforced composites based on atactic PMMA fibers has shown that the processing temperature needs to be between 120-140 ºC and that the processing time is crucial[82-84]. The atactic PMMA fibers are not very stable under high temperature and the orientation of the polymer chains is rapidly lost[80]. A single a-PMMA fiber heated in a hot stage under the microscope results in fiber breakage through Rayleigh instability at 130ºC. In contrast, the wet-spun stereocomplex PMMA fibers retain their shape and orientation up to 160ºC.

The crystalline PMMA stereocomplex regions increase the fiber stability and orientation retention.

2.5. Conclusions

Wet-spinning was shown to be a viable method for producing continuous stereocomplex PMMA fibers. The resulting fibers needed to be thermally annealed in order to obtain a satisfactory degree of crystallinity. The stereocomplex crystallization in the wet-spun fibers proceeded faster than a non-oriented non-fibrous stereocomplex PMMA. The reason for that is the formation of nucleating microcrystallites on the fiber surface from the contact with methanol.

The mechanical properties of the wet-spun stereocomplex PMMA fibers are superior to non-oriented PMMA and comparable to atactic PMMA fibers. The advantage of the stereocomplex PMMA fibers is their stability at high temperatures. This is an important characteristic for composite reinforcement and processing. The disadvantage of the wet-spun SC-PMMA fibers is their brittleness.

CHAPTER 3

PMMA STEREOCOMPLEX FIBERS *via* GEL SPINNING

3.1. Introduction to gel spinning

Gel spinning is a fiber-forming process for high strength fibers through an intermediate gel-like state[96,97]. Stereocomplex PMMA solutions form thermoreversible physical gels in strongly-complexing solvents, therefore it is possible to use gel spinning to make high-strength PMMA fibers. Since atactic PMMA solutions do not form gels, it is not possible to gel-spin atactic PMMA fibers and compare their properties. Similarly, neither iso-PMMA solutions alone, nor syn-PMMA solutions of the polymers in our investigation formed a gel in DMF. Only the mixture of the isotactic and syndiotactic PMMA solutions can form a gel.

Extrusion from the spinneret is the most important phase of the fiber spinning process[95]. A falling fluid jet will break up into droplets. This has been recognized by Lord Rayleigh and is thus termed the Rayleigh instability [93]. In order for a stable and smooth fiber to form, the viscous force has to balance the surface tension (illustration in **Figure 3.1**). The parameters influencing the stability of the fluid jet are: jet diameter D, fluid viscosity η, fluid surface tension σ, jet speed U . The jet is stable over a longer distance L if the fluid is more viscous, the surface tension lower and the jet diameter larger. The analytical expression dealing with jet stability has been found [94,98]:

$$\frac{L}{D} = C\left(\sqrt{We}\left(1+3Oh\right)\right) \qquad \text{Eq. 3.1}$$

Here, C is an empirical constant usually equal to 13[94], We is the Weber number $We = \left(\frac{\rho U^2 D}{\sigma} \right)$ and Oh is the Ohnesorge number $Oh = \left(\frac{\eta}{\sqrt{\rho D \sigma}} \right)$. This theory of jet breakup only gives us an approximation, because there are certain assumptions made about the contribution of inertia in its derivation. In addition to that, our system is non-Newtonian and viscosity is constantly changing as soon as the fluid jet leaves the needle tip. We cannot really know the exact viscosity at the spinneret. However, we can get an estimate of jet breakup, along with general trends. From **Equation 3.1** and definitions of the Weber number and Ohnesorge number, we can see that the jet stability grows with increasing diameter D as well as the speed U. Therefore we have to extrude the liquid at the fastest speed possible to avoid jet breakup. We should also use a large diameter spinneret. In our case the extrusion speed was limited by the speed of the syringe pump. We can modify the extrusion speed by choosing a proper syringe – a large diameter syringe with a small orifice will give a higher extrusion speed. However, if the extrusion speed is too high, it is hard to grab hold of the fiber and guide it to the pickup roller. In addition to that, at high extrusion speeds die swell may occur. Die swell is a phenomenon that occurs when a polymer solution rapidly exits a die[99]. The fluid swells right after the die opening and therefore the diameter of the jet is larger than the diameter of the opening. Die swell is largely dependent upon the shear rate at which we are pushing the fluid through the die.

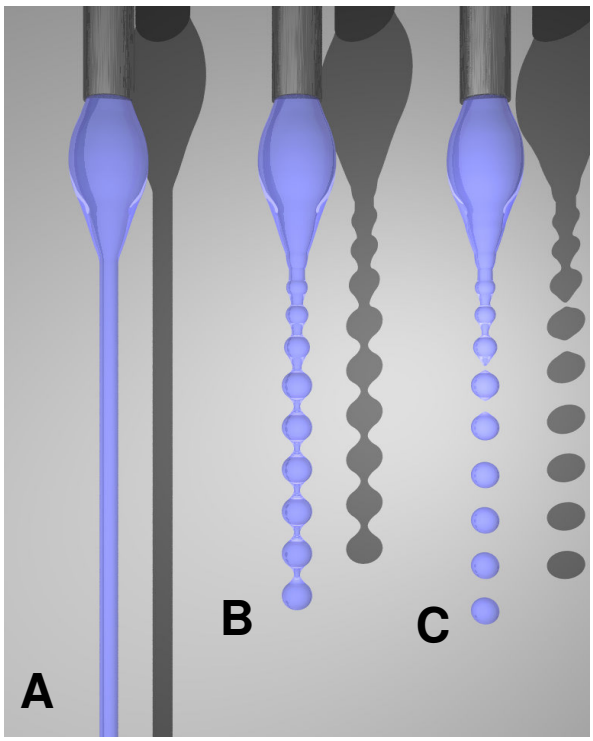

Figure 3.1: Illustration of three different concentration regimes and the influence on fiber formation. (A) 20% DMF concentration and the resulting smooth fiber. (B) 15% concentration results in a beads-on-s-string morphology and (C) 10% concentration results in droplets.

3.2. Experimental

Dimethyl formamide (DMF), dichloromethane and methanol were purchased from Acros Organics. Isotactic-PMMA ((Mw = 300,000, PDI = 9.4, isotactic triads: >95%) and syndiotactic-PMMA (Mw = 50,000, PDI = 1.3, syndiotactic triads: 85%) were purchased from Scientific Polymers Co. All reagents were used without further purification.

Fiber was spun using KDS100 syringe pump (KD Scientific). Differential scanning calorimetry was carried out with Seiko DSC 220. Hitachi S800 FEG and LEO

1530 scanning electron microscopes (SEM) was used for the fiber surface imaging, and Leica RDX polarized light microscope was used for the fiber diameter measurements and birefringence observation. Leica SP-1 laser confocal microscope was use for 3D fiber imaging. Synchotron X-ray crystallography was done using Advanced Photon Source at Argonne National Lab at 0.765335Å along with Mar 3450 area detector.

Iso-PMMA and syn-PMMA and a small amount of pyrromethene 546 fluorescent dye were dissolved in hot DMF to make a solution with iso-:syn-PMMA ratio of 1:1. Since this mixture in DMF forms a gel at room temperature, the hot solution was transferred into a glass syringe (50ml) and was kept at high temperature (~110°C) by wrapping electric heating tape around the syringe. The solution was rapidly squeezed out through the Teflon syringe orifice into a cold methanol (-20°C) bath at 500ml/h. The resulting gel with a variable diameter between 0.6 and 1 mm was uniaxially stretched on a hot plate at 140°C.

3.3. Results and Discussion

DMF is a stereocomplex promoting solvent for PMMA and stereocomplex PMMA solutions in DMF form thermoreversible physical gels. In order to pick the proper solvent from the spinning dope, we have assessed the crystallinity obtained by evaporating the solvent from a solution of the PMMA stereocomplex in two strongly complexing solvents, acetone and DMF. To this end, we have utilized X-ray analysis and DSC analysis. The DSC analysis showed roughly the same melting enthalpy for both experiments (~42 J/g). However, the X-ray analysis has shown that DMF is a better

choice for obtaining highly ordered crystalline stereocomplex PMMA (see **Figure 3.2** and **Figure 3.3**), because the diffraction peaks were sharper.

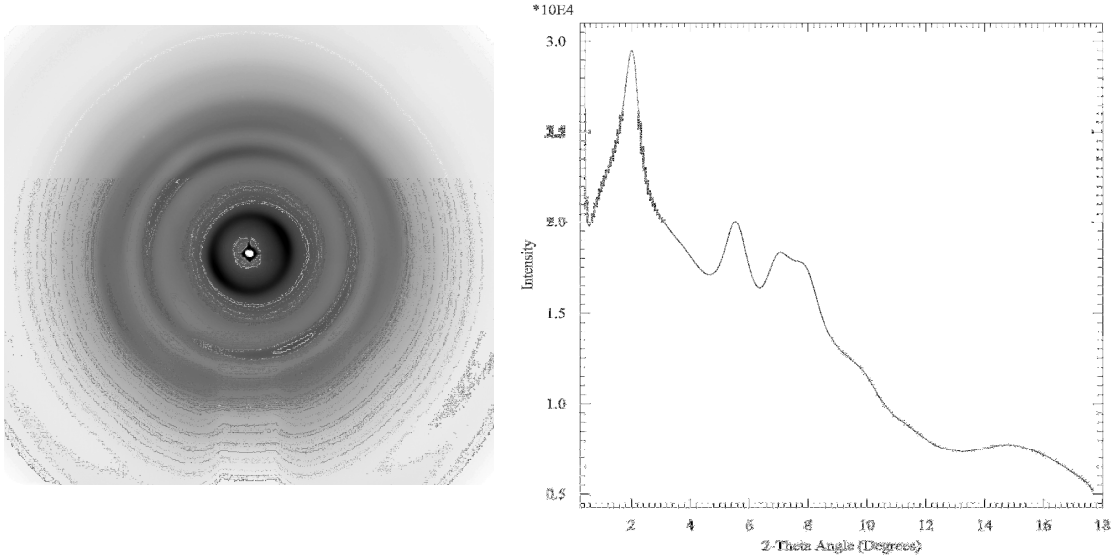

Figure 3.2: X-ray powder diffractogram of stereocomplex PMMA obtained by evaporating a DMF solution. Sharp peaks indicate orientational order of lattice. Peaks correspond to the spacings of 21.9, 7.9, 6.2, 5.6, 4.5, and 3.0 (Å).

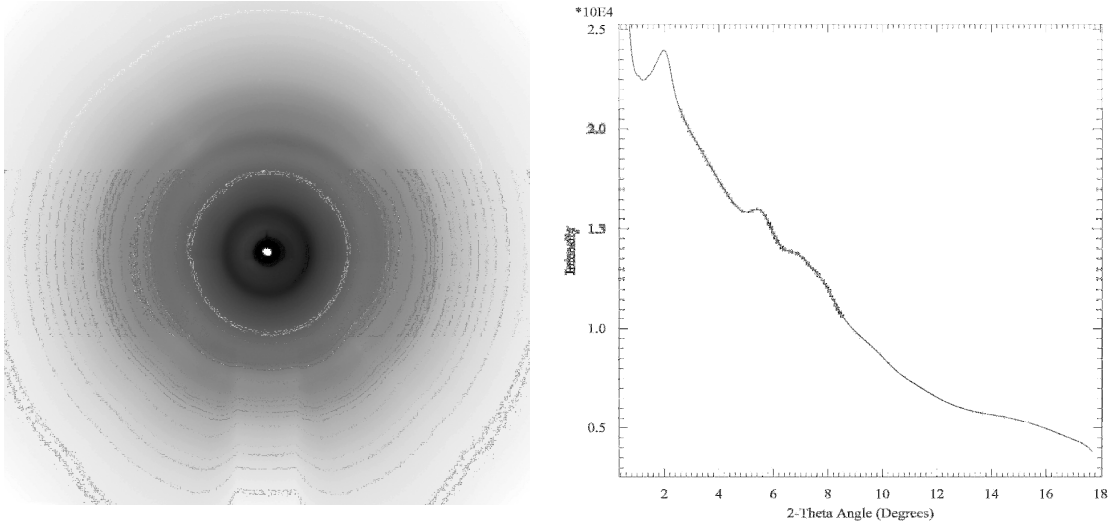

Figure 3.3: X-ray powder diffractogram of stereocomplex PMMA obtained from evaporating an acetone solution. Sharp peaks indicate orientational order of lattice. Peaks correspond to the spacings of 21.9, 7.9, 6.2, 5.6, 4.5, and 3.0 (Å).

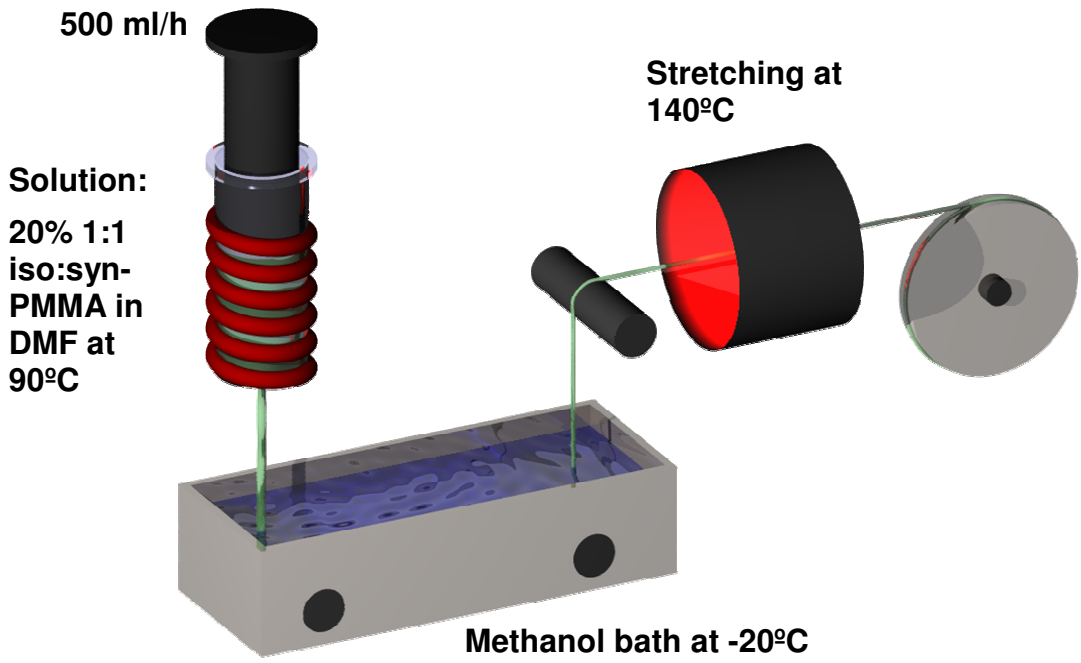

Figure 3.4: Gel-spinning apparatus. The polymer solution is charged into a heated syringe. The solution is injected into a cooling bath so that the fluid jet travels through the air first. The fluid jet is guided through the cooling bath and a gel fiber emerges at the other end. The gel is subsequently stretched into a polymer fiber at elevated temperature, where the solvent also evaporates.

The gel spinning was done using a similar setup as in wet spinning. However, the sample syringe was heated to a sol state for viscosity control and optimum extrusion. The extrusion syringe was not dipped in the cooling bath, but elevated about 3-5 cm above the liquid level. Die swell was observed in that region. The purpose of the air gap is to provide some gentler cooling without a fluid around the jet. The distance from the cooling bath vas not optimized. We added a fiber drawing step to increase the molecular extension and crystallinity (see **Figure 3.4**). The fiber drawing was not performed in line, but rather the gel fiber was collected and subsequently stretched between two rollers and a hot zone.

We have tried gel-spinning with the standard spinnerets, which are very small. The 250 μm spinneret resulted in jet breakup no matter what extrusion speed was used. Therefore we used a syringe with a 1.5 mm wide opening for the spinneret. At the extrusion rate of 500 ml/h, the 20% 1:1 isotactic : syndiotactic PMMA solution could be spun into a continuous fiber. Lower concentration of 15% resulted in beads-on-a-string morphology and at 10% the fluid jet brakes up into droplets due to the Rayleigh instability (illustrated in **Figure 3.1**). In order to characterize the fiber morphology, a small amount of pyrromethene 546 fluorescent dye (<10 ppm) was added to the spinning dope.

Another parameter that had to be carefully controlled was the temperature of the spinning dope. Because viscosity decreases with temperature, the solution needs to be heated just above the gel point in order to make it flow and keep the viscosity as high as possible. Because the stereocomplex PMMA solutions in DMF exhibit gel-point hysteresis (discussed in Chapter 4), the solution was first heated to 105ºC, then slowly cooled to 90ºC and extruded at 500 ml/h.

The thickness of the gel formed in cold methanol bath was between 0.6 and 1 mm. The gels were further stretched at 140°C. The maximum draw ratio achieved was 4. The profile of the resulting drawn fibers was not circular, as shown in **Figure 3.5**. This was due to the stretching of the gel on the take-up reel.

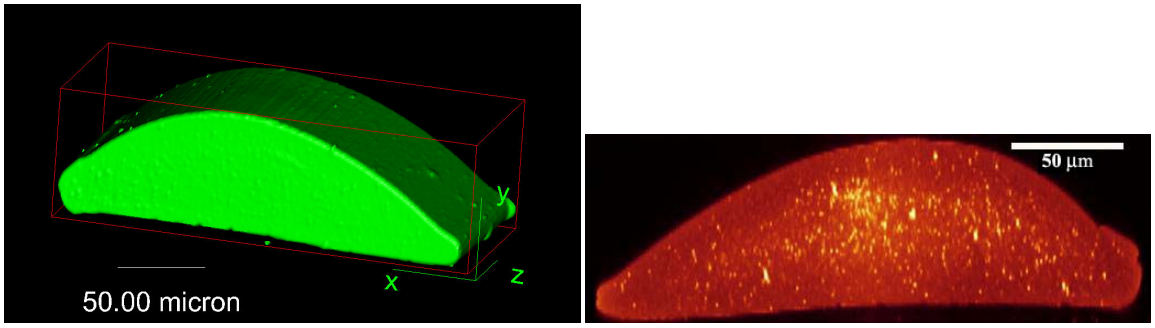

Figure 3.5: A 3D reconstruction (left) of the stretched gel-spun fiber from a series of confocal microscopy images in xy planes (right) in false colors. Z-axis direction is the fiber axis direction.

The drawing process determines the polymer chain orientation. The maximum draw ratio (Λ_{max}) of a single chain attainable is determined by the transition from a random coil into a perfectly extended chain. The end-to-end root mean square distance for a freely-jointed chain is[100,101]:

$$\left\langle r^2 \right\rangle^{1/2} = \sqrt{n}b \qquad \text{Eq. 3.2}$$

where r is the end-to-end distance, n is the number of repeat units and b is the length of each repeat unit. The maximum end-to-end distance of the fully extended chain is simply the product of the number of repeat units and their length[100,101]:

$$r_{\max} = nb \qquad \text{Eq. 3.3}$$

The maximum draw ratio then becomes proportional to the square root of molecular weight:

$$\Lambda_{\max} = \frac{r_{\max}}{\left\langle r^2 \right\rangle^{1/2}} = \sqrt{n} \propto M_w^{0.5} \qquad \text{Eq. 3.4}$$

Any draw ratio higher than this maximum value must be due to chain slippage. Higher molecular weight allows for a larger draw ratio. However, it is not individual molecules that are stretched during gel stretching. The structure being stretched is a transient gel network, where chain entanglements act as nonlocalized junctions[102]. The molecular weight between entanglements in solution is approximated by[100,101]:

$$(M_e)_{sol} = (\rho / c) M_e = M_e / \phi \qquad \text{Eq. 3.5}$$

where M_e is the molecular weight between entanglements in an undiluted polymer melt, ρ is the bulk density of the polymer, c is the weight fraction and ϕ is the polymer volume fraction.

We can see that in order to increase the molecular weight between entanglements in solution, we need to decrease the concentration. However, the concentration should not be decreased below c^*, the critical overlap concentration. Below c^* the polymer chains do not interact with one another and the continuous network cannot form. So far we were only discussing general properties of linear polymers in solution. This is the state in which the polymer solution is above the gel point temperature. During fiber spinning, the polymer solution is ejected from the spinneret and rapidly cooled down. The macromolecular network with low entanglement density is additionally stabilized by the formation of the gel, however we can assume that the number of intermolecular interactions is not much higher than the number of entanglements. Furthermore, the gelation interactions are reversible and thus the chains may slip past each other without affecting the maximum draw ratio. In contrast, entanglements cannot be smoothed out.

We have to stress that the gelation interaction in the case of polyethylene is crystallization of linear polymer chains[103]. In the case of stereocomplex PMMA, the interaction is between helices. It has been shown that the packing of multiple helices is primarily responsible for stereocomplex PMMA gelation[54]. In that case, it is possible for the packed helices to slide past each other. In contrast, gelation crosslinks where multiple polymer chains take part in the formation of the stereocomplex triple helix would act as permanent crosslinks and would influence the maximum draw ratio.

For polyethylene gels it was also found that removing the solvent did not significantly change the number of intermolecular interactions[103]. The dried gels were as stretchable as the wet gels, the only difference being the ideal stretching temperature[103,104]

Analysis of the fiber crossection was further used in the analysis of mechanical properties. The cross-sectional area of multiple fibers was measured and used to calculate Young's modulus by using equation 3.6. Young's modulus was calculated according to the formula[105]:

$$E = \frac{Ml_0}{A} \qquad \text{Eq. 3.6}$$

where E is Young's modulus, M is the slope of the initial linear response, l_0 is the initial fiber length, and A is the cross-sectional area of the fiber.

Mechanical testing (**Figure 3.6**) has shown the fibers to behave as highly oriented brittle fibers. The deformation is close to elastic with a linear response until breakage, however there is appreciable deviation from linearity. Breakage occurs at short extension ratios between 2~4%. The average modulus was found to be 2.5 GPa with the highest values obtained around 3 GPa.

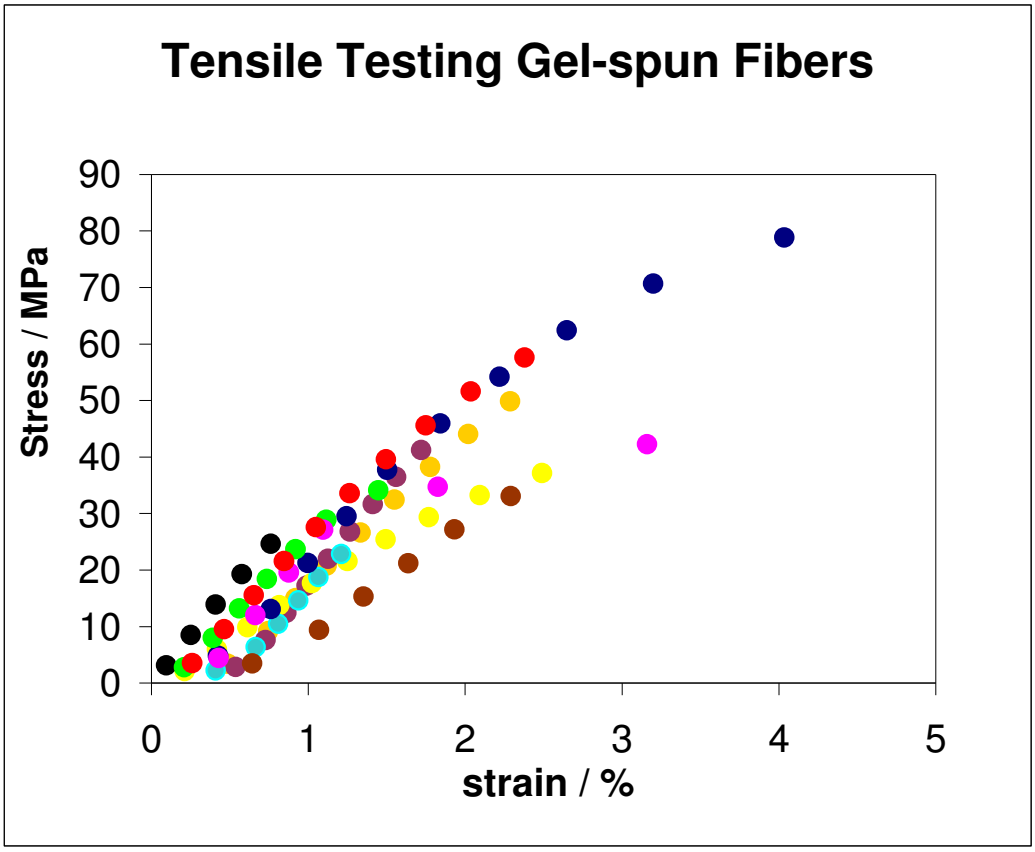

Figure 3.6: The results of mechanical testing of gel-spun stereocomplex PMMA fibers. Each color represents the results of a tensile test. The average modulus is 2.5 GPa.

X-ray analysis was performed to examine the fiber structure and compare to the previously published data on stereocomplex fibers[16,18,106]. The 2-θ plots in **Figure 3.7** and **3.8** exhibit six diffuse peaks found at angles corresponding to the following d-spacings: 21.2 Å, 7.9 Å, 6.4 Å, 5.8 Å, 4.5 Å, and 3.0 Å (shown in **Figure 3.9**). The peaks

corresponding to 21.2Å spacing can be assigned to the helix diameter. The peaks are perpendicular to the meridian direction, which was also the fiber axis direction in the experiment. The full range x-ray (**Figure 3.**8) confirms the smaller angle results without any further structures in different length scales.

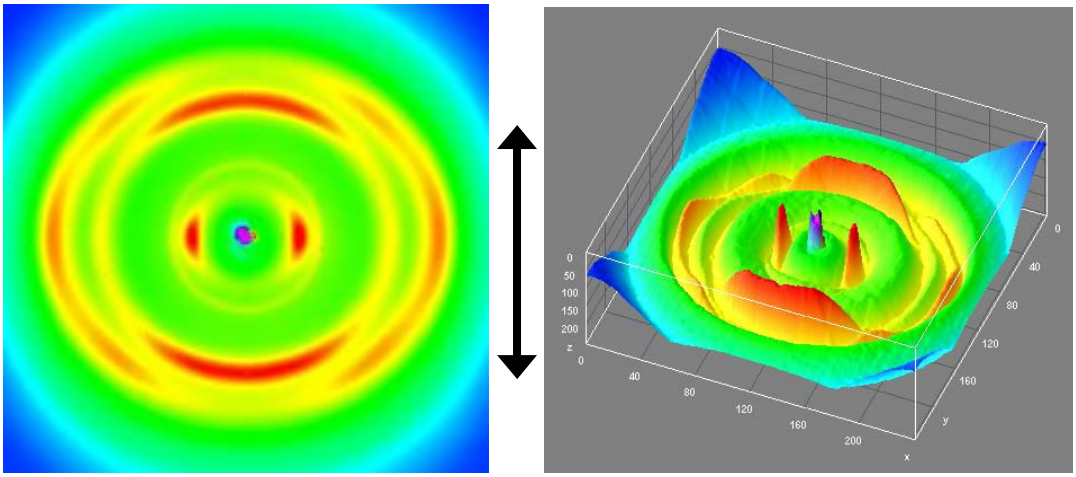

Figure 3.7: X-ray diffractogram in 2D (left) and 3D (right) of a gel-spun stereocomplex PMMA fiber. The fiber axis is denoted by the double-headed arrow.

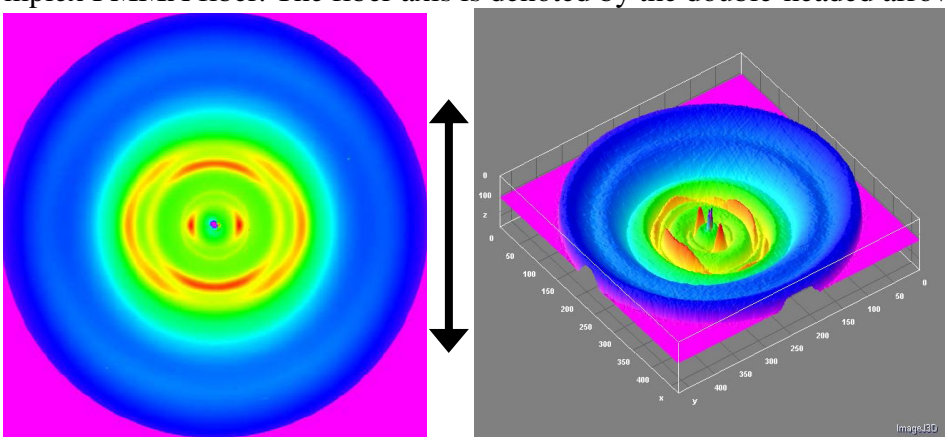

Figure 3.8: The full range X-ray diffractogram of the gel-spun stereocomplex PMMA fiber. The fiber axis is denoted by the double-headed arrow.

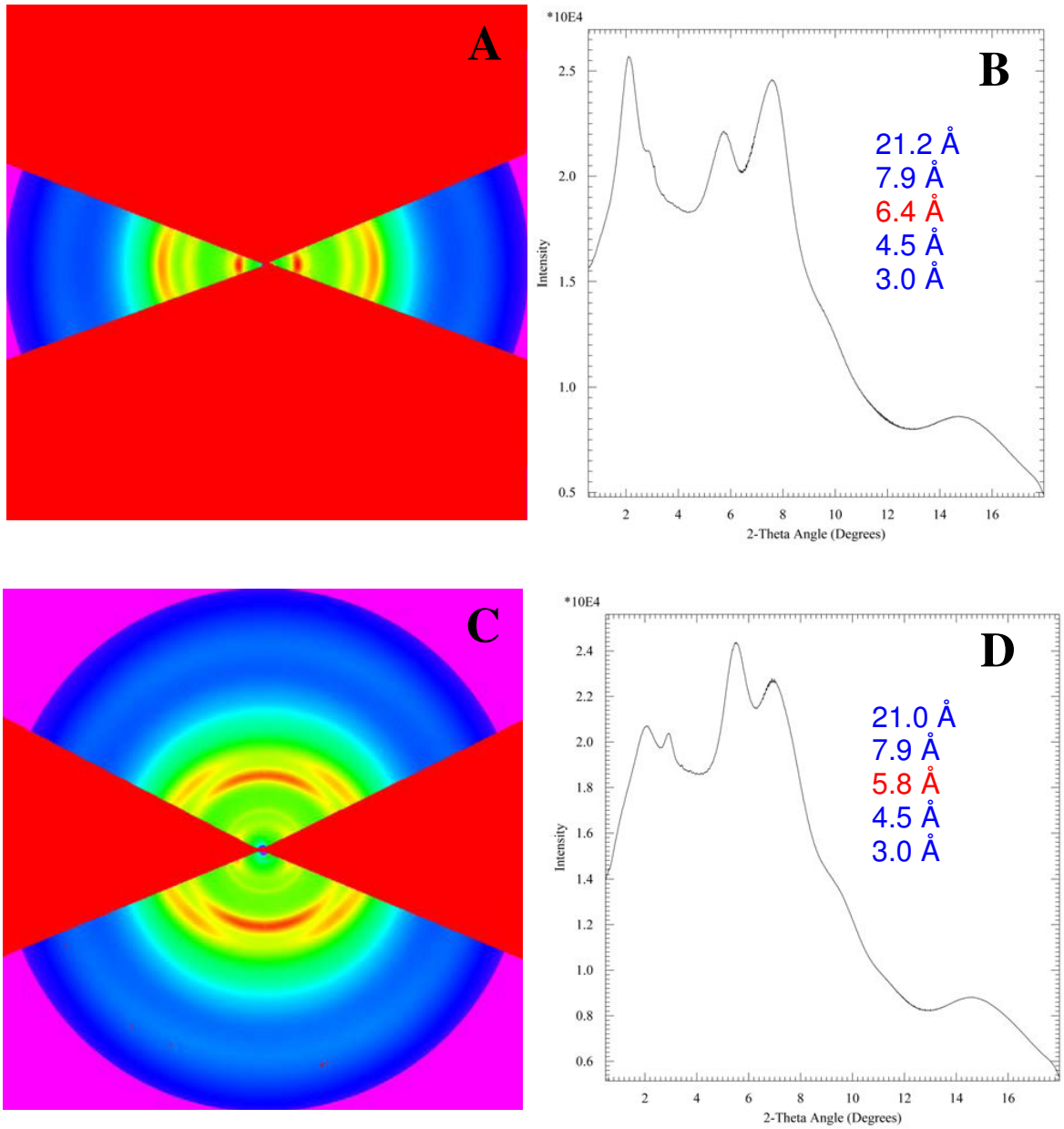

Figure 3.9: The intensity vs. 2θ angle plots for the diffractogram from **Figure 3.8**. Two separate regions are integrated to distinguish the peaks at 5.8Å and 6.4Å. (A) the region integrated and shown in (B) as an intensity vs. 2θ angle plot. Similarly (C) shows the region integrated and plotted in (D) as an intensty vs. 2θ angle plot

The peaks at 7.9Å could belong to the pitch spacing of the syndiotactic PMMA. However, in the model proposed by Kumaki *et al.*[107], the tilt angle between the polymer chain and the helix axis is estimated to be 78° with a 9.2Å pitch. The d-spacing can thus

be calculated as 9.2 Å * *cos (12º)* = 9.0Å. In the alternative quadruple helix model proposed in the same paper, where there are two syndiotactic PMMA chains wrapping around the isotactic PMMA double helix with a tilt angle of 65º from the helix axis, the d-spacing would have been 8.3Å (9.2Å * *cos (25º)*) . Lorentzian deconvolution of the broad doublet peak in the azimuthal scan locates two peaks at approximately 20º from the meridian. This result is similar to the one obtained by Schomaker and Challa[18], where the same reflection was found at 22.5º from the meridian. This implies that perhaps the quadruple helix model also mentioned by Kumaki *et al.*[107] is the correct one. In the quadruple helix model the angle between the polymer chain and the helix axis is 25º[107].

The peak at 6.4Å (9.2Å * *cos (45º)*) is the reflection from the isotactic PMMA double helix. The center of the peak is 45º from the meridian, which corresponds well with the model of the double stranded helix. At 9.2Å pitch and 45º angle, the expected d-spacing is 6.4 Å .

The next peak at 5.8Å corresponds to the spacing between oriented atactic PMMA chains and can therefore be assigned to be the chain dimension. The last peak at 3.0Å is very diffuse. It appears parallel to the chain axis and might be ascribed to the average spacing between side groups on oriented chains.

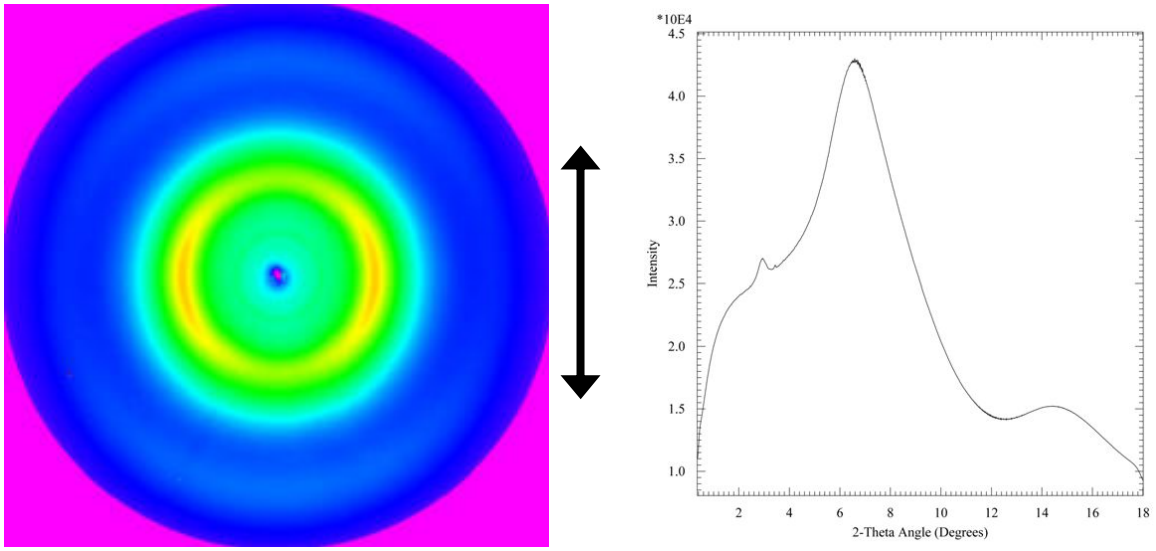

A **B**

Figure 3.10: The full range X-ray diffractogram of a melt-spun atactic PMMA fiber. The double-heade arrow denotes the fiber direction.

The good agreement between the isotactic PMMA double helix structure and the peaks in the X-ray diffractogram reaffirms the structure proposed by Kumaki *et al.*[107]. However, the reflections assigned to the syndiotactic PMMA chain are not in such agreement. The position of the peaks suggests a steeper tilt angle than the 78º proposed for the triple helix model. It is possible that Kumaki *et al.* acquired a different supramolecular structure by their Langmuir-Blodgett procedure. The surprising feature of their procedure is that the stereocomplex PMMA helix was formed in chloroform, which is a non-complexing solvent[30]. Stereocomplex formation has never before been observed in chloroform. It is entirely possible that the special conditions of high surface pressure during Langmuir-Blodget thin film preparation allowed the formation of the stereocomplex PMMA helix. However, it is also possible that the resulting structure is not an equilibrium structure and might be different from the one observed after stretching a stereocomplex PMMA gel in DMF into an oriented fiber as others did[13,16,18,30] or after

gel-spinning as we did. An intuitive explanation would be for the syndiotactic chain to become a bit more compact during fiber drawing and rearrange into a configuration with a tilt angle around 70º, while keeping the stoichiometry and the chain count constant. We thought that perhaps the drawing of the fibers resulted in the stereocomplex PMMA helices rubbing against each other and changing the syndiotactic PMMA tilt angle, because that chain is on the outside of the helix, however an undisturbed sample obtained by evaporating DMF from a solution shows the reflection at the same d-spacings (7.9Å) for the syndiotactic PMMA chains.

The melting temperature of the gel-spun fibers was 177.6°C even without annealing (see **Figure 3.11**). The melting enthalpy was high, 49.9 J/g.

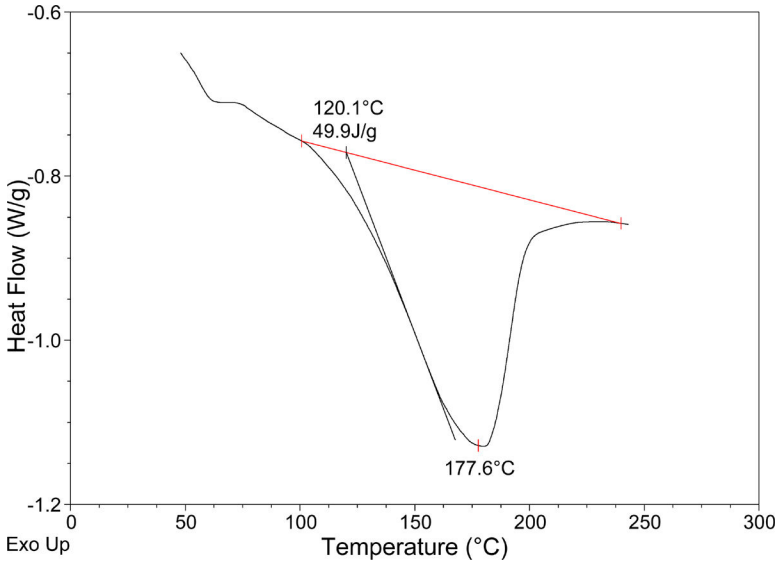

Figure 3.11: The DSC analysis of gel-spun fibers made from a 20% DMF solution. The exotherm points up in the graph. The peak is locatied at 177.6ºC and the melting enthalpy obtained by intergrating the peak area, as defined by the baseline, is 49.9 J/g.

SEM images (**Figure 3.12**) of the fibers show a smooth surface with no crystallites present unlike the wet-spun fibers (see **Figure 2.5**).

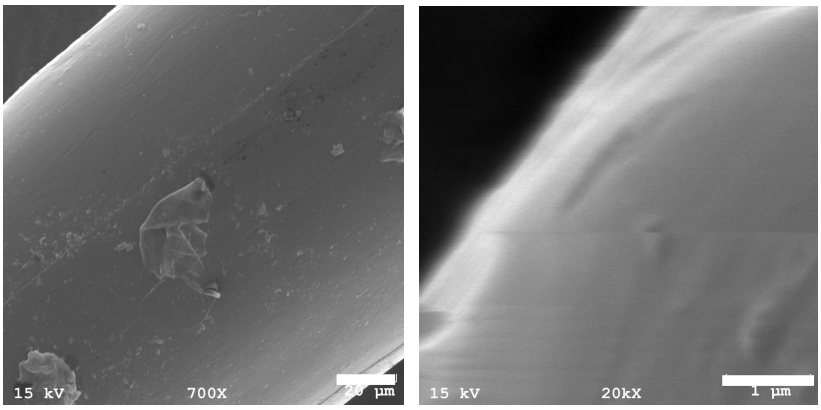

Figure 3.12: SEM images of the gel-spun fiber at different magnifications. The surface is smooth, with no visible microcrystallites present. Scale bars in left and right image represent 20 µm and 1 µm, respectively.

In order to improve the drawability of the gel spun fibers, we attempted to substitute the syn-PMMA with high molecular weight atactic-PMMA (Mw = 996,000). There are short syndiotactic sequences even in the commercially available atactic-PMMA and therefore mixtures of iso-/atactic-PMMA solutions also form gels. Solutions of 15 wt% iso-/atactic-PMMA in 1:2 ratio were viscous enough at 110°C to allow fiber spinning. The draw ratios achieved at 140°C in glycerol were around 20.

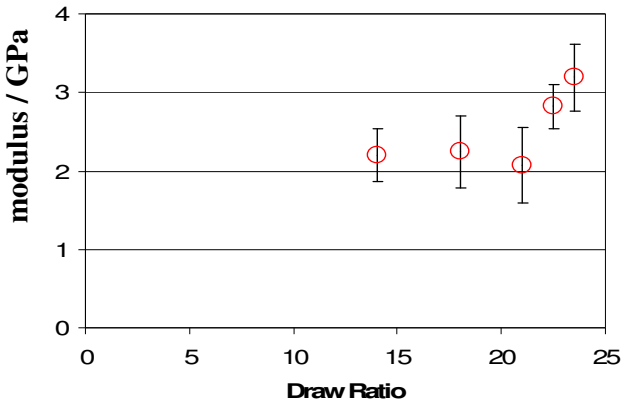

Figure 3.13: Results from drawing the isotactic : atactic PMMA stereocomplex gel-spun fiber. Young's modulus increases with draw ratio once the draw ratio exceeds 20.

In **Figure 3.13** we can see the results of tensile tests on the gel-spun isotactic : atactic stereocomplex. Unfortunately, the weak isotactic : atactic stereocomplex is dissociated when the draw ratio exceeds ~24. The drawing process at 140°C melted the stereocomplex and the stereocomplex formation would again take days of annealing at 140°C. It was not possible to lower the drawing temperature due to the high glass transition of the high molecular weight a-PMMA.

The polymers available for our study had rather low molecular weight for gel-spinning. In general, the molecular weight has to be higher, around $1*10^6$. Such a high molecular weight allows for a much lower concentration of the spinning dope. In our experiment, we have used 20 wt% solution as the spinning dope in order to achieve a high enough viscosity for good spinnability. In order for DMF stereocomplex solutions to behave liquid-like, they have to be heated above the gelation temperature. Under our gel-spinning conditions we heated the polymer solution to 110ºC. The viscosity of the

solution at this temperature has to be around 10 poise for good spinnability. To increase the viscosity of the PMMA mixture solution in DMF, we have used a 1:1 iso- : syn-PMMA mixing ratio instead of 1:2, because the isotactic PMMA that was available has a higher molecular weight.

Because the concentration of the polymer solution we used as the spinning dope was very high, there might be too many coil-coil overlaps formed, which hindered chain extension during the drawing process. The c/c* ratio for the 20% solution in DMF is 10, placing the solution well into the semi-dilute entangled regime[108].

Compared with the wet-spun fibers, the gel-spun fibers have a higher melting point and are therefore superior as a reinforcing agent. The enthalpy of melting was 18 J/g. Compared with the wet-spun fibers that does not seem like a significant increase, however, we have to keep in mind that the iso-:syn-PMMA ratio was 1:1, not 1:2, hence there was excess iso-PMMA not incorporated into stereocomplex formation. Also, the stereocomplex formation happens during the fiber spinning process and no lengthy annealing process is necessary.

3.4. Conclusions

We were able to utilize the thermoreversible gelation of stereocomplex PMMA solutions to produce oriented fibers by gel spinning. The fibers have a high melting point and are resistant to high temperature. The modulus of these gel-spun fibers is comparable to the melt spun atactic PMMA fibers.

We examined the basic structure of the stereocomplex. The X-ray data do not completely agree with the latest triple helix model proposed[107]. However, the data are

consistent with the previously published X-ray diffractograms[13,18]. A quadruple helix model[107] is a better candidate for the basic structure of the stereocomplex.

The formation of iso-/atactic-PMMA stereocomplex is encouraging, because it provides another avenue of composite reinforcement. The free isotactic chains in a semi-crystalline fiber are able to entangle with the surrounding atactic-PMMA matrix and form the stereocomplex, providing good interfacial reinforcement.

CHAPTER 4

ELECTROSPINNING STEREOCOMPLEX SOLUTIONS, WHICH FORM PHYSICAL GELS

4.1. Introduction

We have spun fibers from stereocomplex solutions using wet spinning and gel spinning, and observed that the birefringence is not lost even after treating the fibers at 160ºC. Herein we present a method for electrospinning PMMA stereocomplex solutions and discuss how these solutions behave differently from regular PMMA polymer solutions. We ascribe these differences to the properties arising from the multiple helix stereocomplex formation, namely the possibility of physical gelation.

Electrospinning is a fiber spinning technique capable of producing sub-micron size fibers. The first mention of the technique was almost a century ago in a patent[109] for forming fine fibers under a high electric field. In 1995 the technique was revived by Doshi and Reneker[110] and since then a slew of papers on the topic has appeared[111]. Electrospun fibers have been proposed to be used in a far ranging variety of applications, such as filters[112], superhydrophobic and superoleophobic surfaces[113], composite reinforcement[114], sensors[115], scaffolds for tissue engineering[116], drug delivery[117], supports for enzymes[118] and catalysts[119] and others[120].

The mechanism of electrospinning is fairly well known. A polymer solution is extruded from a syringe and high voltage is applied at the syringe tip. If the electric field

is strong enough so that the charge repulsion on the liquid droplet overcomes the surface tension, the solution is expunged towards a grounded target, forming a Taylor cone[121]. Bending instabilities result in a whipping instability[122-124], which is responsible for making very thin; sub micron size fibers (see **Figure 4.1**). During the electrospinning process, the solution undergoes rapid cooling due to the heat loss from solvent evaporation, if one uses rapidly evaporating solvents. This change in temperature is responsible for water droplet nucleation and growth, resulting in a surface structure[125], similar to the formation of breath figures[126-128]. The speed of the fluid jet is around 5 m/s, making the time of flight in our setup around 0.04 s.

Physical gelation is a phenomenon, where a liquid undergoes a reversible liquid-gel transition. The physical crosslinks in such a gel are reversible, in contrast to chemical gels where the crosslinks are irreversible strong covalent bonds. This reversibility and the associated viscoelastic behavior during the transition from a liquid to a solid is of great interest anywhere where a sharp, reversible transition from liquid to solid is needed, such as fracturing fluids in oil drilling, manufacturing of solid objects through molding, etc. The three dimensional network in a physical gel can undergo changes, as the bonds keep breaking and forming. In this chapter, we show how the process of gelation affects the electrospinning of stereocomplex PMMA solutions.

4.2. Results

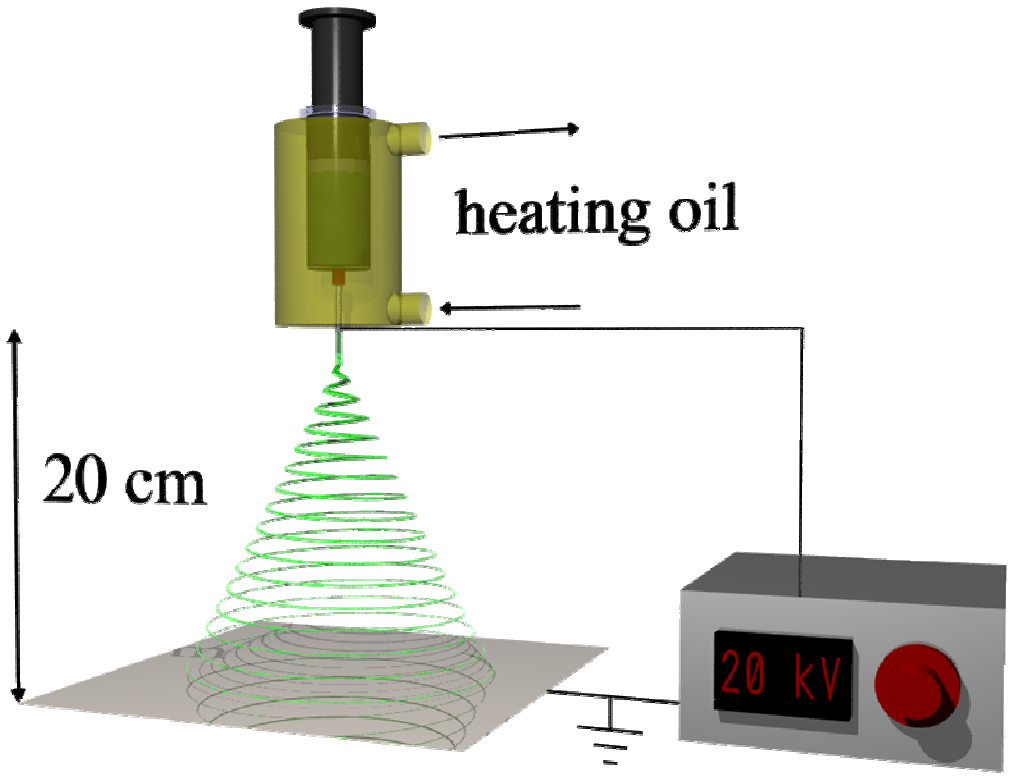

Figure 4.1: A schematic diagram of the electrospinning apparatus. The polymer solution is loaded in a syringe equipped with a non-conductive heating jacket. The needle tip is almost completely covered by the heating jacket to prevent gelation in the needle. The temperature is controlled by an external thermostat with flow-through silicone heating oil. The charged fluid jet undergoes bending and whipping and is collected on a grounded target.

We have dissolved iso-PMMA (MW 300,000, PDI 9.2) and syn-PMMA (MW 50,000, PDI 1.3) (both supplied by Polymer Source) in a 1:2 weight ratio in dimethylformamide (DMF, supplied by Aldrich, 99%) and heated the solution above the gelation temperature. DMF is classified as a "strongly complexing" solvent[21]. The

stereocomplex formation and physical gelation occur rapidly and readily. We have determined the gelation temperatures for different overall polymer concentrations in the range of 1.25-20 wt%, as shown in **Figure 4.2**. Solutions were sealed in glass vials and kept at a set temperature for 30 minutes. After that, the vials were tipped over and, if the solution flowed liquid-like, it was determined to be liquid or sol. If the solution did not flow, it was determined to be a gel. Upon heating, the gel-sol transition is about 22ºC higher than the sol-gel transition upon cooling. This hysteresis is similar in all the concentration ranges previously studied[129].

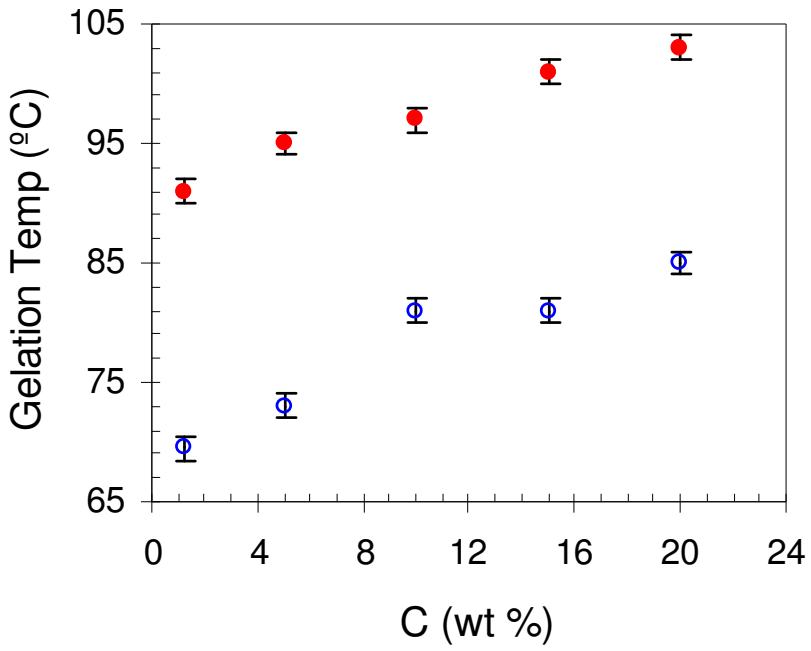

Figure 4.2: Gelation temperature at different concentration of 1:2 iso:syn-PMMA solutions in DMF. Filled circles represent the gel-to-sol transition temperatures upon heating and open circles represent the sol-to-gel transition temperatures upon cooling. The bars represent the range of gelation temperatures for three measurements.

It is not possible to electrospin any material in solid or gel form, therefore we first heated the stereocomplex PMMA/DMF mixtures above their upper gel points. The

solutions were transferred into a custom built electrospinning setup shown above, and kept there until their temperatures reached the equilibrium at selected temperatures.

We first examined the relationship between the concentration and the morphology of the spun fibers at 91ºC. We found that stereocomplex PMMA solutions in DMF above the gelation temperature can be electrospun into continuous fibers at a very low concentration, which is lower than what is necessary for a-PMMA solutions of the same molecular weight[108]. We then examined the influence of temperature of the solution on fiber morphology in the 96~105ºC.

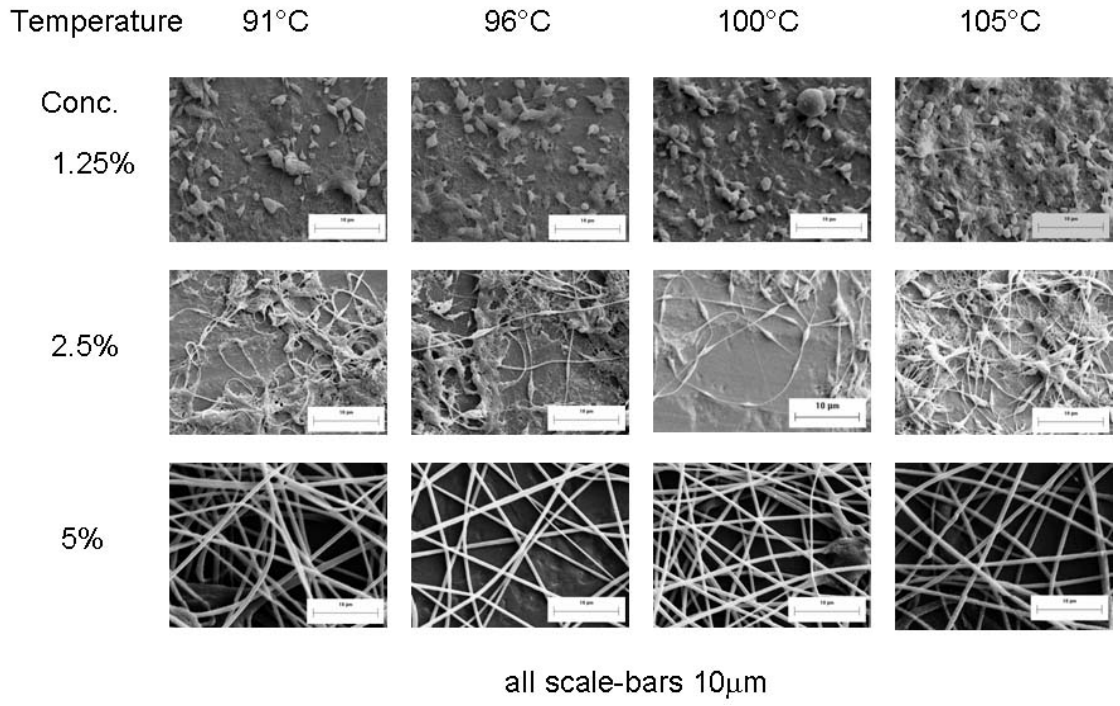

Figure 4.3: The effect of temperature and concentration of the spinning solution on the morphology of the electrospun stereocomplex PMMA. All the scale bars represent 10 μm.

In **Figure 4.3**, we display the different morphologies produced from the stereocomplex solutions in the 1.25 to 5 wt% concentration range at several temperatures. At 1.25 wt%, beads connected with very thin fibers are produced, at 2.5 wt%, the beads are connected with fibers, whose diameter is on the same order of magnitude as the bead diameter, and at 5 wt% smooth stereocomplex fibers are produced. The presence of stereocomplex was confirmed by differential scanning calorimetry (DSC) analysis of the fiber mats, which showed a melting peak at 172ºC.

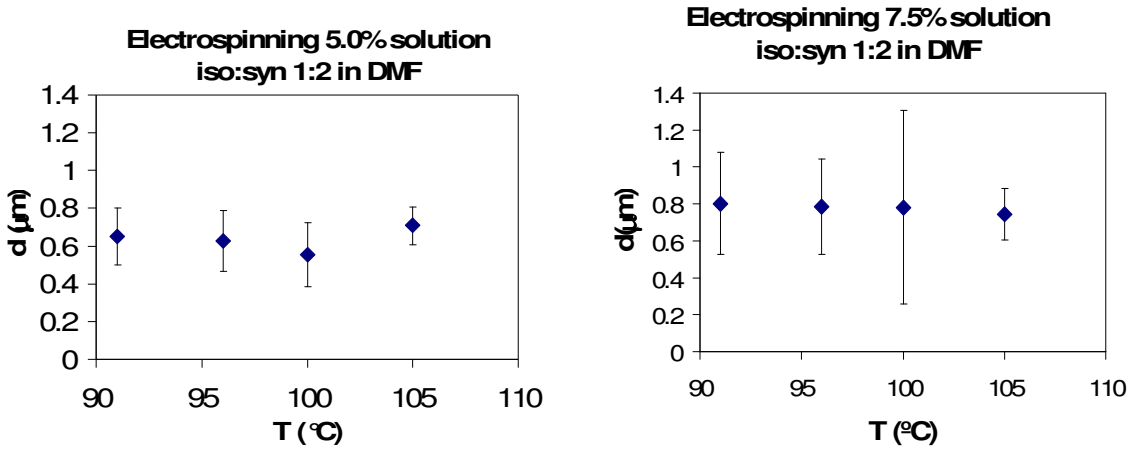

Figure 4.4: The results of fiber diameter measurements of electrospun fibers. Scale bars indicate one standard deviation.

The morphology of the electrospun fibers did not change with temperature, and the diameter of the spun products was also unaffected (see **Figure 4.4**). This behavior is in line with regular polymer solution behavior, because the surface tension and viscosity of the solution do not change drastically with temperature in the range studied. On the other hand, when the PMMA concentration was increased from 5 wt% to 7.5 wt%, the diameter of the electrospun fiber increased from ~0.64 µm to ~0.78 µm.

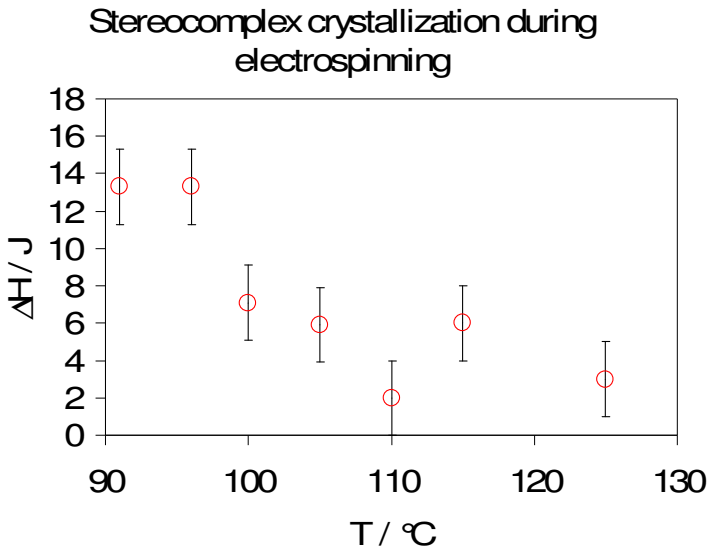

Figure 4.5: The melting enthalpy of electrospun fibers at various spinning temperatures. Vertical bars indicate the error estimated from the measurement due to the challenging definition of the baseline.

To study the effect of processing conditions on crystallinity, we analyzed the DSC traces of 7.5 wt% stereocomplex solutions in detail. We changed the temperature of the oil bath between 91-125ºC and measured the DSC trace for each sample. The fiber mats had similar diameters in each case. The DSC analysis showed a trend towards less crystalline fibers as the spinning temperature increased, as shown in **Figure 4.5**. The error in melting enthalpy was estimated to be 2 J/g, as that was the approximate variation from 3 samples. The samples with high melting enthalpy have less percentage error, because the peak baseline is better defined. The melting peak became more shallow and broad with increasing oil bath temperature (**Figure 4.6**).

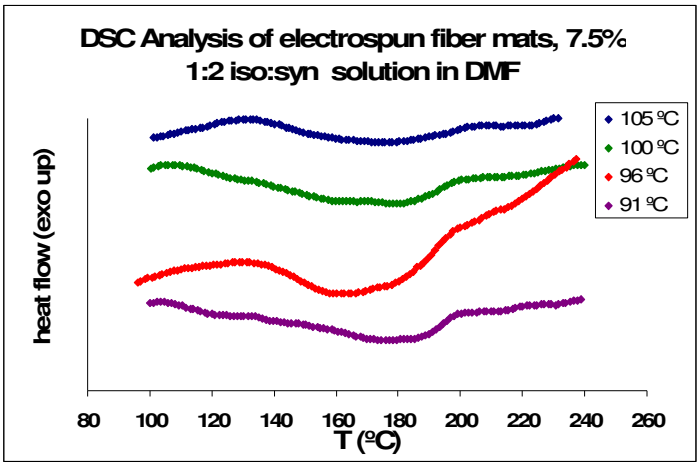

Figure 4.6: Representative DSC traces for 7.5 wt% stereocomplex solution in DMF. The melting peak becomes shallower and narrower with increasing spinning temperature.

In addition, the melting peak location shifted towards lower temperatures, as shown in **Table 4.1.** It has to be mentioned that the melting temperature for the low crystallinity samples is not very accurate, as samples processed under the same conditions differ as much as ± 10ºC. The melting temperatures shown are averages of three samples. It appears that the crystallinity decreases with increasing the temperature from the gel-point.

T(oil bath)/ ºC	T (melting peak) / ºC
91	182
96	172
100	180
105	170
110	160
115	150
125	160

Table 4.1: The melting temperatures of the electrospun stereocomplex fibers from the DSC traces in **Figure 4.6** and the corresponding oil bath temperatures.

The highest melting and most crystalline sample, the 7.5 wt% stereocomplex solution in DMF electrospun at 91ºC oil bath temperature, was analyzed by X-ray diffraction. The resulting diffractogram (**Figure 4.7**) appears symmetric, because the fibers were not oriented on the collection mat. The peaks are very sharp, indicating large crystallite size. The peak locations are the same as in gel-spun fibers discussed in Chapter 3.

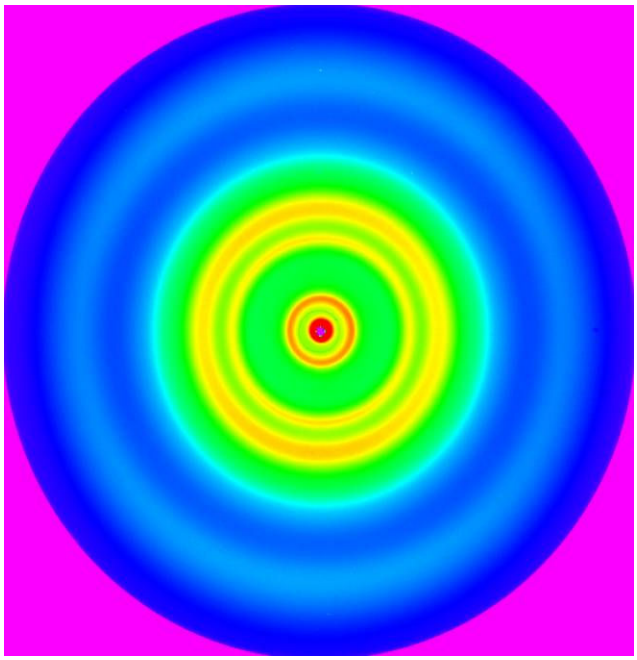

Figure 4.7: X-ray diffractogram of electrospun stereocomplex fibers.

4.3. Discussion

The viscoelasticity and spinnability of a polymer solution is closely related to the solvent type, temperature and polymer concentration. For a good solvent, where polymer-solvent interaction is favored over polymer-polymer interaction, the chains behave like a

single molecule below C*, the overlap concentration, related to molecular weight as $C^* \sim M^{-a} \sim M^{-0.6}$ from the Berry number and Mark-Houwink-Sakurada equation[91]. The parameters were taken from the literature[130]. As the name suggests, polymer chains start to overlap beyond the overlap concentration, and hence the viscosity of the system increases steeply with concentration above it. The values of C* are listed in **Table 4.2** for the solutions used in our experiments. The values were calculated by the Mark-Houwink-Sakurada equation, using the same parameters as Gupta *et al.*[108] (K = 0.015 mL/g, a = 0.66). While the increase in viscosity is linear with concentration for dilute regime, it increases by $C^{5.3}$ in semi-dilute regime[108]. This is due to presence of entanglements that act as temporary cross-links and hence also impart gel-like elasticity to the polymer solution. Gupta *et al*. have determined that a-PMMA solutions in DMF need a concentration ratio C/C* of at least 4 to produce smooth electrospun fibers[108]. This argument of overlap concentration is usually applicable for linear flexible polymer chains. It has been pointed out that the stereocomplex helix formation changes the persistence length of the polymer and makes it more rod-like[54]. In that case the critical overlap concentration becomes lower.

Table 4.2: The critical overlap concentration C* and intrinsic viscosity [η] in DMF

	Mw	[η] (mL/g)	C* (g/mL)
synPMMA	50000	20.4	0.049
isoPMMA	300000	67.5	0.015
aPMMA	350000	74.8	0.013
aPMMA	996000	150.3	0.007
1:2 iso:syn	133000	39.2	0.025
1:1 iso:syn	175000	47.1	0.021

The C/C* ratio of the 5 wt% stereocomplexing mixture that produced smooth fibers was 2 in our case, which is much lower than reported for linear a-PMMA polymers. We can attribute this to the helix formation and physical gelation during the electrospinning process. It has been shown previously that physical gels require a lower concentration to electrospin smooth, continuous fibers[131]. In our case, the comparison with a-PMMA is all the more relevant, as the only difference between the a-PMMA solution and the stereocomplex PMMA solution is the occurrence of physical gelation. During gelation, the polymer chains interact with each other and aggregate into a 3D percolated structure, essentially increasing the effective molecular weight of the system. The polymer chains can do this even below the critical overlap concentration C*. Therefore, C* is not the most important parameter that describes the interactions of a physical gel. The elastic modulus also increases during the gelation process. Recently, Yu et al. have determined that the elasticity of the fluid is more important for electrospun jet stability than the number of entanglements[132]. With solutions that will form physical gels, either argument can explain their peculiar behavior. The polymer chains associate in the solution, forming a crosslinked network. This structure increases the elasticity of the fluid and therefore stabilizes the fluid jet, resulting in smooth, continuous fibers at lower concentrations than those reported for non-complexing linear polymers.

The DSC analysis of crystallinity showed decreasing crystallinity at high oil bath temperatures. Since the oil bath temperature determines the temperature of the polymer solution, we can say that the further the temperature is from the gel point, the less crystalline the fiber. However, the fiber diameter appears to stay the same. These results

imply that the elasticity of the gel increases dramatically and fast, because the elasticity of the fluid jet is high enough to achieve smooth fibers even at high oil bath temperatures. We were expecting the fluid jet to break up at some point if the solution temperature was high enough so that the gelation would not occur during the electrospinning. However, since the fibers are smooth, the temperature drop during electrospinning must be rapid and deep enough to facilitate rapid gelation.

The X-ray analysis shows diffracted peaks at the same d-spacing values as the gel-spun stereocomplex fibers, indicating that the structure of the helix is identical. The peaks are sharp, implying large crystallites.

4.4. Conclusions

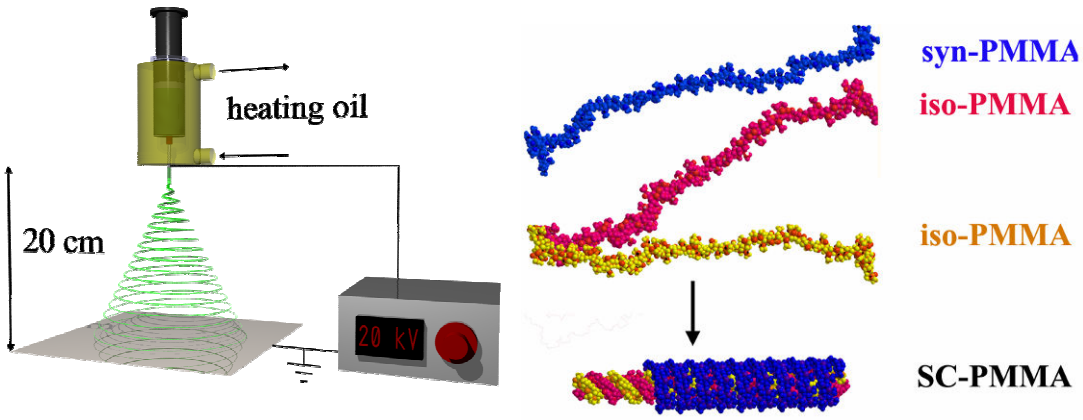

Figure 4.8: The summary of the process occurring during electrospinning. The isotactic and syndiotactic chains from the hot polymer solution come together during the cooling of the liquid jet as it is shot toward the grounded target during electrospinning. They form the stereocomplex helix. The structure portrayed is a triple helix. For further discussion about triple or quadruple helix please see Chapter 3.

By examining the behavior of stereocomplex PMMA solutions during electrospinning, we have found that the heated solutions of stereocomplex PMMA undergo a sol-gel transition during electrospinning (summarized in **Figure 4.8**). The rapid evaporation of the solvent facilitates a temperature drop, which appears sufficient to bring the temperature of the fluid jet below its gelation temperature very quickly. The stereocomplex chains in the helical form pack to generate a percolating network, all of this within a short time frame of around 0.04s. The evidence for this is the appearance of smooth fibers at a concentration lower than that of non-complexing polymer ($C/C^*=4$ for a-PMMA), and the presence of an endothermic melting peak at 172ºC in the DSC trace. The crystallinity of the electrospun fibers is high compared to wet-spun fibers (Chapter 2) and gel-spun fibers (Chapter 3). The melting point achieved is also higher. The formation of a stereocomplex helix has been confirmed by X-ray analysis. These results offer the possibility of forming PMMA stereocomplex fibers that are more temperature resistant than regular a-PMMA fibers. Therefore, electrospun stereocomplex PMMA fibers can be used to reinforce the PMMA matrix in a variety of biomedical applications, because the resultant self-reinforced composites will have much better interfacial strength while retaining the excellent biocompatibility of PMMA. The occurrence of physical gelation during the electrospinning process also opens the possibility of other transitions or reactions occurring during electrospinning.

CHAPTER 5

SELF-REINFORCED COMPOSITE BASED ON STEREOCOMPLEX PMMA FIBERS

5.1. Introduction

We have spun fibers from stereocomplex solutions using wet spinning and gel spinning, and observed that the birefringence is not lost even after treating the fibers at 160ºC. In this chapter we examine if the stereocomplex PMMA fibers can also withstand the conditions of preparing a composite and compare their behavior to atactic PMMA melt spun fibers.

Hot compaction is a widely used method of preparing composites[133]. Particularly self-reinforced composites are often prepared using this method. Usually the process involves compacting two or more polymer sheets in a hot-press. Self-reinforced composites are often made by putting oriented fibers in the hot press and heating them at a set temperature and pressure for a particular length of time[80,82,84,134]. The outer regions of the fibers will melt and fill the interstitial space[133,135]. The fiber core remains oriented and gives the composite strength and toughness. Since the fiber core needs to remain intact, the processing temperature and processing time are extremely important in self-reinforced composite preparation[82,84,133,135]. PMMA self-reinforced composites have been produced by hot compaction by Gilbert, Wright and co-workers[78-84,136-138]. They have

determined that the maximum temperature that can be used for hot compaction is 128ºC and that the processing time needs to be shorter than 1h[82-84,138].

Besides hot compaction, an important method of producing PMMA composites is *in situ* polymerization of methyl methacrylate (MMA). Particularly in applications such as dental fillings and bone cement, this method is often employed[139-141]. The monomer is mixed with initiator and often an accelerator is added[142]. In bone cement formulations, some PMMA polymer is usually pre-dissolved in the mixture to increase the viscosity for easier handling[140,141,143]. Previously, Jagger *et al.* have examined the performance of atactic PMMA fibers during this method of composite preparation and found that the fibers did not improve the material toughness[139,144-149].

In our work, we have used both methods of composite preparation – the hot compaction and the *in situ* polymerization and compared the orientation retention between atactic MMA fibers and stereocomplex PMMA fibers.

5.2. Experimental

PMMA sheets were prepared by taking 1g of PMMA powder (Mw = 350,000, Aldrich, dried overnight in vacuum oven at 1 mmHg and 140ºC) and pressing it in a hot press at 3 bar and 230ºC for 1h. The hot plates were then turned off and the pressure released in order to let the polymer relax. In about 1-2h the temperature of the hot plates and the PMMA sheet reached room temperature and the sheets were taken out of the hot press. The thickness of the sheets produced this way was about 0.5 mm.

Two PMMA sheets were taken to make a self-reinforced composite. In between the sheets, 100 mg of gel-spun PMMA stereocomplex fibers were placed. The sheets were pressed together at 3 bar and 160ºC and examined after 15 min, 1 hr and 6 hr. After that, the hot plates were turned off and allowed to cool down to room temperature. A second sample containing atactic PMMA melt-spun fibers was prepared in the same way.

Thus prepared, the composite was examined in a Leica DMRX polarized light microscope. Furthermore, the composite was broken in a direction perpendicular to the axis of one of the fibers so that the fiber was also broken. This sample was sputtered with gold and analyzed by SEM (Hitachi S800).

The *in situ* polymerization method for composite preparation was adapted from a lab exercise procedure[150]. 20 g of PMMA powder (Mw = 968,000, Aldrich, dried overnight in a vacuum oven at 140ºC and 2 mmHg) was dissolved in 80 g of methyl methacrylate (MMA, Aldrich, as received) monomer. The solution was made by stirring with a magnetic stirrer overnight at 60ºC. Next, 45 mg of finely ground benzoyl peroxide hydrate was added per gram of MMA, for a total of 3.6 g. The powder was mixed in by stirring and gentle heating to 40ºC. After the powder was dissolved, a 10 g aliquot was taken out and mixed well with 0.2 ml of dimethyl paratoluidine (DMPT), which accelerates the polymerization reaction.

The 10 g aliquot was placed in a 25 ml scintillation vial and a thermocouple probe wrapped in aluminum foil was inserted. The aluminum foil is necessary in order to prevent the probe from getting stuck after the polymerization is complete. The vial was wrapped in glass wool to better insulate it and the temperature was recorded through a CASSY Lab platform (Klinger Educational).

Smaller 1 g aliquots were mixed with 0.02 ml DMPT and used together with 100 mg of gel-spun PMMA stereocomplex fibers to prepare self-reinforced composites.

Fiber stability during the polymerization was examined by taking a 1 cm short fiber and gluing it to a microscope slide using epoxy glue. This prevents the fiber from moving around in the field of view during the polymerization. Two fibers, an atactic PMMA melts-spun fiber and a gel-spun PMMA stereocomplex fiber were glued side by side to compare the resistance to solvent during the polymerization. Next, a drop of PMMA solution without DMTP or dibenzoyl peroxide initiator was added and the sample was covered by a cover slip. The concentrations examined were 0% PMMA, 10% PMMA w/w and 20% PMMA w/w, always the high molecular weight PMMA (Mw = 968,000). The sample was then put in a Linkam THMS600 hot stage and observed under a polarized microscope. The sample was heated at 10 ºC/min to 90 ºC, this temperature was kept for 5 minutes and then the sample was cooled down at 1 ºC/min until it reached room temperature. The same experiment with 0%, 10% and 20% w/w high molecular weight PMMA was also performed with the presence of benzoyl peroxide initiator. Furthermore the experiment was performed by adding the initiator and the accelerator

DMTP. A mixture thus prepared had to be quickly transferred onto the fibers on the glass slide in order to be able to do this before the polymerization proceeded far enough for the viscosity to rise so high as to make the transfer impossible. When DMTP was added, the sample was not transferred into the Linkam stage.

5.3. Results

The hot compaction of two PMMA plates was examined in a polarized light microscope. After 15min hot compaction, the phase boundary between the stereocomplex PMMA fibers and the PMMA matrix can still be seen. After 1h, the phase boundary disappears and the fiber can only be detected by using crossed polarizers (**Figure 5.1**). A light blue interference color can be observed under crossed polarizers. The fiber can be seen under crossed polarizers even after 6h of heating at 160ºC. The atactic PMMA fiber cannot be detected even after only 15 min heating. The composite sample that was broken shows the oriented fiber near the fracture point (**Figure 5.1C and 5.1D**).

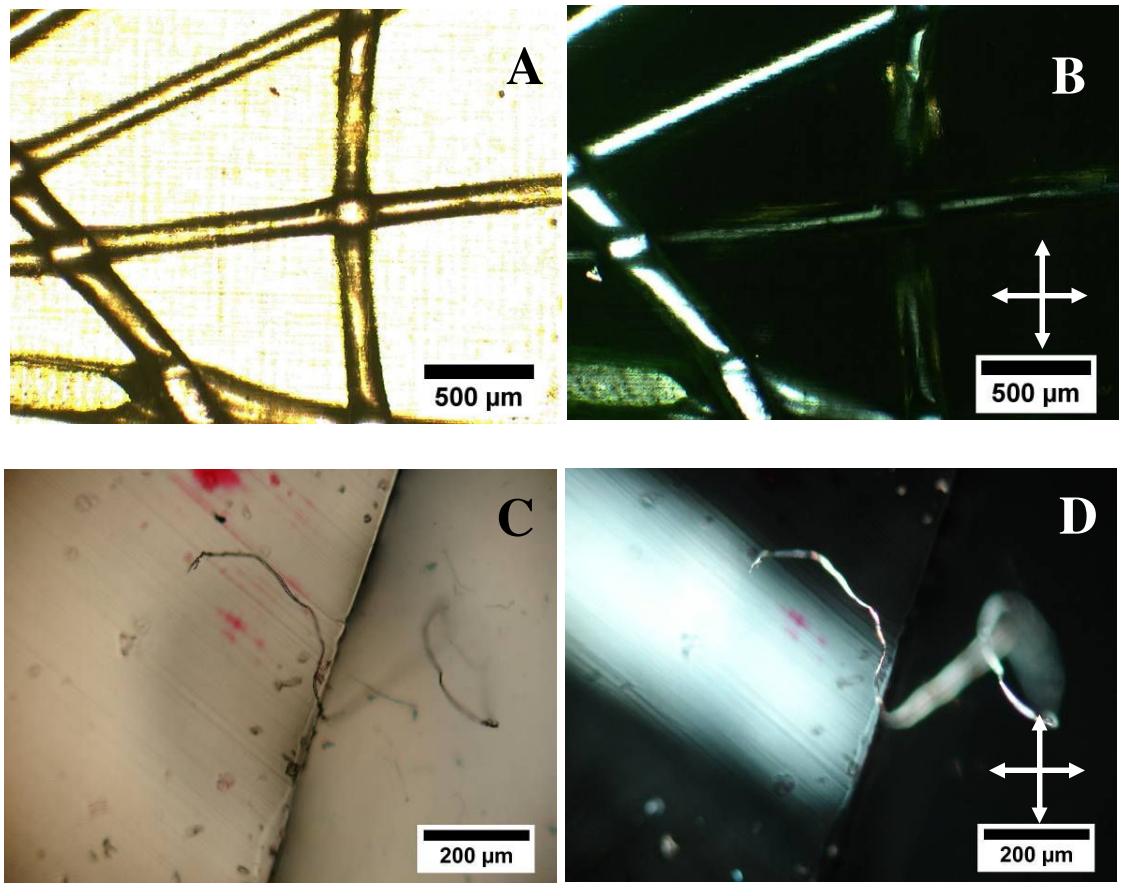

Figure 5.1: (A, B) Self-reinforced PMMA composites with stereocomplex PMMA fibers and a-PMMA by hot compaction after 15min in heat press at 3bar and 160ºC. (A) bright field image and (B) under crossed polarizers. The phase boundaries are still visible. Images in (C, D) show the stereocomplex fiber near a fractured surface after 6h in the heat press. (C) Bright field image does not show any boundaries between the fiber and matrix any more and (D) image under crossed polarizers shows that the fiber is still oriented. The fiber is cleaved perpendicularly at the fracture surface.

The SEM images of the fracture plane do not show any gap between the fiber surface and the matrix (**Figure 5.2**). The fiber location in the SEM image is hard to determine, but appears to be in a slight depression. We have identified the material within this depression as stereocomplex PMMA fiber because the location matched with the location determined from the optical microscopy (**Figure 5.1D**). However, because in SEM we cannot look under crossed polarizers, we cannot be 100% sure that the stereocomplex fiber was present in this depression.

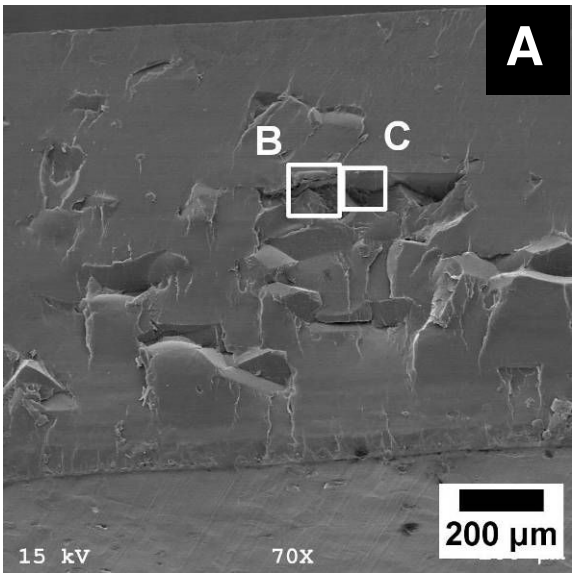

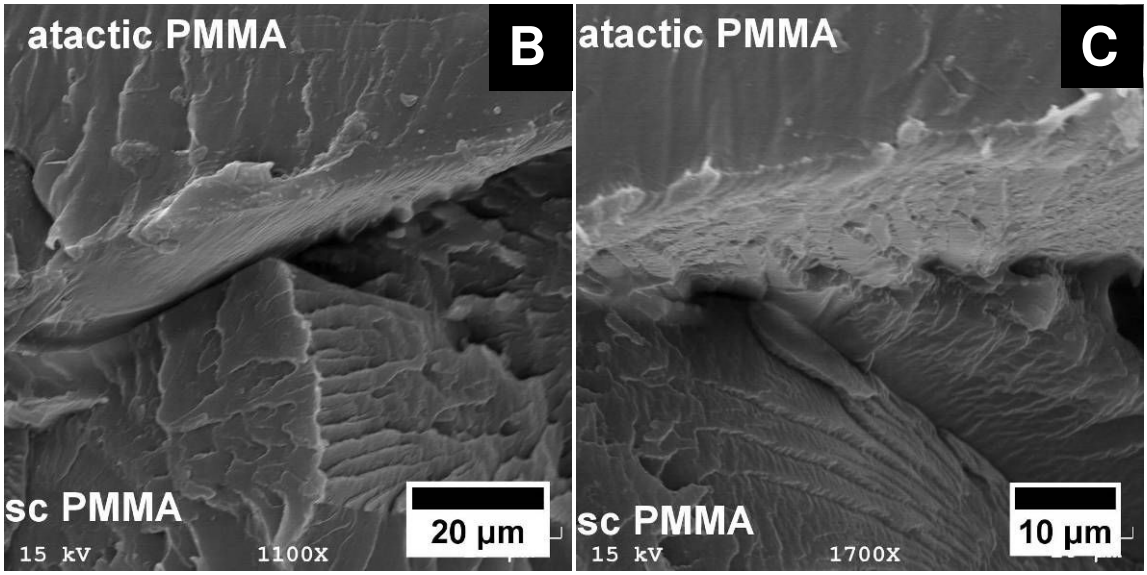

Figure 5.2: (A) The SEM image of the fracture surface from **Figure 5.1C** and **5.1D**. The fiber surface is hardly visible and there is no noticeable delamination or gap between the fiber and the matrix. (B) Zoomed in region indicated on the image (A), showing different fracture surfaces for the atactic PMMA in the upper part of the image and the stereocomplex PMMA (sc PMMA) in the lower part of the image. (C) Another zoomed in region indicated on image (A), showing different fracture surfaces for the atactic PMMA in the upper part of the image and the stereocomplex PMMA (sc PMMA) fiber in the lower part of the image.

The polymerization temperature measurement provided us a temperature profile. The temperature rises up to 90ºC within minutes, which is consistent with previously

published values between 70-90ºC[151]. The subsequent samples were investigated under the microscope by trying to approximate this temperature profile, as shown in **Figure 5.3**.

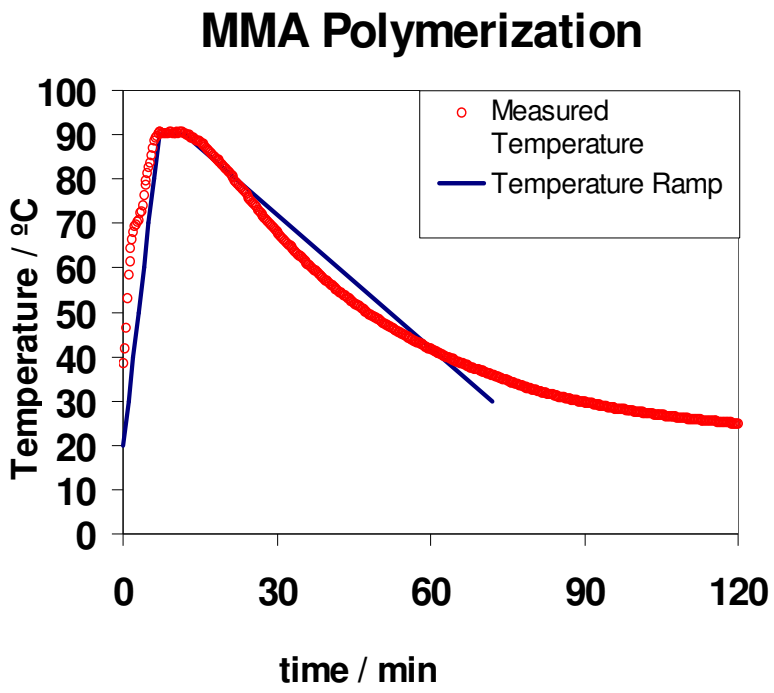

Figure 5.3: Temperature measurement during MMA polymerization (red open circles). The maximum temperature reached was 90ºC. The temperature ramp used in subsequent PMMA fiber stability experiments is shown with blue straight lines.

Both the atactic melt-spun PMMA fibers as well as stereocomplex PMMA fibers dissolved in pure MMA monomer as the temperature was raised, when no high molecular weight a-PMMA was added to the mixture. The atactic fibers dissolved around 40ºC and the stereocomplex PMMA fibers around 60ºC. The atacic fibers could not be detected after the dissolution, but the stereocomplex fibers could be seen under the microscope as a swollen gel. The blue interference color was disappearing from the outside of the fiber towards its core. Under crossed polarizers the remaining gel was not visible. At 10 % w/w PMMA concentration, the atactic fiber dissolved just as readily, while the

stereocomplex fiber persisted until the temperature was raised to 90ºC, however the birefringence could not be detected under crossed polarizers after 5 minutes. At 20% w/w PMMA concentration the atactic PMMA fiber persisted until 45ºC, while the stereocomplex PMMA fiber persisted until the temperature reached 90ºC (the difference shown in **Figure 5.4**). The light blue interference color of the stereocomplex fibers became slightly less bright, but it never completely disappeared for the duration of the experiment. The fiber diameter also decreased slightly. Some of the stereocomplex on the outside of the fiber had apparently been dissolved.

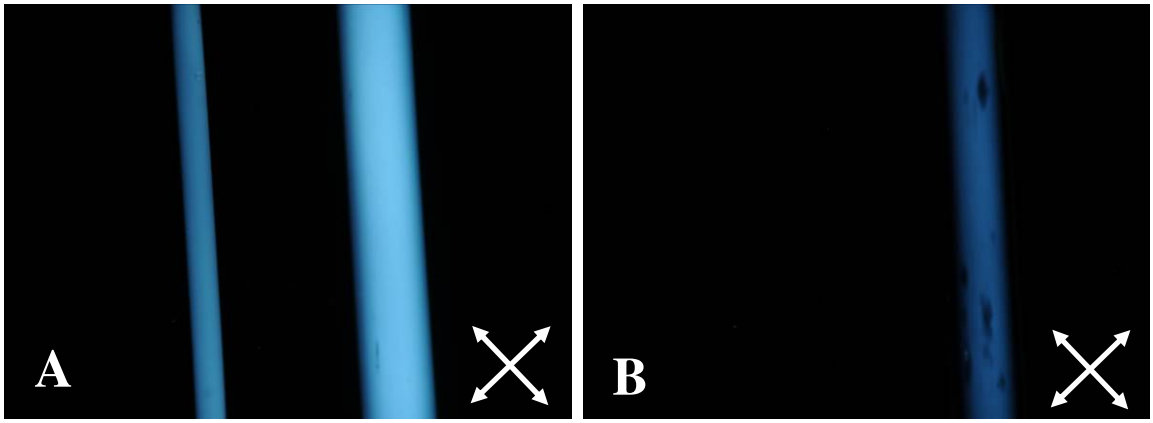

Figure 5.4: Atactic PMMA fiber (left fiber) and stereocomplex PMMA fiber (right fiber) under crossed polarizers under the bone cement setting conditions, with 20 wt% added a-PMMA. Image (A) is at the start of the temperature ramp and image (B) after 5 minutes at 90 ºC. Birefringence is already gone in the atactic fiber, while the stereocomplex fiber retains birefringence.

When the same experiment was repeated with the initiator benzoyl peroxide and a-PMMA added, similar results were obtained. The stereocomplex PMMA fibers lost their birefringence at about the same time into the experiment. The mixture was examined later and found to be liquid. When DMTP was also added to the solution, the polymerization progressed rapidly. Both fibers, atactic PMMA melt spun and the

stereocomplex PMMA gel-spun fiber survived the polymerization. This will be discussed more in the section below.

5.4. Discussion

During the hot compaction experiment the atactic PMMA surrounding the fibers has to be heated well above the glass transition in order to allow the polymer chains to diffuse and entangle with the polymer in the fibers[133]. The fibers making the self-reinforced composite must be able to withstand this high temperature. The atactic PMMA polymer chains thus entangle with the non-crystalline parts of the stereocomplex PMMA fiber, making a composite with favorable adhesion between the fibers and the matrix. This can be seen in **Figure 5.1**, where we can see how the boundary between the fibers and the matrix is disappearing. Since the refractive index of the stereocomplex PMMA and the atactic PMMA is very similar (1.502 for isotactic PMMA, 1.499 for the atactic isomer and 1.497 for the syndiotactic PMMA[152]), we cannot distinguish between the fibers and the polymer matrix once the two are entangled. Furthermore, we can see that even with the disappearance of the phase boundary between the fibers and the polymer matrix, the fibers retain their orientation. This can be seen under crossed polarizers in **Figure 5.1B** and **5.1D.** The stereocomplex PMMA fiber appears light blue, while the surrounding matrix is not oriented and appears as a dark background.

The hot compaction experiments take advantage of the high stability of stereocomplex PMMA fibers towards temperature. The fibers withstand the processing conditions, as evidenced by birefringence retention. In contrast, the atactic PMMA fibers

lose their orientation and cannot be detected by polarized microscopy. That is not surprising, as it has been reported[78,82-84] that the atactic PMMA fibers lose all orientation when processed above 130ºC. We have also shown in Chapter 3 that gel-spun stereocomplex fibers used in our hot compaction experiment are able to withstand the temperature of 160 ºC for a long time.

The surface adhesion between stereocomplex fiber and the a-PMMA matrix is favorable and the gap between the fiber and the matrix is not visible by light microscope. The SEM analysis of the fractured composite (**Figure 5.2**) supports this conclusion, because no crack between the fiber and the polymer matrix is visible. However, the stereocomplex PMMA fiber has a slightly different fracture surface. The atactic PMMA fracture surface is rather smooth, indicating that the polymer cracked cleanly along the fracture direction. In contrast, the stereocomplex PMAM surface is a bit more jagged, with stepwise features running the length of the fiber axis which is perpendicular to the fracture direction (**Figure 5.2B** and **5.2C**). It appears that the mode of fracture is different in the atactic PMMA matrix and the stereocomplex PMMA fiber[153]. We cannot say for sure whether crazing has occurred or not, although it has previously been reported that isotactic-atactic stereocomplexes promote crazing[154].

The experiment with the bulk polymerization of MMA has provided a temperature profile which was used in the subsequent fiber stability experiments. The temperature during the polymerization rises to 90ºC, remains at that level for about 5min and then slowly decreases. These experimental conditions are often used in preparing

PMMA materials, for example in making bone cement[140]. The reinforcing fibers need to be resistant to the monomer during the polymerization. Furthermore, the concentration of PMMA in the MMA solution affects the polymerization kinetics and diffusion and solvation characteristics of the MMA monomer. The polymerization kinetics are affected by what is known as Trommsdorff effect[155]. When the molecular weight becomes high enough, an autoacceleration effect increases the polymerization rate[156]. The viscosity of the system is thus further increased and the diffusion of solvent is hindered.

The stereocomplex PMMA fibers dissolved during the course of experiment when only MMA was used as the solvent. The dissolution proceeded from the outside of the fiber towards its core. The birefringent color was seen disappearing and instead, a gel with no molecular orientation was left. This is consistent with the solvent (MMA monomer) diffusing into the fiber and dissolving the stereocomplex. MMA is classified as a strongly complexing solvent[30] and therefore the gel formation is not a surprise. At higher concentrations of atactic PMMA in the polymerization mixture, the stereocomplex PMMA fibers retain their orientation during the experiment (shown in **Figure 5.4**). This is most likely due to the lower diffusion of the MMA. During the experiments with PMMA dissolved in MMA monomer, no polymerization was taking place. Only the resistance of the fibers to the hot solvent was thus examined.

To better approximate the polymerization conditions, benzoyl peroxide radical initiator was added to the PMMA solution in MMA that was used in the experiments. Benzoyl peroxide is cleaved by DMPT[157] in the preparation of bone cement, but it can

also decompose and produce free radicals spontaneously at temperatures above 60ºC[158]. Therefore the experiments where the benzoyl peroxide was present were thought to be a good simulation of the conditions present during PMMA composite preparation. However, the mixture remained liquid after the experiment and there was no noticeable difference in fiber stability. Most likely the initiation efficiency of benzoyl peroxide was not high enough and/or the temperature not kept high long enough[158]. It is also possible that the radical polymerization was stopped due to the small sample size and no possibility to keep oxygen out of the sample.

In order to come closer to the actual polymerization conditions, DMPT was added to the mixture of PMMA, MMA and benzoyl peroxide. As soon as DMPT is added, the polymerization starts very rapidly. Before the sample could be transferred into the Linkam stage, adjusted to see the fibers in the stage opening, and focused on the microscope, enough time had passed that the temperature ramp was useless. The sample was already rather solid from the MMA polymerization and both fibers, the atactic PMMA melt spun fiber and the stereocomplex PMMA gel-spun fiber, retained their birefringence. However, those results, especially for a-PMMA fiber, may not be trusted, as the quantity of the polymer solution was very small compared to the mass of the glass slide. The microscope glass slide thus acted as a heat sink and therefore the temperature might not have risen to the level expected during bulk polymerization.

In view of the difficulties in observing the actual polymerization taking place under the microscope, we decided to compare the results from the fiber stability test with

0 %, 10 % and 20 % high molecular weight PMMA solutions acting as the medium. In this series, the stereocomplex PMMA fibers are superior to the melt-spun atactic PMMA fibers. The stereocomplex PMMA fibers are able to retain their birefringence, provided that a high enough concentration of high molecular weight atactic PMMA is used in the polymer solution. The pre-dissolved PMMA acts as an MMA solvent diffusion suppressor and prevents the fibers from losing their orientation. Under polymerization conditions, the high-viscosity mixture also promotes the Trommsdorff effect, thus increasing the polymerization rate and further suppressing the solvent diffusion. Stereocomplex PMMA fibers should thus able to retain their orientation throughout the process of composite preparation, as the method of testing employed exposed the fibers to even harsher conditions than are present during the polymerization.

5.5. Conclusion

Stereocomplex PMMA fibers are superior to atactic PMMA fibers in hot compaction composite preparation due to the larger processing window available. They retain their orientation even at prolonged periods of time at 160ºC. The stereocomplex PMMA fibers are also superior when the composite is prepared by *in situ* polymerization of the MMA monomer. The atactic PMMA fibers dissolve in the monomer, while the stereocomplex PMMA fibers can withstand the polymerization conditions, as long as high molecular weight a-PMMA was added and the MMA polymerization was rapidly induced by means of the initiator and DMPT. The monomer solvent can diffuse into the fibers and polymerize there, showing good promise for adhesion enhancement in these self-reinforced composites.

REFERENCES PART A

(1) Atkins, E., "Conformations in polysaccharides and complex carbohydrates"; *J. Biosci.* **1985**, *8*, 375-387.

(2) Kusanagi, H.; Tadokoro, H.; Chatani, Y., "Double Strand Helix of Isotactic Poly(Methyl Methacrylate)"; *Macromolecules* **1976**, *9*, 531-532.

(3) Kusanagi, H.; Chatani, Y.; Tadokoro, H., "The Crystal-Structure of Isotactic Poly(Methyl Methacrylate) - Packing-Mode of Double-Stranded Helices"; *Polymer* **1994**, *35*, 2028-2039.

(4) Saiani, A.; Guenet, J. M., "On the helical form in syndiotactic poly(methyl methacrylate) thermoreversible gels as revealed by small-angle neutron scattering"; *Macromolecules* **1997**, *30*, 966-972.

(5) Fox, T. G.; Garrett, B. S.; Goode, W. E.; Gratch, S.; Kincaid, J. F.; Spell, A.; Stroupe, J. D., "Crystalline Polymers of Methyl Methacrylate"; *Journal of the American Chemical Society* **1958**, *80*, 1768-1769.

(6) Liquori, A. M.; Anzunino, G.; Coiro, V. M.; Dalagni, M.; Desantis, P.; Savino, M., "Complementary Stereospecific Interaction between Isotactic and Syndiotactic Polymer Molecules"; *Nature* **1965**, *206*, 358-362.

(7) Slager, J.; Domb, A. J., "Biopolymer stereocomplexes"; *Advanced Drug Delivery Reviews* **2003**, *55*, 549-583.

(8) Nijenhuis, K. T. In *Thermoreversible Networks*; Springer-Verlag Berlin: Berlin 33, 1997; Vol. 130, p 67-81.

(9) Spevacek, J.; Schneider, B., "Aggregation of Stereoregular Poly(Methyl Methacrylates)"; *Advances in Colloid and Interface Science* **1987**, *27*, 81-150.

(10) Slager, J.; Domb, A. J., "Stereocomplexes based on poly(lactic acid) and insulin: formulation and release studies"; *Biomaterials* **2002**, *23*, 4389-4396.

(11) Jiro Kumaki, T. K., Kento Okoshi, Hiroshi Kusanagi, Eiji Yashima,, "Supramolecular Helical Structure of the Stereocomplex Composed of Complementary Isotactic and Syndiotactic Poly(methyl methacrylate)s as Revealed by Atomic Force Microscopy13"; *Angewandte Chemie* **2007**, *119*, 5444-5447.

(12) Schomaker, E.; Challa, G., "Complexation of Stereoregular Poly(Methyl Methacrylates) .14. The Basic Structure of the Stereocomplex of Isotactic and Syndiotactic Poly(Methyl Methacrylate)"; *Macromolecules* **1989**, *22*, 3337-3341.

(13) Bosscher, F.; Tenbrinke, G.; Challa, G., "Association of Stereoregular Poly(Methyl Methacrylates) .6. Double-Stranded Helical Structure of the Stereo-Complex of Isotactic and Syndiotactic Poly(Methyl Methacrylate)"; *Macromolecules* **1982**, *15*, 1442-1444.

(14) Hatada, K.; Kitayama, T., "Structurally controlled polymerizations of methacrylates and acrylates"; *Polymer International* **2000**, *49*, 11-47.

(15) Kumaki, J.; Kawauchi, T.; Okoshi, K.; Kusanagi, H.; Yashima, E., "Supramolecular helical structure of the stereocomplex composed of complementary isotactic and syndiotactic poly(methyl methacrylate)s as revealed by atomic force microscopy"; *Angewandte Chemie-International Edition* **2007**, *46*, 5348-5351.

(16) Liquori, A. M.; Anzunino, G.; Coiro, V. M.; Dalagni, M.; Desantis, P.; Savino, M., "Complementary Stereospecific Interaction between Isotactic and Syndiotactic Polymer Molecules"; *Nature* **1965**, *206*, 358-&.

(17) D'Alagni, M.; De Santis, P.; Savino, M.; Liquori, A. M., "Comparison Between Far Ultraviolet Absorption Spectra Of Isotactic + Syndiotactic Polymethyl Methacrylate In Solution
"; *Journal of Polymer Science Part B-Polymer Letters* **1964**, *2*, 925-&.

(18) Schomaker, E.; Challa, G., "Complexation of stereoregular poly(methyl methacrylates). 14. The basic structure of the stereocomplex of isotactic and syndiotactic poly(methyl methacrylate)"; *Macromolecules* **1989**, *22*, 3337-41.

(19) Vacatello, M.; Flory, P. J., "Conformational Statistics of Poly(Methyl Methacrylate)"; *Macromolecules* **1986**, *19*, 405-415.

(20) Buter, R.; Tan, Y. Y.; Challa, G., "Radical polymerization of methyl methacrylate in the presence of isotactic poly(methyl methacrylate)"; *Journal of Polymer Science, Polymer Chemistry Edition* **1972**, *10*, 1031-49.

(21) Buter, R.; Tan, Y. Y.; Challa, G., "Radical Polymerization of Methyl-Methacrylate in Presence of Stereoregular Poly(Methyl Methacrylate) .4. Influence of Solvent Type"; *Journal of Polymer Science Part a-Polymer Chemistry* **1973**, *11*, 2975-2989.

(22) Serizawa, T.; Hamada, K.; Akashi, M., "Polymerization within a molecular-scale stereoregular template"; *Nature* **2004**, *429*, 52-55.

(23) Bosscher, F.; Keekstra, D.; Challa, G., "The Influence of Ester Groups on the Stereocomplex Formation Between Different Polyalkylmethacrylates"; *Polymer* **1981**, *22*, 124-126.

(24) Vandenbe.Wb; Hijmans, B.; Piet, P.; Heikens, D., "Complex formations between iso and syndiotactic polymethylmethacrylate in solutions"; *Nature* **1968**, *217*, 949-&.

(25) Kida, T.; Mouri, M.; Akashi, M., "Fabrication of hollow capsules composed of poly(methyl methacrylate) stereocomplex films"; *Angewandte Chemie-International Edition* **2006**, *45*, 7534-7536.

(26) Matsuno, H.; Nagasaka, Y.; Kurita, K.; Serizawa, T., "Superior activities of enzymes physically immobilized on structurally regular poly(methyl methacrylate) surfaces"; *Chemistry of Materials* **2007**, *19*, 2174-2179.

(27) Kawauchi, T.; Kumaki, J.; Yashima, E., "Nanosphere and nanonetwork formations of [60]fullerene-end-capped stereoregular poly(methyl methacrylate)s through stereocomplex formation combined with self-assembly of the fullerenes"; *Journal of the American Chemical Society* **2006**, *128*, 10560-10567.

(28) Chiang, R.; Burke, J. J.; Threlkel.Jo; Orofino, T. A., "Stereocomplex Formation in Solutions of Poly(Methyl Methacrylate)"; *Journal of Physical Chemistry* **1966**, *70*, 3591-&.

(29) Liu, H. Z.; Liu, K.-J., "Stereochemical Interaction between Isotactic and Syndiotactic Poly(methyl methacrylates) in Polar and Nonpolar Solvents"; *Macromolecules* **1968**, *1*, 157-162.

(30) Vorenkamp, E. J.; Bosscher, F.; Challa, G., "Association of Stereoregular Poly(Methyl Methacrylates) .4. Further Study on the Composition of the Stereocomplex"; *Polymer* **1979**, *20*, 59-64.

(31) Gons, J.; Vorenkamp, E. J.; Challa, G., "Radical Polymerization of Methyl-Methacrylate in Presence of Stereoregular Poly(Methyl Methacrylate) .5. Kinetics of Initial Template Polymerization"; *Journal of Polymer Science Part a-Polymer Chemistry* **1975**, *13*, 1699-1709.

(32) Gons, J.; Slagter, W. O.; Challa, G., "Radical Polymerization of Methyl-Methacrylate in Presence of Stereoregular Poly(Methyl Methacrylate) .6. Kinetic Template Effects at Higher Conversion"; *Journal of Polymer Science Part a-Polymer Chemistry* **1977**, *15*, 771-779.

(33) Gons, J.; Vorenkamp, E. J.; Challa, G., "Radical Polymerization of Methyl-Methacrylate in Presence of Isotactic Poly(Methyl Metacrylate) .7. Determination

of Rate Constants for Template Polymerization"; *Journal of Polymer Science Part a-Polymer Chemistry* **1977**, *15*, 3031-3038.

(34) Gons, J.; Straatman, L. J. P.; Challa, G., "Radical Polymerization of Methyl-Methacrylate in Presence of Isotactic Poly(Methyl Methacrylate) .8. Influence of Template Concentration"; *Journal of Polymer Science Part a-Polymer Chemistry* **1978**, *16*, 427-434.

(35) Lohmeyer, J.; Tan, Y. Y.; Challa, G., "Polymerization of Methacrylic-Acid in the Presence of Isotactic Poly(Methyl Methacrylate) as Possible Template"; *Journal of Macromolecular Science-Chemistry* **1980**, *A14*, 945-957.

(36) Odriscoll, K. F.; Capek, I., "Methyl-Methacrylate Copolymerization in the Presence of a Template"; *Journal of Polymer Science Part C-Polymer Letters* **1981**, *19*, 401-407.

(37) Srivastava, A. K.; Nigam, S. K.; Shukla, A. K.; Saini, S.; Kumar, P.; Tewari, N., "Studies on Template Polymerization"; *Journal of Macromolecular Science-Reviews in Macromolecular Chemistry and Physics* **1987**, *C27*, 171-180.

(38) Challa, G.; Tan, Y. Y., "Template Polymerization"; *Pure and Applied Chemistry* **1981**, *53*, 627-641.

(39) Schomaker, E.; Challa, G., "Complexation of Stereoregular Poly(Methyl Methacrylates) .13. Influence of Chain-Length on the Process of Complexation in Dilute-Solution"; *Macromolecules* **1988**, *21*, 3506-3510.

(40) Schomaker, E.; Hoppen, H.; Challa, G., "Complexation of Stereoregular Poly(Methyl Methacrylates) .12. Complexation Process in Dilute-Solution"; *Macromolecules* **1988**, *21*, 2203-2209.

(41) Schomaker, E.; Hoppen, H.; Challa, G., "Complexation of stereoregular poly(methyl methacrylates). 12. Complexation process in dilute solution"; *Macromolecules* **1988**, *21*, 2203-9.

(42) Mrkvickova, L.; Porsch, B.; Sundelof, L. O., "Study of poly(methyl methacrylate) stereocomplexes by size exclusion chromatography and dynamic light scattering"; *Macromolecules* **1999**, *32*, 1189-1193.

(43) Mrkvickova, L.; Stejskal, J.; Spevacek, J.; Horska, J.; Quadrat, O., "Aggregation Behavior of Stereoregular Poly(Methyl Methacrylates) in Dilute-Solution - Light-Scattering and Proton Nmr-Study"; *Polymer* **1983**, *24*, 700-706.

(44) Mrkvickova, L.; Pokorna, V.; Pecka, J., "Study of polymer complexes by size exclusion chromatography coupled with light scattering in combination with fluorescence spectroscopy"; *Macromolecular Symposia* **2000**, *162*, 227-233.

(45) Hatada, K.; Ute, K.; Kitayama, T.; Nishiura, T.; Miyatake, N., "Preparation and Properties of Isotactic and Syndiotactic Poly(Methyl Methacrylate)S, Uniform with Respect to Molecular-Weight"; *Macromolecular Symposia* **1994**, *85*, 325-338.

(46) Kitayama, T.; Fujimoto, N.; Yanagida, T.; Hatada, K., "Synthesis of stereoblock poly(methyl methacrylate) via transformation of isotactic-specific living polymer anion to syndiotactic-specific anion"; *Polymer International* **1994**, *33*, 165-70.

(47) Nishiura, T.; Kitayama, T.; Hatada, K., "Intra- and intermolecular stereocomplex formation of uniform stereoblock poly(methyl methacrylate)"; *Polymer Journal* **1996**, *28*, 1021-1023.

(48) Hatada, K.; Kitayama, T.; Ute, K.; Nishiura, T., "Preparation of stereoregular uniform polymer architectures"; *Kobunshi Ronbunshu* **1997**, *54*, 661-673.

(49) Kumaki, J.; Kawauchi, T.; Ute, K.; Kitayama, T.; Yashima, E., "Molecular weight recognition in the multiple-stranded helix of a synthetic polymer without specific monomer-monomer interaction"; *Journal of the American Chemical Society* **2008**, *130*, 6373-6380.

(50) Guenet, J. M., "Structure versus rheological properties in fibrillar thermoreversible gels from polymers and biopolymers"; *Journal of Rheology* **2000**, *44*, 947-960.

(51) Pyrlik, M.; Rehage, G., "Rheology of Crosslinked Gels with Moderate Auxiliary Valence from Isotactic and Syndiotactic Polymethylmethacrylate"; *Colloid and Polymer Science* **1976**, *254*, 329-341.

(52) Berghams, H.; Donkers, A.; Frenay, L.; Stoks, W.; Deschryver, F. E.; Moldenaers, P.; Mewis, J., "Thermoreversible Gelation of Syndiotactic Poly(Methyl Methacrylate)"; *Polymer* **1987**, *28*, 97-102.

(53) Fazel, N.; Fazel, Z.; Brulet, A.; Guenet, J. M., "Molecular-Structure of Poly Methyl-Methacrylate Thermoreversible Gels"; *Journal De Physique Ii* **1992**, *2*, 1617-1629.

(54) Fazel, N.; Brulet, A.; Guenet, J. M., "Molecular-Structure and Thermal-Behavior of Poly(Methyl Methacrylate) Thermoreversible Gels and Aggregates"; *Macromolecules* **1994**, *27*, 3836-3842.

(55) Fazel, Z.; Fazel, N.; Guenet, J. M., "Swelling and Rheological Properties of Poly Methyl-Methacrylate Thermoreversible Gels"; *Journal De Physique Ii* **1992**, *2*, 1745-1754.

(56) Schomaker, E.; Vorenkamp, E. J.; Challa, G., "Stereocomplexation of Stereoregular Poly(Methyl Methacrylate)S .9. Temperature and Time-Dependence of the Process of Complexation"; *Polymer* **1986**, *27*, 256-260.

(57) Jones, J. L.; Marques, C. M., "Rigid Polymer Network Models"; *Journal De Physique* **1990**, *51*, 1113-1127.

(58) Kawauchi, T.; Kumaki, J.; Okoshi, K.; Yashima, E., "Stereocomplex formation of isotactic and syndiotactic poly(methyl methacrylate)s in ionic liquids leading to thermoreversible ion gels"; *Macromolecules* **2005**, *38*, 9155-9160.

(59) Konnecke, K.; Rehage, G., "Crystallization and Stereo Association of Stereoregular Pmma .2. Crystallization Behavior of the Stereocomplex in Comparison with That of Pure Stereoregular Pmma"; *Makromolekulare Chemie-Macromolecular Chemistry and Physics* **1983**, *184*, 2679-2691.

(60) Lemieux, E.; Prudhomme, R. E., "Crystallization and morphology of isotactic poly(methyl methacrylates)"; *Polymer Bulletin* **1989**, *21*, 621-626.

(61) Schroeder, J. A.; Karasz, F. E.; Macknight, W. J., "Stereoregular Poly(Alkyl Methacrylate)S - Polymer Polymer and Copolymer Polymer Blends"; *Polymer* **1985**, *26*, 1795-1800.

(62) Schomaker, E.; Challa, G., "Complexation of stereoregular poly(methyl methacrylates). 11. A mechanistic model for stereocomplexation in the bulk"; *Macromolecules* **1988**, *21*, 2195-203.

(63) Lemieux, E. J.; Prud'homme, R. E., "Crystallization behaviour of stereocomplexed poly(methyl methacrylates): influence of thermal history"; *Polymer* **1998**, *39*, 5453-5460.

(64) Katime, I.; Quintana, J. R.; Veguillas, J., "Thermal-Behavior of Poly(Methyl Methacrylate) Stereocomplex by Dta"; *Thermochimica Acta* **1983**, *67*, 81-90.

(65) Lemieux, E. J.; Prud'homme, R. E., "Crystallization behavior of stereocomplexed poly(methyl methacrylates): influence of thermal history"; *Polymer* **1998**, *39*, 5453-5460.

(66) Katime, I.; Quintana, J. R.; Veguillas, J., "Stereocomplex formation of PMMA in cosolvent mixtures"; *Polymer* **1983**, *24*, 903-5.

(67) Katime, I. A.; Quintana, J. R., "Study on gels of poly(methyl methacrylate) stereocomplex by light scattering"; *Polymer Journal (Tokyo, Japan)* **1988**, *20*, 459-69.

(68) Konnecke, K.; Rehage, G., "Crystallization and Stereo Association of Stereoregular Pmma .1. Influence of Sequence Length on Crystallization Behavior"; *Colloid and Polymer Science* **1981**, *259*, 1062-1069.

(69) Atkins, P. W. *Physical chemistry*; 6th ed.; Freeman: New York, 1998, p 666.

(70) Allen, P. E. M.; Host, D. M.; Truong, V. T.; Williams, D. R. G., "Some Physical and Mechanical-Properties of Isotactic Atactic Poly(Methyl Methacrylate) Blends and Stereoblocks"; *European Polymer Journal* **1985**, *21*, 603-610.

(71) Urbanek, S.; Tashiro, K.; Kitayama, T.; Hatada, K., "Crystallite modulus of double-stranded helices of isotactic poly(methylmethacrylate): the x-ray measurement and the theoretical calculation"; *Polymer* **1999**, *40*, 3345-3351.

(72) Srinivasarao, M., "Chirality and polymers"; *Current Opinion in Colloid & Interface Science* **1999**, *4*, 147-152.

(73) Wulff, G.; Zweering, U., "Optically active, isotactic homopolymers of alpha-olefins with main-chain chirality and the first preparation of optically active C-3-symmetrical polymers"; *Chemistry-a European Journal* **1999**, *5*, 1898-1904.

(74) Ji, P.; Li, A. D. Q.; Peng, G.-D. In *Linear and Nonlinear Optics of Organic Materials III*; 1 ed.; SPIE: San Diego, CA, USA, 2003; Vol. 5212, p 108-116.

(75) Kawauchi, T.; Kitaura, A.; Kumaki, J.; Kusanagi, H.; Yashima, E., "Helix-sense-controlled synthesis of optically active poly(methyl methacrylate) stereocomplexes"; *Journal of the American Chemical Society* **2008**, *130*, 11889-11891.

(76) Kawauchi, T.; Kumaki, J.; Kitaura, A.; Okoshi, K.; Kusanagi, H.; Kobayashi, K.; Sugai, T.; Shinohara, H.; Yashima, E., "Encapsulation of fullerenes in a helical PMMA cavity leading to a robust processable complex with a macromolecular helicity memory"; *Angewandte Chemie-International Edition* **2008**, *47*, 515-519.

(77) Green, M. M.; Reidy, M. P.; Johnson, R. D.; Darling, G.; O'Leary, D. J.; Willson, G., "Macromolecular stereochemistry: the out-of-proportion influence of optically active comonomers on the conformational characteristics of polyisocyanates. The sergeants and soldiers experiment"; *Journal of the American Chemical Society* **1989**, *111*, 6452-6454.

(78) Gilbert, J. L.; Ney, D. S.; Lautenschlager, E. P., "Self-Reinforced Composite Poly(Methyl Methacrylate) - Static and Fatigue Properties"; *Biomaterials* **1995**, *16*, 1043-1055.

(79) Buckley, C. A.; Lautenschlager, E. P.; Gilbert, J. L., "Deformation Processing of Pmma into High-Strength Fibers"; *Journal of Applied Polymer Science* **1992**, *44*, 1321-1330.

(80) Wright, D. D.; Lautenschlager, E. P.; Gilbert, J. L., "Bending and fracture toughness of woven self-reinforced composite poly(methyl methacrylate)"; *Journal of Biomedical Materials Research* **1997**, *36*, 441-453.

(81) Wright, D. D.; Lautenschlager, E. P.; Gilbert, J. L., "Interfacial properties of self-reinforced composite poly(methyl methacrylate)"; *Journal of Biomedical Materials Research* **1998**, *43*, 153-161.

(82) Wright, D. D.; Gilbert, J. L.; Lautenschlager, E. P., "The effect of processing temperature and time on the structure and fracture characteristics of self-reinforced composite poly(methyl methacrylate)"; *Journal of Materials Science-Materials in Medicine* **1999**, *10*, 503-512.

(83) Wright, D. D.; Lautenschlager, E. P.; Gilbert, J. L., "The effect of processing conditions on the properties of poly(methyl methacrylate) fibers"; *Journal of Biomedical Materials Research* **2002**, *63*, 152-160.

(84) Wright-Charlesworth, D. D.; Lautenschlager, E. P.; Gilbert, J. L., "Hot compaction of poly(methyl methacrylate) composites based on fiber shrinkage results"; *Journal of Materials Science-Materials in Medicine* **2005**, *16*, 967-975.

(85) Wright-Charlesworth, D. D.; Peers, W. J.; Miskioglu, I.; Loo, L. L., "Nanomechanical properties of self-reinforced composite poly(methyl methacrylate) as a function of processing temperature"; *Journal of Biomedical Materials Research Part A* **2005**, *74A*, 306-314.

(86) Johnson, J. A.; Jones, D. W., "The mechanical properties of PMMA and its copolymers with ethyl methacrylate and butyl methacrylate"; *Journal of Materials Science* **1994**, *29*, 870-876.

(87) Jagger, D. C.; Harrison, A., "The effect of chopped poly(methyl methacrylate) fibers on some properties of acrylic resin denture base material"; *International Journal of Prosthodontics* **1999**, *12*, 542-546.

(88) Jagger, D. C.; Harrison, A.; Jandt, K. D., "An investigation of self-reinforced poly(methyl methacrylate) denture base acrylic resin using scanning electron and atomic force microscopy"; *International Journal of Prosthodontics* **2000**, *13*, 526-531.

(89) Challa, G.; Deboer, A.; Tan, Y. Y., "Association of stereoregular poly(methyl methacrylates)"; *Int. J. Polym. Mater.* **1976**, *4*, 239-249.

(90) Schomaker, E.; Tenbrinke, G.; Challa, G., "Complexation of Stereoregular Poly(Methyl Methacrylates) .8. Calorimetric Investigations"; *Macromolecules* **1985**, *18*, 1930-1937.

(91) Larson, R. G. *The structure and rheology of complex fluids*; Oxford University Press: New York, 1999, p 1-342.

(92) Moghbeli, M. R.; Mohammadi, N.; Bagheri, R.; Ghaffarian, S. R., "Wet spinning of low gel content SBR/PMMA core/shell particles dispersed in a good solvent for the shell"; *Polymer* **2003**, *44*, 4011-4019.

(93) Rayleigh, L., "On the instability of a cylinder of viscous liquid under capillary force"; *Philos. Mag.* **1892**, *34*.

(94) Middleman, S. *An introduction to fluid dynamics : principles of analysis and design*; Wiley: New York, 1998, p 111-132.

(95) Barham, P. J., "Strong polymer fibers"; *Physics in Technology* **1986**, *17*, 167-173.

(96) Gupta, V. B.; Kothari, V. K. *Manufactured Fibre Technology*; Chapman & Hall: London, 1997, p 31-188.

(97) Nakajima, T. *Advanced fiber spinning technology*; Woodhead Publishing Ltd. : Cambridge, 1994, p 1-256.

(98) Weber, C., "Zum Zerfall eines Flüssigkeitsstrahles"; *Zeitschrift für Angewandte Mathematik und Mechanik* **1931**, *11*, 136-154.

(99) Gupta, V. B. *Manufactured fiber technology*; Van Nostrand Reinhold International: London, 1995.

(100) Flory, P. J. *Principles of polymer chemistry*; Cornell University Press: Ithaca,, 1953, p 1-672.

(101) Graessley, W. W. *Polymeric liquids and networks : structure and properties*; Garland Science: New York, 2004, p 121-329.

(102) Smith, P.; Lemstra, P. J.; Booij, H. C., "Ultradrawing of high-molecular-weight polyethylene cast from solution: 2. Influence of initial polymer concentration "; *J. Polym. Sci. Pt. B-Polym. Phys.* **1981**, *19*, 877-888.

(103) Smith, P.; Lemstra, P. J., "Ultrahigh strength polyethylene filaments by solution spinning-drawing .3. Influence of drawing temperature"; *Polymer* **1980**, *21*, 1341-1343.

(104) Smith, P.; Lemstra, P. J., "Ultra-high-strength polyethylene filaments by solution spinning-drawing"; *Journal of Materials Science* **1980**, *15*, 505-514.

(105) Sears, F. W.; Zemansky, M. W.; Young, H. D. *College physics*; 7th ed.; Addison-Wesley Pub. Co.: Reading, Mass., 1991, p 1-952.

(106) Bosscher, F.; Tenbrinke, G.; Eshuis, A.; Challa, G., "Crystal-Structure of Isotactic Poly(Methyl Methacrylate)"; *Macromolecules* **1982**, *15*, 1364-1368.

(107) Kumaki, J.; Kawauchi, T.; Okoshi, K.; Kusanagi, H.; Yashima, E., "Supramolecular Helical Structure of the Stereocomplex Composed of Complementary Isotactic and Syndiotactic Poly(methyl methacrylate)s as Revealed by Atomic Force Microscopy13"; *Angewandte Chemie* **2007**, *119*, 5444-5447.

(108) Gupta, P.; Elkins, C.; Long, T. E.; Wilkes, G. L., "Electrospinning of linear homopolymers of poly(methyl methacrylate): exploring relationships between fiber formation, viscosity, molecular weight and concentration in a good solvent"; *Polymer* **2005**, *46*, 4799-4810.

(109) Formalas, A. United States, 1934; Vol. 1,975,504.

(110) Doshi, J.; Reneker, D. H., "Electrospinning Process and Applications of Electrospun Fibers"; *Journal of Electrostatics* **1995**, *35*, 151-160.

(111) Li, D.; Xia, Y. N., "Electrospinning of nanofibers: Reinventing the wheel?"; *Advanced Materials* **2004**, *16*, 1151-1170.

(112) C. Shin, G. G. C., "Water-in-oil coalescence in micro-nanofiber composite filters"; *Aiche Journal* **2004**, *50*, 343-350.

(113) Ma, M.; Hill, R. M.; Rutledge, G. C., "A Review of Recent Results on Superhydrophobic Materials Based on Micro- and Nanofibers"; *Journal of Adhesion Science and Technology* **2008**, *22*, 1799-1817.

(114) Kim, J. S.; Reneker, D. H., "Mechanical properties of composites using ultrafine electrospun fibers"; *Polym. Compos.* **1999**, *20*, 124-131.

(115) Kessick, R.; Tepper, G., "Electrospun polymer composite fiber arrays for the detection and identification of volatile organic compounds"; *Sensors and Actuators B: Chemical* **2006**, *117*, 205-210.

(116) Martins, A.; Reis, R. L.; Neves, N. M., "Electrospinning: processing technique for tissue engineering scaffolding"; *International Materials Reviews* **2008**, *53*, 257-274.

(117) Hadjiargyrou, M.; Chiu, J. B., "Enhanced composite electrospun nanofiber scaffolds for use in drug delivery"; *Expert Opin. Drug Deliv.* **2008**, *5*, 1093-1106.

(118) Zeng, J.; Aigner, A.; Czubayko, F.; Kissel, T.; Wendorff, J. H.; Greiner, A., "Poly(vinyl alcohol) Nanofibers by Electrospinning as a Protein Delivery System and the Retardation of Enzyme Release by Additional Polymer Coatings"; *Biomacromolecules* **2005**, *6*, 1484-1488.

(119) Michael Stasiak, A. S., Andreas Greiner, Joachim H. Wendorff,, "Polymer Fibers as Carriers for Homogeneous Catalysts"; *Chemistry - A European Journal* **2007**, *13*, 6150-6156.

(120) Burger, C.; Hsiao, B. S.; Chu, B., "NANOFIBROUS MATERIALS AND THEIR APPLICATIONS"; *Annual Review of Materials Research* **2006**, *36*, 333-368.

(121) Taylor, G., "Disintegration of Water Drops in Electric Field"; *Proceedings of the Royal Society of London Series a-Mathematical and Physical Sciences* **1964**, *280*, 383-&.

(122) Shin, Y. M.; Hohman, M. M.; Brenner, M. P.; Rutledge, G. C., "Electrospinning: A whipping fluid jet generates submicron polymer fibers"; *Applied Physics Letters* **2001**, *78*, 1149-1151.

(123) Shin, Y. M.; Hohman, M. M.; Brenner, M. P.; Rutledge, G. C., "Experimental characterization of electrospinning: the electrically forced jet and instabilities"; *Polymer* **2001**, *42*, 9955-9967.

(124) Hohman, M. M.; Shin, M.; Rutledge, G.; Brenner, M. P., "Electrospinning and electrically forced jets. I. Stability theory"; *Physics of Fluids* **2001**, *13*, 2201-2220.

(125) Casper, C. L.; Stephens, J. S.; Tassi, N. G.; Chase, D. B.; Rabolt, J. F., "Controlling surface morphology of electrospun polystyrene fibers: Effect of humidity and molecular weight in the electrospinning process"; *Macromolecules* **2004**, *37*, 573-578.

(126) Srinivasarao, M.; Collings, D.; Phillips, A.; Patel, S., "Three-dimensionally ordered array of air bubbles in a polymer film"; *Science* **2001**, *292*, 79.

(127) Sharma, V., Georgia Institute of Technology, 2008.

(128) Barrow, M. S.; Jones, R. L.; Park, J. O.; Srinivasarao, M.; Williams, P. R.; Wright, C. J., "Physical characterisation of microporous and nanoporous polymer films by atomic force microscopy, scanning electron microscopy and high speed video microphotograph"; *Spectroscopy* **2004**, *18*, 577-585.

(129) Chiang, R.; Burke, J. J.; Threlkel.Jo; Orofino, T. A., "Stereocomplex Formation in Solutions of Poly(Methyl Methacrylate)"; *Journal of Physical Chemistry* **1966**, *70*, 3591-3595.

(130) Wagner, H. L., "The Mark--Houwink--Sakurada Relation for Poly(Methyl Methacrylate)"; *Journal of Physical and Chemical Reference Data* **1987**, *16*, 165-173.

(131) Shenoy, S. L.; Bates, W. D.; Wnek, G., "Correlations between electrospinnability and physical gelation"; *Polymer* **2005**, *46*, 8990-9004.

(132) Yu, J. H.; Fridrikh, S. V.; Rutledge, G. C., "The role of elasticity in the formation of electrospun fibers"; *Polymer* **2006**, *47*, 4789-4797.

(133) Ward, I. M.; Hine, P. J., "The science and technology of hot compaction"; *Polymer* **2004**, *45*, 1413-1427.

(134) Alcock, B.; Cabrera, N. O.; Barkoula, N. M.; Reynolds, C. T.; Govaert, L. E.; Peijs, T., "The effect of temperature and strain rate on the mechanical properties of highly oriented polypropylene tapes and all-polypropylene composites"; *Composites Science and Technology* **2007**, *67*, 2061-2070.

(135) Ward, I. M., "Developments in oriented polymers, 1970-2004"; *Plast. Rubber Compos.* **2004**, *33*, 189-194.

(136) Gilbert, J. L., "Complexity in modeling of residual stresses and strains during polymerization of bone cement: Effects of conversion, constraint, heat transfer, and viscoelastic property changes"; *Journal of Biomedical Materials Research Part A* **2006**, *79A*, 999-1014.

(137) Wright-Charlesworth, D. D.; Miller, D. M.; Miskioglu, I.; King, J. A., "Nanoindentation of injection molded PLA and self-reinforced composite PLA after in vitro conditioning for three months"; *Journal of Biomedical Materials Research Part A* **2005**, *74A*, 388-396.

(138) Wright, D. D.; Lautenschlager, E. P.; Gibert, J. L., "Constrained shrinkage of highly oriented poly(methyl methacrylate) fibers"; *Journal of Applied Polymer Science* **2004**, *91*, 4047-4056.

(139) Jagger, D. C.; Harrison, A.; Jandt, K. D., "The reinforcement of dentures"; *J Oral Rehabil* **1999**, *26*, 185-94.

(140) Lewis, G., "Alternative acrylic bone cement formulations for cemented arthroplasties: Present status, key issues, and future prospects"; *Journal of Biomedical Materials Research Part B: Applied Biomaterials* **2008**, *84B*, 301-319.

(141) Lewis, G., "Properties of acrylic bone cement: State of the art review"; *Journal of Biomedical Materials Research* **1997**, *38*, 155-182.

(142) Lewis, G.; Xu, J.; Deb, S.; Lasa, B. V.; Roman, J. S., "Influence of the activator in an acrylic bone cement on an array of cement properties"; *Journal of Biomedical Materials Research Part A* **2007**, *81A*, 544-553.

(143) Lewis, G., "Relative roles of cement molecular weight and mixing method on the fatigue performance of acrylic bone cement: Simplex (R) P versus Osteopal (R)"; *Journal of Biomedical Materials Research* **2000**, *53*, 119-130.

(144) Jagger, D. C.; Harrison, A., "The effect of chopped poly(methyl methacrylate) fibers on some properties of acrylic resin denture base material"; *Int J Prosthodont* **1999**, *12*, 542-6.

(145) Jagger, D. C.; Harrison, A.; Jandt, K. D., "An investigation of self-reinforced poly(methyl methacrylate) denture base acrylic resin using scanning electron and atomic force microscopy"; *Int J Prosthodont* **2000**, *13*, 526-31.

(146) Jagger, D.; Harrison, A.; Vowles, R.; Jagger, R., "The effect of the addition of surface treated chopped and continuous poly (methyl methacrylate) fibres on some properties of acrylic resin"; *J Oral Rehabil* **2001**, *28*, 865-72.

(147) Jagger, D. C.; Harrison, A., "The effect of continuous poly (methyl methacrylate) fibres on some properties of acrylic resin denture base material"; *Eur J Prosthodont Restor Dent* **2000**, *8*, 135-8.

(148) Jagger, D.; Harrison, A.; Jagger, R.; Milward, P., "The effect of the addition of poly(methyl methacrylate) fibres on some properties of high strength heat-cured acrylic resin denture base material"; *J Oral Rehabil* **2003**, *30*, 231-5.

(149) Jagger, D. C.; Alshumailin, Y. R.; Harrison, A.; Rees, J. S., "The effect of the addition of poly (methyl methacrylate) fibres on the transverse strength of repaired heat-cured acrylic resin"; *J Oral Rehabil* **2003**, *30*, 903-8.

(150) Detanv, C. C. *Polymerization of methyl methacrylate (MMA) in bulk to form PMMA* http://ocw.mit.edu/NR/rdonlyres/Chemical-Engineering/10-467Fall-2005/96BA1F28-7EEE-4957-9D44-EC9132DC9DAB/0/10.pdf, 2005. Nov. 11th

(151) Kühn, K. D.; Springer: Berlin ; New York, 2000, p 22-40.

(152) Grohens, Y.; Brogly, M.; Labbe, C.; Schultz, J., "Chain flattening of spin-cast PMMMA on aluminum mirrors: Influence of polymer tacticity"; *European Polymer Journal* **1997**, *33*, 691-697.

(153) Hearle, J. W. S. In *Ellis Horwood series in polymer science and technology*; Ellis Horwood ;
Halsted Press: Chichester, England
New York, 1989, p 454 p.

(154) Allen, P. E. M.; Host, D. M.; Van Tan, T.; Williams, D. R. G., "Some physical and mechanical properties of isotactic-atactic poly(methyl methacrylate) blends and stereoblocks"; *European Polymer Journal* **1985**, *21*, 603-10.

(155) Trommsdorff, E.; Kohle, H.; Lagally, P., "*ZUR POLYMERISATION DES METHACRYLSAUREMETHYLESTERS"; *Makromolekulare Chemie-Macromolecular Chemistry and Physics* **1948**, *1*, 169-198.

(156) Tulig, T. J.; Tirrell, M., "On the onset of the Trommsdorff effect"; *Macromolecules* **1982**, *15*, 459-463.

(157) Joginder Lal, R. G., "Effect of amine accelerators on the polymerization of methyl methacrylate with benzoyl peroxide"; *Journal of Polymer Science* **1955**, *17*, 403-409.

(158) Nozaki, K.; Bartlett, P. D., "The Kinetics of Decomposition of Benzoyl Peroxide in Solvents. I"; *Journal of the American Chemical Society* **1946**, *68*, 1686-1692.

PART B

STRUCTURAL COLOR OF BUTTERFLIES AND BEETLES – CHARACTERIZATION, REPLICATION AND MIMICRY

CHAPTER 6

INTRODUCTION TO STRUCTURAL COLOR OF BUTTERFLIES AND BEETLES

6.1. Structural Color

Structural color, as the name suggests, is color produced by the nanostructured material rather than dye molecules absorbing photons of light. The connection between structures and the iridescent color was made early by Hooke[159]. He observed that the brilliant colors of peacock and duck feathers were destroyed by a drop of water and postulated that alternating layers of thin plates and air might strongly reflect the light. Newton[160] also postulated that the peacock feathers were colored due to the presence of a thin film. After that the explanation of structural color progressed in 19th century with the advent of electromagnetic theory by Maxwell in 1873 and the experimental work on electromagnetic waves by Hertz in 1884. Michelson observed that some beetles reflect circularly polarized light[161] and Lord Rayleigh developed a theory for reflections from a regularly stratified medium[162,163]. His son, the 4th Baron Rayleigh continued the work in microscopic characterization of the iridescent colors of insects and beetles[164]. Raman was also intrigued by the subject[165] and concluded that the colors originate from laminar diffraction[166]. Mason wrote two early reviews on the subject[167,168]. The optical characteristics of some structural color features were pretty well understood at this point and the next breakthrough came in the structural determination with the arrival of an electron microscope[169,170]. Since then, too many structures to list here have been

determined. A bit later, the photonic crystals were discovered, thus putting another piece on the puzzle of the structures that produce color[171].

Structural color is often observed in nature, particularly in the world of insects and especially in butterflies and beetles[172]. Structural color is often associated with the phenomenon of iridescence[173], which is the change of color hue with the angle of incident light and/or the observer. However, that is not always true. Sometimes structural color is not angle dependent. Recently, Kinoshita, Yoshioka and Miyazaki[174,175] have reviewed the physics governing the nanostructures responsible for structural color. Another fairly recent review on photonic structures in biology was written by Vukusic[176]. For general angle dependent optical effects, Pfaff and Reynders[177] have written a review. The structures responsible for the color of various butterflies were categorized by Ghiradella[178] and more recently by Ingram and Parker[179,180]. Two reviews of mechanisms of structural color production in beetles were recently published[181,182]. Here we only give a brief introduction to structural color features in butterflies and beetles. To learn how we might infer the underlying ordered structure from the optical response, let us first list some common structural color elements.

6.2. Thin Film

The simplest structural color element is a thin film. This structure is composed of layer of a material that is thin enough to be comparable to the wavelength of light. The effect can be easily seen in soap bubbles or oil slicks on water. The thickness of the film and the refractive index of the material determine the optical characteristics of this

structure. When a ray of light is incident upon a thin film at an angle ϕ_i , some of the light is reflected and some is refracted in the film to an angle ϕ_r. Some of the light is then reflected at the lower film surface, interfering with the light that was originally reflected at the first surface, as shown in **Figure 6.1**.

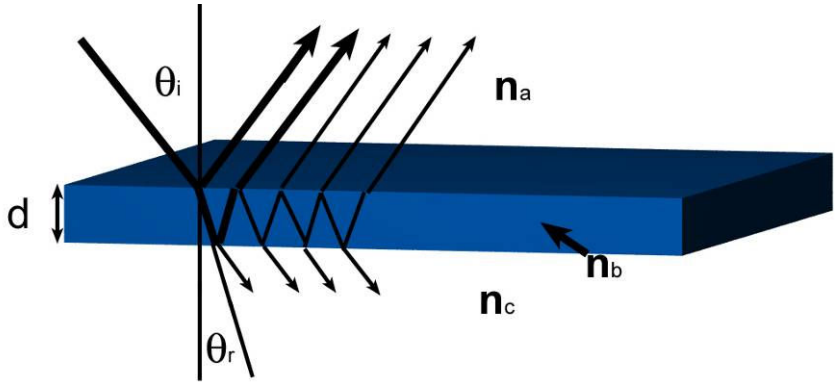

Figure 6.1: Schematic diagram for thin film interference. The light is incident at angle θ_i and reflects fro the top and bottom of the thin film. The angle θ_r is defined by the incident angle and the refractive index and so does the reflected color.

If the film is freestanding, like a soap bubble, the condition for constructive interference is[183]:

$$2n_b\, d \cos\, \theta_r = (m\text{-}1/2)\, \lambda \qquad \text{(Eq. 6.1)}$$

where n_a is the refractive index of the outside medium (air), n_b is the refractive index of the film, d is the thickness of the film, θ_i is the angle of incidence, θ_r is the refracted angle, related to the angle of incidence by Snell's law ($sin\ \theta_r = n_a/n_b \sin \theta_i$) , λ is the wavelength of peak reflectivity and m is an integer. If the film acts in a way similar to an antireflective coating, with another optically thicker material underneath, the constructive interference condition is[184]:

$$2n_b\, d \cos\, \theta_r = m\lambda \qquad \text{(Eq. 6.2)}$$

From the equations 6.1 and 6.2, we can see that the reflected light is blue-shifted with increase in the angle of incidence. To calculate the response at each particular wavelength, one needs to use Fresnel's law and take into account multiple reflections[184].

Thin films are often present as structural color elements in butterflies and beetles, since they are the simplest optical structure. A peculiar example of thin film usage is in making a thin broad-band reflector on the wing of *Argyrophorus argenteus*[185]. Two thin films, one flat and the other tilted, provide constructive interference over a range of angles, effectively making a broadband reflector that is much thinner than a typical one composed of multiple layers of variable thickness (**Figure 6.2**).

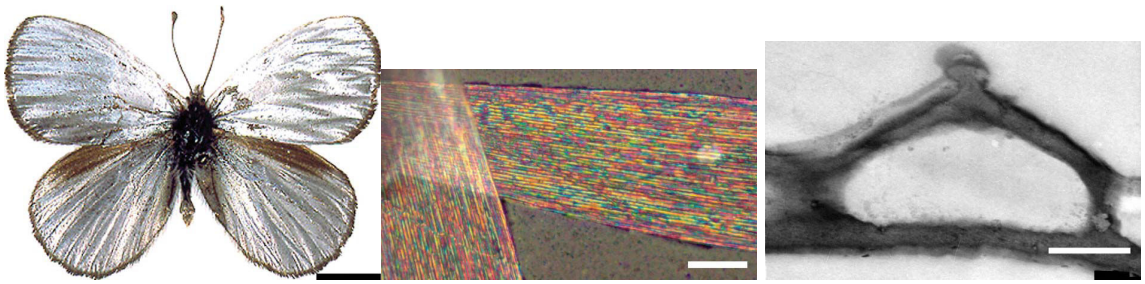

A **B** **C**

Figure 6.2: The silvery butterfly *A. argenteus:* (A) under a reflected light microscope (scale bar 0.5cm), (B) showing the reflections of multiple colors that combine into silvery white (scale bar 15 μm), and (C) the thin film structure responsible for the broadband reflector behavior (scale bar 120nm)[185] (Used by permission, © The Royal Society).

6.3. Multilayer

A stack of thin films atop each other is called a multilayer. It is perhaps one of the most common structural color features present. The optical response is governed by multiple reflections from all the layers in the stack. The reflection was first described

mathematically by Lord Rayleigh[162,163]. To calculate the reflection we conveniently package each reflection Fresnel equation in matrix form and multiply the matrices in the correct order[186]. The whole procedure is conveniently packaged inside a free program called "FreeSnell"[187]. Like with the thin film, the peak reflectance blue-shifts with increasing the angle of incidence. The peak width depends on the refractive index contrast between the two materials used and the peak location depends on the thickness of repeat unit. The repeat unit consists of two layers, one of each material. The maximum reflection is achieved, if the repeat unit *a* is an integer multiple of λ/2, making the thickness of each layer λ/4.[184,186,188] Multilayer principles can be a powerful tool for designing optical components, such as dichroic mirrors, dielectric mirrors, interference filters[186] and even an omni-directional reflector[189].

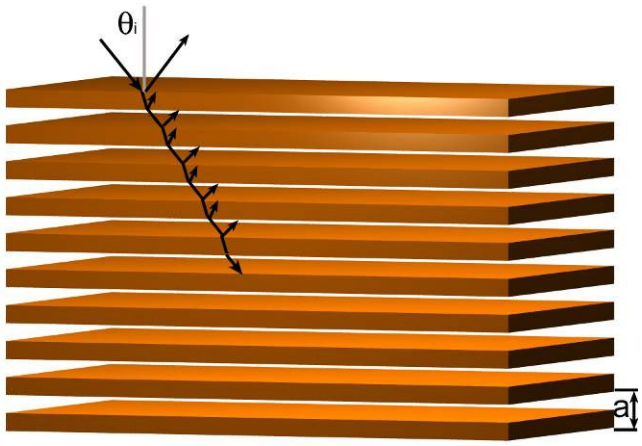

Figure 6.3: Schematic of a multilayer stack.

In butterflies and beetles, the two materials composing the multilayer are often air and chitin. In a sense, only one solid material is used, the other being air. A wonderful example of the multilayer reflection and interaction with light at different incident angles is the butterfly *Papilio palinurus*[190,191]. In this butterfly, the multilayer is bent into

microscopic cups (**Figure 6.4A**). The light interacting with the bottoms of these microcups at at normal incidence is reflected back as yellow, while the light interacting with the sides of the cup is reflected back after two reflections at 45º incident angle and is blue in color (**Figure 6.4B**).

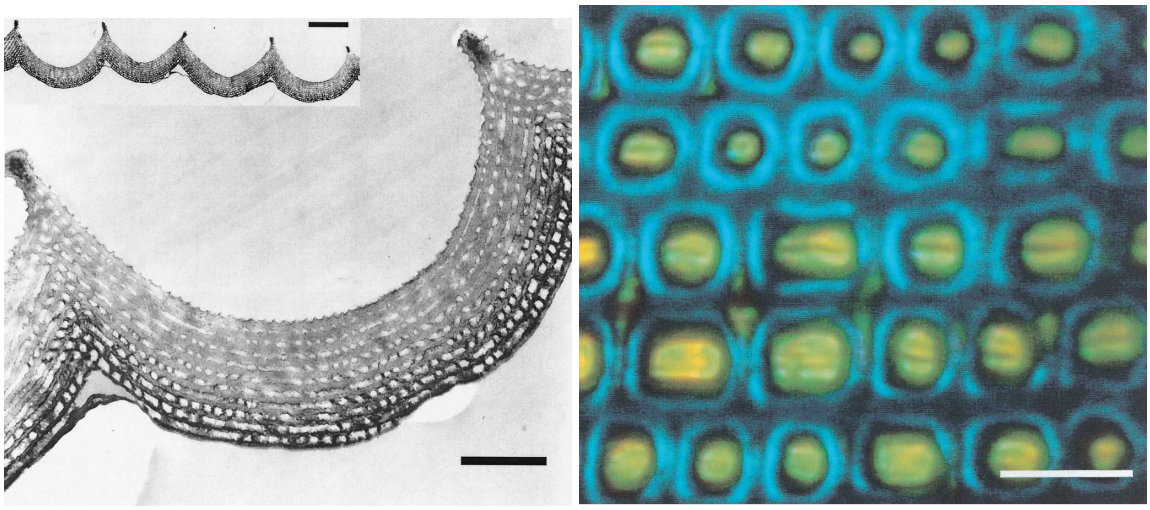

A **B**

Figure 6.4: Micrographs of the butterfly *Papilio palinurus:* (A) Transmission electromicrograph showing multilayer stack curved into a cup (scale bar 1µm, inset 3µm) and (B) the real color image of the microcups showing yellow reflection in the center and the blue on the edges (scale bar 10µm)[190,191] (Used by permission, © The Optical Society of America).

Another classic example is the butterflies in the *Morpho* family. Their metallic blue color is the result of multilayer reflection, combined with a grating-like structure present on the individual wing scales. The multilayer stack in this case consists of plates supported by a central structure, with a tree-like appearance in cross-section [169,170,179,192].

6.4. Diffraction Grating

A classic experiment dealing with light diffraction is Young's double slit experiment[105]. Two thin slits are separated by a known distance and an interference

pattern can be observed on a screen. If we periodically repeat the double slit from Young's experiment, we make a diffraction grating. Each slit acts as a point light source and the light from these light sources interferes to give an interference pattern, which depends on the distance between slits. A diffraction grating can also be thought of as a multilayer turned on its side, as shown in **Figure 6.5**.

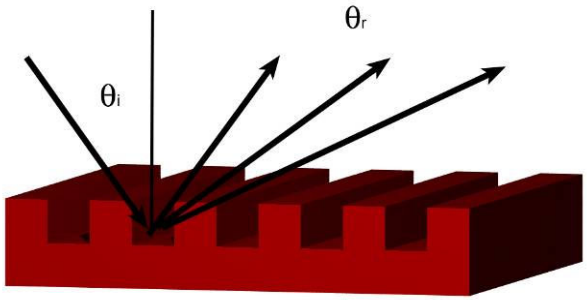

Figure 6.5: Schematic of a reflective diffraction grating.

The equation describing the reflection from a grating is[105]:

$$d\,(\sin\phi_r + \sin\phi_i) = m\lambda \qquad \text{(Eq. 6.3)}$$

where d is the spacing between slits, ϕ_r is the reflected angle, ϕ_i is the incident angle, λ is the wavelength of peak reflectivity and m is an integer. We can see that the wavelength depends on the incident angle as well as the observer angle. The wavelength increases with increasing incident angle, resulting in a red shift. For multilayers and thin films only specular reflection occurs, where the reflected light ray is traveling at exactly the same angle as the incident ray, only opposite in sign.

Diffraction gratings are quite common in nature. A beautiful example is the beetle *Sphaeridiinae gen. sp.* shown in **Figure 6.6**[181].

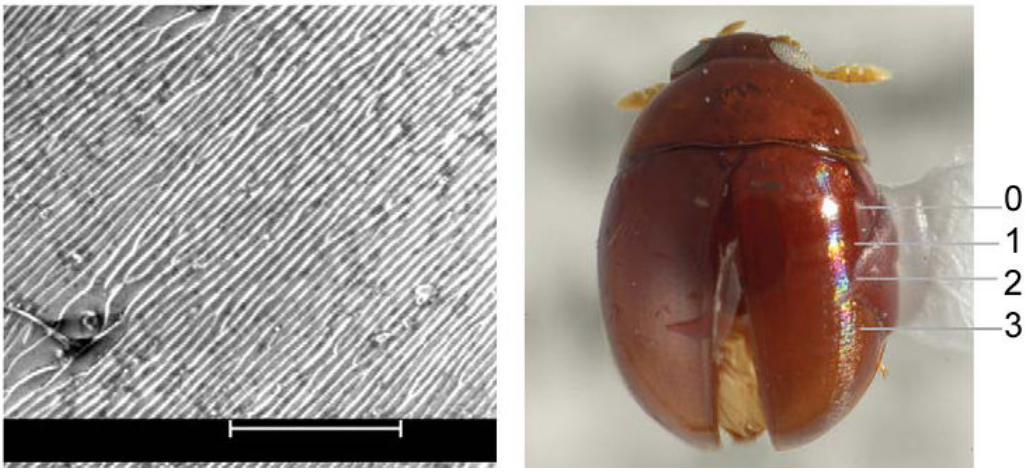

A **B**

Figure 6.6: (A) SEM of diffraction grating on *Sphaeridiinae gen. sp.,* scale bar 20μm and (B) habitus view of the same specimen with zero, first , second and third order spectral colors labelled[181] (Used by permission, © The Royal Society).

6.5. Photonic Crystal

A crystal is a periodic arrangement of atoms or molecules. Just as a crystal presents a periodic potential to an electron propagating through it, so a photonic crystal presents such a potential to a photon. The constituents of the crystal and the geometry of the lattice dictate the conduction properties of the crystal[188]. Waves can travel through such periodic potential without scattering. Furthermore, the lattice can also prohibit the propagation of certain waves. This is called a band gap. To an outside observer, the photonic crystal reflects the light that is in the photonic band gap.

We can also think about the photonic crystals in the same way as molecules and atoms interact with x-rays in crystals. The light is diffracted or reflected according to Bragg's law, where the planes are defined by the Miller indices[193].

The design of a photonic crystal depends on three variables: i) the crystal geometry, ii) the refractive index contrast, and iii) the volume fraction occupied by the material. The periodicity of the structure can propagate in one, two or three dimensions. In the following sections, we shall discuss some of the characteristics of these three types of photonic crystals.

6.5.1. 1D Photonic Crystal

A one-dimensional photonic crystal is basically a multilayer that has already been described in section 6.3. The only difference is how physicists think about the 1D photonic crystals. Instead of multiple reflections, the approach calls for the analysis of band structures[188].

6.5.2. 2D Photonic Crystal

In a two-dimensional photonic crystal, the structure is periodic in two dimensions, such as in **Figure 6.7**. We can envision several different plane directions which would give rise to Bragg diffraction. These planes have different repeat units. Each set of planes behaves similarly to a multilayer. Therefore, the reflected light will be blue-shifted as it interacts with planes that are not perpendicular to the incident beam. Since the width of the reflected peak (the band-gap) for a multilayer depends on the difference in refractive index of the two materials, we can see that multiple plane reflections will overlap in some region of the spectrum, if the reflection peak is wide enough. Thus, we are able to get some reflection at all possible angles, giving rise to a complete directional band gap. However, in order to achieve complete band gap for all polarizations, the difference in the refractive index between the two materials needs to be 3.6.[188] Considering the

refractive indexes of chitin (1.57), keratin (1.5) and melanin (1.3-2.0)[194], we do not expect to see complete band gaps in nature. Therefore, the color reflected from these structures should still differ in hue. Nevertheless, complete band gap for specific polarization can be realized [188].

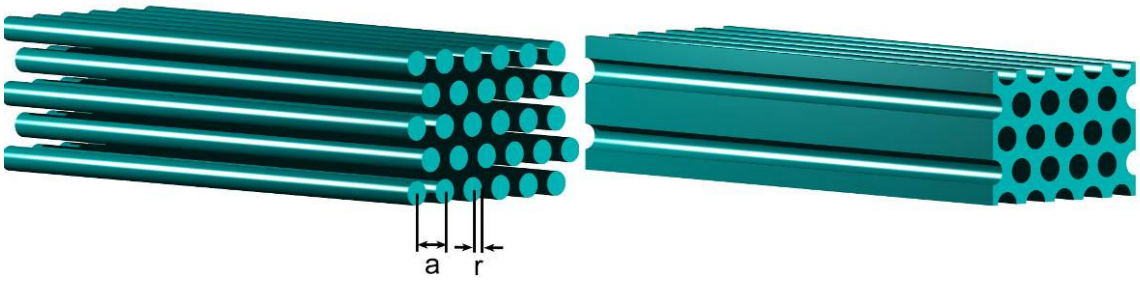

Figure 6.7: Schematic of a 2D photonic crystal. (A) Cylinders packed in hexagonal packing and (B) an inverse structure, which also displays similar characteristics.

The face of the 2D photonic crystal that is perpendicular to the cylinder direction does not exhibit much reflection. Instead, the light travels along and is guided by the surrounding cylinders. This principle, implemented through guiding the light along a single defect, is used in photonic crystal fibers and is hoped to increase the efficiency of photovoltaics[195,196].

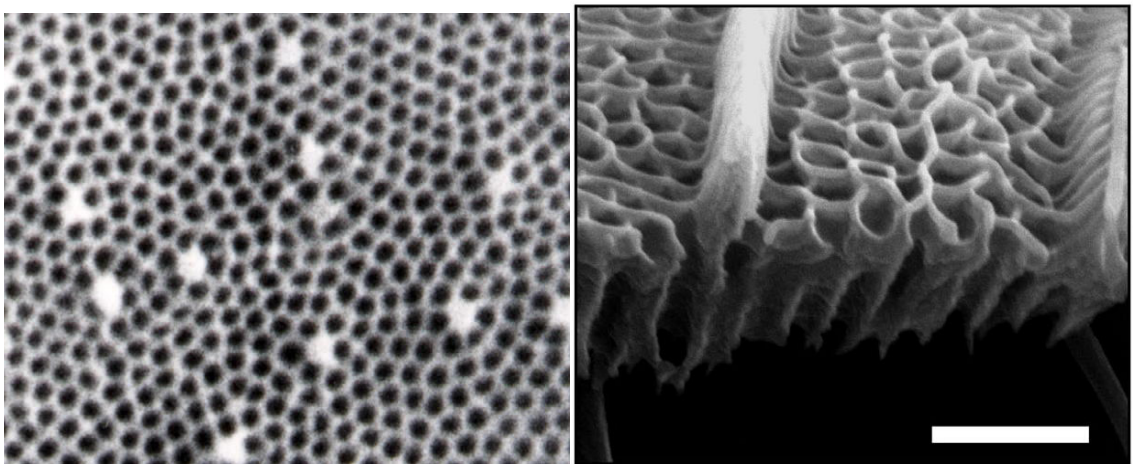

A **B**

Figure 6.8: (A) 2D arrangement of inverse cylinders in the butterfly *Papilio nireus*[197], scale bar 1.4 μm and (B) the same cylinders in SEM, tilted view, scale bar 1μm (Used by permission, © American Association for the Advancement of Science).

A 2D quasiperiodic photonic crystal is used by the butterfly *Papilio nireus* to guide and direct fluorescent light[197] (see Figure 6.8). Likewise, a 2D photonic crystal in the butterfly has been shown to increase the absorption of light[198]. In these two examples, we can see that even quasiperiodic structures can exhibit band-gap characteristics, as has been predicted[199].

6.4.3. 3D Photonic Crystal

Three-dimensional photonic crystals have the unit cell repeating in three dimensions. The same requirements for Bragg reflection as in the 2D photonic crystal lead us to conclude that there is a possibility of a complete photonic band gap in this system. Whereas the 2D photonic crystal has an "open" face at the ends of the cylinders, where light can propagate, a 3D structure is closed on all sides. Similarly to 2D photonic crystals, the geometry, volume fraction and refractive index contrast govern the optical

properties of 3D photonic crystals. Such photonic crystals are essential in making photonic devices for precision light guiding along the defect lines in the perfect crystals[196,200]. However, feasible production of these photonic crystals remains a challenge[200]. Therefore it is interesting to study how these crystals are formed in nature and what structures can be formed. It appears that the 3D photonic crystals are grown in the folds of smooth endoplasmatic reticulum, a sort of a lipid bilayer[201], which opens up wonderful possibilities of making these structures.

Recently Poladian *et al.*[202] have explained properties and appearance of photonic crystals specifically with the properties of natural materials in mind. The appearance of 3D photonic crystals in butterflies and beetles is governed by the fact that the complete photonic band gap is not attainable with natural materials. Therefore, blue shift is expected when the light is incident at the structure at an angle. However, most of the time the grain size of the photonic crystals present in structural color structures is not sufficient to allow the possibility to examine a single grain. Therefore, the outward appearance is usually an average of colors. The geometry of the 3D structure has a profound influence on the optical properties. The optical response will be different if the lattice is simple cubic (SC), body centered cubic (BCC) or face centered cubic (FCC).

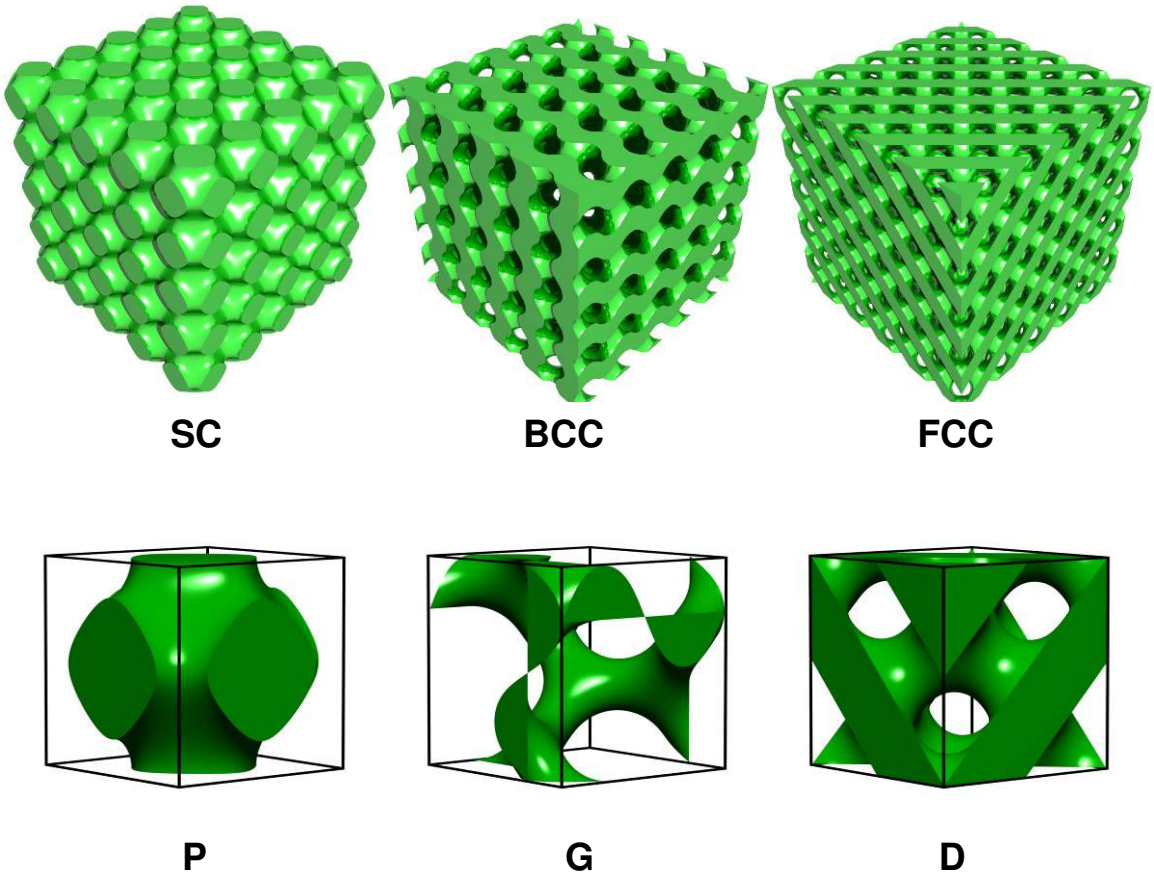

Figure 6.9: The three different cubic packing systems and the corresponding skeleton modes: simple cubic (SC) and primitive P structure, body centered cubic (BCC) and the gyroid G structure, and face centered cubic (FCC) and the corresponding D structure.

Specifically, a single grain in SC would appear more iridescent, having a greater dependence of color on angle than the other two crystalline systems[202]. The cubic structures can be reduced down to skeleton modes, which can be either based on connected cylinders or on minimum energy surfaces[179,203,204], reminiscent of soap bubbles on a cubic grid or lipid/water mixtures[205]. The skeleton structures are the smallest repeat units in the lattice. The structures schematically illustrated in **Figure 6.9** represent the skeleton structures. The SC lattice can be reduced to a 6-coordinated primitive P structure with 90º angles, the FCC to an interconnected 4-coordinated structure with node angles

of 109.47º and the BCC lattice to a 3-coordinated gyroid G structure with node angles of 120º. The gyroid structure is chiral and it can exist in two different handed gyroids. The analysis of band structures of these skeleton modes gives further insight into their optical properties. Namely, the SC lattice with the P skeleton structure is expected to exhibit some linearly polarized reflections. These reflections will also be blue shifted, perhaps in UV. The BCC lattice with the gyroid G structure is expected to have some circularly polarized reflections, which will also be blue shifted. The FCC lattice with D structure is not expected to exhibit polarized reflections. Finally, the effect of volume fraction should shift the center of the reflectance peak position, while the average refractive index influences the width of the reflected peak.

In the world of butterflies, the green hairstreak, *Calophrys rubi* has long been known to have a 3D photonic structure[206,207]. Also, *Mitora gryneus, Parides sesostris* and *Callophrys dumetorum* do [176,202,203]. Beetles from the weevil family such as *Eupholus bennetti*[176], *Eupholus chevrolati*, *Lamprocyphus augustus*[208], *Pachyrrhynchus congestus*[209] and *Metapocyrtus* sp.[210] also exhibit 3D photonic crystal structures. These are currently intensely studied to learn more about the method of their production and photonic properties.

Recently, finite difference time-domain simulations have revealed that even a non-regular structure with a characteristic distance between scattering objects, a so-called "amorphous diamond photonic crystal" behaves very similarly to a photonic crystal[211]. A bandgap is predicted, resulting in a peak at reflection. Some examples in nature have

been proposed to behave in a similar way[212]. Perhaps some colors, especially in bird fethers, that were previously explained by scattering[212-215] can be explained by this mechanism.

6.6. Cholesteric Liquid Crystal

Cholesteric liquid crystals are structures, where the mesogen is arranged in layers that are rotated relative to each other by a certain angle. This gives rise to a helical structure with a pitch p. The optical behavior of this structure is in some ways similar to a multilayer. The main distinction is that there is no difference in refractive index value among different layers, but instead there is director orientation difference among the birefringent layers. Because of this, a polarized ray gets reflected from the layer. Two polarized rays from two different layers then interfere to give circularly polarized light. The handedness of the reflected light is the same as the handedness of the helix. Furthermore, the handedness of the light reflected does not change upon reflection, as it does in reflection from a flat mirror. The light of the opposite handedness is transmitted through the structure. The peak position λ_o and shape (width, $\Delta\lambda$) are dependent on the helix pitch p and the birefringence Δn[216]. The peak position is directly proportional to the helix pitch and the peak width to the birefringence.

$$\lambda_0 = np \qquad \text{(Eq. 6.4)}$$

$$\Delta\lambda = p\Delta n \qquad \text{(Eq. 6.5)}$$

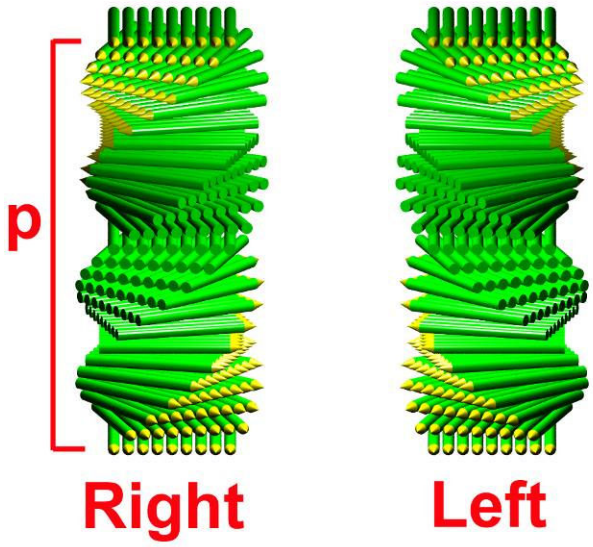

Figure 6.10: The structure of cholesteric liquid crystals. The molecules (or other rod-like entities) are arranged in layers and each layer is rotated relative to the previous by a fixed angle, thus forming a helix. The helices can be left or right handed.

A simple test for the presence of cholesteric structural color building blocks is to view the specimen through a circular polarizer. A great majority of scarabaeid beetles that reflect circularly polarized light display left-handed polarization. Thus, the chiral molecule responsible for inducing the helix pitch might be at least similar across the species or it just happens to have the same chirality. The selective reflection of circularly polarized light was first observed by Michelson[161], and Neville & Cavaney[217] have observed that the chitin fibrils are arranged in a pattern resembling the cholesteric phase. The circular polarizing reflectors appear to be limited to a narrow group of beetles, namely the Scarabaeidae family and further to the subfamilies Rutelinae, Scarabaeidae and Cetoniinae[181].

6.7. Combinations

Besides making the basic building block of structural color in ingenious ways, the world of butterflies and beetles can also teach us a lot about combinations of optical elements to combine, enhance or suppress reflected light effects. For example, the common multilayer is molded into cups on the wings of *Papilio palinurus*, resulting in two reflections of different color. Furthermore we discuss in Chapter 7 how the microcups modify the reflection from the specular reflection expected from a flat multilayer into a spacially more evenly distributed green color. Likewise, the arrangement of tree-like multilayers in the *Morpho* butterflies allows for slight variations in the height of these structures. This irregularity is believed to smooth out the reflective response[175,218], resulting in an even reflection in space instead of dots expected from the grating-like arrangement of the tree-like structures. The melanin pigment at the bottom of the scales in *Morpho* butterflies serves to bring out the blue color by suppressing light scattering. This can be seen very effectively by the appearance of *Morpho sulkowskiy*, which does not have any pigment and appears white, except at the direction of highest blue reflectance. In Chapter 9, we discuss how the surface of the beetle *Chrysina gloriosa* is decorated with focal conic defects, which modify the optical response from the specular iridescent reflector into a brilliant metallic, yet diffuse reflector with no angular dependence of reflected color[219,220]. The *Doxocopa* butterflies use a highly tilted multilayer on their scales to flash blue color from an otherwise dull brown surface. The effect is characterized in Chapter 7. The butterfly *Parides sesostris* uses a combination of 2D and 3D photonic crystal to produce its color[202]. The 2D photonic crystal is used to channel the reflected light from the 3D photonic crystal, thus eliminating iridescence. The

grains of 3D photonic crystals in *Calophrys rubi* are randomly oriented in order to achieve a uniform non-iridescent color on the macro scale. The butterfly *Argyrophorus argenteus* combines two thin films at an angle to build perhaps the worlds' thinnest dielectric wide-band reflector[185]. The examples of such cooperative interactions between optical building blocks are countless in the world of structural color. These combinations and modifications of the basic elements of structural color are important in teaching and inspiring us to manufacture new optical devices, types of color or to modify the existing devices.

6.8. Replication and Mimicry

The brilliant colors of the butterflies and beetles have already inspired researchers to produce optical devices based on their characteristics. A wide-bandwith angle-independent birefringent plastic mirror[221] was reportedly[222] inspired by the colors on the *Morpho* butterflies. Such plastic mirrors are used in liquid crystal displays around the world. An extension of the same approach resulted in photonic fibers for signal transfer[223] and used the same technology for decorating a fiber[224]. A fiber with a flat multilayer embedded within the core has already been commercialized[225]. Recently, the coaxial multilayer approach was used to make structurally colored fibers[226]. All these multilayered structures are made from combining two different polymers. The next step would be to make a multilayer structure based on a polymer-air multilayer, similar to the tree-like structure on the wings of *Morpho* butterflies.

The replication of butterfly wing structures has also received some attention. The motivation behind the effort at replicating structural color features is twofold: i) to

replicate the structure with an artificial material and study the change in optical or other properties, and ii) to explore and confirm or reject the mechanism of color production. The former leads to devices and applications. The fields of interest in this regard are photovoltaics[198], sensors[227], waveguides[228] and other optical devices. The technique that lends itself directly to replicating and modifying these intricate structures is chemical vapor deposition (CVD) and its variants. There were a couple of attempts at replicating the structure of butterfly scales. Huang *et al.* used atomic layer deposition (ALD) to replicate the scales of *Morpho peleides* by depositing a thin layer of Al_2O_3[228]. Their results indicate a color change with increasing the thickness of the deposition, thus demonstrating control over the optical properties. When the chitin template was removed, they observed retention of the blue color. Silver *et al.* have used fluorescent ceramic precursors to make nanocasts of butterfly scales[229]. Chen an co-workers have made large area replicas using ZnO_2 precursors[230]. The resulting structure maintains the iridescent appearance. Weatherspoon *et al.* have used a sol-gel sequential deposition technique to deposit a thin layer of TiO_2 precursor doped with SnO_2 to produce a rutile titania replica after burning out chitin. Rutile is important for making optical devices because of its high refractive index. Zhang *et al.* have recently[198] used the 2D photonic structure on the wings of butterfly *Papilio paris* and *Thaumantis diores* as templates for making a more efficient Graetzel[231] solar cell. These effort in coating and removing the chitin template have shown us, that the nature of color in these butterfly wings truly is structural, as the color is preserved even after burning out all the organic material. Furthermore, these efforts show that the replicated structures can have added functions beyond those used by the butterfly itself.

Another approach in mimicry of the structural color features is building them from bottom up without relying on the natural template. To this end, Watanabe *et al.* have used focused ion beam deposition to make an artificial tree-like structure characteristic of the *Morpho* butterflies[232]. The optical properties of a single tree-like structure were similar to the natural ones. Saito *et al.* have used a different approach[233]. They used nanocasting lithography to make multilayers of varying height, but with the same repeat unit, and have thus replicated the reflection characteristic of the wings of *Morpho rhetenor* very closely. A scale-up effort by Vukusic *et al.* resulted in a 20,000 times larger model, which was then investigated using microwaves[185,234]. The reflection characteristics were found to mimic the original scale, except the wavelengths of light reflected were also scaled up 20.000 times compared to the original scales, thus resulting in reflections in the microwave region of the electromagnetic spectrum.

These research efforts, ranging from structures inspired by nature and structures replicated from nature, to structures directly mimicking nature, show great promise in developing a better understanding of structural color. In addition, such studies show great promise in developing new functional materials. We will describe our own efforts in replication and mimicry in Chapters 8 and 10.

CHAPTER 7

MICROSCOPY METHOD FOR THE CHARACTERIZATION OF STRUCTURAL COLOR ON A SINGLE SCALE

7.1. Introduction

The brilliant iridescent colours seen on some insects are not caused by light absorption of pigments, but rather due to the intricately ordered structures which are comparable to the wavelength of light in size. Light interacts with these structures by reflection, refraction, diffraction, interference and scattering to produce structural colour[235]. The nanostructure is directly correlated with the optical response. In the past decades a lot of effort was devoted to understanding this structure-function relationship. The intricate underlying structures have so far taught us a lot about how light can be manipulated to produce brilliant colors[178]. Recently the biological nanostructures have attracted even more attention, because many examples of periodic biological nanostructures are candidates for 2D and 3D photonic crystals in the visible light region[176].

Many researchers have devoted a lot of time to elucidating the structure using electron microscopy[174,179]. The structure of various iridescent butterflies was elucidated and morphologically classified by Ghiradella[178]. The optical response of the wings was also characterized by various groups[164,167,168,175,234,236,237]. In the optical characterization studies, the single scale characterization stands out in importance, because only such a

method can clearly characterize a particular structural colour feature on the wings. When characterizing the whole wing, various other optical effects can play a role, such as cover scales, wing membrane and non-iridescent scales, etc.[234]. Considerable advancement has been made towards the characterization of the optical properties of individual wing scales. Vukusic and coworkers have mounted a single scale at the tip of a metallic needle and aligned it in a goniometer. They then characterized the reflection and diffraction using lasers of 6 different wavelengths in one plane of incidence[238,239]. Stavenga's group has characterized the reflection pattern of various butterfly species by mounting a single scale on a glass fiber and illuminating it through a hole in a screen[240]. The reflection on the screen was then recorded using a digital camera. A similar setup was previously used Kinoshita's group to record the reflection and diffraction patterns of various *Morpho* butterflies[218]. These efforts allowed the researchers to get great insight into the optical properties of individual wing scales and also propose good models for the behaviour of the reflected light[190,218]. However, there are also some limitations. All these techniques require a special set-up with carefully aligned optical elements. The single scale also has to be individually mounted.

We would like to describe how to characterize single butterfly scales using a microscope. The operation of the microscope does not need any special set-up or mounting of the single scales. The method we describe has recently been mentioned as one of the possibilities for characterizing biological iridescent surfaces[234], however, to our knowledge, the actual method and results obtained with it have not yet been reported.

Iridescence is defined as a phenomenon where the colour varies with the position of the observer[173]. In fact, the reflections of iridescent surfaces vary with the angle of incoming and outgoing rays of light. Therefore the full optical characterization requires measurement of the bidirectional reflection distribution function (BRDF)[241]. BRDF describes all the energy released in the form of light upon illumination of the surface. It describes the light intensity at all possible incoming and outgoing angles and wavelengths.

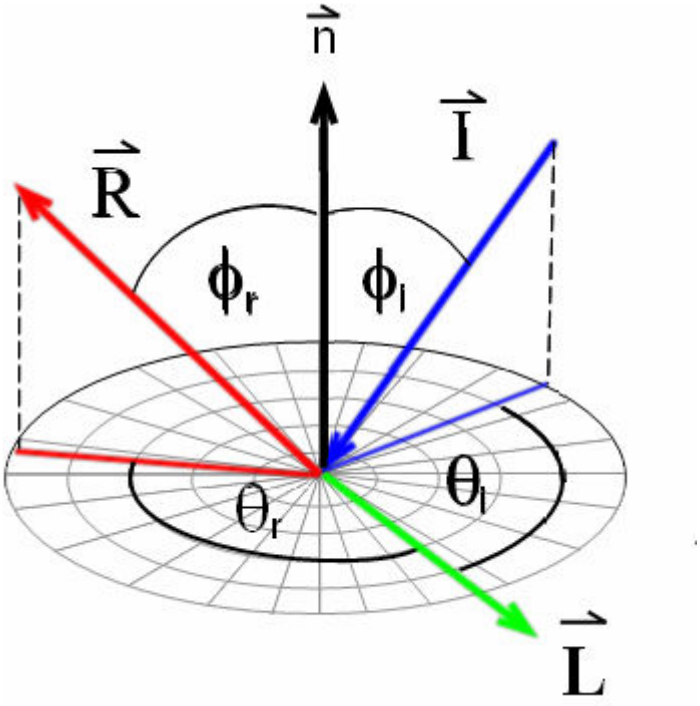

Figure 7.1: The variables in BRDF. The blue arrow shows the direction of incident light and the red arrow the direction of one particular reflection. Angle ϕ_i between the incident ray $\vec{I}$ and the surface normal $\vec{n}$, and angle θ_i between the surface projection of the incident ray and the long axis of the surface $\vec{L}$, define the illumination condition. Angles ϕ_r and θ_r similarly define reflected ray vector $\vec{R}$. Reflectivity for any given combination of these four variables defines the BRDF.

The measurement of BRDF (vectors shown in **Figure 7.**1) requires placement of incoming light $\vec{I}$ at an angle ϕ_i to the surface normal $\vec{n}$ and the detector also at a chosen

angle ϕ_r to the surface normal. In addition to that, the angle θ_i in the plane of the surface between the light source and the long axis $\vec{L}$, as well as the reflected angle θ_r need to be chosen. Reflectivity $\vec{R}$ is then measured. All four variables need to be varied until the full four dimensional space is characterized. The BRDF is formally only defined for one wavelength, therefore to fully characterize the surface, the measurement needs to be repeated for each wavelength separately. To avoid fluorescence measurement, which is not part of the BRDF, a single wavelength should be chosen at the light source and the detector should ideally also be selective for the same wavelength. This prevents fluorescence measurement as long as the emission is at lower wavelengths than the excitation. This condition is rarely met experimentally, due to the time consuming nature of such an experiment. In our work we have simplified the measurement by illuminating the sample with white light and recording an image by a color camera to speed up the characterization. While not formally a characterization of BRDF, this approach does provide insight into the appearance of the subject at various angles. Instead of spectral data, the RGB intensity data can thus be captured.

The challenge in characterizing the optical surfaces in biology stems from the fact that the BRDF of iridescent surfaces is highly anisotropic. In characterizing most other surfaces, such as smooth materials or randomly rough materials, the assumption can be made that the angle between the surface long axis and surface projection of the incoming ray of light (θ_i) does not affect the measurements. In other words, rotations about the surface normal can be ignored. This greatly reduces the number of necessary measurements[242]. The patterning of the iridescent surfaces makes the response different

depending on the incoming and outgoing angle and the only way to discern those relationships is full BRDF characterization.

Another difficulty with measuring the optical properties of biological materials is that the regions and features where optical structures are present are often very small. Manipulation of these small objects can be challenging. In addition, the methods of illumination and reflection measurement need to be suited to the small size (<100μm) of these objects.

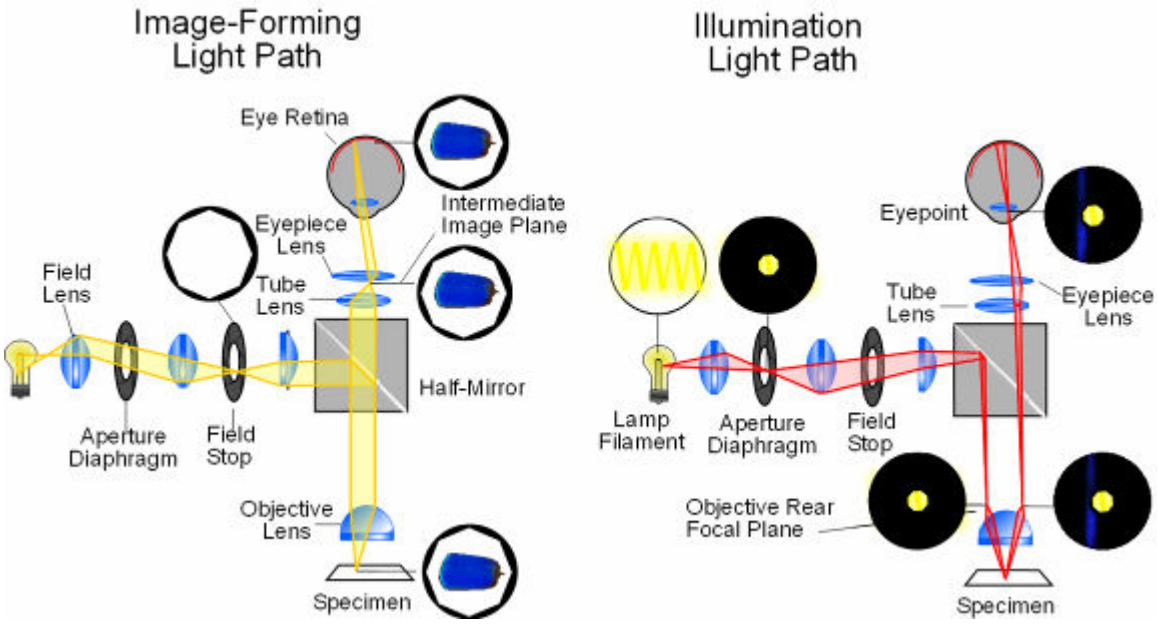

Figure 7.2: The conjugate planes in a reflected light microscope. The image forming path is illustrated with the field stop slightly closed down so that the edges of the iris appear in the field of view when the object (a single *Morpho rhetenor* scale) is in focus. The illumination light path is illustrated starting with the lamp filament, which is in focus. The aperture diaphragm is in the same focal plane and is shown closed down and centered, so that a small bright spot appears in the center of the inverse space image. After the light reflects from the specimen (in this case a single *Morpho rhetenor* scale), the scattering pattern appears in the inverse space image. This image can be seen by using a Bertrand lens.

Let us look at the ray diagram of microscope optical train and see how the microscope can be used for the characterization of the BRDF. There are two light paths in a microscope, each having four focal planes (**Figure 7.2**). The first is the image-forming path and the objects in focus in this path are the field stop, the specimen, the intermediate image plane (where the crosshairs reticule is positioned) and at the retina in the eye. The second is the illumination path and in this path the focal planes are at the filament of the light bulb, the aperture stop, the back of the objective and at eyepoint (at the lens of the eye). By using a Bertrand lens, it is possible to look at the illumination path and its planes.

The microscope objective focuses the light to infinity. The image in this space is called infinity space image or inverse space image, reciprocal space or Fourier space. This image can be seen if the microscope eyepiece is removed or if the microscope is equipped with a Bertrand lens. In this inverse space image the reflected angles ϕ_r and θ_r can be easily characterized simply by recording the image (**Figure 7.3**). The incident light angles ϕ_i and θ_i can also be known by properly adjusting the aperture stop.

The aperture stop controls the angle at which the illuminating light rays enter the sample. By closing the aperture, we are limiting the range of angles at which the rays are incident upon the surface. The aperture is usually centred by means of centring screws. By closing the aperture, we are thus achieving the normal incidence with ϕ_i close to 0º. The angular width of the cone of light incident upon the sample is determined with the size of the aperture iris. Usually, the aperture can be closed down where a range of angles

is ϕ_i ±2º. By manipulating the aperture stop alignment and size we can change the incident angle of light without having to move the sample.

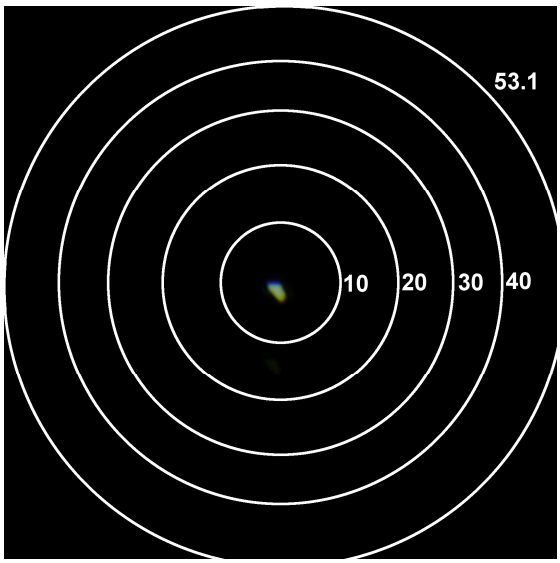

Figure 7.3: The aluminum mirror in inverse space under normal incidence. The concentric circles mark the different angles ϕ_r. The maximum angle that can be observed is limited by the numeric aperture of the objective used, in this case NA = 0.8 = *sin* (ϕ_r), which corresponds to a maximum angle of 53.1º.

7.2. Experimental

The scales of *Morpho rhetenor* and *Papilio Palinurus* were scattered on a microscope slide and imaged with an Olympus BX40 reflected light microscope equipped with a 50x 0.8 NA objective, a mercury lamp, a Bertrand lens and a Nikon D300 camera. The scales were centred manually by adjusting the microscope slide. The field stop was closed down when the inverse space images were obtained to limit the sampling spot size. The aperture stop was also closed down and fixed in the centre or off-

centre, depending on the desired incoming angle ϕ_i. A centred rotating stage was used in order to study the various incidence angles θ_i.

Diffraction patterns in transmission mode were obtained on a Leica RDX microscope equipped with a xenon lamp, a Bertrand lens, a Sony DXC5000 digital camera and a 40x 0.75NA dry/1.25 NA oil immersion objective. The butterfly scales were scattered on the microscope slide and covered with a cover glass. Immersion oil was put on the cover slip but not on the scales.

Laser Scanning Confocal Microscopy was performed using a Leica TCS SP confocal microscope with 514.5 nm excitation wavelength and a 40x 1.25NA oil immersion objective. The samples were immersed in 1.57 refractive index immersion oil (Cargille). The autofluorescence of the chitinous material in the scale was used for imaging.

ImageJ image analysis software (http://rsbweb.nih.gov/ij/) was used to analyze the digital images.

7.3. Results

If we observe a specular reflector[243] such as an aluminium mirror in a reflected light microscope set-up with the Bertrand lens in place, we see a bright speck in the centre of the inverse space (**Figure 7.3**). The size of the speck determines the range of illuminating angles. If we choose a more Lambertian reflector[243], such as Teflon or

Spectralon or a piece of white paper, the light will be scattered throughout the field of view and we might not see the centre speck as clearly. An ideal Lambertian reflector will fill the field of view in inverse space with white light, where the light intensity is related by $I(\phi_r) = I_N \cos(\phi_r)$, where I_N is the intensity at the surface normal. A specular reflector will only show a sharp speck in the centre. In this set-up we can observe the reflection patterns of single butterfly scales. It is helpful to have a dry objective lens with high numeric aperture to be able to observe a wide range of angles, because the maximum reflected angle ϕ_r that can be observed depends on the numeric aperture of the objective (in our case NA = 0.8 = $\sin(\phi_r)$). The incident and reflected angles ϕ_i and ϕ_r can be determined by the distance from the centre of the image, as demonstrated by the concentric rings in **Figure 7.3**. No calibration is necessary to determine these angles, in contrast to a scatterometer with an elliptical mirror. The lenses do not distort the image in any way and the angles are directly correlated. The plane projection angles θ_i and θ_r can be determined by knowing the direction of the long axis $\vec{L}$. The angle θ_r between an observed reflection and the long axis $\vec{L}$ is simply the angle between the vector of the long axis and the vector pointing from the centre of the image to the reflection spot in question.

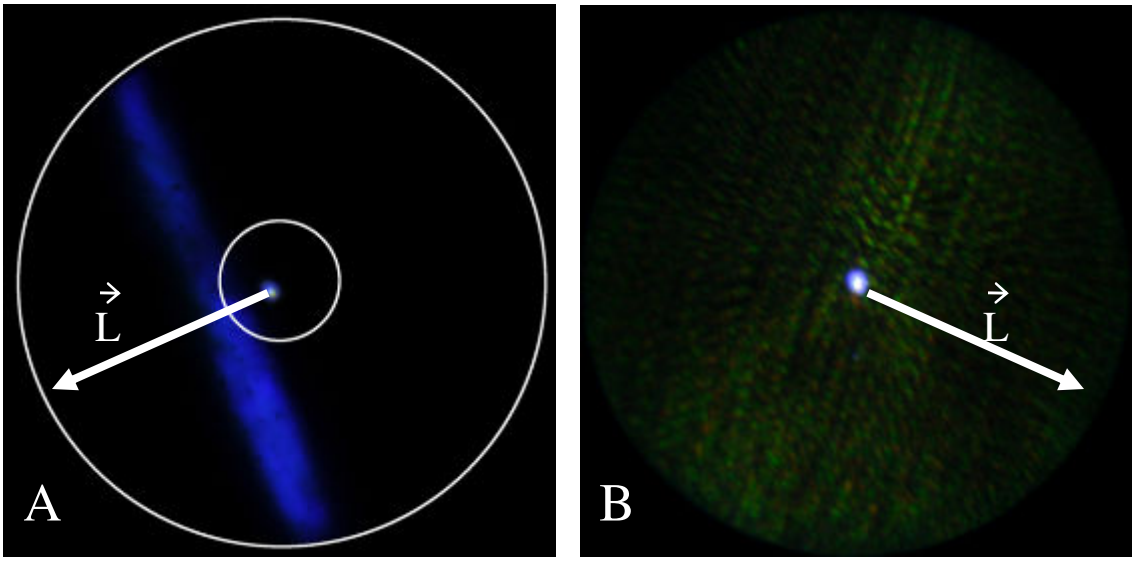

Figure 7.4: The scattering pattern of *Morpho rhetenor* (A) and *Papilio Palinurus* (B).

When we observe a single ground scale of *Morpho rhetenor* in this set-up, we can see (**Figure 7.4A**) the typical scattering pattern as previously reported by Kinoshita *et al.*[218] and Giraldo *et al.*[240] from their experiments on a single scale mounted in a custom set-up. That is a narrow blue streak that is slightly off-centre. By rotating the scale on a centred rotating stage, we can check if there are any changes in the scattering pattern. The narrow blue reflection band that is shifted about 10º off the surface normal rotates about as we rotate the scale, as we can see in **Figure 7.4**. The reflected angles ϕ_r remain the same throughout.

A single scale of *Papilio Palinurus* exhibits a broad scattering pattern (**Figure 7.4B**). Sharp green spots appear throughout the field of view. The pattern appears much

more uniform throughout the whole range of angles. It is interesting to note that all the spots appear green, while the real-space image show yellow bowls with blue rims.

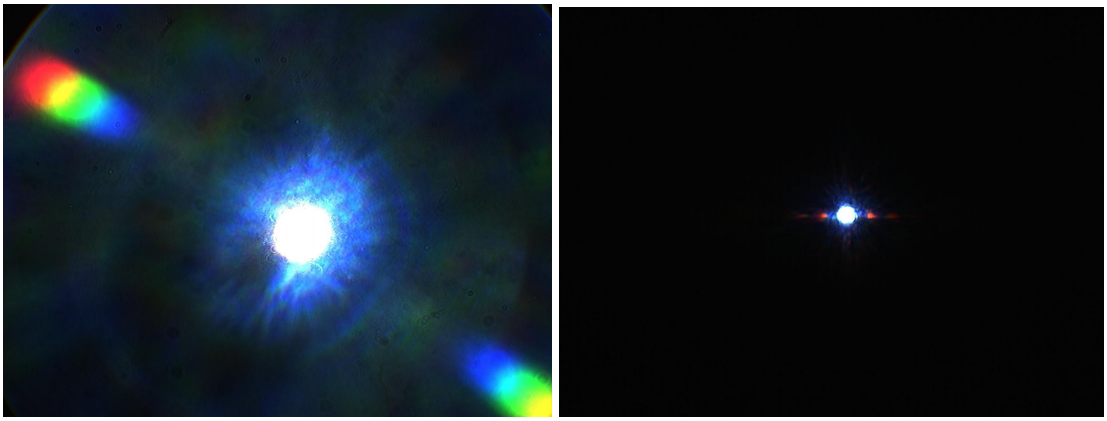

Figure 7.5: Diffraction images in transmission for *Morpho rhetenor* (left) and *Papilio palinurus* (right). The diffraction spots correspond to a characteristic *d* spacing of 750nm in left image and 6μm in the right image.

A similar analysis can be done in the transmission mode (**Figure 7.5**). With the condenser aperture stop closed down and the Bertrand lens swung in, we can observe the diffraction pattern. The spots in the pattern correspond to the diffraction grating distance through the relation $n\lambda = d \sin(\phi)$, where n is an integer noting the order of diffraction, λ is the wavelength, d is the characteristic spacing and $\sin(\phi)$ corresponds to the distance from the centre beam to the diffracted spot in the inverse space image, divided by the maximum distance $NA = 0.95$. The maximum distance to the edge of the inverse space image corresponds to $NA = 0.95$, the highest numeric aperture achievable without immersing the sample in oil. In the case of *Morpho rhetenor* (**Figure 7.5A**), the red green and blue spots correspond to a diffraction grating with a characteristic distance $d = 750$ nm, assuming the red wavelength to be 610 nm, the green at 540 nm and blue at 450 nm. In the case of *Papilio palinurus* (**Figure 7.5B**), the characteristic grating distance is 10 μm.

The normal incidence inverse space images tell us a lot about the iridescent behaviour of the butterfly wing scales. However, in the setup described so far, we are limited in observing a single incident angle ϕ_i. In order to adjust the angle of incidence, we can either tilt the scale with the aid of a spindle stage or we can adjust the illumination alignment. It is simpler to change the illumination alignment, as we do not need any special equipment for that. The aperture stop is equipped with two centring screws that can also be used to adjust the illumination alignment. If we move the closed down aperture stop off centre, we thus change the incident angle ϕ_i. The ray diagrams in **Figure 7.6** illustrate how we can control the incident angle ϕ_i. Because the aperture stop and the back focal plane of the objective are in the same focal planes, we can draw the aperture stop in the back focal plane of the objective instead of drawing the whole diagram. For the reflected light, the aperture stop is not drawn, because it does not affect the reflected light. When we observe the specular reflection from a mirror in this setup, we can see a reflection speck that is not in the centre of the inverse space. This is the location of the reflected light from the mirror. The incident ray can be found by inversion of the image of the speck through the centre of the image. For a mirror, $\phi_i = \phi_r$ and $\theta_i = \theta_r + 180°$. Now we know the exact location of the incident ray. In our case $\phi_i = 30°$ and θ_i has to be determined later, because we are rotating the long axis of the sample on the centred stage. However, the incident ray remains fixed and in our case the incident ray $\vec{I}$ travels in west-east direction, as noted in **Figure 7.6.**

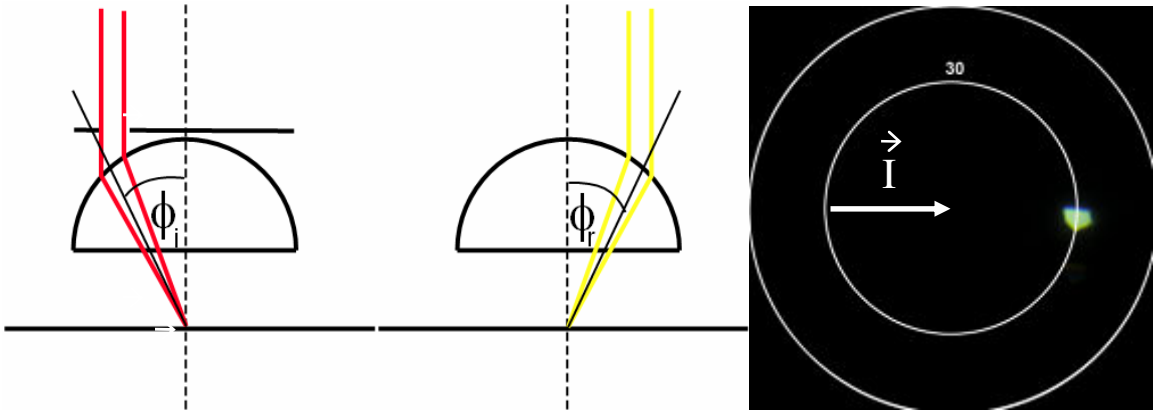

Figure 7.6: The illumination path ray diagrams for incoming light (red) and reflected light (yellow) from a mirror and the resulting image in inverse space. Incoming light angle is adjusted by closing the aperture and moving the iris off centre. Because the aperture stop and the back focal plane of the objective are in the same focal planes, we can draw the aperture stop in the back focal plane of the objective instead of drawing the whole diagram. For the reflected light, aperture stop is not drawn, because it does not affect the reflected light.

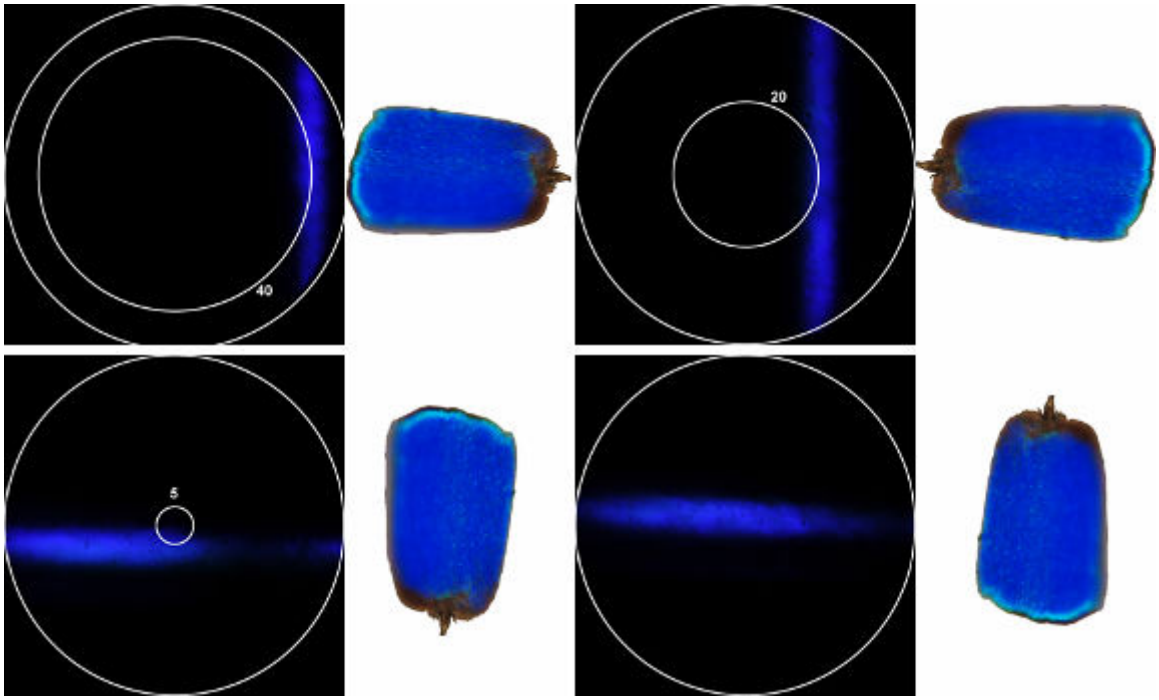

Figure 7.7: Examination of a single scale of *Morpho rhetenor*. Incoming light beam comes from the left side of the image at ϕ_i = 30º. Inverse space images correspond to the scale orientations pictured on the right side of each image. The outermost ring corresponds to the maximum angle of 53.1º that can be measured with this objective (NA=0.8). Circles with numbers indicate the reflected angle ϕ_r in degrees.

When we examine a single scale of *Morpho rhetenor* in this setup, we can observe how the reflection pattern changes at such an incident angle (**Figure 7.7**). Immediately we can see that the blue streak has shifted farther from the centre of the image. By rotating the centred stage, we thus vary the angle θ_i . As in the previous experiment, we observe the same range of angles θ_r and ϕ_r, where the range of ϕ_r is limited by the numeric aperture of the objective. When we rotate the stage, we are changing the direction of the long axis $\vec{L}$ and thus θ_i. During rotation we observe the blue streak rotating. The centre of rotation is not the centre of the inverse space image anymore. Instead, the blue streak appears to be rotating about the point of specular reflection from the mirror. When we measure the angle ϕ_r for the midpoint of the blue streak, we can see that it ranges from 5º to 40º, depending on the orientation of the scale.

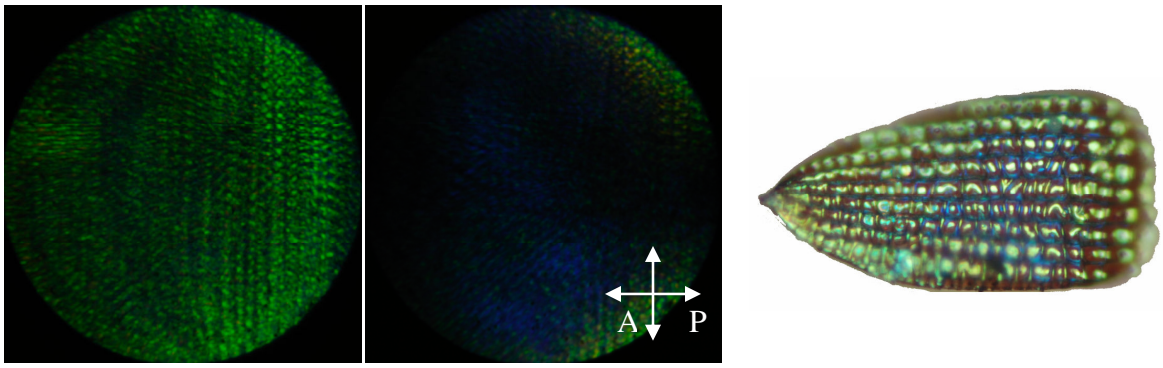

Figure 7.8: *Papilio palinurus* single scale examined with light beam incoming from the left side of the image at ϕ_i = 30º. The middle image is taken with crossed polarizers to show the scattering pattern of the blue bowl rims. The right image shows the orientation of the scale.

The scattering pattern of *Papilio palinurus* with incoming light at ϕ_i = 30º looks very similar to the pattern generated at normal incidence. When we rotate the scale, the

pattern does not change. This is consistent with the macroscopic appearance of *Papilio palinurus*, whose colour remains the same regardless of the observer position.

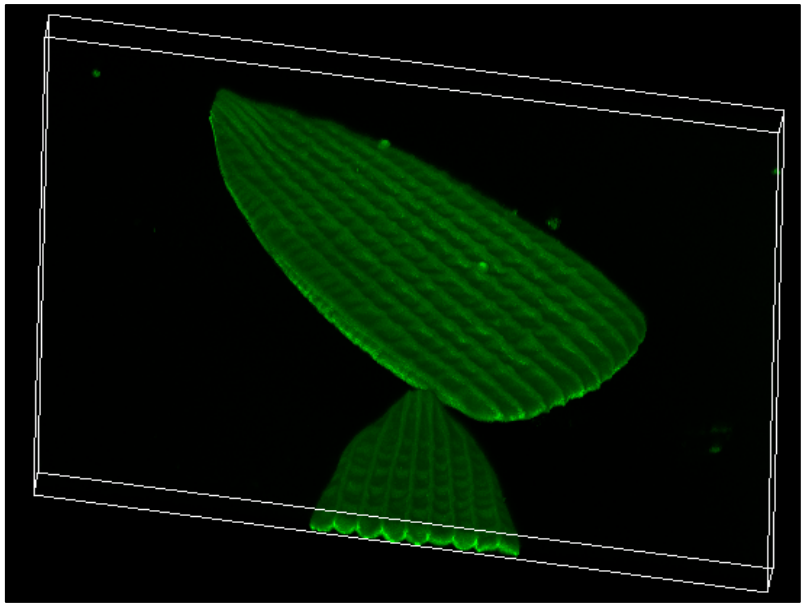

Figure 7.9: 3D reconstruction of laser scanning confocal images of a scale of *Papilio palinurus*. The microbowls responsible for the reflection of the blue and yellow light are clearly visible. The ridges responsible for the diffraction in transmitted light can also be discerned. 3D box size is 250x250x4.3μm.

The 3D reconstruction of the laser scanning confocal image of *Papilio palinurus* shows the morphology of the scale. The microbowls containing the multilayers can be clearly seen. It is these microbowls that are responsible for the reflection mechanism resulting in colour mixing[190,191]. This colour mixing will be dealt with in more details in Chapter 10. The ridges approximately 10μm apart, which are responsible for the diffraction pattern, are also very clearly imaged.

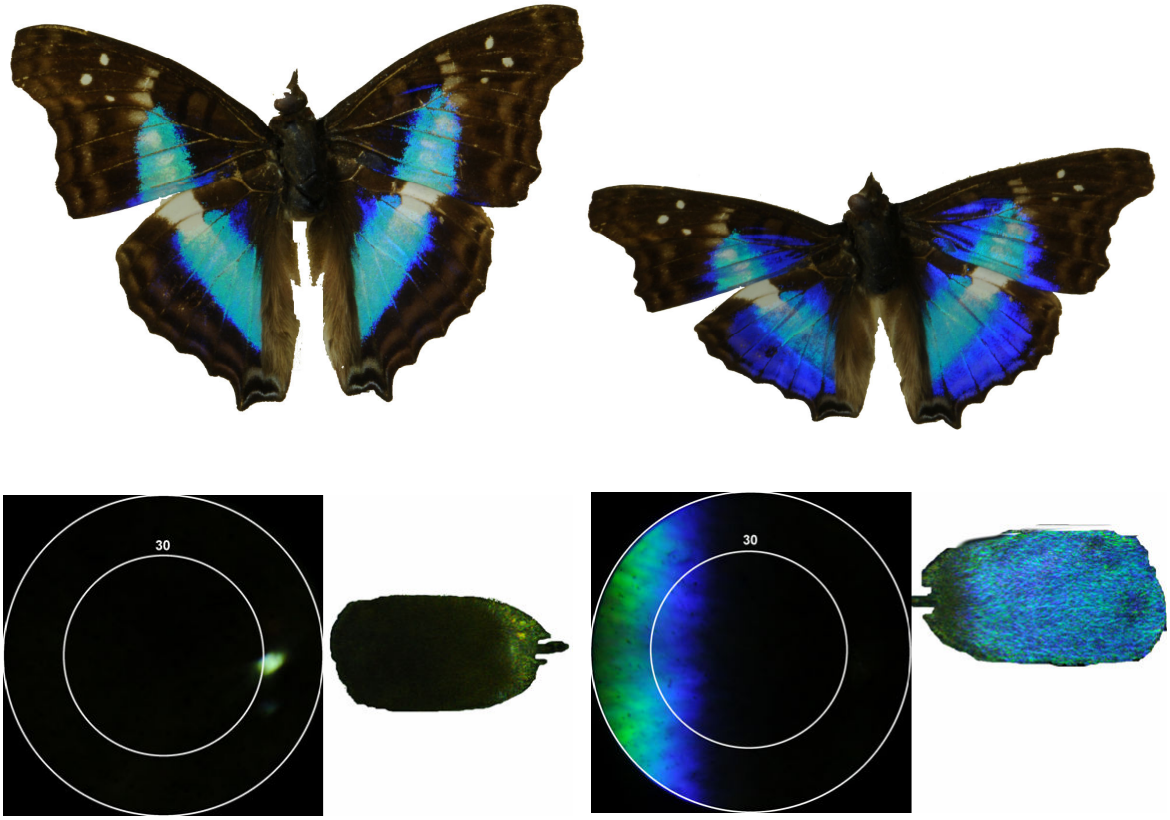

Figure 7.10: The butterfly *Doxocopa seraphina* and the corresponding microscope inverse space images.

Doxocopa seraphina has a very interesting, bright blue color, which can only be seen if the butterfly is tilted in a certain way. It turns out that the bright blue light is reflected, if the light is coming in from the front of the butterfly. The direction of the reflected light is also along the incident beam. We can see that very clearly from the inverse space images in **Figure 7.10**. The incident ray is coming from the left side. When the scale is oriented with its long axis parallel to the incoming light beam, two situations may occur: if the growth direction of the scale is oriented against the beam (stem on the right), the scale appears dark and if the growth direction of the scale is oriented along the light beam (stem on the left), the scale appears bright blue. In inverse space we see that in

the case where the scale appears bright blue, the light is reflected back to the light source and is separated into blue and green hues. Most likely the multilayer reflector on the scutes is placed at a an angle of 30°, similar to *Troides magellanus*[179] and *Ancyluris meliboeus*[244].

7.4. Discussion

The method described for the analysis of the optical properties of microscopic surfaces is very simple and convenient. The main advantage of this method is the availability of microscopes in most biology labs where researchers might study the iridescence. The microscope is also pre-aligned, so the researcher does not need to worry about the proper placement of optical elements. The range of reflected angles that can be studied by this method is limited by the numeric aperture of the objective. Thus, the greatest angle ϕ_r that can be studied is limited by the maximum numeric aperture for dry objectives of 0.95. Dry mounting is necessary, because the iridescence often depends on the refractive index difference between the structures on the wing scale and air. Mounting the specimen in a different refractive index medium will change the optical properties. The range of incident angles that can be studied without a spindle stage[245] is limited by the total internal refraction of light. The critical angle for total internal refraction of an air – glass interface is about 42°. Therefore, light incoming at angles higher than the critical angle will reflect from the bottom surface of the objective lens instead of interacting with the sample. Higher incident angles can be achieved by use of special objective with dark-field collars or by using a spindle stage and rotating the scale.

Inverse space analysis of *Morpho rhetenor* single scale allows us to characterize the BRDF in a large range of reflection angles ϕ_r and θ_r with a single image. The normal incidence analysis confirms the previously reported results[218]. The analysis at 30° incidence angle ϕ_i further illustrates the anisotropic nature of the reflective optical properties. We can see that the reflection pattern strongly depends on ϕ_i as well as θ_i. This observation is similar to the observations made by Berthier *et al.*[246], where the BRDF of multiple *Morpho* scales was measured. In comparison to the method described by Berthier *et al.*, the method described in this article has several advantages. First, the measurements are being done on a single scale instead of a collection of scales. Second, the whole range of angles ϕ_r and θ_r can be observed by taking a single image with a digital camera. Third, the angle θ_i can be easily varied by rotating the centred stage. As we can see from the sample images, the BRDF pattern changes a lot upon changing the angle θ_i. The disadvantages are the fact that the observation space of reflected angles ϕ_r and θ_r is limited by the numerical aperture of the objective and the fact that we are only able to acquire RGB colour data from the digital camera, instead of spectrum traces. In comparison to the imaging scatterometry method recently published by Stavenga *et al.*[247], the main advantage of the inverse space microscopy is its simplicity and availability. Scatterometry requires a custom made elliptical mirror, which is not necessary for microscopy. Since the elliptical mirror stretches the scattering pattern, it is necessary to calibrate the scatterometer in order to use it. All images need to be corrected and the correction is not linear. As far as the incident beam calibration is concerned, the two methods are similar. The placement of the aperture stop needs to be recorded in order to know the incident angle of the light beam, just as the position of the diaphragm needs to

be calibrated in scatterometry. On the other hand, the scatterometry method allows for a far greater range of reflected angles to be studied. The elliptical mirror allows a complete dome of angles up to 90° to be recorded. The sample preparation in scatterometry is also slightly more complicated, as the individual scales need to be specially mounted. For microscopy, they can be simply scattered on the microscope slide, unless a spindle stage is used.

The analysis of the reflection pattern of *Papilio palinurus* reveals a more uniform pattern. There are numerous green spots scattered in ordered rows throughout the observed range of angles. If the light source is not a point source and when there are multiple scales tiled together, this pattern more closely resembles a Lambertian reflector with the intensity distributed throughout the range of reflected angles. The many scales compose a rough surface, where the roughness is approximately random. Therefore the particular green spots can only be seen through a single scale analysis. The confocal image provides us with a 3D model of the scale and demonstrates how the microbowls are arranged.

7.5. Conclusions

The inverse space image analysis is a powerful tool for characterizing the scattering patterns from structured surfaces. We have shown how the microscopy inverse space analysis can be applied towards characterizing the BRDF of single butterfly scales. We have also shown how this method can be used to observe the reflection pattern at incident angles other than normal. We then used this method to characterize the single scales of *Morpho rhetenor, Papilio palinurus* and *Doxocopa seraphina*. For the *Morpho*

rhetenor we have shown how the blue streak is reflected at a number of different incident angles, varying both ϕ_i and θ_i. We have also characterized the diffraction pattern using a microscope. The diffracted spots correspond to the underlying grating structure. The single wing scale of *Papilio palinurus* was also characterized both in reflection and transmission mode. In reflection, multiple green spots were observed. In transmission, the characteristic grating size was determined and confirmed using laser scanning confocal microscopy. *Doxocopa seraphina* was shown to have a limited view iridescence pattern, most likely resulting from a multilayer tilted at 30°.

CHAPTER 8

MODIFICATION AND REPLICATION OF THE STRUCTURAL COLOR FEATURES OF THE BUTTERFLY *Morpho rhetenor*

8.1. Structural Color on the Wings of *Morpho rhetenor*

Among the animals that exhibit structural color, the *Morpho* butterflies are perhaps the best known and one of the most spectacular. The bright blue metallic color is produced by tree-like nanostructures on the wing scales[238]. These structures are placed closely together and they interact with light in two ways: i) as a diffraction grating, resulting from the spacing of the "trees" and ii) as a multilayer, resulting from the spacing of the "branches"[207,218]. The multilayer is slightly tilted relative to the plane of the scale and thus the strongest reflection was observed to be about 10º from the surface normal[240,247,248]. Usually the *Morpho* butterflies have two separate sets of scales – transparent cover scales where the tree-like structures are sparse, and colored ground scales, where the tree-like structures are densely packed[249]. In addition, the ground scales have melanin pigment near the bottom of the scale. The particular species we studied, *Morpho rhetenor*, is known to lack cover scales and also to have the greatest number of "branches" on the tree-like structure (**Figure 8.1**) [174,238,250].

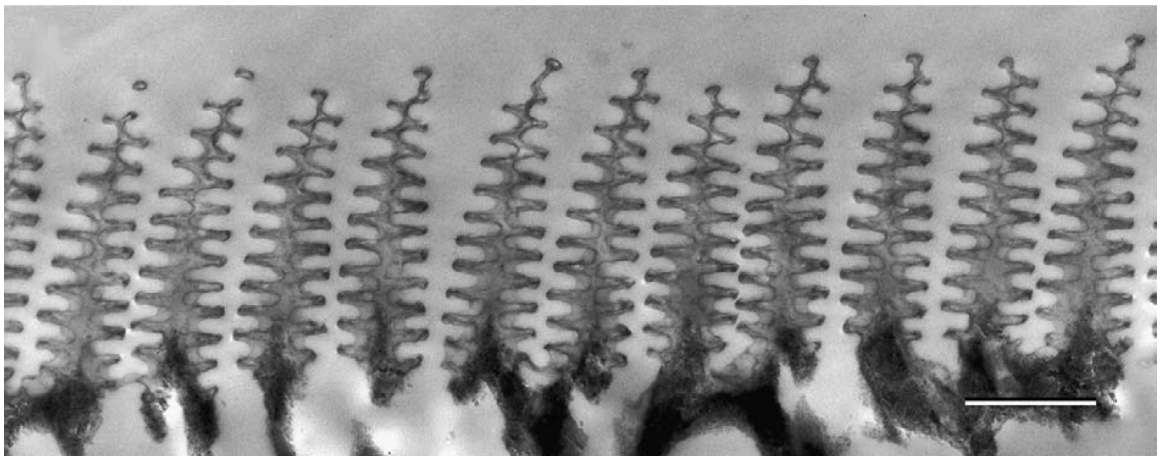

Figure 8.1: TEM image of the tree-like structures responsible for the blue reflection of *Morpho rhetenor*. Scale bar 800nm. Adopted from Vukusic *et al.*[238] (Used by permission, © The Royal Society).

Replication of the structures responsible for the optical properties of butterfly scales has lately attracted a lot of interest [228,229,232,251] due to the peculiar optical characteristics achieved by a single material. Most of the optical properties of these structures arise from a chitin-air interface. Devices and materials made from single material-air interfaces could be easily recycled and there are no adhesion and bonding issues that are often associated with multi-component systems. Structurally colored fibers have already found their application[225,226,252], although these examples all use two polymers to produce a multilayer instead of just one polymer and air. The wing scales of *Morpho sulkowskiy* were also used for vapor sensing[227].

An important aspect in terms of photonic structure replication is the control of refractive index. Ideally we would like to have access to a variety of materials with different refractive indexes. For wide-bandgap structures we need the refractive index contrast between the two materials composing the structure to be as high as

possible[253,254]. Furthermore, the size and thickness of the replicated structure needs to be controlled in order to preserve the size-dependent optical properties. Additionally, the possibility of incorporating dopants and additives into the replicated structures allows us to further extend the functionality of these structures by adding catalysts[255,256], pigments[256], phosphors[229] and other functional materials[257]. Computer-assisted surface sol-gel process has been previously used to replicate biological structures such as diatoms[258]. It was shown that it is possible to replicate these intricate structures with high fidelity using titanium (IV) oxide, which is an important material in optics application due to its high refractive index of 2.5-2.9, depending on the crystal phase[259]. Furthermore, the amorphous titania was converted into rutile by adding tin (IV) oxide as dopant and burning out the biomaterial at low enough temperature where the structural features were preserved. We would like to report on the replication and optical properties of these bio-templated rutile titania structures.

8.2. Methods used for replication and characterization

A 1.5 x 1.5 cm portion of a *Morpho* butterfly wing was attached to a glass slide positioned at a 60^{o} angle inside a fritted glass filtration flask. A computer-controlled pumping system housed in a dry nitrogen glove box was used to infiltrate the immobilized wing scales with a mixture of 0.010 M Ti (IV) isopropoxide and 0.0018 M Sn (IV) isopropoxide in anhydrous 2-propanol, for 10 min. The wing scales were then rinsed three times with anhydrous 2-propanol. The wing scales were then washed with deionized water for 1 min, followed by rinsing three times with anhydrous 2-propanol. The scales were then dried in a stream of warm nitrogen for 5 min. This sequential

infiltration process (alkoxide, 2-propanol wash, deionized water, 2-propanol wash, drying) was repeated 20, 40, 60 or 80 times. Finally, the coated scales were then fired in air at 0.5°C/min to 450°C for 4 h to burn out the chitin template and convert the coating into crystalline titania (**Figure 8.2**).

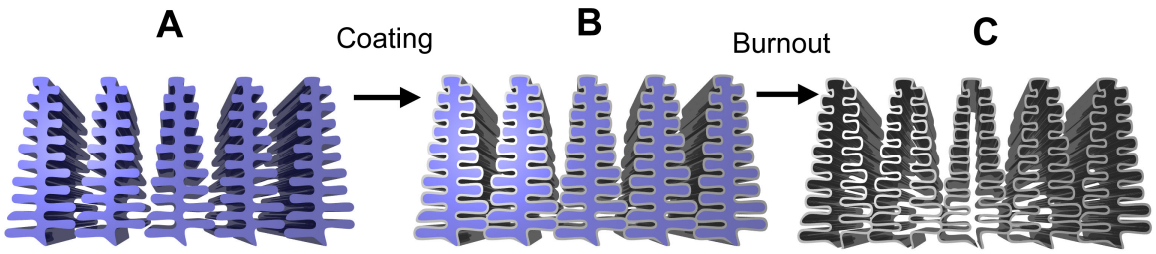

Figure 8.2.: The scheme of the replication process. *Morpho rhetenor* nanostructures (A) were sequentially coated with titania precursors, resulting in a coated structure (B), which was heated to 450ºC to burn out the chitin and convert the amorphous titania into a rutile replica (C).

Coated scales were analyzed in an Olympus BX60 reflected light microscope equipped with a tungsten lamp and a CRAIC SEE 1000 microspectrometer and a Bertrand lens. The reflectance spectra were taken with light aperture closed in order to measure the 90º reflectance. Aluminum mirror was used as a reflectance standard. Q-space analysis to determine the directional reflectance was performed by sliding in the Bertrand lens and taking the picture with a Nikon D300 digital camera equipped with a Martin Microscope adapter.

Multilayer reflectance simulations were done using a transfer-matrix method[253,260] incorporated in the FreeSnell software package. The incident beam angle was set to 15º, because that is the angle at which the multilayers in the scales are tilted. The multilayer

stack approximating the structure of the *Morpho rhetenor* was taken to be 9 alternating layers of chitin and air with the refractive index of chitin of 1.57+0.06i.

8.3. Coating Results

We proceeded with coating in three series of 20, 40, 60 and 80 repeat sol-gel cycles. After 20 cycles, the reflectance spectrum analysis revealed a red shift of the major peak from 434nm to 512nm. The scales appeared green in color under a microscope.

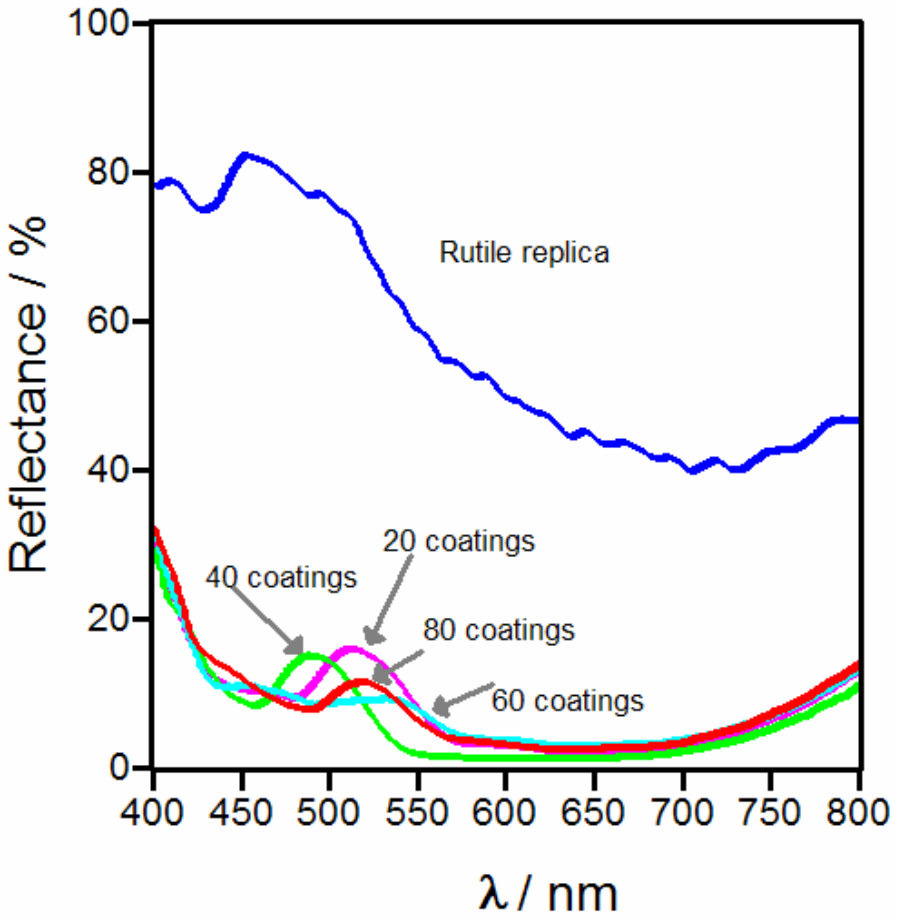

Figure 8.3: Reflectance spectra of coated *Morpho rhetenor* with different number of sol-gel coatings and the rutile replica after the chitin was removed.

After burning out the chitin at 450ºC, the structure collapsed and no color was visible or detected through reflectance measurements. Microscopic investigation showed only collapsed wing scales with no regularity. Coating with 40 and 60 cycles produced similar results. The reflectance peak did not shift further than 514 nm, indicating that the air layers were already filled at 20 coatings. After applying 80 coatings, the pyrolysis did not destroy the underlying nanostructure and the scales appeared shimmering blue under the microscope. The spectral analysis shows a broad peak with high reflectance around 456 nm.

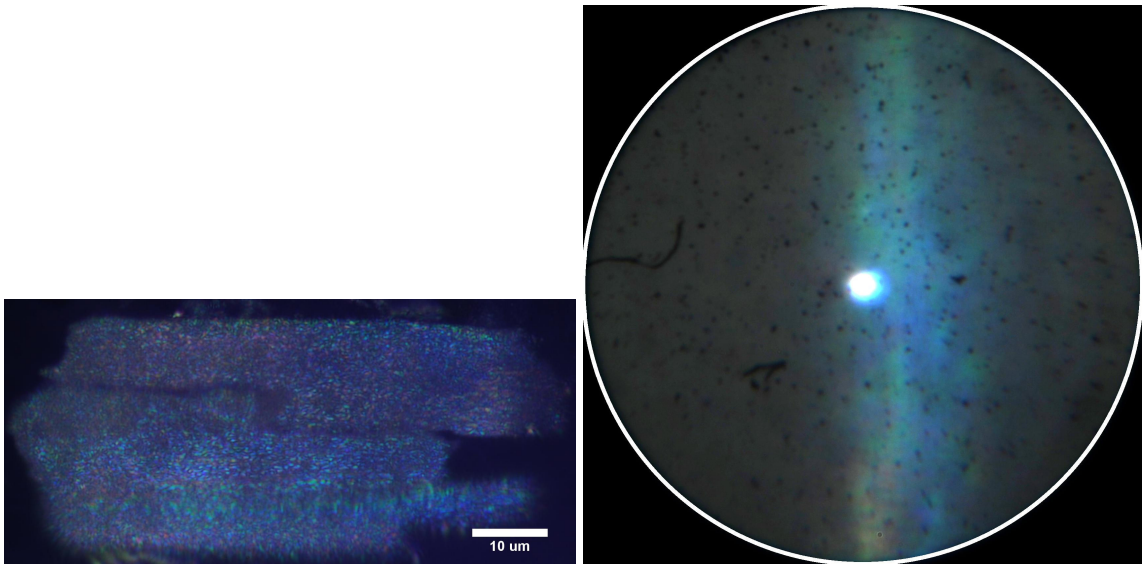

Figure 8.4: The real space (left) and inverse space (or Q-space, right) images of the *Morpho rhetenor* scale replicated with rutile titania.

The Q-space analysis shows a blue streak 15º from the surface normal, implying the preservation of the tilt of the underlying multilayer structure.

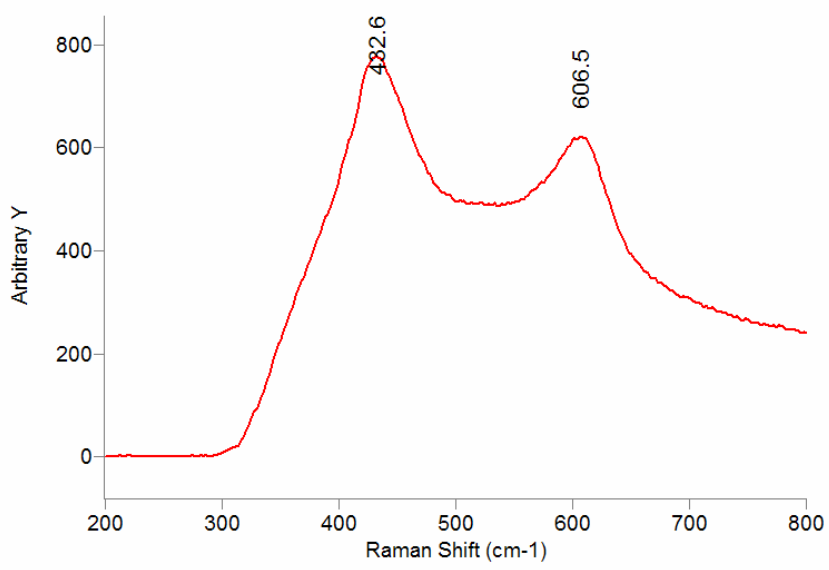

Figure 8.5: The Raman spectrum of the *Morpho rhetenor* replicated scale.

Raman analysis confirms the presence of rutile titania with bands at 433 and 607 wavenumbers. The bands at 433 and 607cm^{-1} are not far from the expected bands for the E_g (448 cm^{-1}) and A_{1g} (612 cm^{-1}) modes of vibration, respectively, for rutile titania[261]. Anatase would have shown three bands at 398, 515 and 640 cm^{-1} for modes B_{1g}, A_{1g} and B_{1g} doubletand E_g respectively[261]. Brookite would have shown two prominent bands for modes B_{2g} (584 cm^{-1}) and A_{1g} (640 cm^{-1})[262].

8.4. Discussion of *Morpho rhetenor* replication

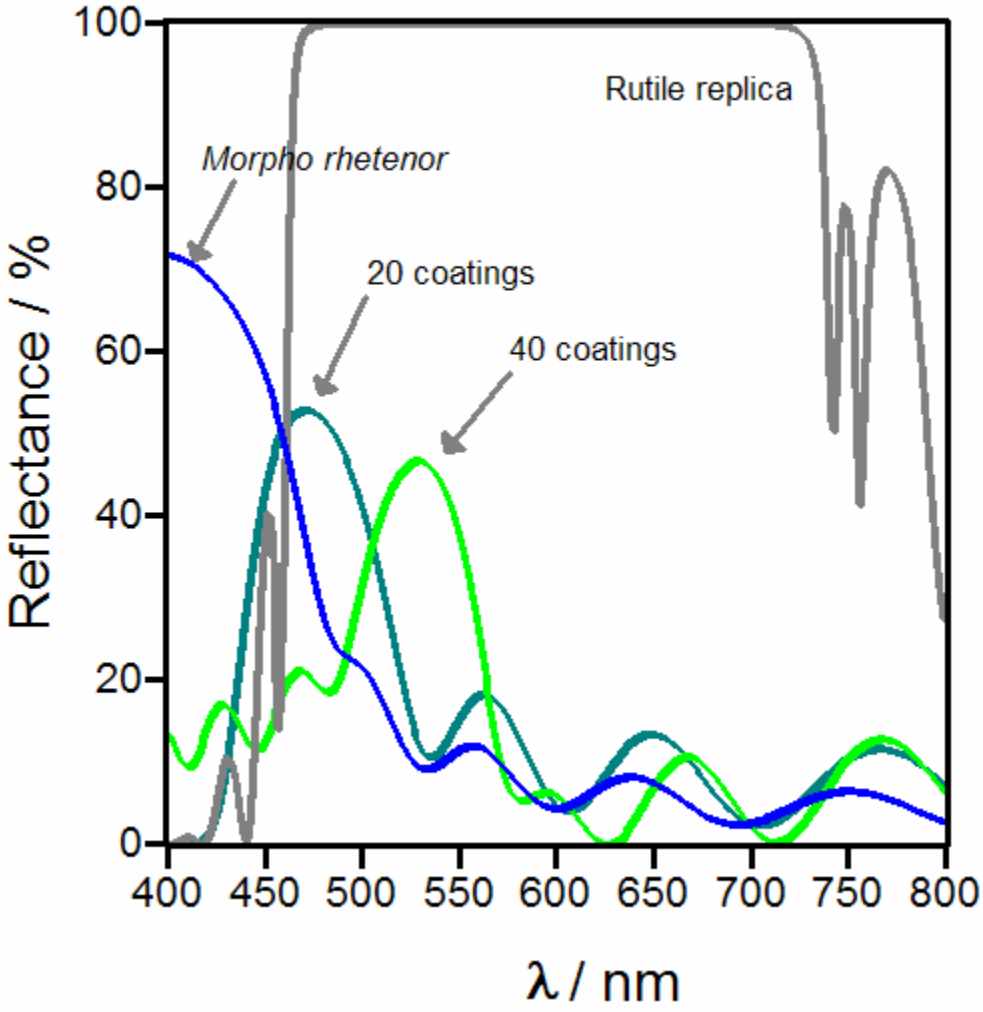

Figure 8.6: The calculated reflectance spectra. Calculations for more than 40 coatings are not shown, because at that point the air spaces between the branches are filled up and the result should therefore be the same as for 40 coatings.

The sol-gel deposition method initially results in an insoluble, amorphous titanium oxide gel, and needs to be fired in order to obtain an amorphous solid titanium oxide. The refractive index of this intermediate is unknown. In order to obtain this refractive index we assumed that the coating of 80 cycles had completely filled the air spaces in the *Morpho rhetenor* multilayer. We then calculated the peak location at

different refractive indexes and concluded that the refractive index of the precursor gel is approximately 1.7 by modifying the refractive index in the calculations until the peak location showed the best match. The peak width also confirms such an estimate. We then calculated the expected reflectivity spectra assuming a filling of 20 nm and 40 nm. Since the air gap between the chitin layers is about 80 nm, the 40 nm coating completely fills the gap. At 20 nm thick coating, the peak reflectance should have been at 475 nm, however our measurement showed the peak after 20 coatings at 514 nm. All the subsequent coatings produced coated scales with peak reflectance very close to 514 nm. If the air gap had not been filled, the peak would have been shifted further towards longer wavelengths. Therefore we conclude that 20 cycles would have already filled the air gaps in the multilayer structure.

However, the coated structure broke down upon pyrolysis if the number of coating cycles was less than 80. Previously it has been shown that 40 coating sol-gel cycles is sufficient to replicate *Morpho* wing scales with high fidelity and to preserve the nanostructures upon burning[251]. However, it needs to be pointed out that those were brown scales on the ventral side. The blue dorsal scales are different in structure. The main difference is the high aspect ratio of the light-producing structures. To compensate, the coating needs to be thicker to withstand the forces present as the gasses exit during chitin pyrolysis and to support its own weight.

The replicated structure is composed of rutile titania, as evidenced by the Raman analysis[261,262]. The two bands at 433 and 607 cm^{-1} are close to the expected bands for

rutile titania[261] and are distinctly different from the three bands that would have appeared for anatase[261] or brookite[262]. The Q-space analysis shows that the reflectance directionality is preserved, which means that the intricate underlying structure was also preserved. However, the blue reflection streak is not as narrow and well-defined as in the natural scales. The reflectance spectrum shows a broad reflectance pattern with high reflectivity in the blue region. This is consistent with the expected reflectance spectrum, which was calculated assuming a refractive index of 2.9. The calculated reflectance spectrum indicates that the reflectance should be high, near 100% over almost the whole visible range. The measured reflectance is high, between 40-80% throughout the visible range. However, the measured spectrum is more jagged and uneven, most likely due to imperfections in the replicated structure.

8.5 *Morpho rhetenor* replication – conclusion

We were able to replicate the optical structure of *Morpho rhetenor* using sequential sol-gel deposition. The resulting rutile replica retains the optical properties of the original scale (directional reflection, peak position) and further modifies them (peak width) due to the higher refractive index of the final structure. The demonstrated process opens a route to replication and manufacture of new materials with a wide band-gap.

CHAPTER 9

IDENTIFICATION OF STRUCTURES RESPONSIBLE FOR THE COLOR OF AN IRIDESCENT GREEN BEETLE *Chrysina (Plusiotis) gloriosa*

9.1. Introduction

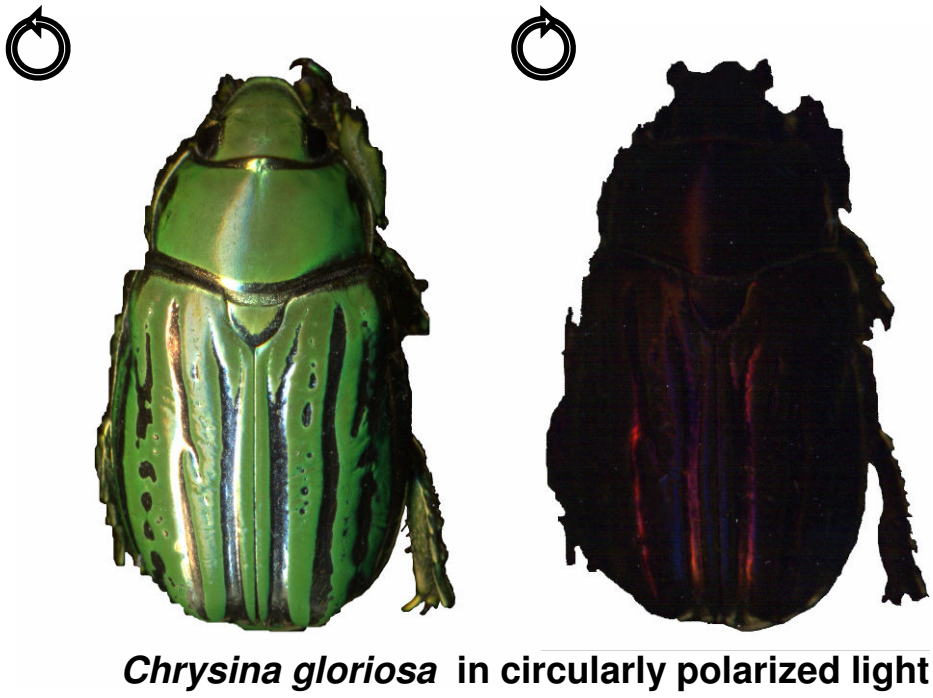

Figure 9.1: The beetle *Chrysina gloriosa* viewed through a left handed circular polarizer and right handed circular polarizer, as indicated by the symbols.

The optical response of exocuticles of many beetles has been found to be similar to that of cholesteric liquid crystals[217,263,264]. The equilibrium director structure of a cholesteric liquid crystal is a helicoid [216,265-267]. The director advances uniformly tracing a helix of pitch *p* as discussed in Chapter 6.7. While the helicoidal structure has been cited as a possible means of generating such an optical response in beetles[235,264,268], the

observed hexagonal pattern remains unexplained, without an attempt made to relate the microstructure to the textures of the cholesteric phase. Previously we have made the connection between the ordered hexagonal structures and surface focal conic cholesteric defects[127]. However, the role of focal conic surface defect in determining the optical response of the beetles has not been investigated. In the optical studies by Jewell et al [220] on *P. boucardi* beetles, similar hexagonal cells are observed to shows dark centers in darkfield and these spots turn yellow in bright field. For both *P. boucardi*[220] and the New Zealand manuka beetle[269], the presence of chiral reflectors with two different pitches satisfying Bragg reflection was cited as responsible for color. Lowery *et al.* [270] simulated their ellipsometric studies on three different species of beetle by using a chirped stack of structurally perturbed chiral resonators. Similarly, Brink *et al.* [271] attributed the reflected spectrum of the red and green scarabaeid beetle *Gymnopleurus virens* to an exocuticle structure which can be simulated using a perturbed cholesteric structure that has an abrupt jump in pitch, and rotation of the cholesteric structure. Hereby we attempt to decipher the role of focal conic defects in color reflection of the beetle *Chrysina gloriosa*.

9.2. Results

Microscopic investigation of the surface of *Chrysina gloriosa* reveals an array of packed hexagonal structures. In fact, they are a mixture of pentagons, hexagons and heptagons and a Voronoi analysis reveals that the packing is less ordered on the more curved parts of the beetle[127]. The color of these multigons changes with variations of the

angle of incident light. With the aperture stop wide open and thus a multitude of incident beams bathing the structure in light, the yellow center appears large, about 5 µm in diameter (**Figure 9.2A**). As the aperture stop is closed down, the yellow center gets smaller and smaller, ending in a tightly focused yellow dot. The surrounding green color takes place of the former yellow spot (**Figure 9.2B**). The interstitial spaces between the cells appear bright green to yellow in color. In dark field illumination (**Figure 9.2C**), the center of the hexagon appears dark. The edges appear yellow and there is a bright green ring in the middle. The interstitial spaces between neighboring cells appear dark. The cell also seems to be divided into slices, where a dark line appears emanating from the center of the hexagon. From this behavior we can see that the reflected light is highly dependent on the incident angle.

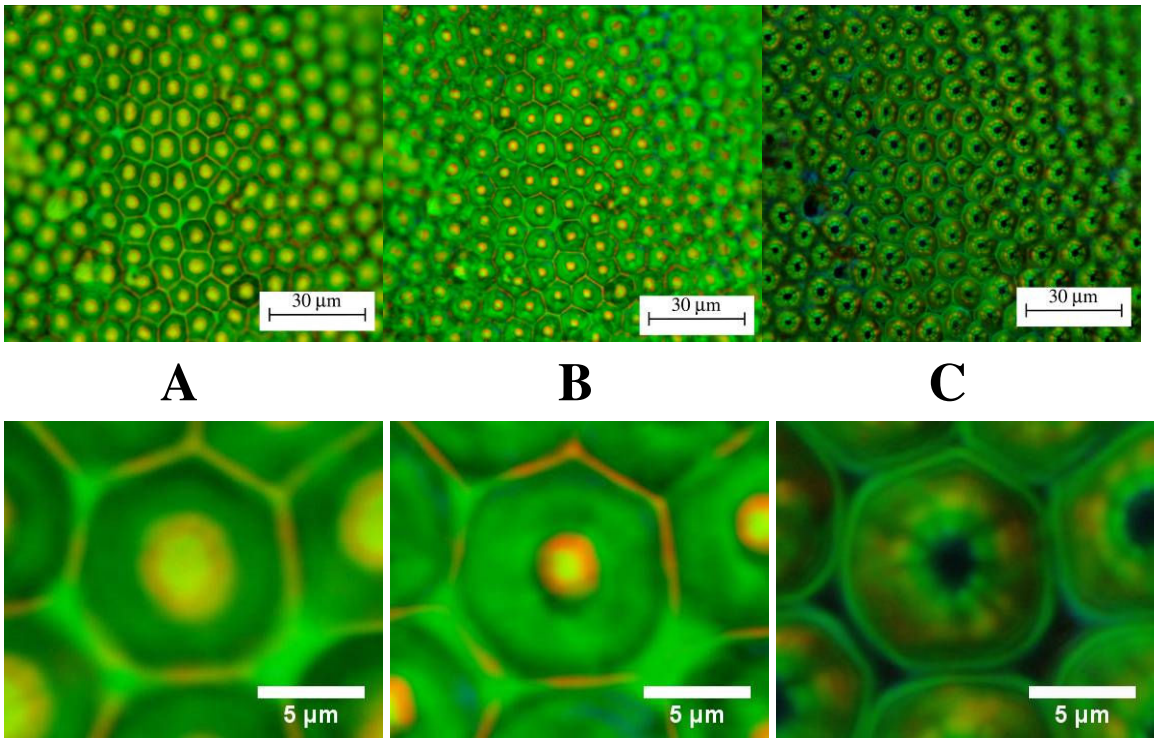

Figure 9.2: *Chrysina gloriosa* under microscope with open aperture (column A), with closed aperture (B) and with dark field illumination (C).

Investigation with a microspectrophotometer yields further insight into the optical characteristics of the elytra. With aperture open and when compared to aluminum mirror as the 100% reflectance standard, the green areas reflect light with a peak at 540 nm (**Figure 9.3**). The sampling area 4x4µm (**Figure 9.3b –** insets**)** is bigger than the actual green or yellow area, hence the spectra include the optical property of the surrounding area. Even so, the characteristic spectra are very consistent at different locations along the sample. The yellow areas reflectance exhibits a strong peak at 560 nm with a small shoulder at 605 nm. The reflectance reaches more than 50%, which should not be theoretically possible given that the reflected light is circularly polarized. This suggests a concentrating or lensing effect.

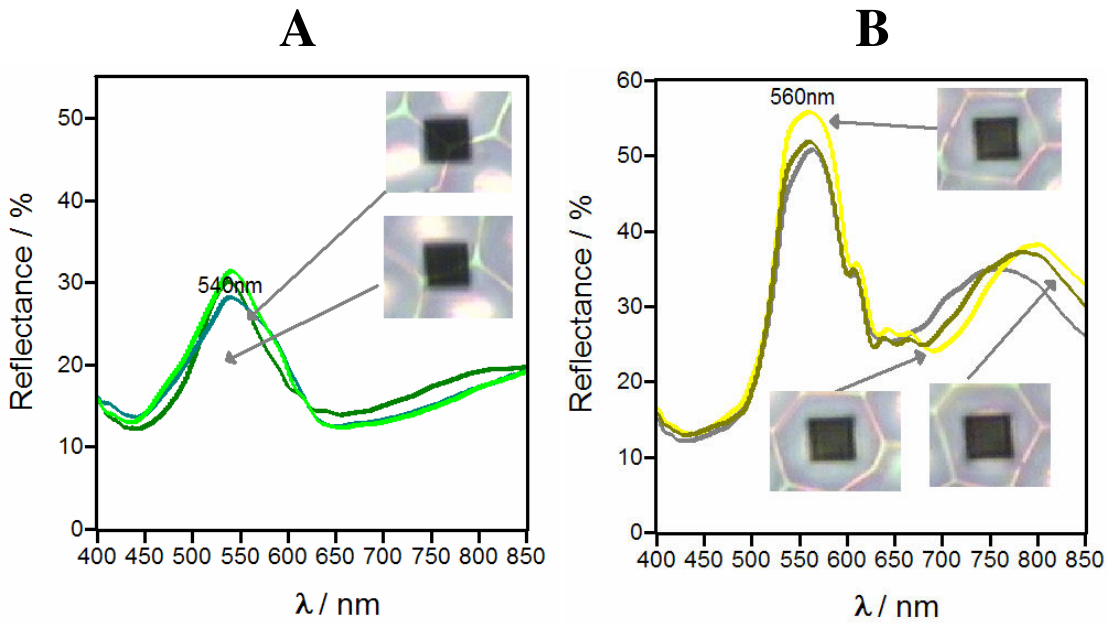

Figure 9.3: Open aperture stop microspectrophotometric investigation. The black squares indicate the sampled area 4x4µm in size. A collection of spectra taken (A) on the green areas and (B) on yellow areas.

We then investigated the reflection by closing down the aperture stop. Again the reflectance was compared to an aluminum mirror (**Figure 9.4**). When the aperture is

closed down so that the incoming beam has an angle variation of 5º, the surface appears unevenly colored. There are sharp yellow dots surrounded by green halos. Furthermore, there are dark areas that do not seem to reflect much light. The green areas exhibited variable reflectance in the range from 40-60%. Again, reflectance over 50% should not be theoretically possible and therefore there might be some light concentration or guiding taking place. The peak position shifted a little bit at different sampling locations, but generally stayed around 525 nm. Yellow dots also exhibited variable reflectance intensity, although the peak locations were more constant. Three peaks were discernible – at 530 nm , 575 nm and 600 nm. The peak at 530 nm seems to be a contribution from a green area that was sampled together with a yellow dot. It was not possible to completely isolate the sampling area so that no green area would be sampled.

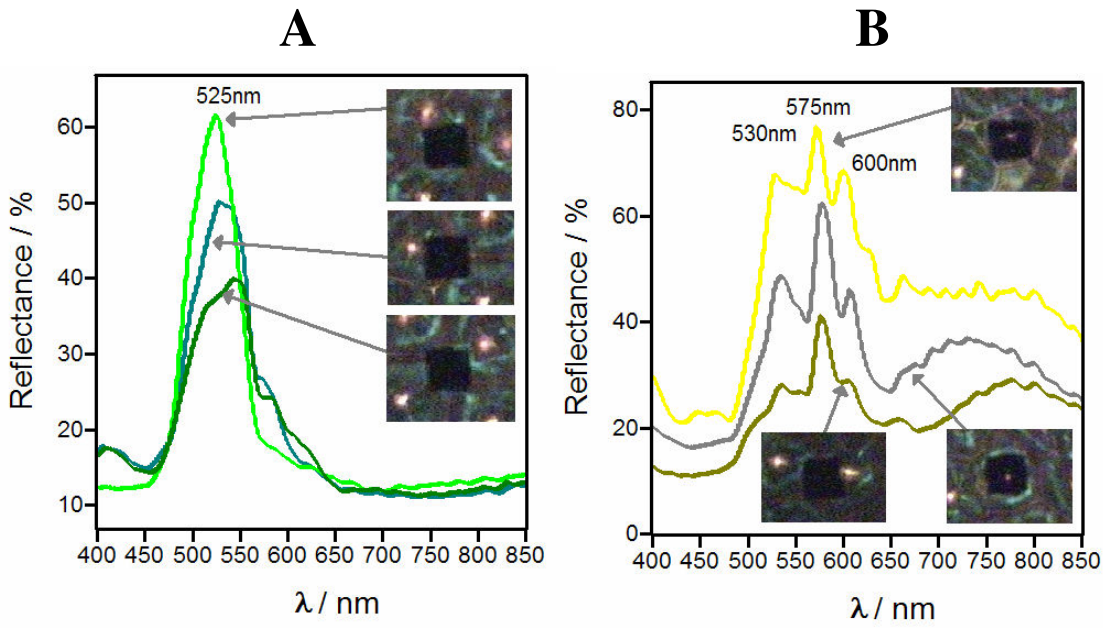

Figure 9.4: Normal incidence narrow incident beam (closed aperture) microspectrophotometric investigation. The black squares indicate the sampled area. A collection of spectra taken (A) on the green areas and (B) on yellow areas.

For the investigation of reflectance at oblique illumination (dark field, **Figure 9.5**.), we could not use the aluminum mirror as the reflectance standard, due to its specular reflectivity. Since the light of a specular reflector is reflected at exactly the same angle from the surface normal as the incoming light, the obliquely illuminating light from the dark-field collar is not reflected into the objective lens. A Lambertian standard was used instead. We used the white scales of the butterfly *Hebomoia glaucippe* as the 100% reflectance standard, because it was shown to approximate a Lambertian reflector[272]. The yellow and green areas in the dark field image are very close together and too small to be sampled separately. Therefore we sampled a number of different locations without separating the colors. The reflectance varies in intensity depending on how much of the sampling area contains reflecting elements. The reflectance peak is located at 556 nm.

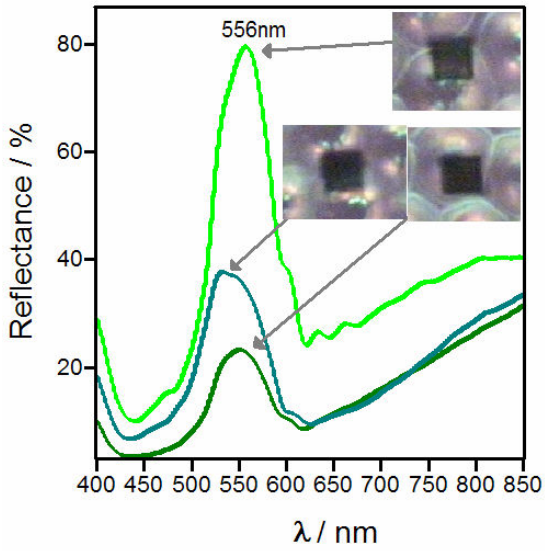

Figure 9.5: Dark field microspectroscopic investigation. The black squares indicate the sampled area.

We then adjusted the incident angle using the technique described in Chapter 7. The incident angle was set to be 25º and the aperture stop was closed down to obtain a 5º narrow beam of light. Aluminum mirror was used as the 100% reflectance standard. The

yellow spots and green halos appear off center relative to the hexagon boundaries under these illumination conditions. The spectra of the green areas (**Figure 9.6A**) vary in intensity and the peak position appears at 550 nm. The spectra measured at the locations of the yellow dots vary in intensity, while the peak position is at 575 nm in this case. No intensities above 50% were measured.

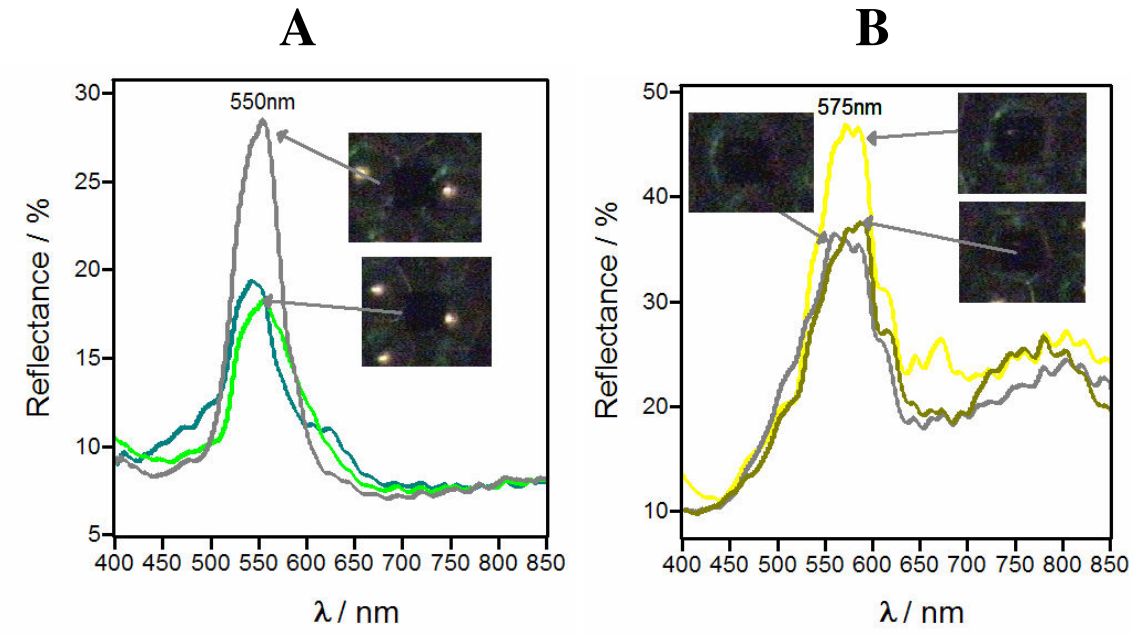

Figure 9.6: **N**arrow incident beam (closed aperture) microspectrophotometric investigation at 25º angle of incidence. The black squares indicate the sampled area. A set of spectra taken (A) on the green areas and (B) on yellow areas.

We also examined the optical response of the beetle elytra in inverse space, as described in Chapter 7. At normal incidence the green light is reflected closer to the surface normal than yellow light (**Figure 9.7a**). The yellow is reflected at angles far from the surface normal. This can be seen more clearly if the picture is taken under crossed polarizers (**Figure 9.8**) where the main beam is extinguished, but the reflection from the cholesteric surface remains the same. Furthermore, the image was split into its RGB components. We can see the blue color reflection is centered around the surface normal.

The green color is more intense close to the surface normal, but is spread throughout. The red color is not reflected at the surface normal, but rather away, at angles greater than 20º.

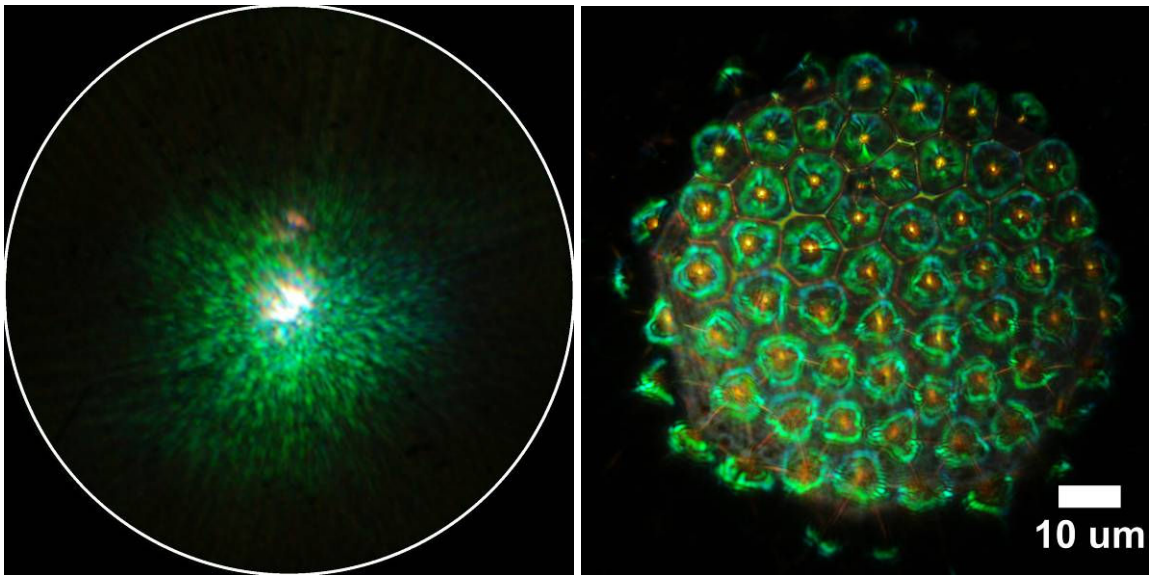

A **B**

Figure 9.7: Inverse space image (A) and real image indicating the illuminated area (B) under normal incidence. The bright white spot in the middle of the inverse space picture is the incident beam.

In real space with closed field stop (**Figure 9.7B**), we can also observe a very interesting phenomenon at the edge of the field stop. Wherever the field stop only covers part of the reflective hexagonal cell, the other half is dark. Surprisingly, it is the part that is covered by the field stop that is bright, while the part that is not covered appears darker and colorless.

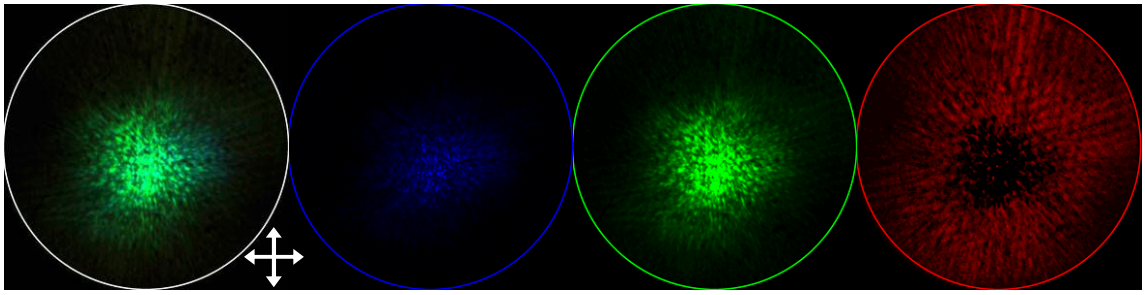

Figure 9.8: Inverse space image under crossed polarizers, with the directions indicated by the arrows. The original image (XPOL) was split into three components: blue, green and red. The intensity of the red component image was also adjusted to make the color more visible.

Since the yellow color is the result of mixing of green and red, we can say that the red image tells us where the yellow color light is reflected. It is somewhat surprising that the yellow color appears to be reflected off-center, while the yellow dots in the real image appear intensely focused. The inverse space analysis also explains why the beetle appears intensely green, although the yellow color is very strong under high magnification. It seems that the yellow color is scattered around, while the green color remains concentrated around the main reflection beam. To further characterize this reflection, we performed the same analysis with an off-center incoming light beam.

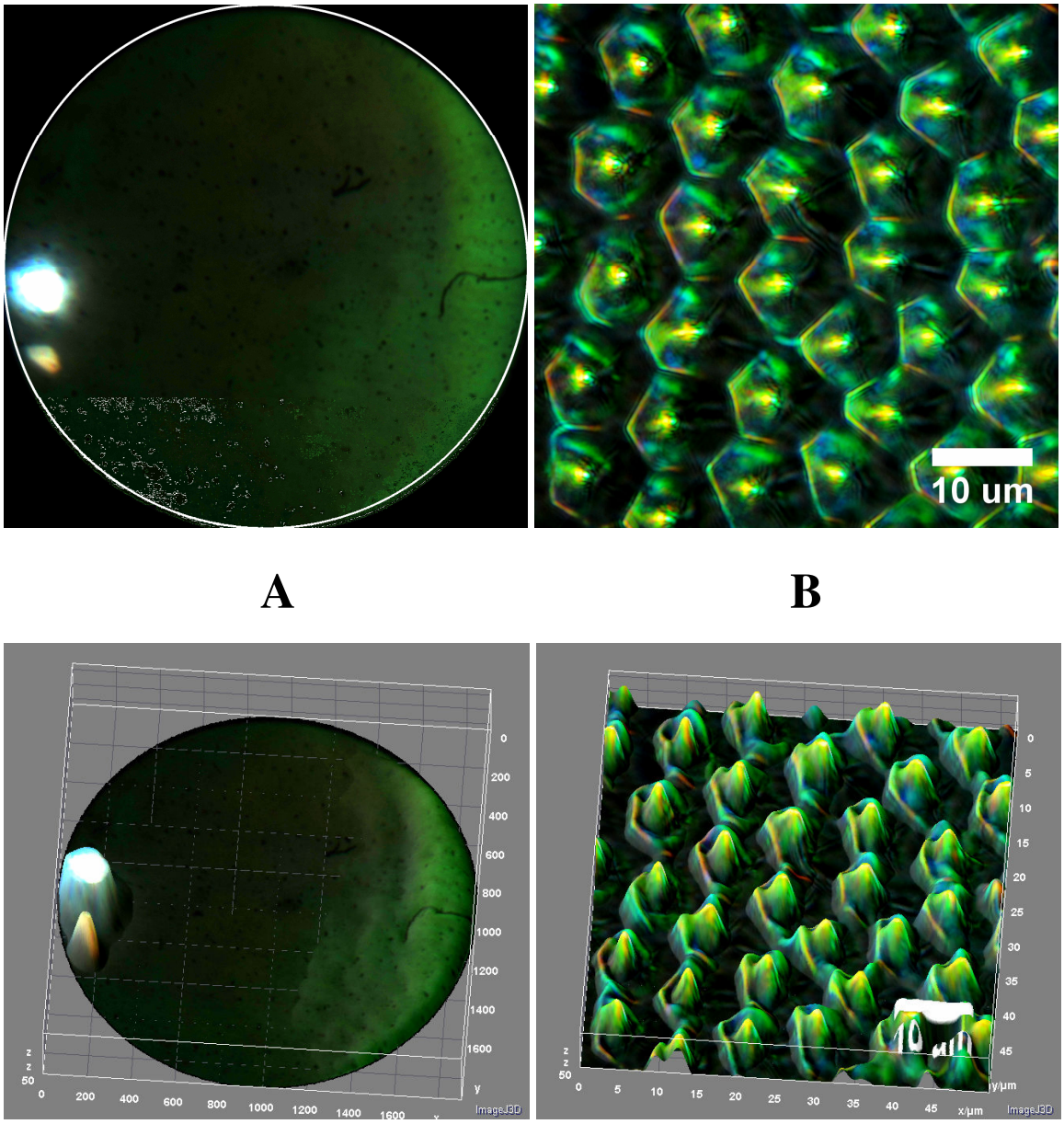

Figure 9.9: Q-space analysis at 30º incident angle. (A)-above is the Q-space image and (A)-below the surface plot of the luminance (intensity). (B)-above the real space image of the area analyzed and (B)-below the surface plot of the luminance (intensity).

The Q-space analysis at 30º incidence (**Figure 9.9**) has shown that the green light is reflected back at the light source. In **Figure 9.9A-**above, we can see that the green light intensity opposite the reflected beam is stronger than the rest of the image. The bright

white spot is the detected reflected beam and the incoming beam is incident on the opposite side of the image. The real space image **figure 9.9B**-above shows that the yellow light is still focused, although in an off-center spot. The green light only appears on the sides of the yellow spot, relative to the incident beam. No green light appears in the region of the hexagon that is oriented on the same side as the incident beam, which is coming from the right-hand side. This can be more clearly seen in the surface plot (**Figure 9.9B**-below), which plots the luminance as a function of image location.

Upon performing these experiments, we tried to keep the sample as flat as possible. In order to flatten it, we used a glass cover slip and noticed a change in the appearance of the reflective structures under the microscope. The hexagons appeared dark, with yellow dots in the middle. In order to investigate the behavior, we applied some immersion oil (n=1.55) and a cover slip to the sample. The sample appeared dark, with yellow dots in the hexagon centers when the aperture stop was narrow (**Figure 9.10A**). Upon opening up the aperture stop, the yellow dots became much larger, however no green color appeared inside the hexagon. Under dark field illumination the green color appears again and the image appears very similar to the dark field image without the immersion oil on top (**Figure 9.2C**). However, the green color at the hexagon edges appears to be absent. Green color is only present in the center of the hexagon, followed by yellow. The dark lines sectioning the hexagon into slices appear more prominent than in the image without immersion oil. At this point it should be noted that the angle of dark field illumination for the 50x objective used in this study is 73º +/- 10º.

The same behavior was observed when water was put on top of the lytra instead of immersion oil.

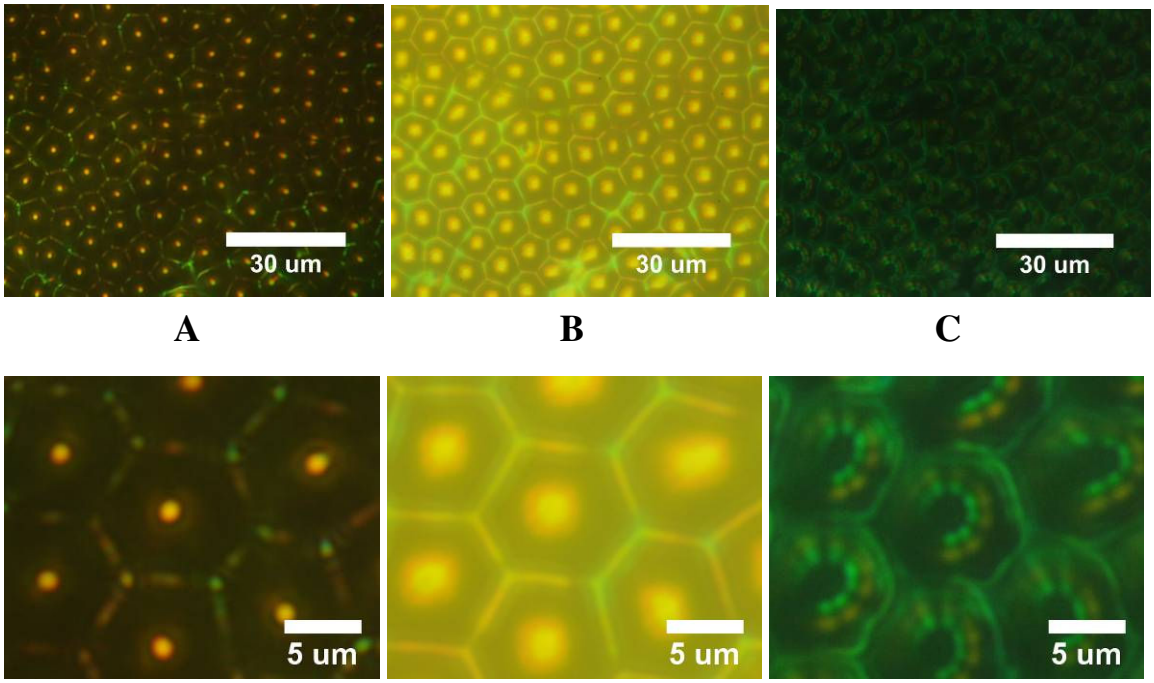

Figure 9.10: The elytra with immersion oil and a cover slip on top. (A) With closed aperture stop, (B) with open aperture stop and (C) in dark field. Images B and C appear washed out due to some light reflecting from the top of the cover slip.

In inverse space under normal illumination the oil covered *Chrisina gloriosa* elytra reflects light quite differently, as evidenced by the inverse space scattergrams. The yellow color is now reflected closer to the surface normal, while the green is reflected at large angles (**Figure 9.11**).

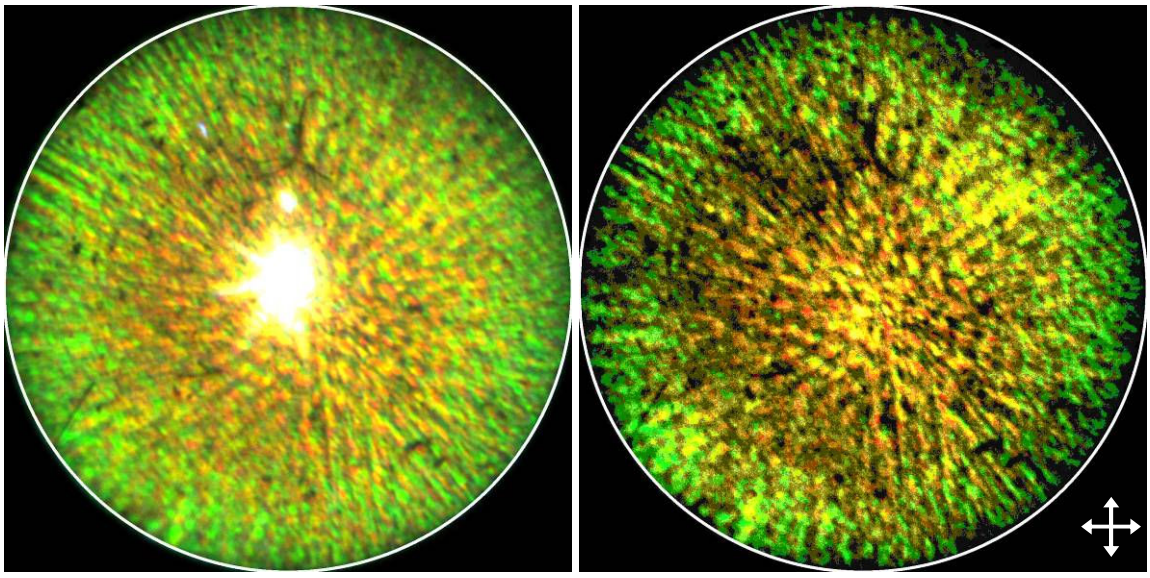

Figure 9.11: Inverse space images of the immersion oil covered elytra under normal illumination. Image (A) has a visible main beam, while image (B) was taken under crossed polarizers. Due to the low light intensity, brightness and contrast of these images had to be adjusted after they were recorded. The crossed arrows indicate the polarizer and analyzer direction.

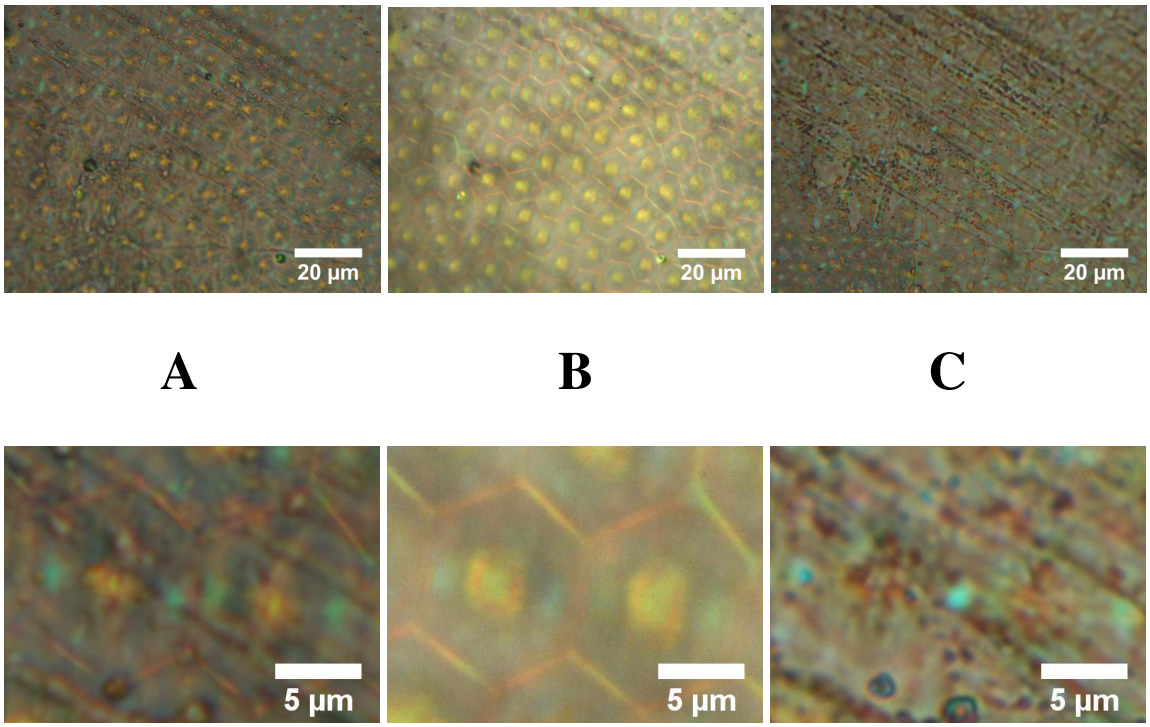

Figure 9.12: The elytra with left handed circular analyzer in place (A) with closed aperture stop, (B) with open aperture stop and (C) in dark field.

In order to investigate the characteristics of reflection of circularly polarized light, we inserted a circular analyzer in the beam path. The resulting microscope image had almost no color (**Figure 9.12**). The green color was completely extinguished, but there was a remnant of the yellow color exhibited as small yellow dots. The dots became bigger with increasing the aperture, the same way as without the circular polarizer shown in **Figure 9.2**. Besides the yellow dots, very small blue dots can be seen when the aperture is closed down. These appear at the edges of the hexagons. In circularly polarized light it is possible to focus on the top of the beetle surface, which is usually obscured by the strong reflections from the structures underneath. We measured the optical distance between the top surface and the position where the yellow dots are in focus (between images **Figure 9.12B** and **Figure 9.12C**. This distance is 4 μm. The Q-space analysis showed only a strong main beam reflection with no color.

We also investigated the structures underneath the reflective surfaces. The native fluorescence of an unknown fluorophore in the elytra was used to image the structures with a laser scanning confocal microscope using a 488 nm argon line. The analysis reveals concentric layered structures underneath the hexagons (**Figure 9.13**). The layer thickness is close to the resolution limit of the microscope. The hexagons appear to have a spiky peak in the middle, with the sides tapering off (**Figure 9.14**). The center of the conical structure viewed from the side also appears brighter than the rest. The visualization of the layers is possible either due to the fluorescent molecule only being present in every other layer or, since the laser is polarized, also due to the orientation of the fluorophore.

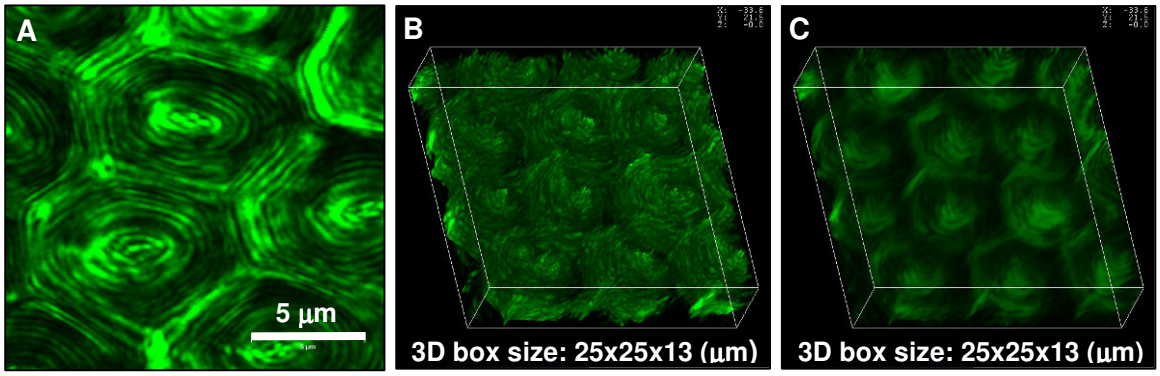

Figure 9.13: Confocal micrographs in fluorescence mode at higher magnification to show detailed structures inside each cell. (A) A xy section image showing bright/dark areas in nearly concentric fashion. (B) and (C) are 3-D images obtained from limited thickness range. The image in (C) shows that the concentric bright/dark regions may be spiraled.

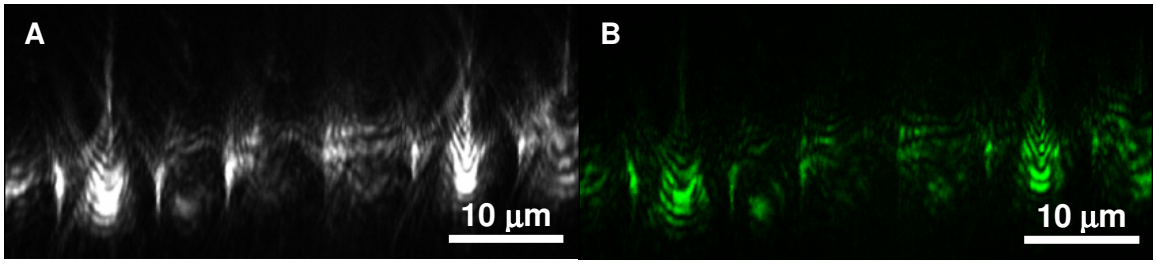

Figure 9.14: Side views (xz section) of the skeleton obtained in reflection mode (A) and in fluorescence mode (B). The seemingly concentric bright/dark regions in **Figure 9.13A** are actually due to the multiple layers of bright/dark regions in the shape of nest arcs, which eventually turn into a conical frame at the top. The apparently incomplete cones/spikes are located behind the complete ones, hence not fully in focal plane resulting in such images.

We also examined the underlying structure using SEM. The elytra was cut using a razor blade or also simply broken off. The SEM images of the surface show a smooth surface with no protrusions. This is consistent with the presence of a waxy layer on top of the optical structures. The thickness of the waxy layer appears to be 1.4 µm. SEM imaging of the cross-section showed no layering in the cleanly cut structure (not shown). However, if the structure is broken, thin fibrils can be observed protruding from the fractured surface. These fibrils are arranged in layers with each subsequent layer having a

different orientation. These layers form a cholesteric structure. The distance between dark layers is about 300 nm, making the pitch of the helix about 600 nm. The diameter of the fibrils seems to vary from the smallest <50 nm to about 5 μm. Most likely the fibrils are just the result of the unclean fracture of oriented material in the elytra.

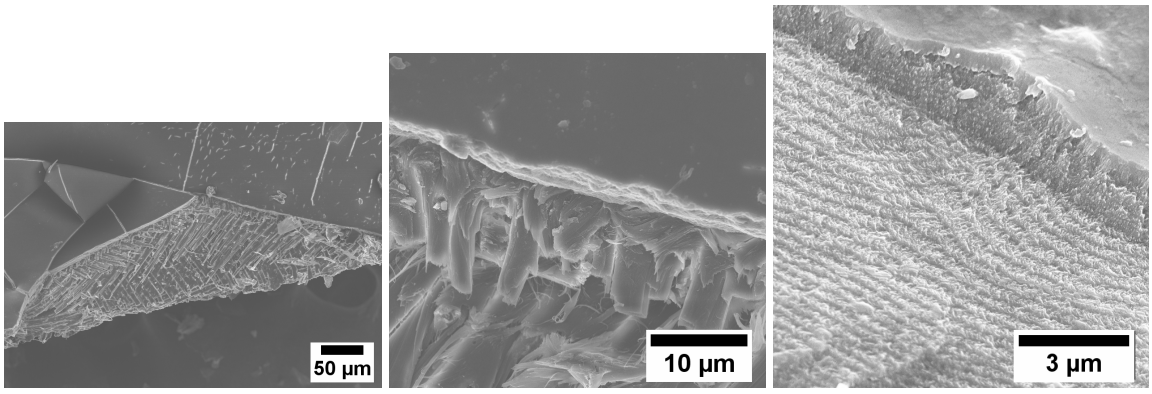

Figure 9.15: The SEM images of the broken elytra. Fibrils can be seen protruding from the fractured surfaces. The top layer is smooth and featureless and is most easlity seen in images (A) and (B). Image (C) shows the layering of the fibrils near the surface. All the samples were prepared by breaking.

9.3 Discussion

The only published example to our knowledge where morphology was compared to cholesteric liquid crystals comes from Pace[273] , where TEM images were presented and it was noted that the beetle *P. gloriosa* has a liquid crystal-like microstructure, which was referred as "Bouligand structure". Bouligand[274] had carried out an extensive study on the similarity of textures observed in crabs and other organisms to cholesteric liquid crystals and explored their role in morphogenesis. TEM studies are influenced by the sample preparation. The surfaces produced by the freeze fracture process can possess a relief due to the anisotropic propagation of fracture and the action of a microtome knife

produces a topography that depends upon the texture of the cut material.[274-276] Perhaps that led to effectively forgetting Pace's interpretation[273] about the relief of this beetle. That is the reason why we focused on confocal microscopy in our study, since it is possible to image the three dimensional microstructure of the beetle elytra in a non-destructive fashion.

First let us discuss the microscopic structure of the focal conic defects at the surface. The confocal images reveal a layered structure with spirals inside the hexagons. The structure is almost identical to the surface structures found by Meister *et al.* on the surface of polymeric cholesteric liquid crystals[275].

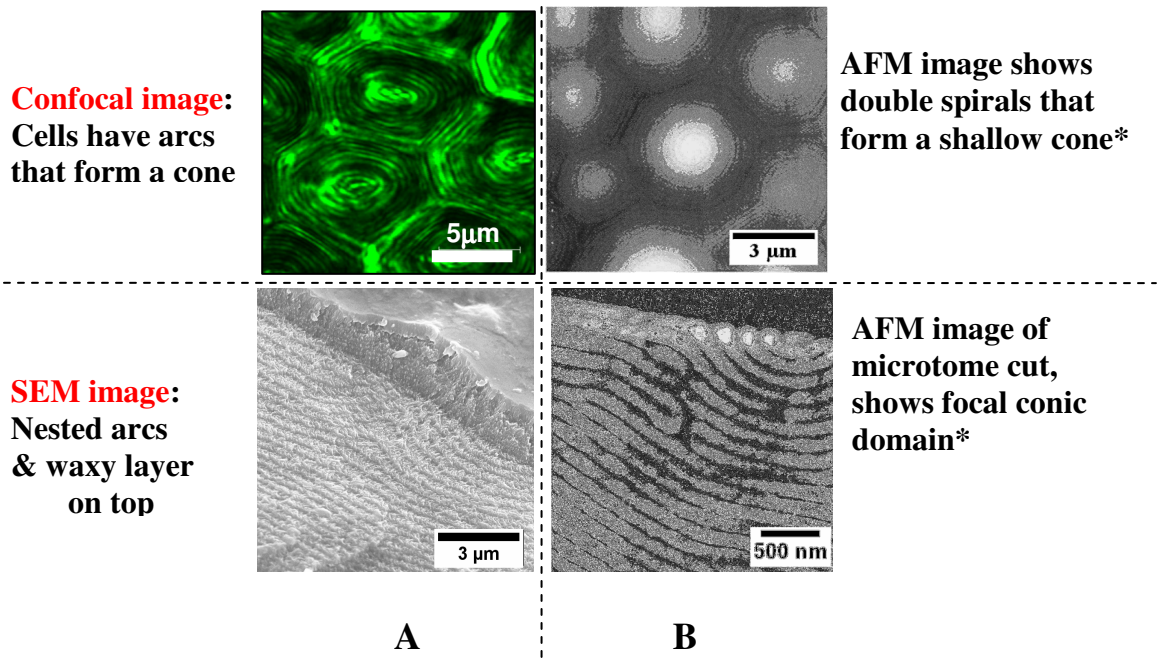

Figure 9.16: A comparison between our (A) data from characterization of *Chrysina gloriosa* and (B) the structures in a paper by Meister[275] *et al* (Used by permission, © by American Physical Society).

From our confocal xy image (**Figure 9.16**), we can see the concentric ring structure. It might be a spiral, but the resolution of the light microscope is not sufficient

to distinguish between rings and a spiral on this scale. Another reason could be that the polarized laser only excites the layers that are not oriented parallel to the polarization direction, thus showing concentric rings. Otherwise, the structure looks remarkably similar to the surface structure found by Meister *et al.*[275] The SEM image shows the cross-section of the elytra and the cholesteric layers are visible. Near the surface we can also see a defect, which is very similar in structure to the ones observed by Maister *et al.*[275] The flat layers start to curve near the surface, producing a reflecting cup.

From the confocal cross-section in the xz plane and **Figure 9.14**, we can also see that the concentric rings are organized in cups, with each subsequent cup being smaller than the previous. The image in **Figure 9.14** is reminiscent of reflections on a spherical mirror – the fluorescent intensity is the highest inside the layered structure approximately in the spot where the focal point of a spherical mirror would be (**Figure 9.17C**). The excitation laser is focused in that spot and therefore the fluorescence intensity is higher. Furthermore, there is a conic plume visible on top of the structure. This sharp peak in **Figure 9.14** cannot be explained by the physical presence of such spikes. However, such effect could be seen if there was a light source between the focal point and the center of the sphere of a spherical mirror. The rays from such a source would be focused above the mirror. If the light source is placed at the focal point, the light is focused to infinity. For a light source close to the focal point, the light is focused far away. Since each fluorescing layer can be considered as a light source, each is focused to a different distance away from the bowl, resulting in a plume-like shape.

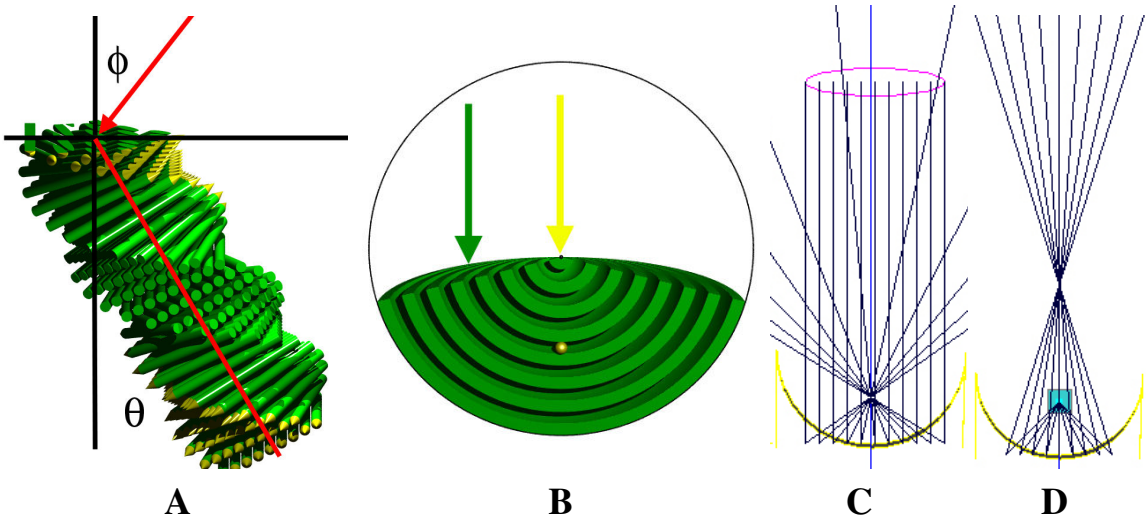

Figure 9.17: (A) Cholesteric helix at the surface with the helix axis oriented at angle θ to the surface normal and incoming light at angle ϕ. (B) Schematic of a layered structure of a focal conic defect at the surface. The yellow dot in the middle of layered structure represents the focal point of a spherical mirror with the greatest radius, which is denoted by the thin black circle around the whole structure. (C) Ray diagram for a spherical mirror for an incident parallel beam. (D) Ray diagram for a light source present between the sphere center and the point of focus.

Since we determined that the architecture of the beetle exoskeleton is similar to a cholesteric focal conic domain at a free surface (see **Figure 9.16**), and we have limited knowledge of all the optical and structural parameters necessary for determining response by ray tracing, we can only make phenomenological arguments. Due to their chiral and periodic helicoidal structure, the cholesteric phase with a pitch comparable to the wavelength of visible light, shows Bragg-like reflection for normal incidence, peaked at wavelength, λ_0, given by $\lambda_0 = np$, where n is the average refractive index. The reflected light is circularly polarized with the same handedness as the cholesteric helix[216]. The peak width of the reflection peak for a pure cholesteric phase is related to birefringence ($\Delta n = n_e - n_o$) by $\Delta\lambda = p\Delta n$ [216,265], where n_o and n_e are the refractive indices for polarizations perpendicular (ordinary) and parallel (extraordinary) to the axis of

anisotropy, respectively. For oblique incidence at an angle ϕ, the reflection for a helix oriented at some angle θ with respect to surface normal, the condition is modified to $S\lambda = np\cos(\phi - \theta)$ as shown in **Figure 9.17A**. When we look at the beetle structure in the white light in a reflection microscope, the Bragg-like reflection is yellow at the center of the cell and green elsewhere. When the range of incidence angles is increased by increasing the aperture size (**Figure 9.2A**), the locus of the yellow reflection expands, implying that by increasing the angle of incidence, *cos (ϕ-θ)* becomes smaller and thus a longer wavelength (yellow as opposed to green) satisfies the condition. In the dark field, when only large angles of incidence are possible, the *cos (ϕ-θ)* term near the center gets even smaller, leading to extinction of color at the center (**Figure 9.2C**).

A possible explanation for yellow color production could be that the yellow dot in the middle is the consequence of focusing the yellow light by the focal conic structure acting like spherical mirror. Further evidence for that are the inverse space images under oblique narrow beam illumination (**Figure 9.9B**), where the yellow dot moves in the direction away from the incident beam. That is consistent with the behavior of focal point in a spherical mirror when the beam is incident at an angle. The spectral analysis shows very little peak shifting for the yellow light peak. This implies that the incident yellow light experiences very similar reflections inside the focal conic structure. Focusing by a spherical mirror could be such an effect. The question arises, why is the beetle not more yellow in color then? A possible explanation would be the very short focal length of the micromirror. Since the light is only focused at a very short distance, that effectively spreads it around at the long distance. The inverse space image, which can also be called

infinity space because the light is focused in infinity, shows the yellow light scattered towards angles away from the normal. This is consistent with the proposed reflection model. The waxy layer also seems to play a role in extinguishing the yellow light and promoting green, however the particular mechanism is no yet understood. From the measurement of optical thickness (4 μm) and the SEM measurement, we cannot estimate the refractive index of the waxy layer. The refractive index calculated from these two measurements would be 2.8 which does not seem reasonable. It is more likely, that the yellow dots were found to be in focus below the bottom surface of the waxy layer, again consistent with the focusing of a spherical reflector, which focuses the light below the center of the sphere.

The green light is a bit more challenging to explain. It appears that the green light arises from the reflection on the sides of the focal conic. The support for this argument comes from the appearance of the cells – the centers are bright yellow, while the sides are green. Furthermore, the peak position of the green peak shifts more prominently in the microspectrophotometric analysis. At normal incidence, the peak appears at 525 nm, at 27º incidence at 55 nm, at dark field illumination (~73 º+-10º) at 556 nm. At open aperture stop where the whole range of angles between 0º and 53.1º are measured, the peak is broader and appears at 540 nm. This analysis suggests that the light is being reflected from a cholesteric helix that lays at an angle greater than 45º to surface normal. Only then will the peak wavelength of light be red-shifted with increasing the angle of incidence. In that case increasing the angle of incidence brings the incoming beam more parallel to the helix axis, resulting in a red shift. How exactly the light travels inside the

focal conic is a very intriguing question. One possibility is that the light gets reflected at the surface. In that case the green light should behave like a regular specular reflector and be reflected along the main beam, with the exit angle being opposite in sign to the entrance angle. However, from the Q-space analysis at 30º incidence we can see that the green light is reflected back to the light source instead (**Figure 9.9A**). From the Q-space analysis at normal incidence, we can also see that the light is reflected back along the main beam and not scattered about too much (**Figures 9.7 and 9.8**). Invoking the spherical mirror hypothesis, this kind of behavior could be explained by two 45º reflections from the sides of the bowl. However, in that case the wavelength shift cannot be explained, as the angle of incidence relative to the helix axis remains the same regardless of the angle of incidence relative to the surface normal. A third option is a wave-guide like mechanism where the light enters on one end of the focal conic and travels along the onion-like layers, exiting on the other side. The real space image under oblique, narrow beam illumination (**Figure 9.9B**) shows no green color on the side of the hexagon close to the incident beam, while the green color is only present on the sides. Furthermore, there appears to be green color present on the side of the hexagon away from the incident beam. The implication is that the light enters on one side of the structure and exits on the other side, provided that the conditions for entering are favorable.

It has to be stressed, that the shape and size of the focal conic domains would definitely influence their reflectance properties. Thus, one could envision making

materials of different colors by having the free surface cholesteric fluid form the defects at different conditions, such as temperature or surface curvature.

9.4. Conclusions

We propose that the cholesteric focal conic domains created at the free surface of a cholesteric liquid crystal chitin can create the perturbed cholesteric relief that can account for the color and the morphology of the exocuticle of the scarabaeid beetles. We further propose a mechanism of light production based on the focal conic defects. This mechanism does not require cholesteric phases with different pitches. The yellow light in this mechanism is focused by the focal conic spherical mirror-like structure, while the blue light enters the focal conic on the side, hitting the layers at an angle and is guided along the layers. While the details of morphogenesis will influence the exact nature of microstructure and observed color for a particular beetle, we infer that each of these mechanisms provides us with inspiration to the design of chiral reflectors. The desired optical response can be achieved by incorporating either a bistable cholesteric phase formed due to free surface that can be solidified or crosslinked to provide stable solid structure, by varying the surface curvature from Gaussian positive to negative, by using controlled anchoring, or by using structures with variable pitch (which can also be accomplished by having a concentration gradient of nematic blended into a cholesteric fluid [277]).

CHAPTER 10

MIMICRY OF THE STRUCTURAL COLOR FEATURES OF THE BUTTERFLY *Papilio palinurus* BY BOTTOM-UP SELF ASSEMBLY

10.1. Structural Color on the Wings of *Papilio palinurus*

The green color on the wings of a butterfly *Papilio palinurus* originates from the hierarchical microstructure of individual wing scales that are tiled on the wing. Each wing scale is about 100 μm long and contains multiple 4-10 μm diameter bowls, which in turn are lined with a multilayer stack of eleven alternating layers of air and chitin, each 100 nm thick[191]. . It is well known that the multilayer films produce iridescent-reflectance over a well-defined range of wavelengths, making them apt for applications as diverse as optical filters, anti-reflectance coatings for lenses, heat transmission coatings, and so forth[189,278-282]. Vukusic[191] elucidated that the distinct green color of the wings is the result of additive color mixing of yellow and blue, involving a combination of two reflections off the multilayer in the bowl; the yellow color is due to the reflection from the bottom of the bowl at normal incidence and the blue results from two 45º reflections at the edge of the bowl[191].

The polarization of the ray reflecting from the edge is changed upon each reflection and thus the edge is visible in a reflection mode microscope under crossed polarizers. The elegance of this structure has inspired us to mimic it using simple bottom-up self-assembly methods.

In this chapter, we describe the colours and colour mixing quantitatively using the language of color science. We then describe the result of mimicking[232,252] the optical effects found on the wing scale of *Papilio palinurus* by atomic layer deposition of multilayers of titanium dioxide and aluminium oxide over a polymer film with an ordered array of nearly monodisperse micron size holes formed using breath figure templated assembly[283].

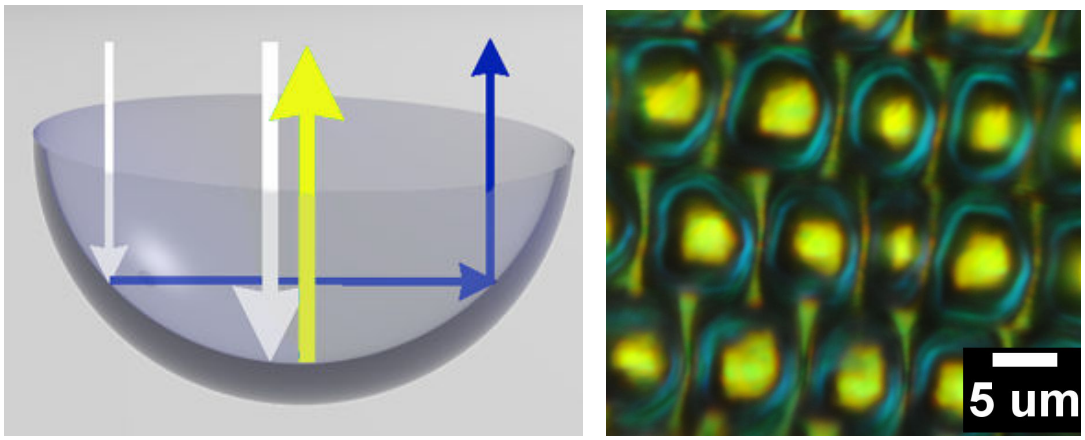

A B

Figure 10.1: (A) The mechanism of light reflection in a microbowl. White arrows denote white incoming light and the yellow and blue arrow the reflected light. (B) The microbowls on the wing of *Papilio palinurus* as seen under an optical microscope.

To better illustrate the additive color mixing, we have taken reflectance spectra of individual wing scale on a reflected light microspectrophotometer. We sampled a 4x4 μm spot by using a 50x lens. The yellow centre of the microbowl and the blue edges were sampled separately. The illumination condition was also adjusted by closing down the aperture stop so that the light was incident normal to the surface. The reflectivity of the yellow spot was almost 100% compared to an aluminium mirror. The reflectivity of the blue region was lower, peaking at about 40% (**Figure 10.2).** In contrast with these values, the previously reported values are 40% for the yellow and blue combined[190]. The

measurements at microscopically separate regions had not been previously reported to our knowledge. The high reflectivity measured can be explained by the spot measurement at the high magnification. When we measured the reflectivity of the wing scale with a 20x lens, the reflectivity values were in line with the previously reported ones. At 20x it is not possible to separately measure the differently coloured regions. Moreover, there are many dark regions on the wing scale that do not reflect light. These regions do not contribute to the reflectivity and thus the macroscopic measurements can be very different from the microscopic ones. Furthermore, the microbowl on the wing scale might be focusing the light from a slightly larger area into one small, bright spot, resulting in a high reflectivity of the yellow color measured with the microspectrophotometer.

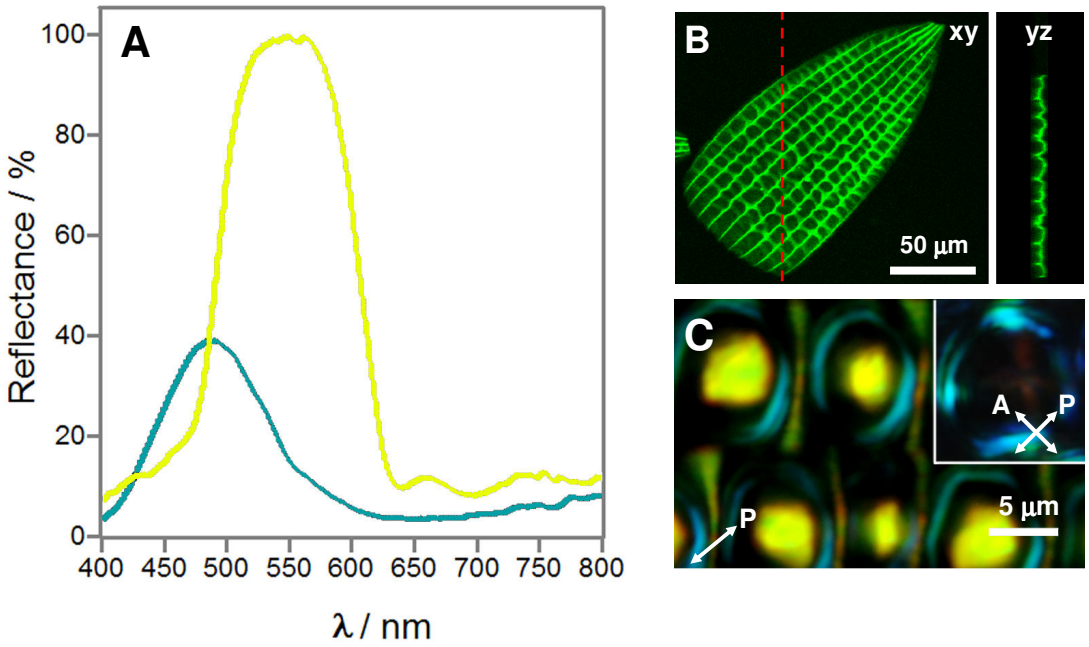

Figure 10.2: (A) The reflectance spectra of microbowls on the surface of a scale of *Papilio Palinurus.* The curve with nearly 100% reflectivity was taken observed on a yellow region and the less reflective curve on a blue region. (B) Confocal micrograph of a wing scale of *Papilio palinurus* obtained in fluorescence mode. The xy image was taken 5 µm below the top of a wing scale. The yz image is taken along the red dotted line of the xy image. (C) Optical micrograph of *Papilio palinurus* obtained in polarized light. The inset in the upper right corner shows the same structures under crossed polarizers.)

Vukusic et al[190]. noted that the colour of Papilio palinurus is green, despite mixing two complementary colours - blue and yellow. Usually we would expect the additive mixture of these two colors to result in white or blueish grey. It was also pointed out that it is possible to mix certain "blues" and yellows in such a way that the result is a green colour[190]. Since we were able to measure the individual colour spectra, we also set about describing the colour mixing quantitatively. From the yellow and blue spectra we calculated the CIE chromaticity coordinates[284]. These values tell us how a standard human observer would perceive the colors. The colour space is described by three vectors which have a relation with the three receptors in the eye in terms of the colour perceived. Since this is a vector space, we could theoretically also describe the perception of an animal, if we knew its receptor characteristics and as long as the animal also had three colour receptors (a trichromate)[285]. We then plotted the resulting colours in the CIE chromaticity diagram[286]. We can indeed see (**Figure 10.3)** that the line connecting the blue and yellow lies well away from the white point and never crosses it. This line describes all the colour hues accessible through additive colour mixing. Thus the colour of Papilio palinurus is not white but green. If we calculate the coordinates of the resulting mixed colour by weighting the contribution of the yellow and blue with their respective luminance values, we can see that the result is a yellowish green colour. From the location of the two colours on the CIE diagram we can see that they are quite far apart. That means there are many mixed colours attainable through additive mixing of these two colours[285,287]. The contribution of each colour to the mixed colour could be modified by changing the ratios of reflective yellow and blue area fractions[287]. On the CIE diagram we can also see that, under D65 illumination, which simulates daylight illumination, the blue falls outside the sRGB triangle. This means that any pictures taken with a digital camera cannot do justice to the brilliant appearance of these scales under the microscope, because sRGB is the standard colour space in use by the digital cameras. If we switch the illumination to CIE illuminant A (an incandescent light, not shown), the yellow colour

falls outside the sRGB range. If the camera operates in AdobeRGB, the blue colour can be captured in D65, and the yellow in incandescent light will be on the edge of the gamut.

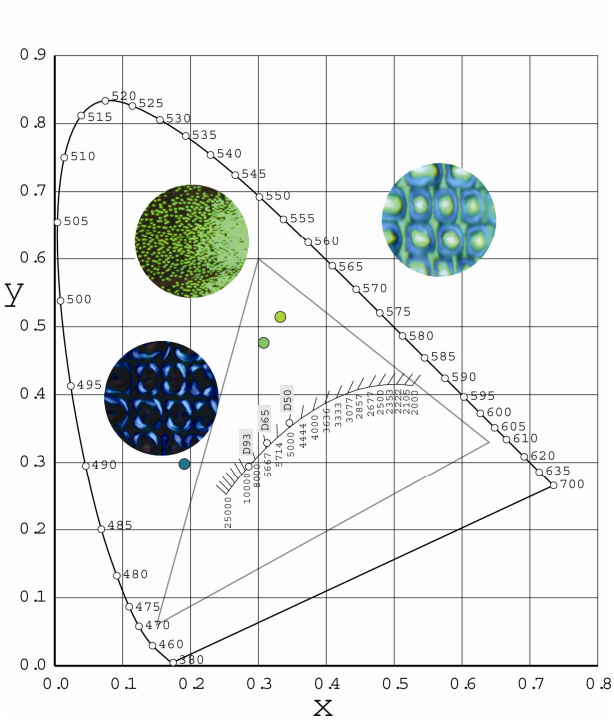

Figure 10.3: The colors of *Papilio palinurus* in the CIE chart. The blue spot is shown together with a microscope image under crossed polarizers under high magnification. The green spot is shown next to a piece of wing under low magnification. The yellow spot is shown next to a picture of the bowls under high magnification, where the yellow colour dominates. The triangle denotes the sRGB gamut.

10.2. Self-Assembly Method for Mimicry of the Structural Color Features of Papilio Palinurus

The approach envisioned for the mimicry of the structural features responsible for the color on the wing of *Papilio palinurus* was to first produce micron-sized bowls and then coat them with a multilayer. The method employed for the production of the bowls was breath figure templated assembly[283]. The bowls were then coated by atomic layer deposition of multilayers of titanium dioxide and aluminum oxide[288] (See **Figure 10.4**).

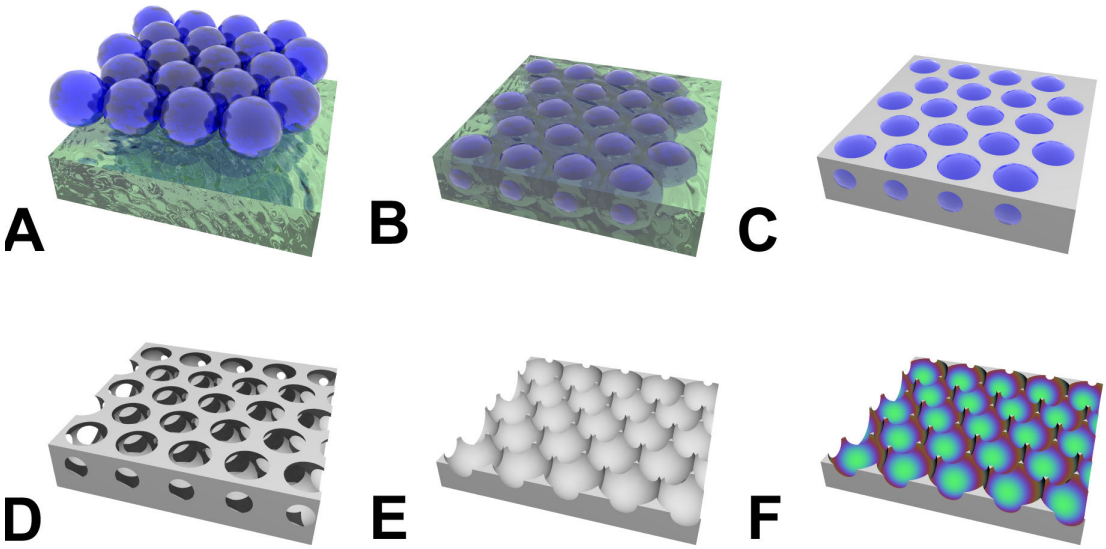

Figure 10.4: The steps in making an artificial butterfly wing by self assembly: (A) Water droplets condense and pack above a polymer solution, (B) water droplets sink into the polymer solution, (C) solvent evaporates, leaving behind a solid polymer interspersed with water droplets (D) water droplets evaporate, leaving behind an ordered, porous polymer film, (E) the top of the film is peeled off, leaving behind an array of microbowls, and (F) the microbowls are coated with a multilayer using atomic layer deposition.

10.2.1. Breath Figure Templated Assembly

In order to mimic the optical effects found on the wing scale the key starting component is an array of microbowls. We use a bottom-up self-assembly method known as "breath figure templated assembly" [127,283,289,290] to make such an array. When a stream of humid air air (relative humidity around 80 %) is passed over a dilute (1% w/w) polymer solution (polystyrene, M_w 50.000, carboxy terminated) in a volatile solvent (carbon disulfide), evaporative cooling promotes condensation of water droplets[291,292]. These drops grow and self-assemble into a hexagonally ordered array (**Figure 10.4A**), eventually sinking into the polymer solution (**Figure 10.4B**). After the solvent evaporates away (**Figure 10.4C**), the water drops evaporate, leaving their imprint in the polymer in the form of an ordered array of air bubbles, with typical diameters between 300 nm and

10 μm (**Figures 10.4D, 10.5A**). By blowing moist air over polystyrene dissolved in carbon disulfide, we produced a holey film with micron sized cavities. We then peeled the top off using adhesive tape, resulting in a polymer film with an ordered array of micron sized bowls (**Figures 3e, 10.5B**). The bowls are reminiscent of the structures on the wing scales of *Papilio palinurus*, but the optical effect requires a multilayer stack which was obtained by atomic layer deposition (**Figure 10.4F**).

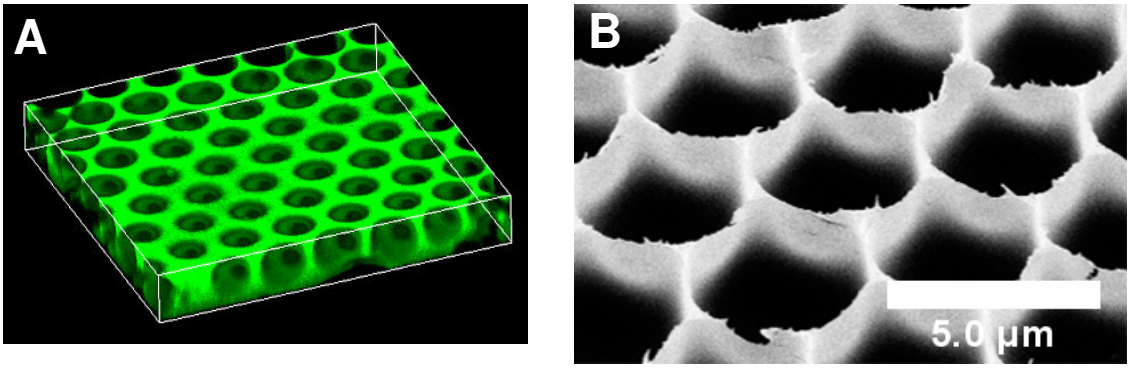

29.7 × 29.7 (3.7 μm^3 Confocal microscope: 3D reconstruction of the breath figure

SEM image of microbowls after peeling

Figure 10.5: The structure of the breath figure templated assembly, (A) before and (B) after peeling off the top half.

10.2.2. Multilayer Reflectance Simulation

To replicate the optical effect of the individual wing scale, we first simulated the reflectance of a multilayer stack composed of alternating layers of amorphous titanium oxide, TiO_2 (refractive index n=2.5) and amorphous aluminum oxide, Al_2O_3 (n=1.5). The method used was the standard transfer matrix method with the Fresnel coefficients present in 2x2 matrices, each representing a dielectric layer [253]. The Fresnel coefficients

represent the fraction of reflected to the fraction of transmitted light at each interface and they depend on the refractive indices of both media and the incident angle of light.

FreeSnell software package was used for the simulations[293]. In the calculations the two cases were considered – the first where the ray of light is incident at the normal to the surface of a multilayer and the second case where the ray of light is incident upon the multilayer at an angle of 45º. These two cases correspond to the light illuminating a microbowl. At the bottom, the angle of incidence of light is normal to the surface, and at the edges, the angle of incidence is 45º. An attempt was made in the calculations to provide the proper layer thicknesses for the greatest separation between the two peaks of reflected light in these two cases. However, because of the limitations of the apparatus for atomic layer deposition, the total thickness of the multilayer also had to be kept below 300 nm. The calculations showed that alternating 20 nm layers of TiO_2 and Al_2O_3 would give a similar optical effect as seen on the *Papilio palinurus*. From the calculated spectra we calculated the predicted colors according to the CIE color space with the CIE A illuminant. The CIE A illuminant is a tungsten lamp, which is what was used in our microscope to illuminate the samples. The CIE tristimulus values thus calculated were converted into CIE L*a*b coordinates and entered into Adobe Photoshop to make color patches representing the expected colors at the bottom of the bowls (normal incidence) and at the edges (45º incidence) (see **Figure 10.6** for 5 alternating layers and **Figure 10.7** for 8 alternating layer). We can see that the color at 45º incidence is always blue shifted compared to normal incidence, as expected for a multilayer reflector. Furthermore, the peak width becomes smaller with increasing the number of layers. This occurs because

we are using a sub-optimal number of layers. If the number of layers is 10 or more, the peak width does not change that much anymore[186]. We can also see that the peak position shift slightly into the blue with increasing the number of layers.

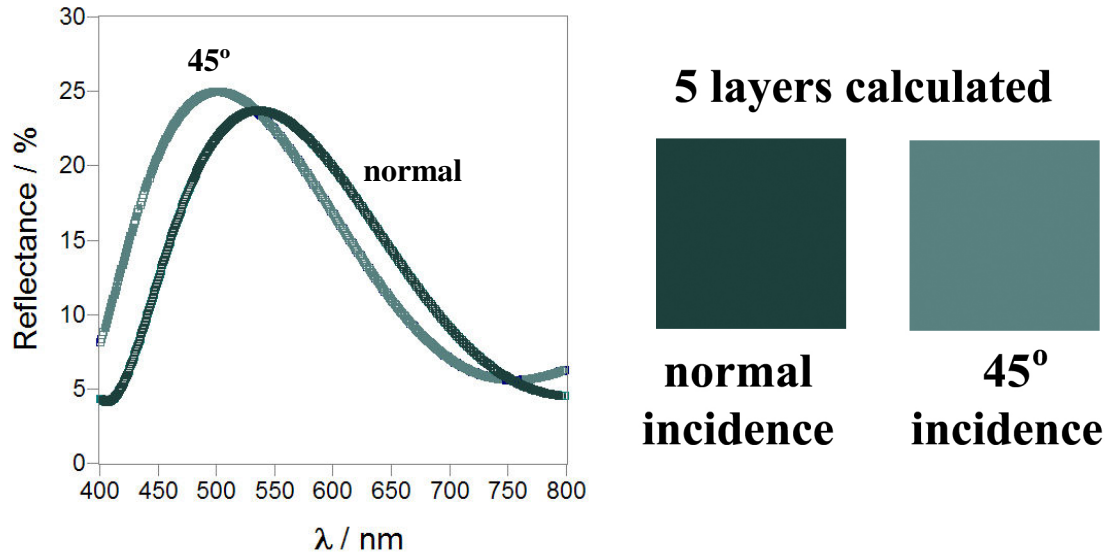

Figure 10.6: Calculated reflectance spectra for 5 alternating TiO_2/Al_2O_3 layers 20 nm each.

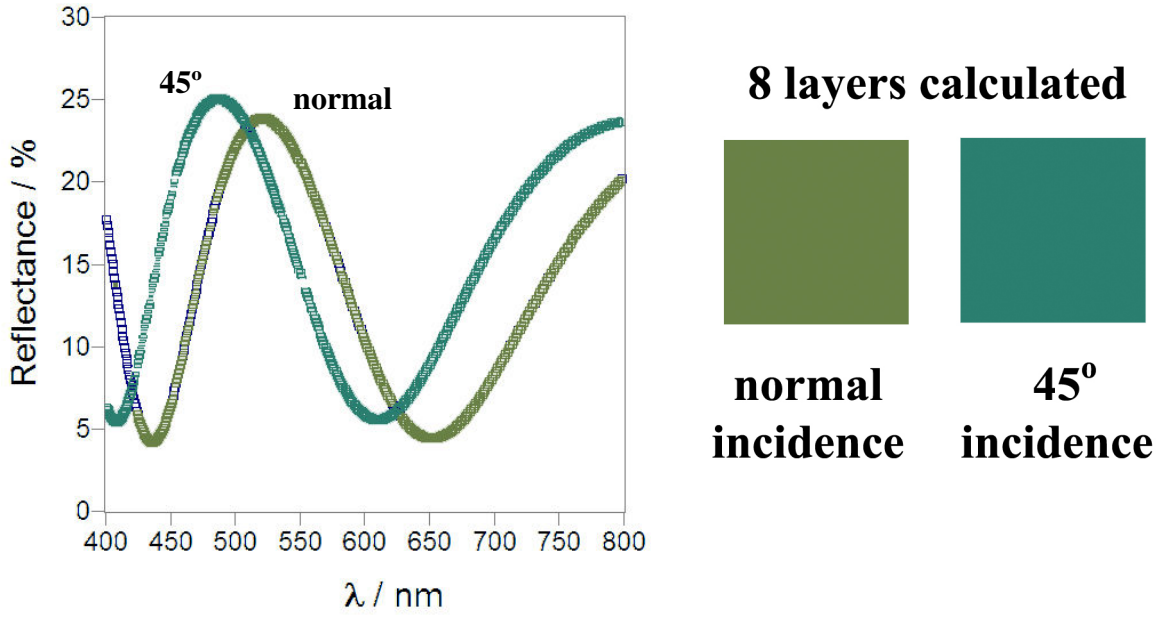

Figure 10.7: Calculated reflectance spectra for 8 alternating TiO_2/Al_2O_3 layers 20 nm each.

10.2.3. Atomic Layer Deposition (ALD)

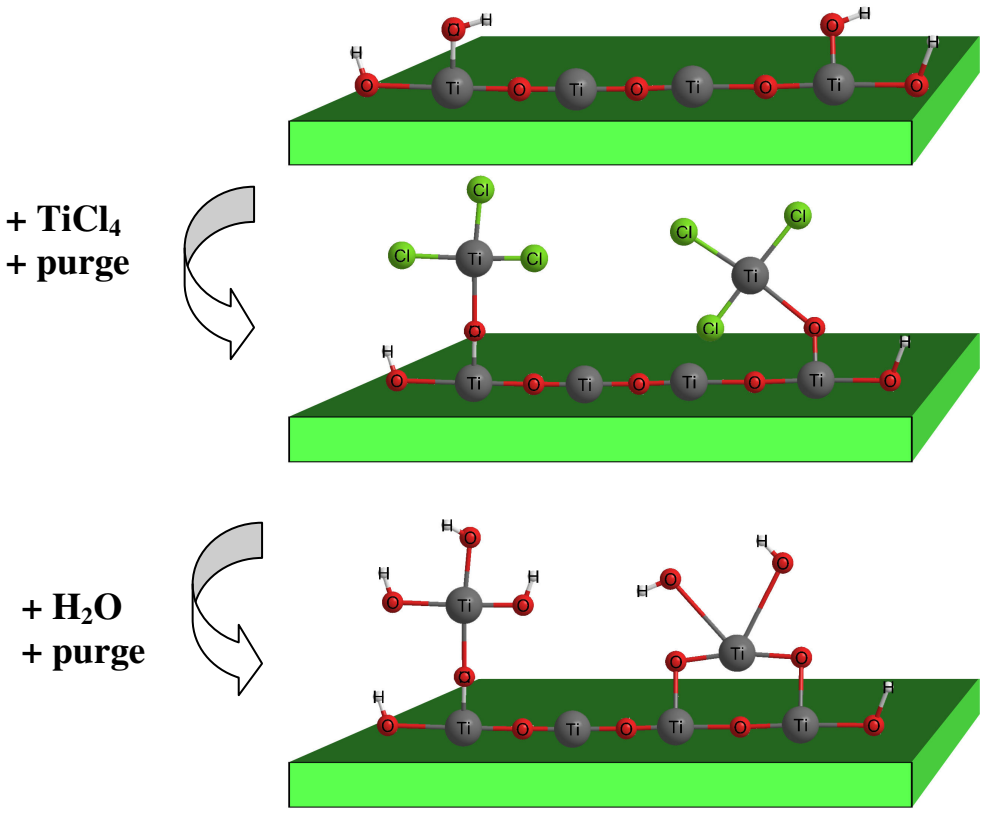

Figure 10.8: ALD process. The precursor is deposited on the surface, where it reacts with the nucleophilic groups. The surface is purged of the un-adsorbed precursor and hydrolyzed by water vapor. This process is repeated until a desired thickness is achieved.

The layers of Al_2O_3 and TiO_2 were deposited using atomic layer deposition technique with a custom designed apparatus[294,295]. Schematic diagram is shown in **Figure 10.8**. Volatile liquid precursors trimethylaluminum and titanium(IV)tetrachloride were deposited on the surface of the microbowls. Then water vapor was used to hydrolyze the precursors into their respective hydroxides. Another layer of the precursor was then deposited onto the reactive hydroxyl groups. This process was repeated until the desired

material thickness was achieved. The automated process controls which precursor is deposited during the cycle and thus multilayers of Al_2O_3 and TiO_2 of custom thickness were produced. The peeled breath figure templated polymer structure was coated with 5 alternating layers of Al_2O_3 and TiO_2, the thickness of each layer was set to be 20 nm and examined. After that, the structure was placed in the ALD apparatus again and further 3 alternating layers were deposited for a total of 8 alternating layers, 20 nm each. The starting layer in the coating was TiO_2.

10.3. Characterization of the artificial structures

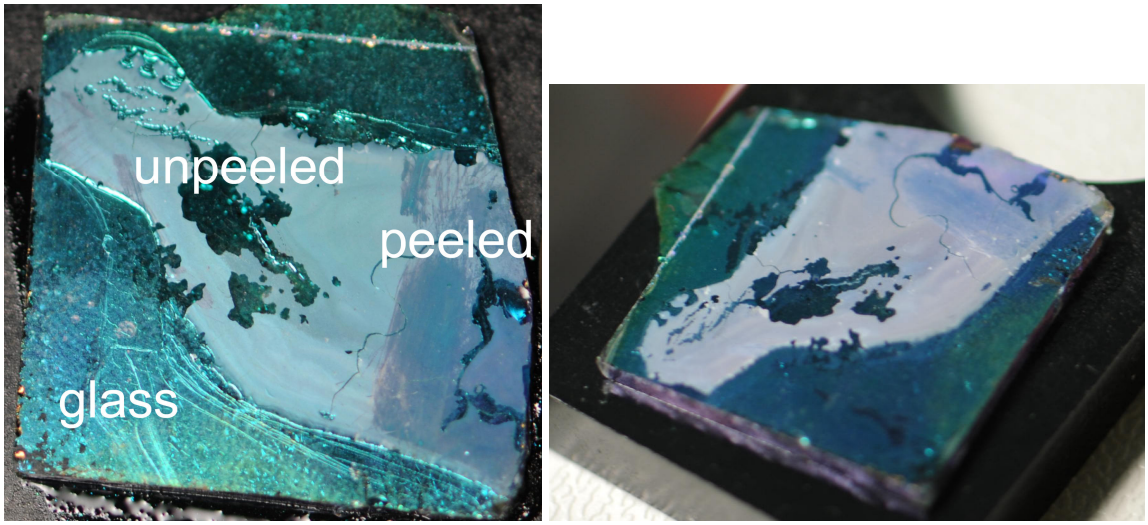

A **B**

Figure 10.9: The ALD coated porous polymer film with the light coming from behind the camera (A) and from the side (B). There are three regions on the glass slide – "glass" is the region where the glass was directly coated with the multilayer. "Unpeeled" is the region where the porous polymer film was coated as received from breath figure templated assembly. "Peeled" is the region where the top of the porous film was peeled off before ALD.

The macroscopic appearance of the ALD coated polymer film is already very different from the flat multilayer. As we can see in **Figure 10.9**, the color of the flat multilayer on glass is brilliant green. However, the peeled and ALD coated polymer film is blue. Furthermore, the color of the peeled film does not change much with varying the angle of incoming light, while the flat multilayer changes from green (**Figure 10.9A**) to blue (**Figure 10.9B**). The unpeeled polymer film has a similar hue as the flat multilayer, however it appears lighter in color. This might be due to the light scattering of all the micron-sized holes.

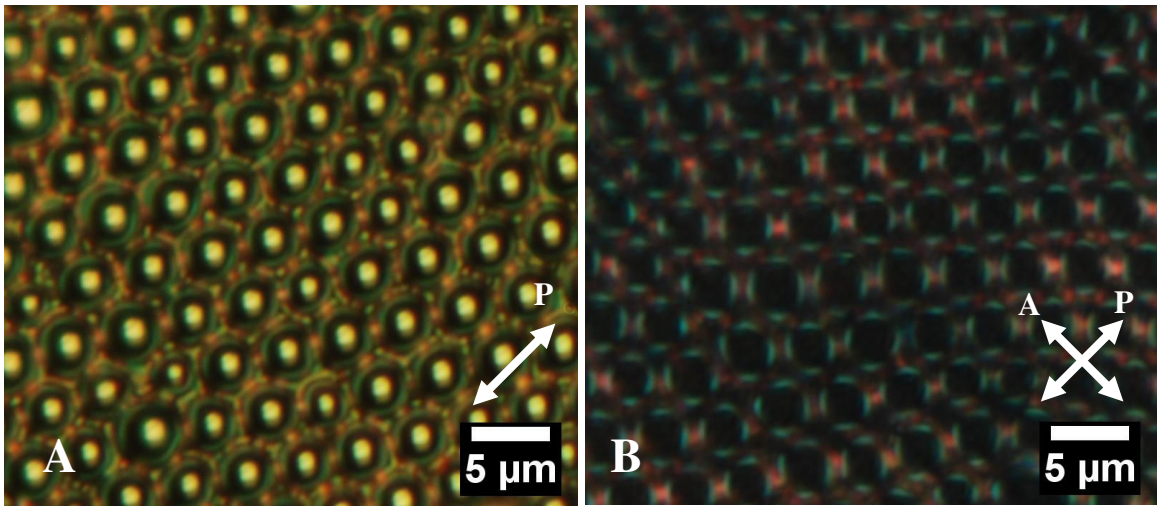

Figure 10.10: Micrographs of the peeled breath figures coated with 5 alternating TiO_2/Al_2O_3 layers 20 nm thick. An image taken (A) with only the polarizer in the light path, and (B) under crossed polarizers.

The peeled breath figures coated with 5 alternating layers of TiO_2/Al_2O_3 appear very similar to the original *Papilio palinurus* optical structures under a microscope (**Figure 10.10A**). The bottom of the bowls appears very bright and has a yellowish hue. The sides of the bowls are of a greenish blue hue. The rims of the bowls are also dimmer than the original *Papilio palinurus* brilliant blue rims. Under crossed polarizers (**Figure**

10.10B) the center reflection is extinguished and the side reflections become more prominent. The side reflections do not appear as rings, because light that is polarized perpendicular to the surface normal does not get reflected. This was checked by placing a rotatable polarizer in the illumination path. The side reflection is extinguished in the same direction as the polarization direction (**Figure 10.10A**). Under crossed polarizers the second extinction is caused by cutting off of light by the analyzer. Another color with a red hue appears to be present in the interstices between the microbowls. The optical effect is analogous to that seen on the *Papilio palinurus* scales.

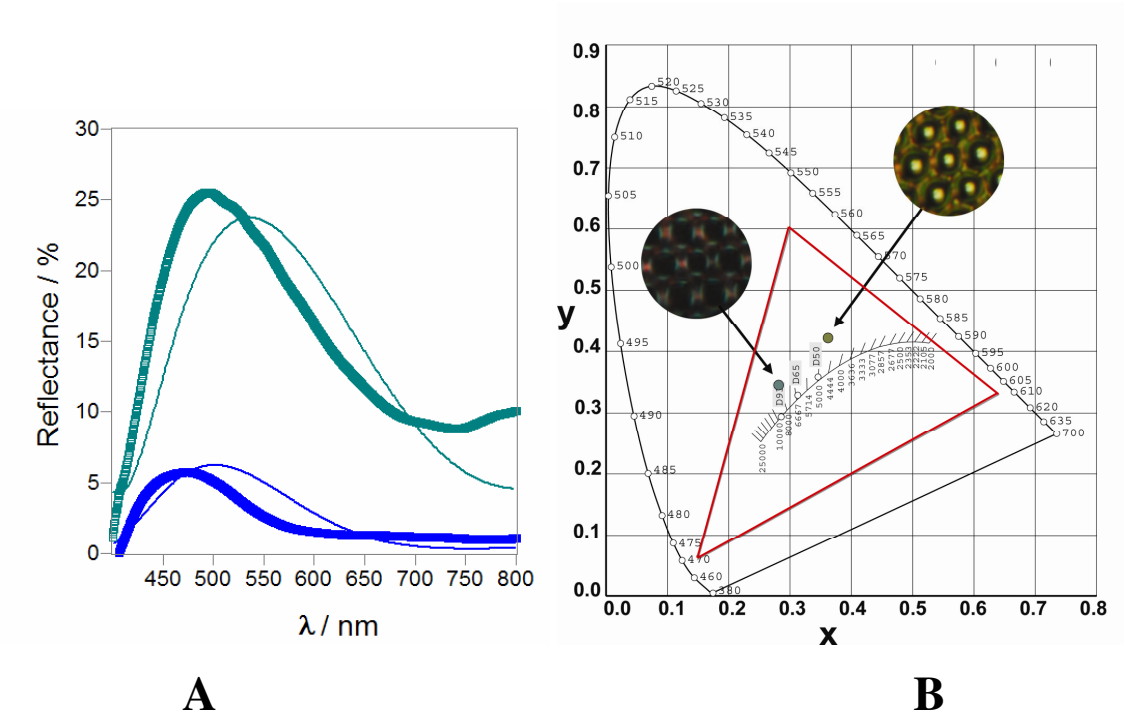

Figure 10.11: (A) The reflectance spectra of the peeled and ALD coated (5 layers) breath figure templated assembly and (B) the corresponding CIE diagram. The relative reflectivity is in reference to an aluminum mirror. The colors of the curves roughly represent the respective colors in the micrographs. The thin curves in (A) are the calculated values for a 5 layer alternating stack of TiO_2/Al_2O_3. The thick curves are the measured spectra. The low reflectivity curve was taken under crossed polarizers to extinguish the bottom reflection. The reflectivity is not calibrated in this case and the Y-scale has arbitrary units.

Due to the smaller size of the microbowls, we were not able to measure the two colors separately by the microspectrometer. Therefore we measured the reflectance under crossed polarizers to evaluate the spectrum of the side reflections. The spectral analysis of the 5-layered structure shows a blue shift for the spectrum taken under crossed polarizers (**Figure 10.11A**). This shift can be explained by the different incident angle for the ray reflecting from the side of the bowl. We were not able to get a meaningful intensity calibrated spectrum under crossed polarizers, therefore the units on the ordinate scale are arbitrary. The spectrum is thus scaled in the ordinate so that the intensity is comparable to the calculated spectrum after two 45º reflections. The intensity units for the spectrum taken without polarizers correspond to the relative intensity versus an aluminum mirror. Although the reflectance measured under crossed polarizers is not quantitative in terms of intensity, the location and shape of the peak and thus the hue and saturation information are preserved. In comparison with the calculated spectra, the measured spectra have peaks at slightly lower wavelengths. This could be explained by the ALD layer thickness being lower than desired. Also, the measured spectrum has slightly higher reflectivity at high wavelengths. The reason for that could be light scattering from the breath figure which appears milky white before it is coated using ALD. On the CIE diagram the two resulting colors are located in the same direction from the white point as the colors of *Papilio palinurus.* They appear in the green-yellow quadrant.

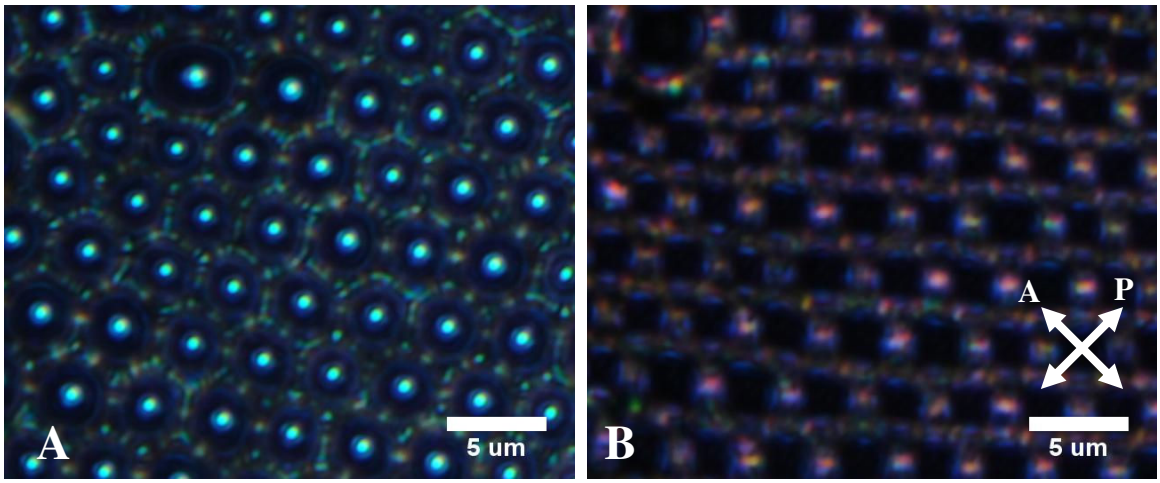

Figure 10.12: Micrographs of the peeled breath figures coated with 8 alternating TiO_2/Al_2O_3 layers 20 nm thick (A) Image taken with only the polarizer in the light path, and (B) Image taken under crossed polarizers.

The breath figure coated with 8 alternating layers TiO_2 and Al_2O_3 has a different hue from the one coated with 5 alternating layers. The bottom of the bowls reflects a greenish light blue and the edges reflect a dark blue (**Figure 10.12A**). Again, if a polarizer is put in the light path, the portion of the ring where the polarization is perpendicular to the reflecting surface is not reflected back. Under crossed polarizers the dark-blue reflections can be seen more clearly, along with the red color on the edges (**Figure 10.12B**).

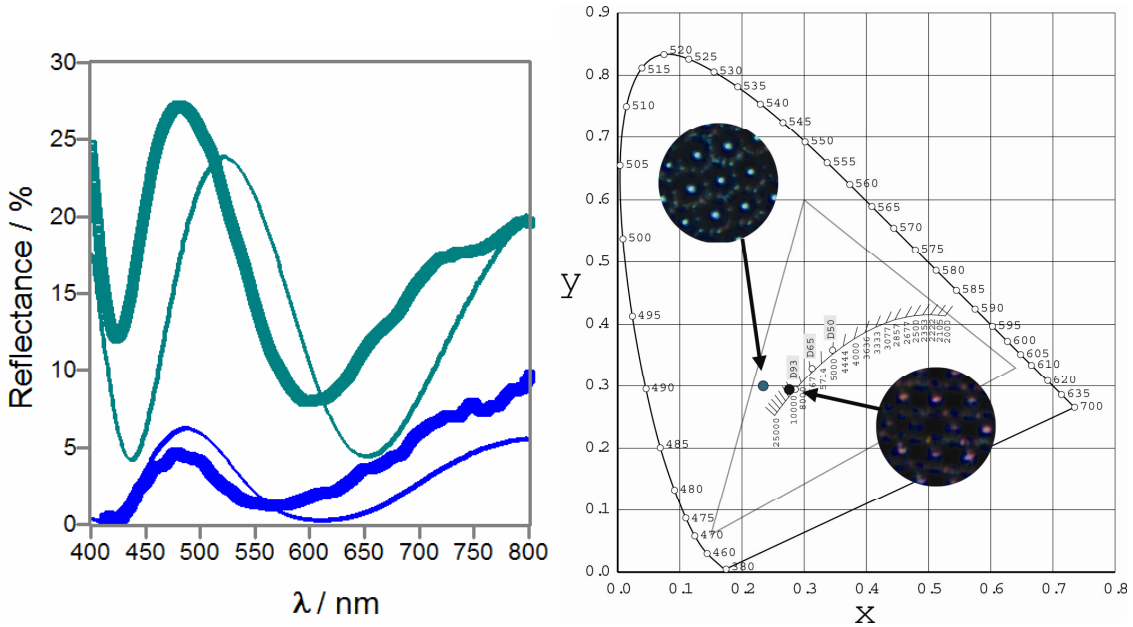

Figure 10.13: : (A) The reflectance spectra of the peeled and ALD coated (8 layers) breath figure templated assembly and (B) the corresponding CIE diagram. The relative reflectivity is in reference to an aluminum mirror. The colors of the curves roughly represent the respective colors in the micrographs. The thin curves in (A) are the calculated values for an 8 layer alternating stack of TiO_2/Al_2O_3. The thick curves are the measured spectra. The low reflectivity curve was taken under crossed polarizers to extinguish the bottom reflection. The reflectivity is not calibrated in this case and the Y-scale has arbitrary units.

The spectral analysis of the 8 layer coated structure shows good qualitative agreement with the predicted spectra (**Figure 10.13A**). However, the measured peak reflection appears substantially blue shifted compared to the calculated peak. Since the sample was taken out of the ALD chamber and then further coated another time, it is possible that the thickness of the last three layers was smaller than desired. The spectrum taken under crossed polarizers does not appear to be blue shifted by much compared to the overall reflectivity. The reason for that could be a measurement error. The spectrum appears noisy and the peak is located in the region between 400 and 500 nm where the tungsten

lamp used in the measurement has a rather low intensity. Therefore it was not possible to obtain a better spectrum. We can also see the overall background appears higher in this sample. We believe that the background can be attributed to light scattering from the small structures in the breath figure. In the CIE diagram (**Figure 10.13B**) we can see that the two colors are located very close together. Since all the colors available through color mixing lie on the line connecting the two chromaticity values, that means there are not many color available through additive color mixing in this case. However, it is possible that the measurement under crossed polarizers has a substantial error and therefore the color mixing cannot be easily described in this case.

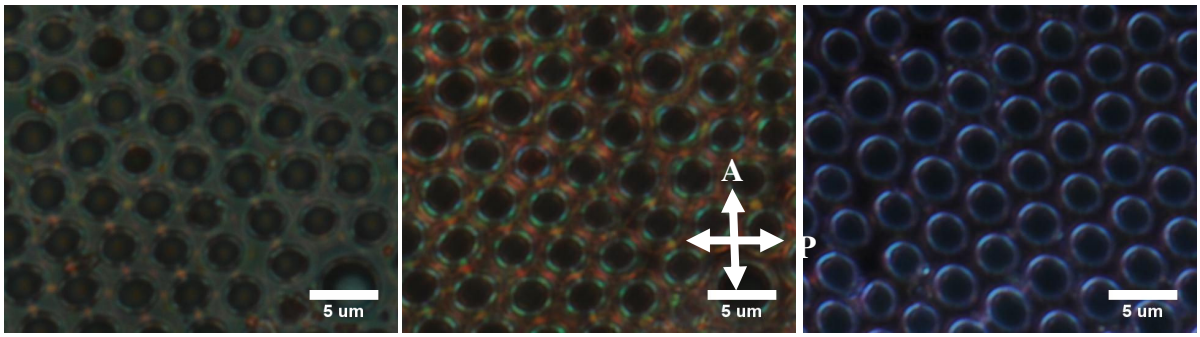

A **B** **C**

Figure 10.14: Micrographs of unpeeled ALD coated breath figure: (A) under normal illumination, (B) under crossed polarizers, and (C) under dark field illumination.

The unpeeled and coated breath figure structure also has some very interesting optical properties. Under normal illumination (**Figure 10.14A),** we can see some contributions from the underlying structure connecting the cavities. This becomes more obvious under crossed polarizers (**Figure 10.14B**), where the connecting interstices obtain a red color. This means there is some polarization change when light interacts with these structures. The red dots visible in the peeled structures under crossed polarizers are most likely also

the result of this interaction. The rings around the cavity appear green-blue colored under crossed polarizers. The melatope is present, but hardly visible. Again the polarization of the light interacting with the ring is changed. These effects are also observed in the breath figure structures without ALD coating, however not as pronounced and not so brightly colored. Perhaps the polymer molecules in these confined spaces are oriented, giving rise to birefringence in these small regions. In dark field illumination (**Figure 10.14C**), we can again see the rings around the cavities are scattering light, which is blue colored due to the sharper angle of incidence. The reflection spectra of these structures are dominated by the reflectivity of the flat multilayer. We were not able to take the spectra of the peculiar colors present in the interstices due to their small size.

10.4 Conclusions

We were thus able to mimic the optical effect on the individual wing scales of *Papilio palinurus* using breath figure templated assembly as the starting point for the structure. The spectral analysis of the regions responsible for the two colours on the wing of *Papilio palinurus* shows us that these two colours are spaced quite far apart on the CIE colour diagram and therefore many colours between the points are possible through additive colour mixing. The nanoscale construction of the bio-mimicry structure proceeded in a few simple steps, and involved no etching or microfabrication tools or templates. The template for the array of microbowls is an array of water droplets which nucleate, grow, imprint and evaporate on their own under the unique conditions of breath figure templated assembly. The peeling step is very simple and no special equipment is needed. The stepwise ALD process proceeds at low temperature and is well known and established; however, as far as we know it has never been applied to build a bio-mimicry structure from scratch. The resulting structure exhibits all the major optical

characteristics of the natural structure of *Papilio palinurus* – an array of microbowls, reflection of light involving polarization change, separation of white light into two colours due to the underlying multilayer structure and additive colour mixing of these two colours. Although an array of microbowls exhibiting the polarization change has been realized before[296], the colour mixing and complete bottom-up self-assembly were not. We believe that the demonstrated principle of manipulation of the microstructure of the optical multilayer could find an interesting application in making brilliantly coloured materials with access to many different colours through colour mixing, as well as micro-arrays of focusing dichroic mirrors.

REFERENCES PART B

(159) Hooke, R. *Micrographia* London,, 1667.

(160) Newton, I. *Opticks: or, A treatise of the reflexions, refractions, inflexions and colours of light. Also two treatises of the species and magnitude of curvilinear figures*; Printed for S. Smith, and B. Walford: London,, 1704.

(161) Michelson, A. A., "Metallic Coloring in Birds and Insects"; *Philos. Mag.* **1911**, *21*, 554-67.

(162) Rayleigh, "On the propagation of waves through a stratified medium, with special reference to the question of reflection."; *Proceedings of the Royal Society of London Series a-Containing Papers of a Mathematical and Physical Character* **1912**, *86*, 207-226.

(163) Rayleigh, "On the reflection of light from a regularly stratified medium"; *Proceedings of the Royal Society of London Series a-Containing Papers of a Mathematical and Physical Character* **1917**, *93*, 565-577.

(164) Rayleigh, L., "Studies of Iridescent Colour, and the Structure Producing it. IV. Iridescent Beetles"; *Proceedings of the Royal Society of London. Series A, Containing Papers of a Mathematical and Physical Character (1905-1934)* **1923**, *103*, 233-239.

(165) Raman, C. V., "On iridescent shells - Part I: Introductory"; *Proceedings of the Indian Academy of Sciences-Animal Sciences* **1934**, *1*, 567-573.

(166) Raman, C. V., "On iridescent shells - Part II: Colours of laminar diffraction"; *Proceedings of the Indian Academy of Sciences-Animal Sciences* **1934**, *1*, 574-589.

(167) Mason, C. W., "Structural Colors in Insects. I"; *The Journal of Physical Chemistry* **1926**, *30*, 383-395.

(168) Mason, C. W., "Structural Colors in Insects. II"; *The Journal of Physical Chemistry* **1927**, *31*, 321-354.

(169) Anderson, T. F.; Richards, A. G., "An electron microscope study of some structural colors of insects"; *J. Appl. Phys.* **1942**, *13*, 748-758.

(170) Lippert, W.; Gentil, K., "*Elektronenmikroskopische Studien Uber Micellare Strukturen Bei Schmetterlingsschuppen Vom Morpho-Typ"; *Zeitschrift Fur Wissenschaftliche Mikroskopie Und Fur Mikroskopische Technik* **1952**, *61*, 95-100.

(171) Yablonovitch, E., "Photonic Band-Gap Crystals"; *J. Phys.: Condens. Matter* **1993**, *5*, 2443-2460.

(172) Srinivasarao, M., "Nano-optics in the biological world: Beetles, butterflies, birds, and moths"; *Chem. Rev.* **1999**, *99*, 1935-1961.

(173) Meadows, M. G.; Butler, M. W.; Morehouse, N. I.; Taylor, L. A.; Toomey, M. B.; McGraw, K. J.; Rutowski, R. L., "Iridescence: views from many angles"; *Journal of The Royal Society Interface* **2009**, *6*, S107-S113.

(174) Kinoshita, S.; Yoshioka, S.; Miyazaki, J., "Physics of structural colors"; *Reports on Progress in Physics* **2008**, *71*, -.

(175) Kinoshita, S.; Yoshioka, S., "Structural Colors in Nature: The Role of Regularity and Irregularity in the Structure"; *ChemPhysChem* **2005**, *6*, 1442-1459.

(176) Vukusic, P.; Sambles, J. R., "Photonic structures in biology"; *Nature* **2003**, *424*, 852-855.

(177) Pfaff, G.; Reynders, P., "Angle-Dependent Optical Effects Deriving from Submicron Structures of Films and Pigments"; *Chemical Reviews* **1999**, *99*, 1963-1982.

(178) Ghiradella, H., "Light and Color on the Wing - Structural Colors in Butterflies and Moths"; *Appl Optics* **1991**, *30*, 3492-3500.

(179) Ingram, A. L.; Parker, A. R., "Review. A review of the diversity and evolution of photonic structures in butterflies, incorporating the work of John Huxley (The Natural History Museum, London from 1961 to 1990)"; *Philosophical Transactions of the Royal Society B: Biological Sciences* **2008**, *363*, 2465-2480.

(180) Parker, A. R., "515 million years of structural colour"; *Journal of Optics a-Pure and Applied Optics* **2000**, *2*, R15-R28.

(181) Seago, A. E.; Brady, P.; Vigneron, J.-P.; Schultz, T. D., "Gold bugs and beyond: a review of iridescence and structural colour mechanisms in beetles (Coleoptera)"; *Journal of The Royal Society Interface* **2009**, *6*, S165-S184.

(182) T. Lenau, M. B., "Colours and Metallic Sheen in Beetle Shells - A Biomimetic Search for Material Structuring Principles Causing Light Interference"; *Advanced Engineering Materials* **2008**, *10*, 299-314.

(183) Heavens, O. S. *Optical Properties of Thin Solid Films*; Dover Publications: New York, 1991.

(184) Heavens, O. S. *Optical Properties of Thin Solid Films*; Dover Publications: New York, 1991.

(185) Vukusic, P.; Kelly, R.; Hooper, I., "A biological sub-micron thickness optical broadband reflector characterized using both light and microwaves"; *Journal of The Royal Society Interface* **2009**, *6*, S193-S201.

(186) Macleod, H. A. *Thin-film optical filters*; 3rd ed.; Institute of Physics Pub.: Bristol ; Philadelphia, 2001.

(187) Jaffer, A., "The FreeSnell Thin-Film Optical Simulator"; *http://people.csail.mit.edu/jaffer/FreeSnell/* **2003**.

(188) Johnson, S. G.; Joannopoulos, J. D. *Photonic crystals : the road from theory to practice*; Kluwer Academic Publishers: Boston, 2002.

(189) Fink, Y.; Winn, J. N.; Fan, S.; Chen, C.; Michel, J.; Joannopoulos, J. D.; Thomas, E. L., "A Dielectric Omnidirectional Reflector"; *Science* **1998**, *282*, 1679-1682.

(190) Vukusic, P.; Sambles, R.; Lawrence, C.; Wakely, G., "Sculpted-multilayer optical effects in two species of Papilio butterfly"; *Applied Optics* **2001**, *40*, 1116-1125.

(191) Vukusic, P.; Sambles, J. R.; Lawrence, C. R., "Structural colour - Colour mixing in wing scales of a butterfly"; *Nature* **2000**, *404*, 457-457.

(192) Ghiradella, H., "Structure of iridescent lepidopteran scales: Variation on several themes"; *Ann. Entomol. Soc. Am.* **1984**, *77*, 637-645.

(193) Vukusic, P., "Manipulating the Flow of Light with Photonic Crystals"; *Physics Today* **2006**, *59*, 82-83.

(194) Shawkey, M. D.; Morehouse, N. I.; Vukusic, P., "A protean palette: colour materials and mixing in birds and butterflies"; *Journal of The Royal Society Interface* **2009**, *6*, S221-S231.

(195) Knight, J. C.; Broeng, J.; Birks, T. A.; Russel, P. S. J., "Photonic band cap guidance in optical fibers"; *Science* **1998**, *282*, 1476-1478.

(196) Russell, P., "Photonic crystal fibers"; *Science* **2003**, *299*, 358-362.

(197) Vukusic, P.; Hooper, I., "Directionally controlled fluorescence emission in butterflies"; *Science* **2005**, *310*, 1151.

(198) Zhang, W.; Zhang, D.; Fan, T.; Gu, J.; Ding, J.; Wang, H.; Guo, Q.; Ogawa, H., "Novel Photoanode Structure Templated from Butterfly Wing Scales"; *Chemistry of Materials* **2009**, *21*, 33-40.

(199) Chan, Y. S.; Chan, C. T.; Liu, Z. Y., "Photonic Band Gaps in Two Dimensional Photonic Quasicrystals"; *Physical Review Letters* **1998**, *80*, 956.

(200) D. J. Norris, Y. A. V., "Chemical Approaches to Three-Dimensional Semiconductor Photonic Crystals"; *Advanced Materials* **2001**, *13*, 371-376.

(201) Ghiradella, H. T.; Butler, M. W., "Many variations on a few themes: a broader look at development of iridescent scales (and feathers)"; *Journal of The Royal Society Interface* **2009**, *6*, S243-S251.

(202) Poladian, L.; Wickham, S.; Lee, K.; Large, M. C. J., "Iridescence from photonic crystals and its suppression in butterfly scales"; *Journal of The Royal Society Interface* **2009**, *6*, S233-S242.

(203) Michielsen, K.; Stavenga, D. G., "Gyroid cuticular structures in butterfly wing scales: biological photonic crystals"; *Journal of The Royal Society Interface* **2008**, *5*, 85-94.

(204) Ghiradella, H., "Structure and Development of Iridescent Butterfly Scales - Lattices and Laminae"; *J Morphol* **1989**, *202*, 69-88.

(205) Hyde, S.; Andersson, S.; Larsson, K.; Blum, Z.; Landh, T.; Lidin, S.; Ninham, B. W. *The Language of Shape*; Elsevier Science B. V.: Amsterdam, 1997.

(206) Morris, R. B., "Iridescence from Diffraction Structures in Wing Scales of Callophrys-Rubi, Green Hairstreak"; *Journal of Entomology Series a-Physiology & Behaviour* **1975**, *49*, 149-154.

(207) Ghiradella, H.; Radigan, W., "Development of Butterfly Scales .2. Struts, Lattices and Surface-Tension"; *J Morphol* **1976**, *150*, 279-297.

(208) Galusha, J. W.; Richey, L. R.; Gardner, J. S.; Cha, J. N.; Bartl, M. H., "Discovery of a diamond-based photonic crystal structure in beetle scales"; *Physical Review E* **2008**, *77*, -.

(209) Welch, V.; Lousse, V.; Deparis, O.; Parker, A.; Vigneron, J. P., "Orange reflection from a three-dimensional photonic crystal in the scales of the weevil Pachyrrhynchus congestus pavonius (Curculionidae)"; *Physical Review E* **2007**, *75*, -.

(210) Parker, A. R.; Welch, V. L.; Driver, D.; Martini, N., "Structural colour - Opal analogue discovered in a weevil"; *Nature* **2003**, *426*, 786-787.

(211) Edagawa, K.; Kanoko, S.; Notomi, M., "Photonic amorphous diamond structure with a 3D photonic band gap"; *Physical Review Letters* **2008**, *100*, -.

(212) Shawkey, M. D.; Saranathan, V.; Palsdottir, H.; Crum, J.; Ellisman, M. H.; Auer, M.; Prum, R. O., "Electron tomography, three-dimensional Fourier analysis and

colour prediction of a three-dimensional amorphous biophotonic nanostructure"; *J R Soc Interface* **2009**.

(213) Prum, R. O.; Torres, R.; Williamson, S.; Dyck, J., "Two-dimensional Fourier analysis of the spongy medullary keratin of structurally coloured feather barbs"; *Proc. R. Soc. Lond. Biol. Sci.* **1999**, *266*, 13-22.

(214) Prum, R. O., "Phylogenetic fourier analysis of the biophysics and evolution of avian structural colors"; *Integr. Comp. Biol.* **2002**, *42*, 1297-1298.

(215) Prum, R. O.; Torres, R. H., "A Fourier tool for the analysis of coherent light scattering by bio-optical nanostructures"; *Integr. Comp. Biol.* **2003**, *43*, 591-602.

(216) Chandrasekhar, S. *Liquid Crystals*; Cambridge University Press: Cambridge, 1977.

(217) Neville, A. C.; Caveney, S., "Sacarabaeid beetle exocuticle as optical analogue of cholesteric liquid crystals"; *Biological Reviews of the Cambridge Philosophical Society* **1969**, *44*, 531-&.

(218) Kinoshita, S.; Yoshioka, S.; Kawagoe, K., "Mechanisms of structural colour in the Morpho butterfly: cooperation of regularity and irregularity in an iridescent scale"; *P Roy Soc Lond B Bio* **2002**, *269*, 1417-1421.

(219) Sharma, V.; Crne, M.; Park, J. O.; Srinivasarao, M.; *Science* **2009**, under review.

(220) Jewell, S. A.; Vukusic, P.; Roberts, N. W., "Circularly polarized colour reflection from helicoidal structures in the beetle Plusiotis boucardi"; *New Journal of Physics* **2007**, *9*.

(221) Weber, M. F.; Stover, C. A.; Gilbert, L. R.; Nevitt, T. J.; Ouderkirk, A. J., "Giant Birefringent Optics in Multilayer Polymer Mirrors"; *Science* **2000**, *287*, 2451-2456.

(222) *Polymer-Based Mirror Outshines All Others*, http://www.sciencedaily.com/releases/2000/04/000404205617.htm, 2000. 24 March 2009

(223) Ibanescu, M.; Fink, Y.; Fan, S.; Thomas, E. L.; Joannopoulos, J. D., "An All-Dielectric Coaxial Waveguide"; *Science* **2000**, *289*, 415-419.

(224) Hart, S. D.; Maskaly, G. R.; Temelkuran, B.; Prideaux, P. H.; Joannopoulos, J. D.; Fink, Y., "External Reflection from Omnidirectional Dielectric Mirror Fibers"; *Science* **2002**, *296*, 510-513.

(225) Asano, M. Y., JP), Kuroda, Toshimasa (Osaka, JP), Shimizu, Susumu (Kanagawa, JP), Sakihara, Akio (Kanagawa, JP), Kumazawa, Kinya (Kanagawa, JP), Tabata, Hiroshi (Yokohama, JP); Nissan Motor Co., Ltd. (Yokohama, JP),Tanaka Kikinzoku Kogyo K.K. (Tokyo, JP),Teijin Limited (Osaka, JP): United States, 2001.

(226) Gauvreau, B.; Guo, N.; Schicker, K.; Stoeffler, K.; Boismenu, F.; Ajji, A.; Wingfield, R.; Dubois, C.; Skorobogatiy, M., "Color-changing and color-tunable photonic bandgap fiber textiles"; *Opt. Express* **2008**, *16*, 15677-15693.

(227) Potyrailo, R. A.; Ghiradella, H.; Vertiatchikh, A.; Dovidenko, K.; Cournoyer, J. R.; Olson, E., "Morpho butterfly wing scales demonstrate highly selective vapour response"; *Nat Photon* **2007**, *1*, 123-128.

(228) Huang; WangWang; Wang, Z. L., "Controlled Replication of Butterfly Wings for Achieving Tunable Photonic Properties"; *Nano Letters* **2006**, *6*, 2325-2331.

(229) Silver, J.; Withnall, R.; Ireland, T. G.; Fern, G. R.; Zhang, S., "Light-emitting nanocasts formed from bio-templates: FESEM and cathodoluminescent imaging studies of butterfly scale replicas"; *Nanotechnology* **2008**, 095302.

(230) Chen, Y.; Gu, J.; Zhu, S.; Fan, T.; Zhang, D.; Guo, Q., "Iridescent large-area ZrO[sub 2] photonic crystals using butterfly as templates"; *Applied Physics Letters* **2009**, *94*, 053901-3.

(231) Gratzel, M., "Photoelectrochemical cells"; *Nature* **2001**, *414*, 338-344.

(232) Watanabe, K.; Hoshino, T.; Kanda, K.; Haruyama, Y.; Kaito, T.; Matsui, S., "Optical measurement and fabrication from a Morpho-butterfly-scale quasistructure by focused ion beam chemical vapor deposition"; *Journal of Vacuum Science & Technology B: Microelectronics and Nanometer Structures* **2005**, *23*, 570-574.

(233) Saito, A.; Miyamura, Y.; Nakajima, M.; Ishikawa, Y.; Sogo, K.; Kuwahara, Y.; Hirai, Y.; 6 ed.; AVS: 2006; Vol. 24, p 3248-3251.

(234) Vukusic, P.; Stavenga, D. G., "Physical methods for investigating structural colours in biological systems"; *Journal of The Royal Society Interface* **2008**.

(235) Srinivasarao, M., "Nano-optics in the biological world: Beetles, butterflies, birds, and moths"; *Chemical Reviews* **1999**, *99*, 1935-1961.

(236) Ghiradella, H.; Aneshansley, D.; Eisner, T.; Silberglied, R. E.; Hinton, H. E., "Ultraviolet Reflection of a Male Butterfly: Interference Color Caused by Thin-Layer Elaboration of Wing Scales"; *Science* **1972**, *178*, 1214-1217.

(237) Kinoshita, S.; Yoshioka, S.; Miyazaki, J., "Physics of structural colors"; *Rep. Prog. Phys.* **2008**, *71*, 30.

(238) Vukusic, P.; Sambles, J. R.; Lawrence, C. R.; Wootton, R. J., "Quantified interference and diffraction in single Morpho butterfly scales"; *P Roy Soc Lond B Bio* **1999**, *266*, 1403-1411.

(239) Morehouse, N. I.; Vukusic, P.; Rutowski, R., "Pterin pigment granules are responsible for both broadband light scattering and wavelength selective absorption in the wing scales of pierid butterflies"; *Proceedings of the Royal Society B: Biological Sciences* **2007**, *274*, 359-366.

(240) Giraldo, M. A.; Yoshioka, S.; Stavenga, D. G., "Far field scattering pattern of differently structured butterfly scales"; *Journal of Comparative Physiology a-Neuroethology Sensory Neural and Behavioral Physiology* **2008**, *194*, 201-207.

(241) Nicodemus, F. E., "Directional Reflectance and Emissivity of an Opaque Surface"; *Appl. Opt.* **1965**, *4*, 767-773.

(242) Matusik, W.; Pfister, H.; Brand, M.; McMillan, L. In *Proceedings of the 14th Eurographics workshop on Rendering*; Eurographics Association: Leuven, Belgium, 2003.

(243) Lavin, E. P. *Specular reflection*; American Elsevier Pub. Co.: New York,, 1971.

(244) Vukusic, P.; Sambles, J. R.; Lawrence, C. R.; Wootton, R. J., "Limited-view iridescence in the butterfly Ancyluris meliboeus"; *Proceedings of the Royal Society B: Biological Sciences* **2002**, *269*, 7-14.

(245) Bloss, F. D. *The spindle stage : principles and practice*; Cambridge University Press: Cambridge ; New York, 1981.

(246) Berthier, S.; Charron, E.; Boulenguez, J., "Morphological structure and optical properties of the wings of Morphidae"; *Insect Science* **2006**, *13*, 145-158.

(247) Stavenga, D. G.; Leertouwer, H. L.; Pirih, P.; Wehling, M. F., "Imaging scatterometry of butterfly wing scales"; *Optics Express* **2009**, *17*, 193-202.

(248) Yoshioka, S.; Kinoshita, S., "Wavelength-selective and anisotropic light-diffusing scale on the wing of the Morpho butterfly"; *P Roy Soc Lond B Bio* **2004**, *271*, 581-587.

(249) Ghiradella, H., "Structure of Butterfly Scales - Patterning in an Insect Cuticle"; *Microsc Res Techniq* **1994**, *27*, 429-438.

(250) Kinoshita, S.; Yoshioka, S., "Structural colors in insects, particularly in morpho butterflies"; *Sen-I Gakkaishi* **2003**, *59*, P35-P39.

(251) Michael R. Weatherspoon, Y. C., Matija Crne, Mohan Srinivasarao, Kenneth H. Sandhage,, "3D Rutile Titania-Based Structures with <I>Morpho</I> Butterfly Wing Scale Morphologies13"; *Angewandte Chemie* **2008**, *120*, 8039-8041.

(252) Saito, A.; Miyamura, Y.; Nakajima, M.; Ishikawa, Y.; Sogo, K.; Kuwahara, Y.; Hirai, Y., "Reproduction of the Morpho blue by nanocasting lithography"; *Journal of Vacuum Science & Technology B* **2006**, *24*, 3248-3251.

(253) Born, M.; Wolf, E. *Principles of Optics*; 6th ed.; Pergamon Press: New York, 1980.

(254) Joannopoulos, J. D. *Photonic crystals : molding the flow of light*; 2nd ed.; Princeton University Press: Princeton, 2008.

(255) Sánchez, E.; López, T.; Gómez, R.; Bokhimi; Morales, A.; Novaro, O., "Synthesis and Characterization of Sol-Gel Pt/TiO2Catalyst"; *Journal of Solid State Chemistry* **1996**, *122*, 309-314.

(256) Ni, M.; Leung, M. K. H.; Leung, D. Y. C.; Sumathy, K., "A review and recent developments in photocatalytic water-splitting using TiO2 for hydrogen production"; *Renewable and Sustainable Energy Reviews* **2007**, *11*, 401-425.

(257) Schubert, U., "Chemical modification of titanium alkoxides for sol-gel processing"; *Journal of Materials Chemistry* **2005**, *15*, 3701-3715.

(258) Michael R. Weatherspoon, Matthew B. D., Guojie Wang, Ye Cai, Samuel Shian, Simon C. Jones, Seth R. Marder, Kenneth H. Sandhage,, "Thin, Conformal, and Continuous SnO_{<FONT SIZE='-1'>2</FONT>} Coatings on Three-Dimensional Biosilica Templates through Hydroxy-Group Amplification and Layer-By-Layer Alkoxide Deposition13"; *Angewandte Chemie International Edition* **2007**, *46*, 5724-5727.

(259) Martinu, L.; Poitras, D., "Plasma deposition of optical films and coatings: A review"; *Journal of Vacuum Science & Technology A: Vacuum, Surfaces, and Films* **2000**, *18*, 2619-2645.

(260) Heavens, O. S. *Optical properties of thin solid films*; Dover Publications: New York, 1991.

(261) Balachandran, U.; Eror, N. G., "Raman spectra of titanium dioxide"; *Journal of Solid State Chemistry* **1982**, *42*, 276-282.

(262) G. A. Tompsett, G. A. B., R. P. Cooney, J. B. Metson, K. A. Rodgers, J. M. Seakins,, "The Raman spectrum of brookite, TiO_2 (*Pbca, Z* = 8)"; *Journal of Raman Spectroscopy* **1995**, *26*, 57-62.

(263) Caveney, S., "Cuticle reflectivity and optical activity in scarab beetles - role of uric acid"; *Proceedings of the Royal Society of London Series B-Biological Sciences* **1971**, *178*, 205-&.

(264) Neville, A. C. *Biology of fibrous composites: Development beyond the cell membrane*; Cambridge University Press: Cambridge, 1993.

(265) de Gennes, P. G.; Prost, J. *The Physics of Liquid Crystals*; 2nd ed.; Oxford University Press, USA, 1995.

(266) Kleman, M.; Lavrentovich, O. D. *Soft matter physics: an introduction*; Springer-Verlag Inc.: New York, 2003.

(267) Bouligand, Y. In *Bifurcation Theory, Mechanics and Physics*; Bruter, C. P., Arangol, A., Lichenrowicz, A., Eds.; D. Riedel Publishing Company: Dordecht, 1983.

(268) Bertheier, S. *Iridescences: The Physical Color of Insects*; Springer, 2007.

(269) De Silva, L.; Hodgkinson, I.; Murray, P.; Wu, Q. H.; Arnold, M.; Leader, J.; McNaughton, A., "Natural and nanoengineered chiral reflectors: Structural color of manuka beetles and titania coatings"; *Electromagnetics* **2005**, *25*, 391-408.

(270) Lowrey, S.; De Silva, L.; Hodgkinson, I.; Leader, J., "Observation and modeling of polarized light from scarab beetles"; *Journal of the Optical Society of America a-Optics Image Science and Vision* **2007**, *24*, 2418-2425.

(271) Brink, D. J.; van der Berg, N. G.; Prinsloo, L. C.; Hodgkinson, I. J., "Unusual coloration in scarabaeid beetles"; *Journal of Physics D-Applied Physics* **2007**, *40*, 2189-2196.

(272) Wijnen, B.; Leertouwer, H. L.; Stavenga, D. G., "Colors and pterin pigmentation of pierid butterfly wings"; *Journal of Insect Physiology* **2007**, *53*, 1206-1217.

(273) Pace, A., "Cholesteric liquid crystal-like structure of cuticle of Plusiotic gloriosa"; *Science* **1972**, *176*, 678-&.

(274) Bouligand, Y., "Liquid crystals and biological morphogenesis: Ancient and new questions"; *Comptes Rendus Chimie* **2008**, *11*, 281-296.

(275) Meister, R.; Halle, M. A.; Dumoulin, H.; Pieranski, P., "Structure of the cholesteric focal conic domains at the free surface"; *Physical Review E* **1996**, *54*, 3771-3782.

(276) Berreman, D. W.; Meiboom, S.; Zasadzinski, J. A.; Sammon, M. J., "Theory and simulation of freeze fracture in cholesteric liquid crystals"; *Physical Review Letters* **1986**, *57*, 1737-1740.

(277) Broer, D. J.; Lub, J.; Mol, G. N., "Wide band reflective polarizers from cholesteric polymer networks with a pitch gradient"; *Nature* **1995**, *378*, 467-469.

(278) Ohring, M. *The Materials Science of Thin Films*; Academic Press: San Diego, 1992.

(279) Scharf, T. *Polarized light in liquid crystals and polymers*; John Wiley & Sons, Inc: Hoboken, NJ, 2007.

(280) Fowles, G. R. *Introduction to Modern Optics*; 2nd ed.; Dover Publications, Inc: New York, 1989.

(281) Z. Wu, J. W., A. Nolte, L. Zhai, R. E. Cohen, M. F. Rubner,, "Deformable Antireflection Coatings from Polymer and Nanoparticle Multilayers"; *Advanced Materials* **2006**, *18*, 2699-2702.

(282) King, J. S.; Graugnard, E.; Summers, C. J., "Photoluminescence modification by high-order photonic bands in TiO[sub 2]/ZnS:Mn multilayer inverse opals"; *Applied Physics Letters* **2006**, *88*, 081109.

(283) Srinivasarao, M.; Collings, D.; Philips, A.; Patel, S., "Three-dimensionally ordered array of air bubbles in a polymer film"; *Science* **2001**, *292*, 79-83.

(284) Wyszecki, G.; Stiles, W. S. *Color science: concepts and methods, quantitative data and formulas*; Wiley: New York,, 1967.

(285) Kuehni, R. G.; Schwarz, A.; Oxford University Press: Oxford ; New York, 2008, p xi, 391 p.

(286) Hoffmann, G. *ColorCalc PostScript Code*, http://www.fho-emden.de/~hoffmann/colcalc03022006.txt. December 8th 2008

(287) Wyszecki, G.; Stiles, W. S. *Color Science: Concepts and Methods, Quantitative Data and Formulae*; 2nd ed.; John Wiley: New York, 1982.

(288) Markku Leskelä, M. R., "Atomic Layer Deposition Chemistry: Recent Developments and Future Challenges13"; *Angewandte Chemie International Edition* **2003**, *42*, 5548-5554.

(289) Song, L.; Bly, R. K.; Wilson, J. N.; Bakbak, S.; Park, J. O.; Srinivasarao, M.; Bunz, U. H. F., "Facile microstructuring of organic semiconducting polymers by the

breath figure method: Hexagonally ordered bubble arrays in rigid-rod polymers"; *Advanced Materials* **2004**, *16*, 115-+.

(290) Erdogan, B.; Song, L. L.; Wilson, J. N.; Park, J. O.; Srinivasarao, M.; Bunz, U. H. F., "Permanent bubble arrays from a cross-linked poly(para-phenyleneethynylene): Picoliter holes without microfabrication"; *Journal of the American Chemical Society* **2004**, *126*, 3678-3679.

(291) Barrow, M. S.; Jones, R. L.; Park, J. O.; Wright, C. J.; Williams, P. R.; Srinivasarao, M., "Studies of the formation of microporous polymer films in "breath figure" condensation processes"; *Mod. Phys. Lett. B* **2008**, *22*, 1989-1996.

(292) Barrow, M. S.; Jones, R. L.; Park, J. O.; Srinivasarao, M.; Williams, P. R.; Wright, C. J., "Physical characterisation of microporous and nanoporous polymer films by atomic force microscopy, scanning electron microscopy and high speed video microphotography"; *Spectr.-Int. J.* **2004**, *18*, 577-585.

(293) Jaffer, A. *The FreeSnell Thin-Film Optical Simulator*, http://people.csail.mit.edu/jaffer/FreeSnell/, 2003. May 12th 2008

(294) Gaillot, D. P.; Graugnard, E.; Blair, J.; Summers, C. J., "Dispersion control in two-dimensional superlattice photonic crystal slab waveguides by atomic layer deposition"; *Applied Physics Letters* **2007**, *91*, 181123.

(295) Graugnard, E.; Gaillot, D. P.; Dunham, S. N.; Neff, C. W.; Yamashita, T.; Summers, C. J., "Photonic band tuning in two-dimensional photonic crystal slab waveguides by atomic layer deposition"; *Applied Physics Letters* **2006**, *89*, 181108.

(296) Coyle, S.; Prakash, G. V.; Baumberg, J. J.; Abdelsalem, M.; Bartlett, P. N., "Spherical micromirrors from templated self-assembly: Polarization rotation on the micron scale"; *Applied Physics Letters* **2003**, *83*, 767-769.